

# **Nanocomposites based on fluorescent carbogenic nanoparticles for biomedical applications**

**by**

**Joanna Daria Stachowska**



A thesis submitted in partial fulfilment for the requirements for the degree of  
Doctor of Philosophy at the University of Central Lancashire

**April 2021**

# STUDENT DECLARATION FORM



Type of Award

Doctor of Philosophy

School

School of Pharmacy and Biomedical Sciences

**1. Concurrent registration for two or more academic awards**

\*I declare that while registered as a candidate for the research degree, I have not been a registered candidate or enrolled student for another award of the University or other academic or professional institution

**2. Material submitted for another award**

\*I declare that no material contained in the thesis has been used in any other submission for an academic award and is solely my own work

**3. Collaboration**

Where a candidate's research programme is part of a collaborative project, the thesis must indicate in addition clearly the candidate's individual contribution and the extent of the collaboration. Please state below:

N.A.

**4. Use of a Proof-reader**

\*No proof-reading service was used in the compilation of this thesis.

Signature of Candidate

*Joanna Stachowska*

Print name:

JOANNA DARIA STACHOWSKA

# ABSTRACT

Carbon dots (C-dots) constitute a new class of carbon-based nanomaterials that combine remarkable colloidal stability, easy-to-modify surface, strong fluorescence with heavy metal-free composition and environmentally benign nature. The dynamic presence of these nanoemitters in biomedical research is directly related to their great promise as highly sensitive optical sensors, surveillance probes, antimicrobial agents and traceable nanosystems for drug delivery. To this end, the current thesis highlights the applicability of three different types of C-dots based nanosystems within the biomedical field and provides novel insights into their exciting photo-optical and structural properties.

First, a large gallery of novel photoluminescent powders and suspensions was derived via pyrolytic treatment of citric acid and urea at 230°C. The use of either dialysis or filtration as a size separation strategy led to the generation of four distinct families comprising of sixteen fluorescent nanomaterials in which the emissive signal predominantly arises from C-dots with embedded fluorophores, a blend of molecular fluorophores, a mixture of C-dots with unbound molecular fluorophores as well as cyanuric acid-rich C-dots. Within each one of the CA/urea derived family, the chemical composition and optical properties can be systematically tuned by adjusting the molar ratio between the precursors. During synthesis, urea is consumed for the synthesis of molecular fluorophores and the build-up of carbogenic cores, while post-synthesis urea serves as the solid diluent matrix that suppress their self-quenching effect in a powder form. The combination of excellent fluorescent properties under a broad range of excitation wavelengths (QY $\approx$ 11-32%) together with the pH-responsive nature indicated that these nanoscopic emitters are ideal candidates for the cellular labelling and multicolour imaging applications.

Second, a large gallery of novel magnetic C-dots (C/Fe-NPs) was synthesized through a facile one-step thermal decomposition of iron (III) acetylacetonate in the presence of highly fluorescent C-dots precursor derived from CA/ethanolamine at 230°C. The systematic incorporation of iron into the C-dots matrix led to generation of nine

diverse C/Fe-NPs which optical and magnetic properties were modified in a controlled manner by adjusting the C/Fe ratios. The use of other materials (such as amines, polymers, polyetheramine) as the carbon-rich precursors resulted in an extended five series of C/Fe-NPs that all combine their magnetic nature with high levels of fluorescent emissions. Incorporation of gadolinium while following a modified synthetic approach further improved the magnetic properties of the C/Fe-NPs without compromising their fluorescent properties. Overall, the C/Fe-NPs with advanced magnetic, fluorescent and antimicrobial performance carry promise for magnetically-guided detection and labelling of cancer cells.

Third, a novel approach to synthesise yellow C-dots based nanopowders was developed in order to further fabricate a highly fluorescent chitosan/C-dots based nanocomposites. This pioneering approach relied on the oxidation of primarily blue CNP300 (derived via thermal decomposition of CA/ethanolamine mixture at 300°C) under harsh conditions and originated from the structural changes of molecular fluorophores. This simple experimental protocol allowed to separate a predominantly green fluorescent fraction (QY≈3-10%) without the use of sophisticated chromatography techniques. Furthermore, the conjugation of as-prepared C-dots with chitosan (CS/C-dots) at room temperature led to fabrication of polymeric nanocomposites that can accommodate a variety of therapeutic drugs and biologically important molecules. The drug release profile from the fluorescent CS/C-dots nanocarrier with antimicrobial finish constitute a promising feature for the development of traceable drug delivery nanosystems.

In conclusion, this research presents time and cost efficient strategies to generate different types of multifunctional C-dots and their polymeric nanocomposites with superior optical properties and versatile chemical composition. Significantly, the thesis provides further evidence that the environmentally benign C-dots can effectively supplant highly engineered fluorescent materials.



# TABLE OF CONTENTS

<b>ABSTRACT .....</b>	<b>2</b>
<b>TABLE OF CONTENTS.....</b>	<b>4</b>
<b>ACKNOWLEDGEMENTS .....</b>	<b>8</b>
<b>LIST OF FIGURES .....</b>	<b>10</b>
<b>LIST OF TABLES .....</b>	<b>26</b>
<b>ABBREVIATIONS .....</b>	<b>27</b>
<b>CHAPTER 1: Introduction.....</b>	<b>30</b>
1.1 General overview of nanomaterials.....	31
1.2 Carbon-based nanomaterials.....	33
1.2.1 Brief history .....	33
1.2.2 Synthesis methods .....	34
1.2.2.1 Top-down approach.....	35
1.2.2.2 Bottom-up strategy.....	37
1.2.3 Carbogenic nanoparticles.....	41
1.2.3.1 Classification .....	41
1.2.3.2 Photoluminescence mechanism.....	45
1.2.3.3 Rationale for research work .....	52
1.2.3.4 Limitations .....	54
1.2.4 Toxicity.....	55
1.3 Nanocomposites .....	57
1.4 Biomedical applications .....	59
1.4.1 Bioimaging .....	59
1.4.2 <i>In vivo</i> fluorescence imaging .....	60
1.4.3 Optical sensors .....	63
1.4.4 Antimicrobial agents .....	66
1.4.5 Drug delivery nanosystems .....	67

1.5 Study aims .....	68
1.6 References.....	70
<b>CHAPTER 2: Experimental section .....</b>	<b>77</b>
2.1 Materials .....	78
2.2 Synthesis protocols .....	78
2.2.1 Urea-based carbon dots .....	78
2.2.2 Magnetic C-dots .....	79
2.2.3 Hybrid magnetic nanoparticles .....	80
2.2.4 Carbogenic nanoparticles.....	81
2.2.5 Chitosan-carbon dots based nanocomposites .....	82
2.2.6 CS-CNP@Vancomycin drug delivery nanosystem .....	83
2.3 Characterization methods.....	84
2.3.1 X-Ray Photoelectron Spectroscopy (XPS).....	84
2.3.2 Fourier-transform Infrared Spectroscopy (FTIR) .....	84
2.3.3 Raman Spectroscopy .....	85
2.3.4 Nuclear Magnetic Resonance Spectroscopy (NMR).....	86
2.3.5 UV-Visible Spectroscopy (UV-VIS) .....	86
2.3.6 Fluorescence Spectroscopy (PL) .....	87
2.3.7 Fluorescence lifetime .....	88
2.3.8 Quantum yield measurements (QY).....	90
2.3.9 Elemental Analysis.....	91
2.3.10 Powder X-ray Diffraction (PXRD).....	92
2.3.11 Dynamic Light Scattering (DLS) .....	93
2.3.12 Fluorescence Microscopy .....	93
2.3.13 Scanning / Transmission Electron Microscopy (SEM, STEM, TEM) .....	94
2.3.14 Faraday force magnetometry.....	96
2.3.15 Mössbauer spectroscopy .....	98
2.3.16 Thermogravimetric Analysis (TGA).....	99
2.3.17 Bacterial culture techniques .....	99
2.3.17.1 <i>Escherichia coli</i> and <i>Staphylococcus aureus</i> bacterial strains .....	99

2.3.17.2 Sterilisation procedure .....	99
2.3.17.3 Culturing method .....	100
2.3.17.4 Antimicrobial testing.....	101
2.3.18 Mammalian cell culture techniques.....	102
2.3.18.1 HeLa cervix cancer cell line .....	102
2.3.18.2 Recovery of the cells from the cell bank .....	102
2.3.18.3 Subculturing / passaging of adherent cells.....	103
2.3.18.4 Cell counting using haemocytometer .....	103
2.3.18.5 Freezing down the cells .....	104
2.3.18.6 Cell viability determined by MTT assay .....	105
2.3.18.7 Bioimaging .....	106
2.3.19 Collaborators contribution .....	107
2.4 References.....	109
<b>Chapter 3: Novel photoactive carbon dots with dual optical properties for bioimaging and pH-sensing applications .....</b>	<b>112</b>
3.1 Introduction .....	113
3.2 Novelty and predominance over existing materials .....	114
3.3 Results and discussion.....	115
3.2.1 Characterization .....	116
3.2.2 Liquid-state fluorescent properties.....	125
3.2.3 Solid-state optical properties .....	134
3.2.4 Biological applications .....	136
3.2.5 Photoluminescent properties at various pH .....	138
3.2.5.1 Liquid-state solutions.....	139
3.2.5.2 Solid-state powders .....	142
3.3 Conclusion .....	144
3.4 References.....	146
<b>Chapter 4: Iron based carbogenic nanoparticles with exceptional optical, magnetic and antimicrobial properties.....</b>	<b>151</b>

4.1 Introduction .....	152
4.2 Novelty and predominance over existing materials .....	153
4.3 Results and discussion.....	154
4.3.1 Optimization of magnetic C-dots synthesis parameters.....	156
4.3.2 Systematic study of iron incorporation into carbogenic nanoparticles.....	163
4.3.3 Comparison of magnetic C-dots with other carbon-rich magnetic NPs .....	184
4.4 Conclusion .....	193
4.5 References.....	195
<b>CHAPTER 5: Fluorescent chitosan-carbon dots based nanocomposites as nanocarriers for drug delivery applications .....</b>	<b>201</b>
5.1 Introduction .....	202
5.2 Novelty and predominance over existing materials .....	203
5.3 Results and discussion.....	204
5.3.1 Carbon dots as a highly fluorescent nanotracers.....	204
5.3.2 Biocompatible nanocomposites based on chitosan and carbon dots .....	216
5.3.3 Fluorescent CS-CNPs nanocarrier for traceable drug delivery application....	225
5.4 Conclusion .....	229
5.5 References.....	231
<b>CHAPTER 6: General conclusion and future work.....</b>	<b>237</b>
6.1 General conclusion.....	238
6.2 Future work.....	241
<b>CHAPTER 7: Appendices .....</b>	<b>242</b>

## ACKNOWLEDGEMENTS

Firstly, I would like to thank Dr Marta Krysmann for giving me an opportunity to undertake the PhD studies as well as initial help and plentiful advices while getting used to a new university, research field and life in the UK. Secondly, I am forever thankful to Dr Antonios Kelarakis for directing my research, giving me an opportunity to work in the cell culture laboratory, knowledgeable discussions about science all around the world as well as being always available for asking questions. Our long research meetings made me not only a better Chemist but also a more mature person and a better human being. Thus, for all your help and patience sincere thank you!

Additionally, I am sincerely grateful to Dr Claire Mellor for help and guidance in the cell culture laboratory as well as an emotional support in the most stressful last stage of the PhD studies. Furthermore, I would like to express my gratitude to Dr Monika Gamża for her help with magnetization measurements, many advices, enormous kindness and knowledgeable scientific conversations. Moreover, thank you Dr Monika Gamża for being absolutely the best role model for less experienced researchers! Furthermore, I would like to say words of appreciation to Dr Abdullah Isreb, Dr Anna Kirkham and Dr Jioji Tabudravu. Thank you for showing me what set of skills should have a great lecturer, all your help as well as interesting discussions about science. And last but not least, I would like to say words of gratitude to absolutely fantastic Technician's which were always willing to help me and answer all questions concerning to the laboratory equipment's. Thank you so much Tamar, Peter, Sameera, Tess, John, Daaren and Alex for being absolutely the best at your job.

I would like also to express my gratitude to many collaborators from other institutions that contributed to the physicochemical characterisation of presented in this thesis nanomaterials. Among them, I would like to acknowledge Professor Engin Burgaz from the Ondokuz Mayıs University (Turkey), Professor Stephen Yeates and Dr Joshua Moore from the University of Manchester (United Kingdom), Dr Diogo Fernandes from the Malvern Panalytical (United Kingdom), Dr Anna Sz wajca from the Adam Mickiewicz University (Poland) and MSc Elżbieta Gumieniczek-Chłopek, MEng Tomasz Strączek and Professor Czesław Kapusta from the AGH University of Science and Technology (Poland).

During my studies at UCLan I met some wonderful people, both inside and outside the laboratories. I would like to especially acknowledge Beatrice, Rober, Alice, Natasha, Sarah, Joshua, Karolina, Magda, TCee, NKechi, Anna, Zeinab, Mo, Dariya, Thelma, Zoya, Jean-Baptiste, Krzysztof, Cindy, Chahinez, Megan, Szymon, Oliver, Christopher, Ella, Mohammed, Charlie, Yang and Spyros. You helped me to keep balance between work and social life and made this journey unforgettable for what I am forever grateful.

And most importantly, I would like to especially thank my wonderful boyfriend for always making me laugh when I was upset or stressed as well as my beloved family and friends in Poland for all your encouraging words from the beginning till the end. I could have not done it without your unconditional love and emotional support! You all have always seen the best in me, thus I would like to dedicate this thesis to you and my unforgettable best friend Martusia [\*].

# LIST OF FIGURES

Figure 1.1 Scheme presenting a comparison of nanosized particles in contrast to larger-sized biological cells or materials (Adapted from Ref. 7). .....	32
Figure 1.2 The schematic illustration of different structures of carbon based nanomaterials in the order of their discovery (Adapted from Ref. 9).....	33
Figure 1.3 The molecular models of various $sp^2$ -hybridized carbon nanostructures with diversified dimensionalities: $C_{60}$ Buckminsterfullerene (a), graphitic onions or nester giant fullerenes (b), carbon nanotube (c), nanohorns or nanocones (d), nanotoroids (e), graphene (f), 3D-graphite crystal (g), Haeckelite surface (h), graphene nanoribbons (i), graphene clusters (j), helicoidal carbon nanotube (k), carbon chains (l), 3D Schwarzsche crystals (m), carbon nanofoams (n), 3D nanotube networks (o) and 2D nanoribbons network (p) (Adapted from Ref. 12). .....	34
Figure 1.4 The schematic illustration of top-down and bottom-up strategies leading to preparation of C-dots (Adapted from Ref. 15).....	35
Figure 1.5 TEM images presenting the transformation of MWCNTs into GQDs under oxidative treatment (Adapted from Ref. 21). .....	37
Figure 1.6 Schematic representation of the synthetic approach leading to preparation of fluorescent carbon dots from crude biomass (Adapted from Ref. 22). .....	37
Figure 1.7 Schematic illustration of CQDs fabrication from orange and lemon peel via carbonization procedure. The final CQDs can be used for cell labelling and as chemical sensors (Adapted from Ref. 26). .....	38
Figure 1.8 The scheme of the formation of polymeric C-dots from polyacrylamide solution via hydrothermal treatment (a) along with the TEM images of CPDs synthesized by 24h (b), 72h (c), 96h (d) (Adapted from Ref. [27]) and general illustration of the formation mechanism of CPDs (e) (Adapted from Ref. 28).....	39

Figure 1.9 The schematic illustration of the possible formation mechanism of N,S-CNPs with the use of L-cysteine as a carbon source (a) together with the high-resolution TEM images of N,S-CNPs with various crystallization degree (Adapted from Ref. 29). ....	40
Figure 1.10 The scheme of the microwave-assisted synthesis and purification steps of green-emissive and blue-emissive carbon dots derived from urea and citric acid (Adapted from Ref. 34). ....	41
Figure 1.11 The scheme presenting the surface-state engineering of C-dots with excitation-dependent or excitation-independent luminescent properties (a) and the PL spectra showing independent (b) or dependent (c) of $\lambda_{\text{ex}}$ positions of the emission peaks (Adapted from Ref. 40). ....	42
Figure 1.12 TEM image (a), XRD pattern (b), FTIR spectra (c), XPS survey (d), XPS C1s spectra (e), UV-Vis absorption spectra (ABS) and emission spectra (f) of aC-dots (Adapted from Ref. 43). ....	44
Figure 1.13 The data presenting the XPS survey spectrum (a), high-resolution XPS C1s spectra of CF (b) and gC-dots (c), Raman spectrum (d), FTIR spectra (e), XRD pattern (f), high-resolution TEM image of the edge of gC-dots (g) and schematic illustration of hexagonal graphene network with zigzag and armchair directions (h) (Adapted from Ref. 46). ....	45
Figure 1.14 The PL and absorption spectra, the size distribution and corresponding images under the UV light of blue, green, yellow and red emissive carbon dots (a-d) together with the schematic model for the tunable luminescence of C-dots with various oxidation degrees (e) (Adapted from Ref. 50). ....	46
Figure 1.15 The images of aqueous dispersions of N-doped C-dots under UV light showing the multicolour fluorescence (a), structure of multicolour C-dots (b) and schematic illustration of the proposed energy level and electron transition diagrams of multicolour C-dots (c) (Adapted from Ref. 51). ....	47
Figure 1.16 The scheme presenting values of the energy gap of $\pi - \pi^*$ transitions calculated based on density functional theory as a function of the number of fused	



aromatic rings with the inset structures of graphene molecules used for calculation (Adapted from Ref. 53). .....	48
Figure 1.17 Fluorescent microscopy images of gC-dots with an excitation wavelength of 360 nm (a), HRTEM images with different diameters (b-g), optical images of C-dots solutions illuminated under daylight (left) and UV light (right) (h), PL spectra with blue, green, yellow and red emission (i), the relationship between PL properties and the size of gC-dots (j) and the HOMO-LUMO gap dependence on the size of graphite fragments (k) (Adapted from Ref. 54). .....	49
Figure 1.18 Schematic illustration of the synthetic pathways leading to the formation of several molecular fluorophores during the bottom-up chemical synthesis of carbon dots (Adapted from Ref. 57). .....	50
Figure 1.19 The representation of typical absorption spectra (a,b) and PL spectra (c,d) corresponding to molecular fluorophores (Type I) and carbogenic nanoparticles (Type II) (Adapted from Ref. 58). .....	50
Figure 1.20 Schematic representation of the emission characteristics of different photoactive aromatic species produced through the pyrolytic treatment of CA and EA mixture (a) and hydrothermal treatment of CA and EN (b) which demonstrate the consumption of organic fluorophores (blue colours) during the synthesis step for the build-up of the carbogenic cores (black and red colours) (Adapted from Ref. 61 and Ref. 49). .....	52
Figure 1.21 The graphical representation of luminescence quenching schematics of amorphous and crystalline C-dots with varied content of $sp^2$ -hybridized carbon domains (Adapted from Ref. 62). .....	53
Figure 1.22 MTT assay results for <i>in vitro</i> cytotoxicity testing of various concentrations of nitrogen doped C-dots against HeLa cells after 24h (Adapted from Ref. 64). .....	56
Figure 1.23 The graphical illustration of switching phenomena of organic-inorganic nanocomposites induced by different stimuli (Adapted from Ref. 3). .....	58

Figure 1.24 Confocal fluorescence microscopy images of HeLa cells incubated with 200µg/mL of C-dots for 4 hours. The images were captured in the bright field as well as with the use of blue, green, red and merged channels. The cell nuclei were stained with DAPI dye as presented in blue channel (Adapted from Ref. 23). ....	60
Figure 1.25 Subcutaneous injection of C-Dots (images on the top) and C <sub>ZnS</sub> -Dots (images at the bottom) in the bright field (a), as-detected fluorescence (b,d) along with color-coded images (c,e) (Adapted from Ref. 84). ....	61
Figure 1.26 Intradermal injection of CZnS salt doped C-dots in the bright field (a), as-detected fluorescence (b) and color-coded images. The images inserted below represent the dissected axillary lymph node (LN) of the mouse (Adapted from Ref. 23). ....	61
Figure 1.27 Intravenous injection of C-dots in the bright field (a), as-detected fluorescence (b) and color-coded images (c). The dissected kidneys (a'-c') and liver (a''-c'') are in the same order and Bl represents bladder while Ur - urine (Adapted from Ref. 84). ....	62
Figure 1.28 <i>Ex vivo</i> imaging of C-dots biodistribution in harvested liver (1), spleen (2), lung (3), kidneys (4), muscle (5), intestine (6) and heart (7) after three injection routes: intravenous (top), subcutaneous (middle), intramuscular (bottom) (Adapted from Ref. 64). ....	63
Figure 1.29 PL spectra of carbon dots in PBS buffer with various pH values under $\lambda_{ex}$ = 380nm while inserted images show the colour change under UV light exposure (a), linear relationship between the PL intensity ratio and pH values (b), confocal fluorescence images of carbon dots incubated with HeLa cells in buffered solutions with nigericin at different pH (c) (Adapted from Ref. 85). ....	64
Figure 1.30 The fluorescence response of BCDs in the presence of various metal ions with concentration 100 mM (a) together with the fluorescence emission spectra of BCDs after addition of different concentrations of Fe <sup>3+</sup> and the linear calibration plot for F <sub>0</sub> /F versus different concentrations of Fe <sup>3+</sup> (b) (Adapted from Ref. 91). ....	65

Figure 1.31 The schematic illustration of the dual-emission fluorescent sensing of $\text{Cu}^{2+}$ ions based on CdSe/ZnS-Cdots hybrid nanosystem (Adapted from Ref. 93). .....	66
Figure 1.32 The schematic representation of the cell walls of Gram-positive and Gram-negative bacteria (Adapted from Ref. 101). .....	67
Figure 1.33 The design of multifunctional nanocarrier for targeted delivery applications (A) with possible routes of action (B), including inactivation of the cell surface receptors (a), intercellular release of therapeutic substance (b), controlled release of gene therapeutic materials (c) or intracellular decay of radioactive materials (d) (Adapted from Ref. 103). .....	68
Figure 2.1 Picture of the sample of C/Fe-NPs prior (A) and during (B) and after (C) finished purification procedure. ....	80
Figure 2.2 Pictures showing the transformation of a partially carbonized viscous dark orange material CAEA230 (A) to a black powder of CNP300 (B). ....	81
Figure 2.3 Photos of the samples suggesting the presence (A) and absence (B) of low molecular weight particles in the dialysis water. ....	82
Figure 2.4 The energy-level diagram representing the states involved in Raman spectra (Adapted from Ref. 4). ....	85
Figure 2.5 The schematic presentation of the Jablonski diagram (Adapted from Ref. 7) .....	87
Figure 2.6 The scheme presenting the possible fluorescence decays upon pulsed excitation while emitted fluorescence is measured in a time-resolved manner (Adapted from Ref. 7). ....	89
Figure 2.7 Schematic explanation of the Bragg's law conditions (Adapted from Ref. 3). ....	92
Figure 2.8 The schematic illustration of the fluorescence microscope (Adapted from Ref. 16). ....	94

Figure 2.9 Scheme of SEM (A), TEM (B) and STEM (C) imaging techniques (Adapted from Ref. 17). .....	95
Figure 2.10 The scheme presenting the principle of Faraday balance utilized for magnetic susceptibility measurements (Adapted from Ref. 19). .....	96
Figure 2.11 The representative shapes of $^{57}\text{Fe}$ Mössbauer spectra of iron-bearing materials (Adapted from Ref. 22). .....	98
Figure 2.12 The photos of a streak (A) and control (B) plates with the cultures of <i>Staphylococcus aureus</i> . .....	101
Figure 2.13 The photos of agar spread plates containing different concentrations of <i>S.aureus</i> cultures, prepared by ten-fold serial dilution ranging from $10^{-1}$ (A) up to $10^{-8}$ (H). .....	102
Figure 2.14 The photos of the cells under the optical microscope after reaching approximately 20% confluency (A), 50% confluency (B) and 95% confluency (C). .....	103
Figure 2.15 The schematic representation of the grid of a haemocytometer along with magnified a living cells (A) as well as a blue coloured dead cells (B) (Adapted from Ref. 31). .....	104
Figure 2.16 The photos of the immature cells adhered to the cover slip (A) and after 24 hours incubation at $37^{\circ}\text{C}$ (B). .....	106
Figure 3.1 Scheme presenting the synthetic and purification strategies leading to the formation of four distinct series of fluorescent suspensions and powders derived via pyrolytic treatment of CA/urea precursors mixture.....	116
Figure 3.2 STEM images of CU03D (A), CU25D (B), CU50D (C) and CU100D (D). .....	117
Figure 3.3 XRD patterns (A) and FTIR spectra (B) for CU03D, CU25D, CU50D and CU100D. ....	118
Figure 3.4 The $^1\text{H}$ -NMR (A) and $^{13}\text{C}$ -NMR (B) spectrum of CU50D and citrazinic acid. The d-DMSO solvent peaks are marked as a dashed black line. ....	118

Figure 3.5 The mechanism depicting the formation of CU-dots derived from CA/urea precursors mixture (Adapted from Ref. 43).....	119
Figure 3.6 The $^1\text{H}$ -NMR (A) and $^{13}\text{C}$ -NMR (B) spectrum of CU50D1 along with the side products which diffuse through the dialysis membrane. The d-DMSO solvent peaks are marked as a dashed black line. ....	121
Figure 3.7 FTIR spectra of CU50D1, CU50F1, CU50F and CU50D. ....	121
Figure 3.8 XRD patterns (A) and FTIR spectra (B) for CU03F, CU25F, CU50F and CU100F. ....	123
Figure 3.9 The $^1\text{H}$ -NMR (A) and $^{13}\text{C}$ -NMR (B) spectra of CU50F, biuret, urea and cyanuric acid (CYA). The d-DMSO solvent peaks are marked as a dashed black line...	124
Figure 3.10 STEM image of CU50F1 (A) together with the FTIR spectra (B) and photos of aqueous dispersions of pre-CU50F1 (C) and CU50F1 (D). ....	125
Figure 3.11 The $^{13}\text{C}$ -NMR spectrum (A) and the XRD patterns (B) of CU50F1 compared to CYA. The d-DMSO and $\text{D}_2\text{O}$ solvent peaks are marked as dashed and dotted black lines in $^{13}\text{C}$ -NMR spectrum.....	125
Figure 3.12 UV-Vis spectra (A) and photos under the UV light (B) of aqueous dispersions of CU03D, CU25D, CU50D and CU100D. The concentration of the solutions was equal to 0.1 mg/mL.....	126
Figure 3.13 Liquid-state photoluminescent spectra of aqueous dispersion of CU03D (A), CU25D (B), CU50D (C) and CU100D (D). The concentration of the solutions was equal to 0.1 mg/mL. ....	127
Figure 3.14 The plots demonstrating the integrated PL intensity of CU03D (A), CU25D (B), CU50D (C) and CU100D (D) materials dissolved in extra pure water as a function of optical absorbance. The results were collected at 365 nm, 425nm, 480nm and 510 nm excitation wavelengths. ....	128
Figure 3.15 Liquid-state PL lifetime decays of aqueous dispersions of CU03D (A), CU25D (B), CU50D (C) and CU100D (D) recorded at $\lambda_{\text{ex}} = 375$ nm. ....	128

Figure 3.16 Liquid-state fluorescence lifetime decays of aqueous dispersions of CU03D (A), CU25D (B), CU50D (C) and CU100D (D) at $\lambda_{\text{ex}} = 450$ nm. ....	129
Figure 3.17 The UV-Vis spectra (A), PL lifetime decays measured at $\lambda_{\text{ex}} = 375$ nm and $\lambda_{\text{ex}} = 450$ nm (B) and the PL spectra (C) of aqueous dispersions of CU50D1. The concentration of the solutions was equal to 0.01 mg/mL. ....	130
Figure 3.18 UV-Vis spectra of aqueous dispersions of F-series CU-dots (A) along with the photo revealing their blue luminescence after UV illumination (B). The concentration of the solution was equal to 0.1 mg/mL. ....	130
Figure 3.19 Liquid-state photoluminescent spectra of aqueous dispersion of CU03F (A), CU25F (B), CU50F (C) and CU100F (D) powders. The concentration of the solutions was equal to 0.1 mg/mL. ....	131
Figure 3.20 The plots demonstrating the integrated PL intensity of CU03F (A), CU25F (B), CU50F (C) and CU100F (D) samples dissolved in ultra-pure water as a function of optical absorbance. The results were collected at 365 nm, 425 nm, 480 nm and 510 nm excitation wavelength. ....	132
Figure 3.21 Liquid-state fluorescence lifetime decays of aqueous dispersions of CU03F (A), CU25F (B), CU50F (C) and CU100F (D) at $\lambda_{\text{ex}} = 375$ nm. ....	133
Figure 3.22 Liquid-state fluorescence lifetime decays of aqueous dispersions of CU03F (A), CU25F (B), CU50F (C) and CU100F (D) at $\lambda_{\text{ex}} = 450$ nm. ....	133
Figure 3.23 The PL spectra (A), plots of integrated PL intensity as a function of optical absorbance ( $\lambda_{\text{ex}} = 365, 425, 480$ and $510$ nm) (B) and PL lifetime decays recorded at $\lambda_{\text{ex}} = 375$ and $450$ nm (C) for aqueous dispersion of CU50F1. ....	134
Figure 3.24 Fluorescent microscopy images of CU100F powder on a glass slide illuminated by ultraviolet (A), blue (B) and green (C) excitation wavelength and the fluorescence emission spectra of CU03F (D), CU25F (E), CU50F (F) and CU100F (G) powders recorded at $\lambda_{\text{ex}} = 300-580$ nm. ....	135
Figure 3.25 Solid-state PL lifetime decays of CU25F, CU50F and CU100F recorded at $375$ nm (A-C) and $450$ nm (D-F). ....	136

Figure 3.26 The cell viability of human cancer cervix HeLa cell line calculated from MTT assay after their incubation with D-series (A) and F-series (B) of CU-dots for 24 hours. The data is expressed as mean $\pm$ SD of triple experiments while percentage of cytotoxicity is represented comparatively to untreated controls. ....	137
Figure 3.27 Fluorescent microscope images of HeLa cell line incubated with 50 $\mu$ g/mL of CU100D and CU100F nanoparticles presenting their multicolour emission at various excitation wavelengths. ....	137
Figure 3.28 pH dependence of the PL intensity of aqueous dispersions of CU50D (A) and CU50F (B) recorded at varied excitation wavelengths: 380 nm (blue circles), 420 nm (red triangles), 460 nm (green squares) and 500 nm (dark yellow pentagons). ....	139
Figure 3.29 Liquid-state fluorescence lifetime decays of aqueous dispersions of CU03D (A), CU25D (B), CU50D (C), CU100D (D) with neutral pH, pH=2 (orange colour) and pH=11 (cyan colour) at $\lambda_{\text{ex}}$ = 375 nm. ....	140
Figure 3.30 Liquid-state fluorescence lifetime decays of aqueous dispersions of CU03D (A), CU25D (B), CU50D (C), CU100D (D) with neutral pH, pH = 2 (orange colour) and pH = 11 (cyan colour) at $\lambda_{\text{ex}}$ = 450 nm ....	141
Figure 3.31 Liquid-state fluorescence lifetime decays of aqueous dispersions of CU03F (A), CU25F (B), CU50F (C), CU100F (D) with neutral pH, pH=2 (orange colour) and pH=11 (cyan colour) at $\lambda_{\text{ex}}$ = 375 nm. ....	141
Figure 3.32 Liquid-state fluorescence lifetime decays of aqueous dispersions of CU03F (A), CU25F (B), CU50F (C), CU100F (D) with neutral pH, pH=2 (orange colour) and pH=11 (cyan colour) at $\lambda_{\text{ex}}$ = 450 nm. ....	142
Figure 3.33 Solid-state PL spectra of CU25F (A-C), CU50F (D-F) and CU100F (G-I) nanopowders with pH $\approx$ 2 (left), neutral pH (middle) and pH $\approx$ 11 (right).....	143
Figure 3.34 Solid-state PL lifetime decays of CU25F, CU50F and CU100F nanopowders with various pH recorded at 375 nm (A-C) and 450 nm (D-F). ....	144
Figure 4.1 Scheme presenting the formation of PL-CAEA180 and CNP230 derived from the mixture of citric acid (CA) and ethanolamine (EA).....	154

Figure 4.2 Scheme presenting the formation and purification of magnetic C-dots via thermal treatment of Fe(acac) <sub>3</sub> and PL-CAEA180 precursors mixtures.....	155
Figure 4.3 Scheme presenting the controlled self-assembly of C-dots (B,C) on the surface of Fe-NPs (A).....	155
Figure 4.4 TGA curves of magnetic C-dots and synthesis precursors (A) together with their FTIR spectra depicting the purity of post-synthesized C/Fe-NPs (B). ....	156
Figure 4.5 The XRD patterns (A), EDS spectra (B) and photos of C/Fe-NPs (C) and bare C/Fe-NPs (D) with attached external magnets. ....	157
Figure 4.6 FTIR spectra of C/Fe-NPs, Fe-NPs, CNP230, PEG400 and Fe(acac) <sub>3</sub> (A) together with the photos of Fe-NPs (B) and C/Fe-NPs (C) with external magnet.....	158
Figure 4.7 Photos of C/Fe-NPs with external magnet synthesized by 30 minutes up to 5 hours (A-F) along with their XRD patterns (G). ....	158
Figure 4.8 Schematic mechanism presenting the formation of magnetic C-dots over a specific period of time (A) (Adapted and changed from Ref. 51) together with an illustration depicting the differences in their morphology and magnetic properties after 30 minutes or 3 hours of synthesis (B). ....	159
Figure 4.9 FTIR spectra (A) and TGA curves (B) of C/Fe-NPs synthesized from 30 minutes up to 5 hours. ....	160
Figure 4.10 PL spectra recorded at $\lambda_{\text{ex}} = 375$ nm for exemplary C/Fe-NPs synthesized by various time (A) along with the scheme presenting the thickness of the fluorophore outer layer at various synthesis stages (B). ....	161
Figure 4.11 Fluorescence lifetime decays of C/Fe-NPs 30 min and C/Fe-NPs 1-5h aqueous dispersions measured at $\lambda_{\text{ex}} = 375$ nm. ....	162
Figure 4.12 Fluorescence lifetime decays of C/Fe-NPs 30 min and C/Fe-NPs 1-5h aqueous solutions recorded at $\lambda_{\text{ex}} = 450$ nm. ....	163
Figure 4.13 TEM image (A), size histogram plotted on the basis of 150 fields (B) and the XRD pattern (C) of CNP230 (A,B - Adapted from Ref. 42).....	164



Figure 4.14 The UV-Vis spectra of aqueous dispersion of CNP230 (A) together with its photo under the UV lamp (B). The sample concentration was equal to 0.01 mg/mL.	164
Figure 4.15 The PL spectra (A) and fluorescence lifetime decays recorded at excitation wavelength 375 nm and 450 nm (B) of CNP230. The sample concentration was equal to 0.01 mg/mL.	165
Figure 4.16 TEM image (A) and size histogram plotted on the basis of 395 fields (B) of C/17Fe-NPs.	166
Figure 4.17 Photos of Fe-NPs (A) and C/Fe-NPs (B-I) with an external magnet together with the X-Ray diffraction patterns of all sample (J).	167
Figure 4.18 TGA curves of magnetic C-dots (A) along with the scheme illustrating the thermal induced shrinkage of outer carbon shell in C/17Fe-NPs (B).	168
Figure 4.19 Photos of C/31Fe-NPs with an external magnet in a close or far distance.	168
Figure 4.20 Magnetization results recorded at room temperature (296K) and at temperature around -200°C (70K) for selected C/Fe-NPs.	170
Figure 4.21 Normalized Mössbauer spectra of C/28Fe-NPs (A), C/31Fe-NPs (B), C/27Fe-NPs (C), C/17Fe-NPs (D) at room temperature and with an external 0.5T magnetic field.	171
Figure 4.22 FTIR spectra of magnetic C-dots with diversified iron content.	172
Figure 4.23 High-resolution C1s and Fe2p XPS spectra of C/31Fe-NPs (A-B) and C/23Fe-NPs (C-D).	173
Figure 4.24 The UV-Vis spectra of aqueous dispersions of C/Fe-NPs (A) together with the photos of C/31Fe-NPs, C/24Fe-NPs, C/17Fe-NPs under the daily (left) and ultraviolet (right) light (B).	174
Figure 4.25 PL spectra of aqueous solutions of iron oxide-based nanoparticles (A) and magnetic C-dots with varied iron content (B-I). The samples concentration was 0.01 mg/mL.	175

Figure 4.26 PL spectra of magnetic C-dots aqueous dispersions recorded for the maximum emission peak at $\lambda_{\text{ex}} = 375$ nm (A) and higher wavelength peak at $\lambda_{\text{ex}} = 450$ nm (B).	176
Figure 4.27 Time-resolved PL decay curves for aqueous dispersions of magnetic C-dots at $\lambda_{\text{ex}} = 375$ nm.	177
Figure 4.28 The range of average PL lifetimes of selected magnetic C-dots as a detection function at $435 \leq \lambda_{\text{em}} \leq 585$ nm. The relevant PL emission peaks were measured at $\lambda_{\text{ex}} = 375$ nm.	178
Figure 4.29 Time-resolved PL decay profiles for aqueous solutions of magnetic C-dots at $\lambda_{\text{ex}} = 450$ nm.	179
Figure 4.30 Plots showing the impact of Fe content on both magnetic (brown line) as well as fluorescent (blue line) properties of selected magnetic C-dots.	179
Figure 4.31 The MTT assay results for HeLa cells incubated with CNP230 (A) and Fe-NPs (C) for 24 h together with the fluorescence microscope images of HeLa cells with internalised CNP230 (B).	180
Figure 4.32 The MTT assay results presenting the in vitro cytotoxicity of magnetic C-dots against the HeLa cell line after incubation for 24h. The data is expressed as mean $\pm$ SD of triple experiments while percentage of cytotoxicity is represented comparatively to untreated controls.	181
Figure 4.33 Fluorescent microscope images of HeLa cells with internalized C/31Fe-NPs (A) and C/17Fe-NPs (B) showing their multicolour imaging capabilities at UV ( $\lambda_{\text{ex}} = 366$ nm), blue ( $\lambda_{\text{ex}} = 488$ nm) and green ( $\lambda_{\text{ex}} = 512$ nm) excitation wavelengths.	182
Figure 4.34 Plots showing the variations of the PL intensity recorded at $\lambda_{\text{ex}} = 365$ nm for C/31Fe-NPs (A) and C/17Fe-NPs (B) dispersions over 7 days. The concentration of the samples was equal to 0.1 mg/mL.	182
Figure 4.35 The plots representing an impact of selected metal ions in aqueous solutions of C/31Fe-NPs on the maximum PL intensity recorded at $\lambda_{\text{ex}} = 375$ nm (A) and $\lambda_{\text{ex}} = 450$ nm (B).	183

Figure 4.36 Photos of PEG@Fe-NPs (A), EA@Fe-NPs (B), EN@Fe-NPs (C), C/31Fe-NPs (D), PEA@Fe-NPs (E) and BPEI@Fe-NPs (F) along with their X-Ray diffraction patterns (G).....	185
Figure 4.37 FTIR spectra of amine (A) and polymer (B) functionalized magnetic nanoparticles.....	186
Figure 4.38 UV-Visible absorption spectra of aqueous dispersion of C@Fe-NPs. The concentration of the samples was equal to 0.1 mg/mL. ....	187
Figure 4.39 The PL spectra of aqueous dispersions of EA@Fe-NPs (A), EN@Fe-NPs (B), PEG@Fe-NPs (C), BPEI@Fe-NPs (D), PEA@Fe-NPs (E) and C/31Fe-NPs (F) with concentration of 0.01 mg/mL. ....	188
Figure 4.40 The PL lifetime decays of aqueous dispersions of C/Fe-NPs and C@Fe-NPs recorded at $\lambda_{ex}=375$ nm. ....	189
Figure 4.41 The PL lifetime decays of aqueous solutions of C/Fe-NPs and C@Fe-NPs recorded at $\lambda_{ex}=450$ nm. ....	189
Figure 4.42 The cumulative chart summarizing the liquid-state optical properties of various carbon-rich magnetic nanoparticles at $\lambda_{ex}=375$ nm (A) together with zeta potential values of their aqueous dispersions (B). ....	190
Figure 4.43 Scheme presenting the synthesis and purification strategies of Gd-doped magnetic C-dots via thermal treatment of Gd-DTPA or Gd(acac) <sub>3</sub> , Fe(acac) <sub>3</sub> and PL-CAEA180 precursors mixtures.....	191
Figure 4.44 Photos of Gd1@C/Fe-NPs (A-G) with an external magnet along with the X-Ray diffraction patterns of all sample (H). ....	191
Figure 4.45 Photos of Gd2@C/Fe-NPs (A-G) with an external magnet together with the X-Ray diffraction patterns of all sample (H).....	192
Figure 4.46 PL spectra of aqueous solution of Gd-DTPA (A) and Gd(acac) <sub>3</sub> (B) with concentration of 0.1 mg/mL. ....	192

Figure 4.47 PL spectra of Gd1@C/Fe-NPs (A) and Gd2@C/Fe-NPs (B) recorded for the maximum emission peak at $\lambda_{\text{ex}} = 375$ nm. The samples concentration was equal to 0.1 mg/mL. ....	193
Figure 5.1 The scheme presenting both the synthetic and purification routes that lead to fabrication of photoluminescent suspensions ( $\lambda_{\text{ex}}=365\text{nm}$ ) and powders derived from the pyrolytic treatment of CA/EA precursors mixture.....	205
Figure 5.2 The scheme showing the same synthesis and purification approaches applied for fluorophore-rich (CNP300) and biomass-derived (B-dots) photoluminescent suspensions and powders. ....	205
Figure 5.3 TEM images of CNP300 (A - Adapted from [43]) and B-dots (B - Adapted from Ref. 3). ....	206
Figure 5.4 FTIR spectra (A) and XRD patterns (B) of CNP300oxG (a), CNP300oxB (b) and CNP300non-ox (c) together with the photos of corresponding powders. ....	207
Figure 5.5 Liquid-state UV-Vis spectra (A,D,G), photos under UV illumination (B,E,H) and PL spectra(C,F,I) of 0.1 mg/mL aqueous dispersions of CNP300non-ox (A-C), CNP300oxB (D-F) and CNP300oxG (G-I).....	208
Figure 5.6 Fluorescence lifetime decay curves of 0.1 mg/mL aqueous dispersions of CNP300non-ox, CNP300oxB and CNP300oxG at $\lambda_{\text{ex}} = 375$ nm (A,B,C) and $\lambda_{\text{ex}} = 450$ nm (D,E,F). ....	209
Figure 5.7 The plots of integrated PL intensity of CNP300oxB (A) and CNP300oxG (B) as a function of optical absorbance at 365 nm, 425 nm, 480 nm and 510 nm with calculated quantum yield values.....	210
Figure 5.8 Fluorescent microscope images of HeLa cancer cell line incubated with 50 $\mu\text{g/mL}$ of CNP300oxG (A), CNP300oxB (B) and CNP300non-ox (C) under the bright field, UV, blue and green excitation wavelengths. ....	211
Figure 5.9 The solid-state PL spectra of CNP300oxB (A) and CNP300oxG (B) together with the PL lifetime decays of CNP300oxG recorded at $\lambda_{\text{ex}} = 375$ nm and $\lambda_{\text{ex}}=450$ nm (C). ....	212

Figure 5.10 XRD pattern (A) and FTIR spectra (B) of B-dots. ....	212
Figure 5.11 The UV-Vis spectra (A), photo under the UV illumination (B), PL spectra (C) and PL lifetime decays (D) of aqueous dispersion of B-dots with concentration of 0.1 mg/mL. The fluorescence microscopy images (E) showing the multicolour nature of B-dots after being internalized by HeLa cells. ....	214
Figure 5.12 The MTT assay results presenting the viability of HeLa cells incubated with various concentrations of CNP300non-ox (A), CNP300oxB (B), CNP300oxG (C) and B-dots (D) for 24 and 48 hours. The data is expressed as a mean $\pm$ SD of triple experiments while percentage of cell viability is represented comparatively to untreated controls. ....	215
Figure 5.13 Scheme presenting a coupling reaction between fluorescent carbon dots (A) and DCC reagent (B) followed by precipitation of DCU side product and generation CS-CNP nanocomposite (C). ....	217
Figure 5.14 FTIR spectra (A) and XRD patterns (B) of non-pure CS-CNP nanocomposite (dark yellow colour) containing a co-product dicyclohexylurea (green colour). ....	217
Figure 5.15 FTIR spectra (A), Raman spectra (B) and the liquid-state particles size distribution measured by DLS (C) for CS-CNP300oxB and CNP300oxB. ....	218
Figure 5.16 FTIR spectra of CS-CNP300oxG and its components (A) together with the XRD patterns (B) of CS-CNP300oxG (a), chitosan (b) and CS-CNP300oxB (c) along with the photos of their powders. ....	219
Figure 5.17 PL spectra (A,D), PL lifetime decays (B,E) and UV-Vis spectra (C,F) of CNP300oxB and CS-CNP300oxG. The concentration of aqueous dispersions was equal to 0.1 mg/mL. ....	221
Figure 5.18 The solid-state PL emission spectra of CS-CNP300oxB (A) and CS-CNP300oxG (B) together with the PL lifetime decays of CS-CNP300oxG recorded at $\lambda_{\text{ex}}$ = 375 nm and $\lambda_{\text{ex}}$ =450 nm (C). ....	222
Figure 5.19 The results from MTT assay showing the viability of HeLa cells incubated with various concentrations of CS-CNP300oxB (A) and CS-CNP300oxG (B) for 24 and 48	

hours. The data is presented as a mean $\pm$ SD of triple experiments and percentage of cell viability is relative to untreated control cells. ....	223
Figure 5.20 Fluorescence microscopy images representing the cellular uptake of 100 $\mu\text{g/mL}$ CS-CNP300oxG (left) and CS-CNP300oxB (right) by HeLa cells. ....	224
Figure 5.21 The comparison between the PL intensity of the maximum emission peaks (A) as well as the average PL lifetimes (B) of CS-CNP300oxB and CNP300oxB in various solvents. ....	224
Figure 5.22 FTIR spectra of CS-CNP@Van, vancomycin and CS-CNP300oxB.....	225
Figure 5.23 SEM images of CS-CNP300oxB (A) and CS-CNP@Van nanocarrier (B). ....	226
Figure 5.24 PL spectra (A) and PL lifetime decays (B) of 0.1 mg/mL aqueous dispersion of CS-CNP@Vancomycin recorded at various excitation wavelengths. ....	227
Figure 5.25 The cytotoxicity from MTT assay of HeLa cells incubated with CS-CNP@Van for 24 hours at various concentrations (A) together with fluorescence microscopy images of HeLa cells with internalized CS-CNP@Van (B) under the bright field and ultraviolet, blue and green $\lambda_{\text{ex}}$ . ....	228
Figure 5.26 The UV-Vis spectra of pure vancomycin (A) as well as CS-CNP@Van nanosystem (B).....	228
Figure 5.27 The photos showing the gelation behaviour of CS-CNP@Van at concentration of 9.5wt% (A), 16.5wt% (B) and 24.5wt% (C) together with the drug release profile of vancomycin antibiotic from CS-CNP@Van nanosystem (D).....	229

## LIST OF TABLES

Table 3.1 Deconvolution results for C1s, O1s and N1s spectra .....	120
Table 3.2 Composition and PL behaviour of D-, D1-, F- and F1-series.....	136
Table 3.3 The results from antimicrobial studies presenting the reduction in <i>E.coli</i> or <i>S.aureus</i> bacterial colonies incubated with D-series and F-series CU-dots for 24 hours at 37°C .....	138
Table 4.1 Elemental analysis results for magnetic C-dots synthesized at different time intervals.....	161
Table 4.2 Elemental analysis results for magnetic C-dots, Fe-NPs and CNP230 .....	165
Table 4.3 The results from antimicrobial studies presenting the number of colony forming units (CFU) for agar plates incubated with selected C/Fe-NPs and either <i>E.coli</i> or <i>S.aureus</i> for 24 hours at 37°C .....	184
Table 4.4 Elemental analysis results for various C@Fe-NPs and C/31-Fe-NPs.....	185
Table 5.1 The results from antimicrobial studies presenting the reduction of <i>E.coli</i> and <i>S.aureus</i> colonies incubated with various C-dots for 24 hours at 37°C.....	216

## ABBREVIATIONS

<b>NPs</b>	Nanoparticles
<b>NCs</b>	Nanocomposites
<b>CNPs / C-dots</b>	Carbogenic nanoparticles
<b>aC-dots</b>	Amorphous C-dots
<b>gC-dots</b>	Graphitic C-dots
<b>CU-dots</b>	Carbon dots prepared from citric acid/urea mixture
<b>CNP230</b>	Carbogenic nanoparticles after synthesis at 230°C
<b>CNP300non-ox</b>	Carbogenic nanoparticles after pyrolysis at 300°C
<b>CNP300oxB</b>	Oxidized CAEA300 with blue fluorescence in liquid-state
<b>CNP300oxG</b>	Oxidized CAEA300 with green fluorescence in liquid-state
<b>CS-CNP300ox</b>	Chitosan–carbogenic nanoparticles based nanocomposite
<b>Van</b>	Vancomycin
<b>CS-CNP@Van</b>	CS-CNP300oxB nanocarrier conjugated with vancomycin
<b>GQDs</b>	Graphene quantum dots
<b>SQDs</b>	Semiconductor quantum dots
<b>SWCNTs</b>	Single-wall carbon nanotubes
<b>MWCNTs</b>	Multi-walled carbon nanotubes
<b>CA</b>	Citric acid
<b>EA</b>	Ethanolamine
<b>CAEA180</b>	Precursor of CNPs after synthesis at 180°C
<b>EN</b>	Ethylenediamine
<b>BPEI</b>	Branched polyethyleneimine with $M_w \sim 800$ (g/mol)
<b>PEG<sub>400</sub></b>	Polyethylene glycol with $M_w=400$ (g/mol)
<b>PEA</b>	Polyetheramine Jeffamine® D-230
<b>EA@Fe-NPs</b>	Ethanolamine-derived Fe-NPs
<b>EN@Fe-NPs</b>	Ethylenediamine-derived Fe-NPs
<b>PEA@Fe-NPs</b>	Jeffamine® D-230-derived Fe-NPs



<b>PEG@Fe-NPs</b>	Polyethylene glycol-derived Fe-NPs
<b>BPEI@Fe-NPs</b>	Branched polyethyleneimine-derived Fe-NPs
<b>DPE</b>	Diphenyl ether
<b>DMAP</b>	4-(dimethylamino)pyridine
<b>DCC</b>	N,N'-dicyclohexylcarbodiimide
<b>DCU</b>	Dicyclohexylurea
<b>AA</b>	Acetic acid
<b>Fe-NPs</b>	Magnetite nanoparticles
<b>C/Fe-NPs</b>	Magnetic C-dots
<b>C@Fe-NPs</b>	Carbon-rich magnetic nanoparticles
<b>Gd1@C/Fe-NPs</b>	Gd-doped magnetic C-dots prepared from Gd-DTPA
<b>Gd2@C/Fe-NPs</b>	Gd-doped magnetic C-dots prepared from Gd(acac) <sub>3</sub>
<b>Fe(acac)<sub>3</sub></b>	Iron (III) acetylacetonate
<b>Gd-DTPA</b>	Gadopentetic acid
<b>Gd(acac)<sub>3</sub></b>	Gadolinium (III) acetylacetonate
<b>D-series</b>	CU-dots purified via extensive dialysis
<b>D1-series</b>	Collected run-off material from dialysis of CU-dots
<b>F-series</b>	CU-dots purified via extensive filtration
<b>preF1-series</b>	pre-oxidized CU-dots residue from the filtration step
<b>F1-series</b>	post-oxidized CU-dots residue from the filtration step
<b>MTT</b>	3-(4,5-dimethylthiazolyl-2)-2,5-diphenyltetrazolium bromide
<b>DMEM</b>	Dulbecco's Modified Eagle Medium
<b>FBS</b>	Fetal Bovine Serum
<b>MWCO</b>	Molecular weight cut-off
<b><i>E. coli</i></b>	<i>Escherichia coli</i>
<b><i>S. aureus</i></b>	<i>Staphylococcus aureus</i>
<b>f<sub>CA/urea</sub></b>	molar ratio of citric acid to urea
<b>CTA</b>	Citrazinic acid

<b>IPCA</b>	imidazo(1,2-a)pyridine-7-carboxylic acid, 1,2,3,5-tetrahydro-5-oxo-
<b>CYA</b>	Cyanuric acid
<b>HPPT</b>	4-hydroxy-1H-pyrrolo(3,4-c)pyridine-1,3,6(2H,5H)-trione
<b>d-DMSO</b>	deuterated dimethyl sulfoxide
<b>D<sub>2</sub>O</b>	deuterium oxide
<b>PL</b>	Photoluminescence
<b><math>\tau</math></b>	Lifetime component
<b><math>\tau_{avg}</math></b>	Average fluorescence lifetime
<b>IRF</b>	Instrument Response Factor
<b><math>\lambda_{ex}</math></b>	Excitation wavelength
<b><math>\lambda_{em}</math></b>	Emission wavelength
<b><math>\zeta</math></b>	Zeta potential
<b>M<sub>s</sub></b>	Magnetization saturation
<b>QY</b>	Quantum yield
<b>FTIR</b>	Fourier Transform Infrared Spectroscopy
<b>EDS</b>	Energy Dispersive X-Ray Spectroscopy
<b>XPS</b>	X-Ray Photoelectron Spectroscopy
<b>XRD</b>	X-Ray Powder Diffraction
<b>TEM</b>	Transmission Electron Microscopy
<b>SEM</b>	Scanning Electron Microscopy
<b>STEM</b>	Scanning-Transmission Electron Microscopy
<b>NMR</b>	Nuclear Magnetic Resonance
<b>VSM</b>	Vibrating sample magnetometer
<b>TGA</b>	Thermogravimetric analysis
<b>DLS</b>	Dynamic Light Scattering
<b>UV-Vis</b>	Ultraviolet- Visible
<b>TCSPC</b>	Time-correlated Single Photon Counting

# **CHAPTER 1:**

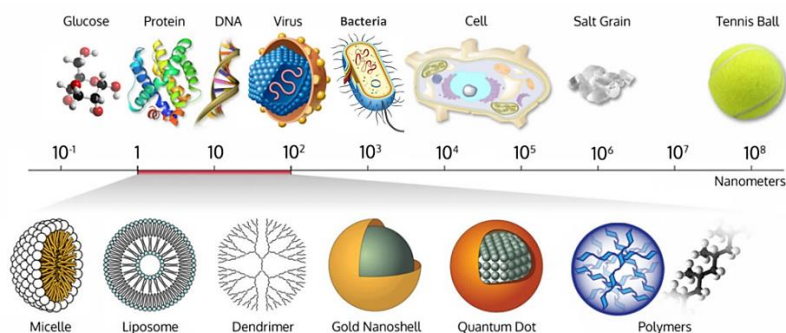
## **Introduction**

*“Nothing in life is to be feared, it is only to be understood. Now is the time to understand more, so that we may fear less”*

*Maria Skłodowska-Curie*

## 1.1 General overview of nanomaterials

Nanotechnology as a field of science focuses on engineering - design, synthesis, characterization and application - of novel nanomaterials that possess at least one dimension less in size than 100 nm [1]. Over the last decade, nanomaterials have attracted an enormous scientific attention due to their wide-spread applications in various fields, such as electronics, sensors, catalysis, microfluidic lateral flow devices, photonics, pharmaceuticals and medical diagnostics [2]. The development of nanomaterials with desired shape, size and structures can be controlled by the selection of appropriate synthesis method as well as through adjustment of parameters for manufacturing process. In regard to classification, nanomaterials can be categorized by their various dimensions, such as zero dimension (0D), one dimension (1D), two dimension (2D) as well as three dimension (3D). In detail, the 0D nanomaterials possess all dimensions at the nanoscale, while the 1D, 2D or 3D have one, two or three dimensions at the macroscale, accordingly [3]. More specifically, the dimensionality - 0D, 1D, 2D, 3D - is dependent on the electron movement along the dimensions in nanoscopic materials, while in 0D nanomaterials the electrons are entrapped in a dimensionless space, in 1D nanomaterials the electrons can move along x-axis that size is less than 100 nm while in 2D and 3D nanomaterials the electrons movement is taking place along the x,y-axis as well as x,y,z-axis, accordingly [4]. Nevertheless, among all a vast attention is attributed to zero dimensional nanoparticles (NPs) with three external nanoscale dimensions [5], which are classified as organic, inorganic or hybrid, depending on their intrinsic components. To that end, inorganic NPs are based on diversified inorganic components (i.e. metallic NPs), organic nanoparticles are composed of simple polymeric building blocks (i.e. carbon dots) while hybrid nanomaterials comprise engineered NPs (i.e. carbon-coated magnetic NPs) [6]. Importantly, NPs can easily penetrate through the bacterial and mammalian cells owing to their nanoscopic nature (**Figure 1.1**), thus hold an enormous potential to be used for diverse biomedical applications, such as fluorescent nanotracers for imaging of bacterial or cancer cells as well as efficient nanocarriers with outstanding loading capacity for the purpose of targeted drug delivery [6].



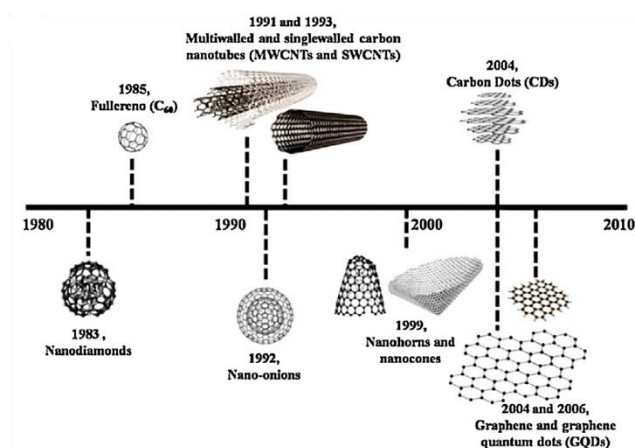
**Figure 1.1** Scheme presenting a comparison of nanosized particles in contrast to larger-sized biological cells or materials (Adapted from Ref. 7).

In contrast to bulk precursors, nanoparticles demonstrate novel and unique physicochemical properties owing to a high surface area to volume ratio, which means that the nanodomains possess a considerably higher surface area than the equivalent mass of the bulk material. In addition, at the nanoscale level the behaviour of matter can be dominated by quantum confinement effect, which impact on the electrical, magnetic and optical properties of nanomaterials. In detail, this behaviour corresponds to the movement of electrons that could either rotate or shift among particular energy levels of nanostructured materials, which by definition refer to materials containing the interconnected nanoscopic constituents within their structure [2, 5, 6]. For instance, in smaller iron oxide-based nanoparticles (size below 20nm) electrons rotate in the same directions while for the macroparticles (size above 20 nm) with the same composition the rotation of electrons take place in opposite directions. Thus, knowing that the total magnetic field strength of magnetic NPs constitute a sum of the magnetic fields of individual electrons, the alignment of the electrons in the same directions in nanoscopic domains significantly enhance their overall magnetic properties [6]. In summary, a common use of nanoparticles has been widely reported in a variety of customer products, including: cosmetics and sunscreens (titanium oxide NPs), beer bottles (clay NPs), bicycles (carbon NPs) as well as sheets and clothing (silver NPs) [6]. Therefore, the generation of novel types of nanoparticles with controlled structural, morphological and electronic properties is a key task to make an impact on the advancement of the science and everyday life in the future perspective.

## 1.2 Carbon-based nanomaterials

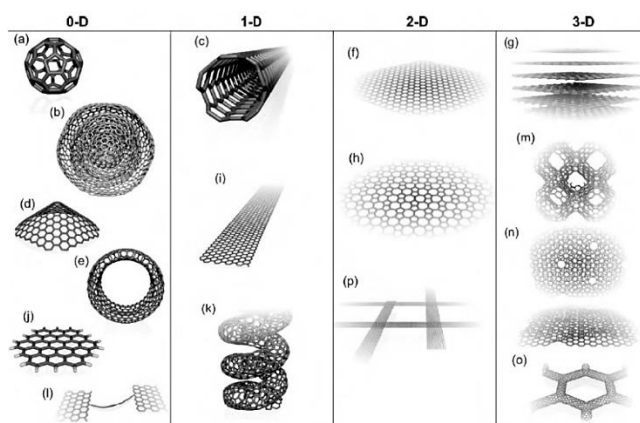
### 1.2.1 Brief history

The great interest of scientists about new physics and chemistry of nanocarbons has started from 1985 (**Figure 1.2**), when the group of Kroto et al. discovered a cage-like carbon molecule of  $C_{60}$  Buckminsterfullerene with 0.7 nm diameter (**Figure 1.3a**) [8].



**Figure 1.2** The schematic illustration of different structures of carbon based nanomaterials in the order of their discovery (Adapted from Ref. 9).

Soon after, in 1991 the study of carbon nanotubes began from a report delivered by Sumio Iijima, which confirmed that the structure of multi-walled carbon nanotubes (MWCNTs) was based on nested graphene tubules displaying fullerene-like caps (**Figure 1.3c**). The MWCNTs were produced via arc-discharge between graphite electrodes without metal catalysts and in inert atmosphere [10]. Additionally, in 1993 the group of Iijima et al. reported the synthesis of single-walled carbon nanotubes (SWCNTs) with the use of carbon arc and metal catalysts [11]. However, a few years later in 2000 other graphitic nanostructures were fabricated, such as nanohorns and nanocones (**Figure 1.3d**) or carbon rings (**Figure 1.3e**) [12]. More recently, in 2004 the graphene with a two-dimensional crystalline structure (**Figure 1.3f**) was isolated via the exfoliation of graphite. In the same year, a fluorescent carbon fraction was fortuitously isolated by Xu et al. during the purification of SWCNTs via electrophoretic method [13]. Later on, this fluorescent carbon material was named as carbon dots by Sun et al. in 2006 [14].



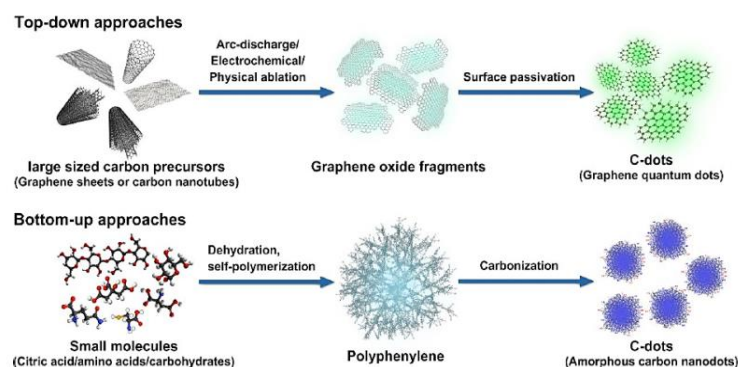
**Figure 1.3** The molecular models of various  $sp^2$ -hybridized carbon nanostructures with diversified dimensionalities:  $C_{60}$  Buckminsterfullerene (a), graphitic onions or nester giant fullerenes (b), carbon nanotube (c), nanohorns or nanocones (d), nanotoroids (e), graphene (f), 3D-graphite crystal (g), Haeckelite surface (h), graphene nanoribbons (i), graphene clusters (j), helicoidal carbon nanotube (k), carbon chains (l), 3D Schwarzite crystals (m), carbon nanofoams (n), 3D nanotube networks (o) and 2D nanoribbons network (p) (Adapted from Ref. 12).

To date, scientists still try to explore the potential of carbon-based nanomaterials and modify their intrinsic structure in accordance to desired further applications. Owing to the fact that carbon nanotubes and fullerenes are characterized by poor dispersibility in water as well as a weak fluorescence in the visible light region, the preparation carbon dots and graphene quantum dots become tempting for many researchers that work on development of fluorescent nanomaterials via facile methods for biomedical applications [15].

### 1.2.2 Synthesis methods

Since last decade, several methods have been used for preparation of carbon-based nanomaterials, which can be modified during synthesis step or post-treatment [15, 16]. In general, the synthetic methods can be classified into two main groups, namely top-down as well as bottom-up strategies (**Figure 1.4**). The top-down approaches involve the cutting of a large sized carbon precursors (e.g. graphene sheets, carbon nanotubes) into nano-sized graphene quantum dots through chemical or physical methods, while the bottom-up approaches are based on the polymerization and

carbonization of various small molecules (e.g. carbohydrates, amino acids, citric acid) into carbon dots via chemical reactions [15].



**Figure 1.4** The schematic illustration of top-down and bottom-up strategies leading to preparation of C-dots (Adapted from Ref. 15).

### 1.2.2.1 Top-down approach

In detail, the most popular top-down methods that are commonly used for the fabrication of carbon nanomaterials include: arc discharge, laser ablation as well as acidic oxidation [15].

#### Arc discharge

The preparation of carbon dots via arc discharge method was originated in 2004 by the group of Xu et al., which accidentally fabricated three types of carbogenic nanoparticles (CNPs) with various relative molecular mass while preparing SWCNTs [13]. The as-synthesized CNPs displayed a blue-green, yellow and orange fluorescence at 365nm, which was further supported by the presence of abundant –COOH groups on their surface [13, 15]. Overall, the carbon-based nanomaterials prepared by this method are characterized by good water dispersibility and have a large particles size distribution [15].

#### Laser Ablation

Laser ablation method utilizes a high-energy laser pulse to irradiate the pavement of carbon-rich material into a thermodynamic state, in which both high pressure and temperature are generated. The rapidly generated heat evaporates to a plasma state, the vapours crystallize and as a result the nanoparticles are being formed [15]. Carbogenic nanoparticles were synthesized for the first time via laser ablation method



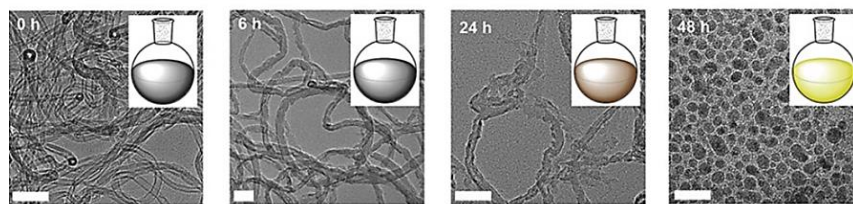
by the group of Sun et al. in 2006, while hot-pressing of cement and graphite powder mixture that was further ablated with Q-switched Nd:YAG laser (1064 nm, 10 Hz). The produced carbon nanoparticles exhibited no detectable fluorescence, even after their further heating in nitric acid solution (up to 2.6M) for 12 hours [14]. Overall, laser ablation method leads to effective generation of carbon nanodomains with good water solubility, narrow size distribution as well as fluorescence characteristics. Nevertheless, the significant drawbacks of this preparative method are the complicated procedure as well as limitation of a large scale synthesis of as-prepared CNPs [15].

#### Electrochemical method

Synthesis of carbon dots via electrochemical method exploits a redox reaction in the electrochemical cell, while the electric current is applied between two electrodes, separated from each other by the electrolyte solution [17]. In general, electrochemical synthesis provide an ease of tuning the particle size as well as their intrinsic luminescence properties under ambient temperature [15]. The first electrochemical synthesis of blue luminescent nanocrystals exfoliated from the MWCNTs was reported by Zhu et al. in 2007 [18]. They demonstrated the novelty of using this method for preparation of graphitic carbon dots from MWCNTs-based electrode [17-19]. In another report, Liu et al. described a facile electrochemical oxidation of graphite electrode in alkaline alcohols, which led to synthesis of CNPs for cellular imaging of the mice cells [20].

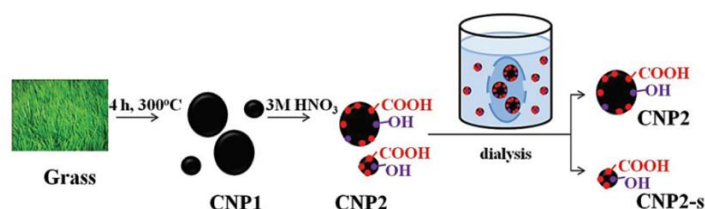
#### Acidic oxidation

The acid oxidation treatment have been commonly utilized to exfoliate and subsequently decompose bulk carbon into nano-sized particles while simultaneously introduce the hydrophilic groups (eg. -OH, -COOH) on the surface of carbon dots, which impact on the enhanced water solubility as well as fluorescence characteristics [15]. Exemplary, Qu et al. demonstrated the preparation of oxygen-rich graphene quantum dots (GQDs) from MWCNTs as a carbon precursor, which under the oxidative treatment with nitric acid were broken down into zero-dimensional oxygen-rich GQDs, as displayed in **Figure 1.5** [21].



**Figure 1.5** TEM images presenting the transformation of MWCNTs into GQDs under oxidative treatment (Adapted from Ref. 21).

In another report, Krysmann et al. utilized the nitric acid oxidative treatment to break down the post-synthesized carbonaceous material into smaller nanodomains, while enriching their surface with plentiful  $-\text{COOH}$  and  $-\text{OH}$  functional groups (**Figure 1.6**) [22].



**Figure 1.6** Schematic representation of the synthetic approach leading to preparation of fluorescent carbon dots from crude biomass (Adapted from Ref. 22).

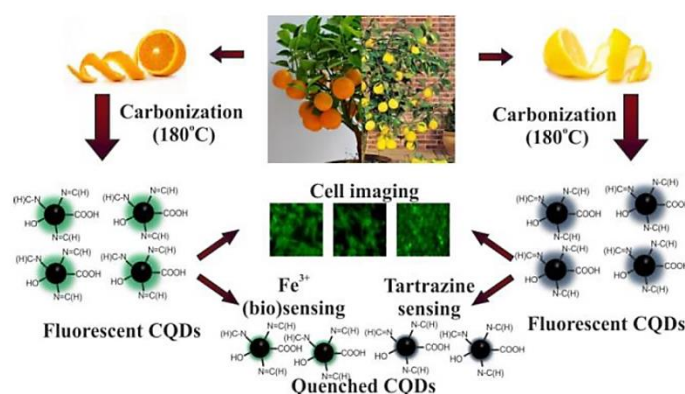
### 1.2.2.2 Bottom-up strategy

On the other side, the synthesis of CNPs via bottom-up approaches is based on the thermal decomposition method, microwave-assisted pyrolysis, hydrothermal and solvothermal synthesis as well as electrochemical method [15]. While comparing both strategies, bottom-up approach is cost-efficient, environmentally benign and can be easily scaled-up [15].

#### Thermal decomposition

Thermal decomposition synthesis is an effective and low cost method, which is commonly utilized to fabricate the carbon dots with controlled morphology and tunable optical properties. The surface chemical properties resulting from the C-dots formation and surface passivation processes can be precisely designed by selection of suitable passivating agents and carbon sources [23]. For the first time, thermal carbonization approach of suitable molecular precursors towards fluorescent C-dots was introduced by Bourlinos et al. in 2008 [24]. In this protocol, surface functionalized

carbogenic nanoparticles with sizes less than 10 nm were fabricated via one-step pyrolysis method, implying two different chemical routes for fabrication of either hydrophilic or hydrophobic NPs [24]. In another report, Wang et al. reported in 2015 the facile synthesis of various CNPs prepared through pyrolytic treatment of malic acid, glycolic acid or citric acid with N-rich urea precursor at 250°C for 1h. Then, the purified via dialysis carbon dots displayed a low cytotoxicity towards the human osteogenesis sarcoma cell line as well as a remarkable cell labelling capabilities [25]. In recent report, Chatzimitakos et al. synthesized carbon dots from fresh lemons and oranges peels after their pyrolytic treatment at 180°C for 2 hours (**Figure 1.7**). The proposed inexpensive carbonization treatment of the organic waste was in agreement with green chemistry aiming to reduce both the generation of toxic by-products as well as the use of organic solvents. In regard to biomedical applications, the low toxicity of as-prepared carbon dots as well as their abilities to complex Fe(III) highlighted their potential to be used as a probe for monitoring of Fe<sup>3+</sup> in living cells [26].

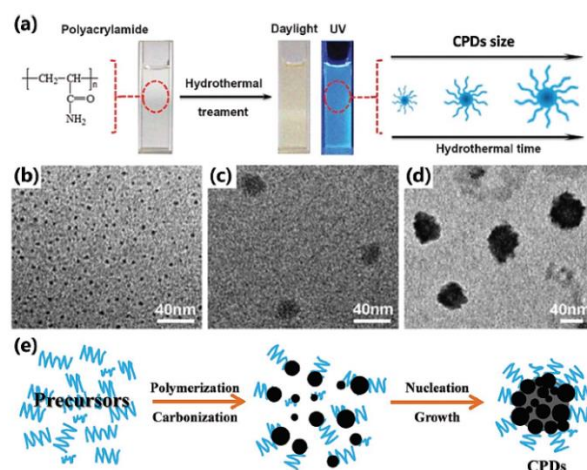


**Figure 1.7** Schematic illustration of CQDs fabrication from orange and lemon peel via carbonization procedure. The final CQDs can be used for cell labelling and as chemical sensors (Adapted from Ref. 26).

### Hydrothermal / Solvothermal synthesis

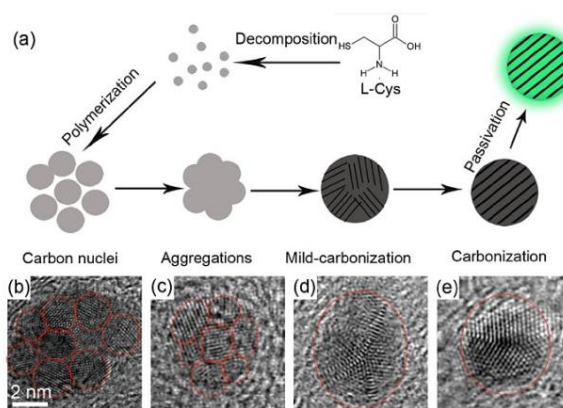
Typically for hydrothermal or solvothermal methods, polymers or small organic molecules are dissolved in water (hydrothermal method) or organic solvent (solvothermal method) and as-prepared precursors mixture is further transferred into a Teflon-lined stainless steel autoclave. Subsequently, the heating at high temperature of the precursors mixture leads to the generation of carbon seeding cores, which grow in a controllable manner into nanodomains with an approximate particle size of 10 nm

[15]. The facile synthesis of C-dots via hydrothermal treatment of polyacrylamide dispersion was reported by Gu et al. Besides generation of highly fluorescent polymeric carbon dots (CPDs), they observed a fast cellular endocytosis of these nanoemitters and proposed their utilization for rapid biolabeling and diagnosis of human prostate adenocarcinoma cells [27]. Regarding the reaction mechanism, it is believed that after nucleation step the polymer molecules present in the solution attach to the surface of nucleus, which dehydrates and carbonizes into graphitic-like carbon skeleton. In addition, longer reaction time enhance the formation of bigger clusters with enlarged sizes (**Figure 1.8b-d**), owing to the aggregation of several micronucleus formed in the initial reaction stage, which further grow and carbonize into CPDs with multiple subdomains (**Figure 1.8e**) [27, 28].



**Figure 1.8** The scheme of the formation of polymeric C-dots from polyacrylamide solution via hydrothermal treatment (a) along with the TEM images of CPDs synthesized by 24h (b), 72h (c), 96h (d) (Adapted from Ref. 27) and general illustration of the formation mechanism of CPDs (e) (Adapted from Ref. 28).

On the other hand, the group of Song et al. reported synthesis of N,S-CNPs via one-step hydrothermal route (100°C, 12 hours) from L-cysteine and  $\text{NH}_3\cdot\text{H}_2\text{O}$  mixture. They suggested that the formation of N,S-CNPs could be based on five stages, involving the decomposition, self-polymerization, aggregation, carbonization as well as surface passivation (**Figure 1.9a**). In addition, the suggested formation mechanism was further supported by high-resolution TEM results (**Figure 1.9b-e**), which displayed the formation of gradually impeccable lattice structures [29].



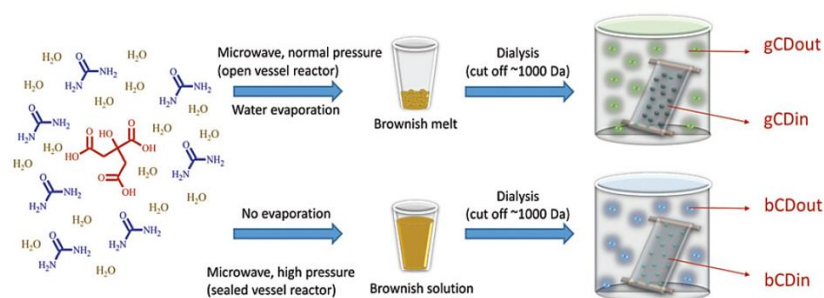
**Figure 1.9** The schematic illustration of the possible formation mechanism of N,S-CNPs with the use of L-cysteine as a carbon source (a) together with the high-resolution TEM images of N,S-CNPs with various crystallization degree (Adapted from Ref. 29).

In another report, Zhu et al. reported a facile synthesis of carbon dots with the highest QY up to 80% via hydrothermal treatment of citric acid and ethylenediamine precursors mixture. The significant high product yield under hydrothermal conditions implied its desirable application as biosensor for detection of  $\text{Fe}^{3+}$  ions in living cells [30]. In more recent reports, Sharma et al. noted a facile solvothermal synthesis of urea-based carbon dots from citric acid, urea and dimethylformamide, which reacted at 200°C for 12 h. The as-prepared carbon dots exhibited a spherical structure with the average size being in the range of 2-10 nm as well as presented a successful cell-labelling capabilities in human umbilical vein endothelial cells [31].

#### Microwave-assisted pyrolysis

The microwave pyrolysis approach has been well-established owing to faster synthesis procedure than regular thermal or hydrothermal methods, utilized for fabrication of carbon dots [15, 23]. The first synthesis of carbon dots via microwave pyrolysis was reported by Zhu et al. in 2009, who heated an aqueous solution of glucose and polyethylene glycol in 500W microwave oven for 5 or 10 minutes. With time, the solution changed colour from transparent to yellow and dark brown, which indicated the formation of C-dots with PL properties dependent on the duration of microwave heating. In addition, the authors noticed the poor luminescence properties of non-passivated carbon dots [32]. In another study conducted by Liu et al., carbon dots were

synthesized via single-step microwave-assisted method using diethylene glycol as the reaction medium and a sucrose as a carbon source [33]. The as-prepared within only one minute microwave irradiation carbon dots were characterized by green fluorescence upon 360 nm excitation and an average diameter of 5 nm. Moreover, the excellent dispersibility in water, low cytotoxicity and efficient uptake by C6 glioma cells implied their potential use for tumor cell labelling [33]. In more recent study, the group of Kasprzyk et al. prepared highly fluorescent C-dots from citric acid/urea mixture, while using a microwave oven operating at 300W (**Figure 1.10**). After dialysis step, the suspensions of the final products displayed either green or blue luminescence, which was dependent on the conditions of synthesis process that was carried out either in opened or sealed vessel reactor, respectively [34]. In general, the microwave-assisted carbonization is simple, rapid and environmentally friendly method that leads to an ease of commercialization of as-prepared carbogenic nanoparticles [23, 35].



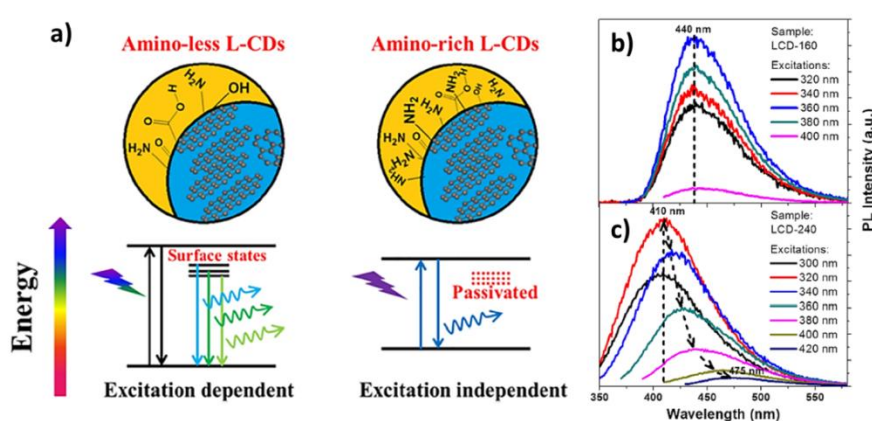
**Figure 1.10** The scheme of the microwave-assisted synthesis and purification steps of green-emissive and blue-emissive carbon dots derived from urea and citric acid (Adapted from Ref. 34).

## 1.2.3 Carbogenic nanoparticles

### 1.2.3.1 Classification

Carbon nanoparticles (C-dots) are a type of fluorescent carbon-based nanomaterials that are composed of  $sp^2/sp^3$  carbon and nitrogen/oxygen-based groups. According to the intrinsic structure, carbon dots can be categorized as graphene quantum dots (GQDs), crystalline carbon quantum dots or amorphous carbon nanodots (CNPs) [23, 36-38]. Although various terms relate to carbogenic nanoemitters in the literature, this thesis investigates the properties of C-dots with respect to the nature of their

carbogenic cores, that can be distinguished as highly graphitic (referred hereafter as gC-dots) or completely amorphous (referred hereafter as aC-dots) [39]. Besides obvious structural dissimilarities of gC-dots and aC-dots, both types share a common photoluminescence (PL) behaviour, defined as an ability of fluorescent nanomaterial to emit the light after the irradiation of its solution or powder with particular excitation energy. In detail, the luminescent properties of C-dots are dependent on the abundance of surface functional groups (i.e. C-O, C=O, O=C-OH), which can introduce trapping states with diversified energy levels and then allow carbogenic nanodomains emit the light that varies with excitation energy. Thus, the excitation dependence of photoluminescence phenomenon can be controlled by engineering the surface states in C-dots (**Figure 1.11a**). In detail, when the surface states are not fully passivated, the emission modes related to C=O, C-O and O=C-OH surface states with a series of specific energies dominate the PL spectra accordingly to the excitation energy, which impact on the excitation-dependent emission behaviour (**Figure 1.11a,c**). In contrast, after complete passivation, the emission is based on the radiative  $\pi$ - $\pi^*$  transition of  $sp^2$  carbon, which owing to a single transition mode with a certain energy impact on the excitation independence (**Figure 1.11a,b**). In general, especially nitrogen-rich organic precursors with short chains are commonly used as an effective candidate to achieve the controlled surface passivation, which further determine the character of C-dots photoluminescence phenomenon [40].

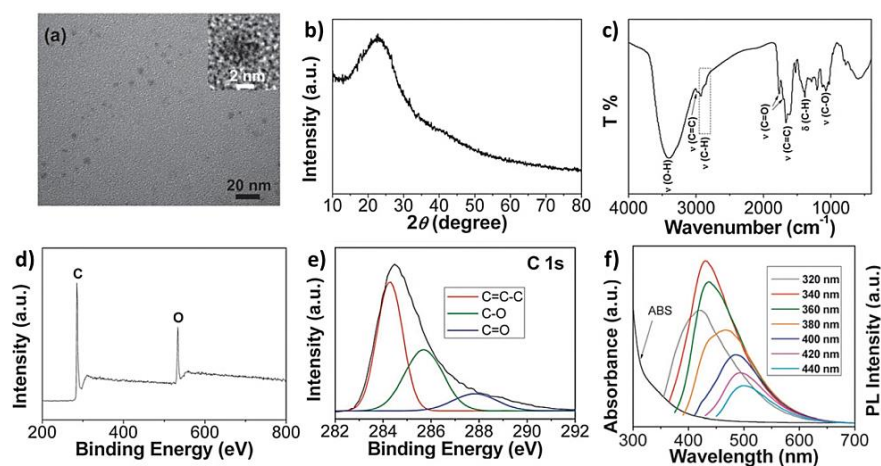


**Figure 1.11** The scheme presenting the surface-state engineering of C-dots with excitation-dependent or excitation-independent luminescent properties (a) and the PL spectra showing independent (b) or dependent (c) of  $\lambda_{\text{ex}}$  positions of the emission peaks (Adapted from Ref. 40).



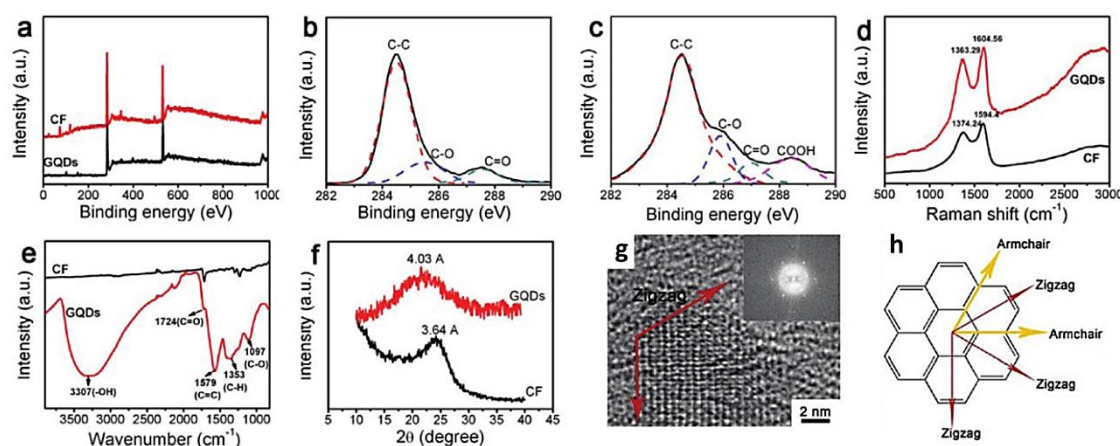
Besides multicolour luminescence properties and long-term resistance to photo bleaching, C-dots also possess a bio-friendly nature, negligible toxicity, easy-to-modify surface, electron donating and accepting capabilities, excellent colloidal stability as well as biocompatible nature that imply their compatibility with living tissues inside the body. Thus, the combination of all of these features facilitate the application of carbon dots in various biomedical applications, such as cancer therapy, biosensing, chemosensing, cellular imaging and drug delivery, or in energy conversion, solar cells, photocatalysis and the light emitting diodes (LEDs) [16, 36, 40, 41]. Importantly, the above mentioned intriguing properties make C-dots also superior to conventionally used luminescent inorganic semiconductor quantum dots (SQDs) or fluorescent organic dyes [16, 17, 36, 40, 42]. To expand the potential applications of C-dots in biomedical fields, these eco-friendly nanoemitters are usually modified with functional ligands or biomolecules (i.e. DNA, proteins, polymers, organic molecules) via physical mixing or chemical bonding that correspond to the electrostatic interactions or coupling reactions, respectively [36]. In regard to the characteristic intrinsic features of aC-dots reported in the literature, Zhou et al. notified a facile synthesis of carbon dots from a peach gum polysaccharide via hydrothermal method with diameter in the range of 1-5 nm (**Figure 1.12a**). The XRD pattern of as-prepared aC-dots displays only a single broad peak at  $2\theta = 23.1^\circ$  (**Figure 1.12b**) attributed to the amorphous carbon phase, while the FTIR spectra (**Figure 1.12c**) reveals the presence of several functional groups (i.e.  $-\text{OH}$ ,  $\text{C-H}$ ,  $\text{C=O}$ ,  $\text{C=C}$ ,  $\text{C-O}$ ) that impart their dispersibility in diversified solvents. The XPS survey demonstrates the  $\text{C1s}$  peak at 284.5eV and  $\text{O1s}$  peak at 531.8eV (**Figure 1.12d**), while further deconvolution of  $\text{C1s}$  spectra results in the recognition of  $\text{C=C-C}$ ,  $\text{C-O}$  and  $\text{C=O}$  surface functional groups (**Figure 1.12e**). In regard to optical properties, the UV-Vis absorption spectrum of aC-dots demonstrates a weak absorption bands at 340 nm assigned to aromatic  $\pi$  orbitals, while PL spectra confirmed their excitation-dependent emission behaviour (**Figure 1.12f**) [43].





**Figure 1.12** TEM image (a), XRD pattern (b), FTIR spectra (c), XPS survey (d), XPS C1s spectra (e), UV-Vis absorption spectra (ABS) and emission spectra (f) of aC-dots (Adapted from Ref. 43).

Besides aC-dots, a vast attention is attributed to gC-dots with graphitic cores that also possess a unique physicochemical properties (i.e. extensive surface area, good dispersibility in a number of solvents, high conductivity) [44, 45]. In reference to the literature, Peng et al. fabricated gC-dots via a facile one-step acidic treatment of carbon fibres (CF) [46]. The detailed physicochemical characterization of gC-dots revealed that the average size of each nanodomain was around 4 nm (**Figure 1.13g**), while the edge structure was predominantly parallel to the zigzag orientation (**Figure 1.13g,h**). The X-Ray Photoelectron Spectroscopy (XPS) patterns of gC-dots and carbon fibres demonstrates the C1s peak at 284.8eV and the O1s peak at 532eV, which after deconvolution proved the presence of C=C, C-O and C=O bonds (**Figure 1.13b**) together with the -COOH groups on the surface (**Figure 1.13c**). The collected Raman spectra are governed by two characteristic D and G peaks (**Figure 1.13d**) related to disordered and ordered  $sp^2$  carbon atoms, whereas the ratio of the relative intensity of the D band over G band ( $I_D/I_G=0.9$ ) implied a significant graphitization degree. In addition, the Fourier Transform Infrared (FTIR) spectra confirms the presence of -OH, C=O, C=C, C-H and C-O (**Figure 1.13e**), which were introduced during the oxidation process to the edges. The X-ray powder diffraction (XRD) pattern of gC-dots displays a broad (002) peak centered at around 21.5 degrees (**Figure 1.13f**) with broader interlayer spacing ( $d=0.403$  nm) than that of graphite, thus confirms the generation of plentiful oxygen-containing groups after the oxidation [46].



**Figure 1.13** The data presenting the XPS survey spectrum (a), high-resolution XPS C1s spectra of CF (b) and GQDs (c), Raman spectrum (d), FTIR spectra (e), XRD pattern (f), high-resolution TEM image of the edge of GQDs (g) and schematic illustration of hexagonal graphene network with zigzag and armchair directions (h) (Adapted from Ref. 46).

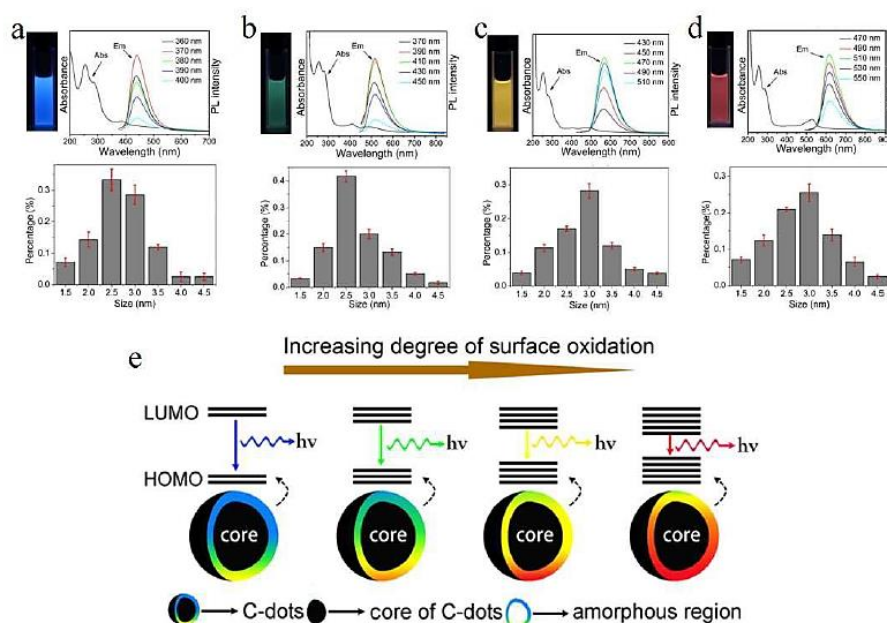
### 1.2.3.2 Photoluminescence mechanism

To date, the photoluminescence mechanism of carbon dots is still a subject of debate among researchers [21, 37, 47-49]. The synthesis of C-dots from different precursors and via various approaches usually leads to fabrication of additional components with complicated structures. In general, to date two mainstream of luminescence origin have been adopted: intrinsic state emission (i.e. quantum confinement effect, core states, electron-hole radiative recombination) as well as defective state emission. In detail, the defective state emission relates to the surface states (i.e. molecule state, edge state, defect state) as well as surface energy traps (i.e. emissive trap sites) [48]. Nevertheless, the majority of the literature reports refer to the molecular fluorescence, surface state as well as quantum confinement effects as a possible mechanisms of PL origin [21].

#### Surface state

Till now, surface state is the most widely accepted PL mechanism for C-dots emission that corresponds to the degree of surface oxidation as well as surface functional groups [21, 47]. Many studies confirmed that the higher degree of surface oxidation is related to the greater amount of surface defects. Then, these defects can trap excitons

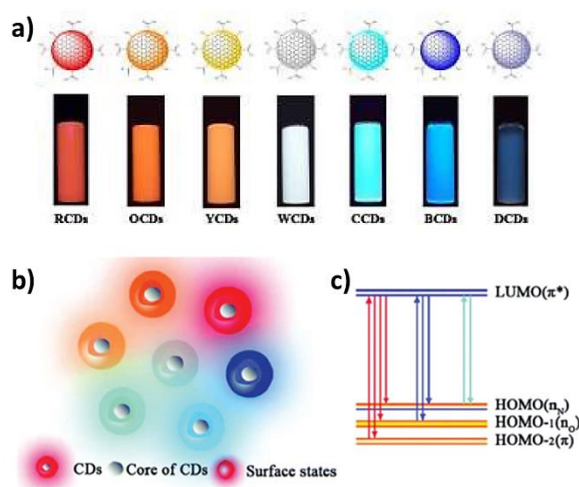
and the radiation from the recombination of trapped excitons impact on the red-shift of PL emission [21, 50]. To this point, Ding et al. reported the preparation of a series of purified carbon dots with excitation-independent luminescence, which varied from blue to red under the UV illumination, while using column chromatography as a separation strategy (**Figure 1.14a-d**). Owing to similar particle sizes with a broad size distribution (**Figure 1.14a-d**), they implied that the surface states were a dominant factor to control the variable PL behaviour of as-prepared C-dots. In addition, they stated that surface oxidation could produce defects that act as a capture centres for excitons and cause the surface-state related luminescence. On the other side, the band gap between the highest occupied molecular orbital (HOMO) and the lowest unoccupied molecular orbital (LUMO) strongly correspond to the incorporated oxygen species (**Figure 1.14e**). Thus, the reduction of the band gap along with the increment of oxygen content on C-dots pavement impact on the red-shifted emission, which originates from the increased degree of surface oxidation [50].



**Figure 1.14** The PL and absorption spectra, the size distribution and corresponding images under the UV light of blue, green, yellow and red emissive carbon dots (a-d) together with the schematic model for the tunable luminescence of C-dots with various oxidation degrees (e) (Adapted from Ref. 50).

In addition, some researchers correlate the surface states with the presence of surface functional groups (molecular states). It is believed that different functional groups on

C-dots pavement, such as C=N or C=O, may introduce various fluorophore molecules or energy levels in carbon dots [21]. For instance, the group of Zhang et al. reported the fabrication of multicolour N-doped carbon dots with tunable emission from dark blue to red or even white (Figure 1.15a,b). They noted that the PL behaviour of these nanoemitters was dependent on the surface functional groups instead of degree of oxidation, owing to the similar oxygen content in all materials. In regard to PL mechanism (Figure 1.15c), the electron transitions may take place between from the highest occupied molecular orbital (HOMO) to the  $\pi^*$  orbital of the lowest unoccupied molecular orbital (LUMO). However, the presence of abundant functional groups such as C=N or C=O can introduce two new energy levels (HOMO and HOMO-1) besides the characteristic HOMO-2( $\pi$ ) energy level, which leads to generation of new effective electron transitions from the HOMO and HOMO-1 energy levels to the LUMO( $\pi^*$ ). Thus, this phenomenon cause the shifting of emission towards longer wavelengths, while the electrons in N-related defect states return to the HOMO [51].

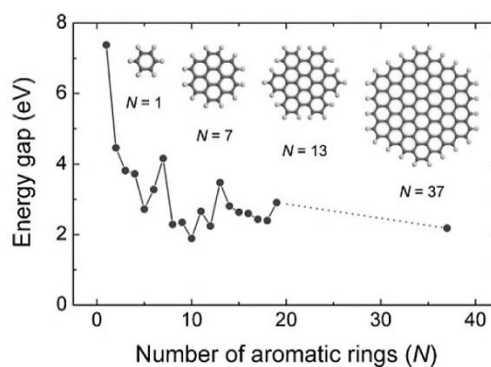


**Figure 1.15** The images of aqueous dispersions of N-doped C-dots under UV light showing the multicolour fluorescence (a), structure of multicolour C-dots (b) and schematic illustration of the proposed energy level and electron transition diagrams of multicolour C-dots (c) (Adapted from Ref. 51).

### Quantum confinement effect

The quantum confinement effect occurs when the size of quantum dots is smaller than their exciton Bohr radius [52]. In general, the bulk graphene displays an atomic layered sheet with  $sp^2$ -bonded carbon atoms and is considered as a two-dimensional crystal

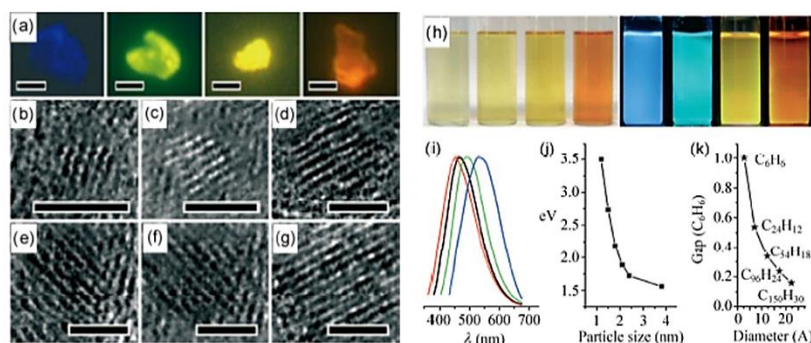
with a zero band gap. On the other side, graphene quantum dots as a zero-dimensional quantum confined system have a unique properties arising from both graphene as well as a light constituent elements [21]. Thus, the band gap of conjugated  $\pi$ -domains of the graphene quantum dots with an ideal graphitic core and a fewer surface functional groups is considered to be their true intrinsic photoluminescence centre [37, 52]. However, the density functional theory calculations demonstrated previously that the band gap gradually increase from ca. 3 eV in gC-dots composed of 20 aromatic rings up to 7 eV for benzene molecule (**Figure 1.16**) [53]. Therefore, the adjustment of the size of conjugated  $\pi$ -domains of gC-dots tune the PL behaviour, whereas blue-shift emission is observed for a smaller sizes of nanodomains [37].



**Figure 1.16** The scheme presenting values of the energy gap of  $\pi - \pi^*$  transitions calculated based on density functional theory as a function of the number of fused aromatic rings with the inset structures of graphene molecules used for calculation (Adapted from Ref. 53).

In addition, the quantum confinement effect of C-dots could be expressed as a dependence of their sizes on the light emission [37]. In regard to literature reports, Li et al. developed gC-dots with sizes in the range of 1.2 nm to 3.8 nm via electrochemical method. The examined by the fluorescence microscope PL properties of gC-dots (**Figure 1.17a**) varied sensitively along with the nanodomains size, resulting in the UV light emission for small domains (1.2 nm diameter) and near-infrared emission for larger domains (3.8 nm diameter) (**Figure 1.17b-j**). Additionally, in order to confirm that the strong emission of gC-dots arise from the quantum-sized fragments of graphite, the as-prepared carbon quantum dots were also treated with hydrogen plasma, to remove the oxygen species from the graphite structure. However, experiments showed no obvious change in the PL spectra of gC-dots before and after

utilization of this procedure. In addition, theoretical calculations further agreed that strong emission originates from the quantum-sized graphite fragments of gC-dots, owing to the gradual decrement of the HOMO-LUMO gaps along with increment of the size of graphene fragments (**Figure 1.17k**) [54].



**Figure 1.17** Fluorescent microscopy images of gC-dots with an excitation wavelength of 360 nm (a), HRTEM images with different diameters (b-g), optical images of C-dots solutions illuminated under daylight (left) and UV light (right) (h), PL spectra with blue, green, yellow and red emission (i), the relationship between PL properties and the size of gC-dots (j) and the HOMO-LUMO gap dependence on the size of graphite fragments (k) (Adapted from Ref. 54).

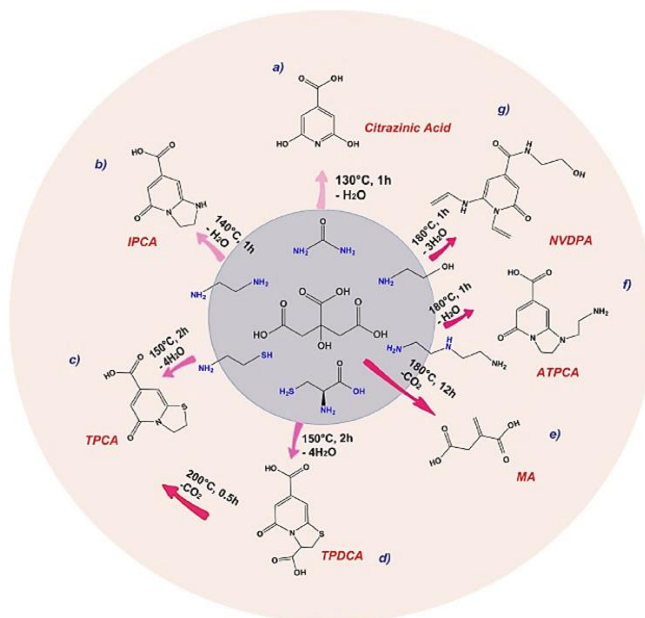
### **The synergistic effect of the surface state and the quantum confinement effect**

To date, some reports indicated the synergistic effect of the surface state and quantum confinement effect on the luminescence properties of carbon dots [21]. For instance, Bao et al. suggested that the PL of C-dots arise from surface state emission whereas the energy gap is controlled by both size as well as surface properties of carbon dots. The results demonstrated that the increase of the degree of surface oxidation or the particle size impact on the red-shift of C-dots emission wavelength due to the smaller energy gaps [55]. In other report delivered by Liu et al., a series of full colour emitting carbon dots were synthesized via one-pot hydrothermal method and purified through silica gel column chromatography. The results stated that the fluorescence properties of the crystalline core-shell C-dots could be finely modulated by changing the shell consisting of the surface functional moieties (surface trap states) as well as by tuning the size of the crystalline carbogenic core (quantum confinement effects) [56].

### **Molecular fluorescence**

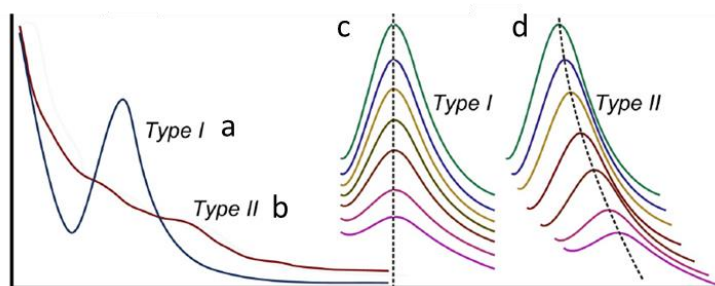


Recent studies demonstrated that the fabrication of additional fluorescent impurities during the bottom-up synthesis processes (i.e. molecular fluorescence) have a major contribution towards the overall emission of C-dots, as demonstrated in **Figure 1.18**. [21, 57].



**Figure 1.18** Schematic illustration of the synthetic pathways leading to the formation of several molecular fluorophores during the bottom-up chemical synthesis of carbon dots (Adapted from Ref. 57).

In general, the optical properties arising from carbogenic domains can be characterized by broad absorption spectra (**Figure 1.19b**) and the  $\lambda_{\text{ex}}$ -dependent PL behaviour (**Figure 1.19d**), while for the molecular fluorophores a well-pronounced absorption peak attributed to  $\pi$ - $\pi^*$  transitions (**Figure 1.19a**) and the  $\lambda_{\text{ex}}$ -independent PL emission (**Figure 1.19c**) are observed [58].

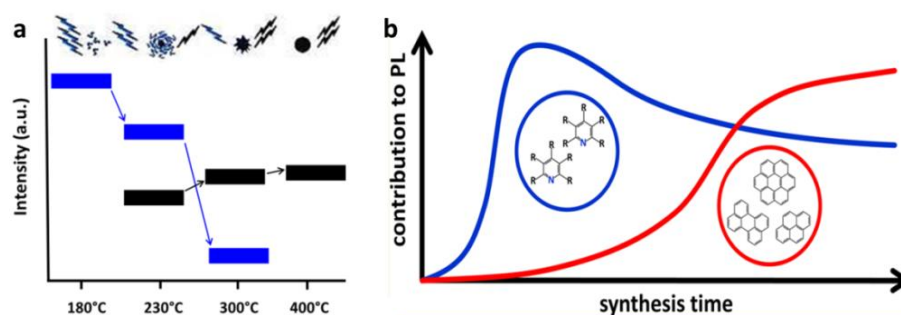


**Figure 1.19** The representation of typical absorption spectra (a,b) and PL spectra (c,d) corresponding to molecular fluorophores (Type I) and carbogenic nanoparticles (Type II) (Adapted from Ref. 58).

To date, the effect of an independent fluorophore on the luminescence properties of carbon dots has been carefully investigated [22, 57, 59, 60]. For instance, Song et al. noted that the high quantum yield fluorescence of carbon dots prepared via carbonization of citric acid and ethylenediamine corresponded to the presence of additional fluorescent molecule (imidazo(1,2-a)pyridine-7-carboxylic acid, 1,2,3,5-tetrahydro-5-oxo-, IPCA). Thus, they suggested that as-prepared C-dots were a mixture of IPCA, nanosized carbon cores and polymer clusters, whereas ICPA fluorophore had a significant contribution towards the molecular state PL and displayed a strong blue luminescence under the UV light, together with the excitation wavelength-independent PL behaviour [59]. In addition, Schneider et al. investigated the impact of the molecular fluorophores on the photoluminescent properties of citric acid-based carbon dots, derived from three different nitrogen-rich sources. The authors proved that besides carbon nanostructures all final materials were rich in molecular fluorophores, which molecules were attached to C-dots pavements instead of being free in the solution. In addition, the detail spectroscopic study revealed that these organic compounds were a fluorescent derivatives of citrazinic acid and their molecules were covalently attached to C-dots pavement [60]. Besides that, the group of Giannelis et al. suggested the formation mechanism of carbogenic nanoparticles derived from pyrolytic treatment of citric acid (CA) and ethanolamine (EA), which displayed a dual photoluminescence emission. In detail, they concluded that the pyrolysis of precursors mixture at 180°C generates the molecular precursor of C-dots with high quantum yield ( $\Phi \approx 50\%$ ) and strong PL properties, while the rise of temperature up to 230°C facilitate the formation of carbogenic cores along with the molecular fluorophores (**Figure 1.20a**). Nevertheless, the significant contribution of carbogenic domains towards the dual emission behaviour was observed for the products carbonized at temperature 300°C or above, for which the PL properties arise mainly from the carbogenic cores (**Figure 1.20a**) [61]. Furthermore, the similar examination related to the formation mechanism of internal carbon dots structure as well as their optical properties was conducted by Ehrat et al [49]. Thus, they concluded that during the hydrothermal treatment of citric acid and ethylenediamine (EN)



precursors mixture the carbon dots are formed within 30 minutes and their size maintain the same along with longer exposure to heat. On the other side, the prolonged synthesis time impact on the occurrence of the substantial changes in C-dots internal structure, which initially consist of the fluorescent molecules based on citrazinic acid while with time the aromatic domains appear with embedded molecular fluorophores (**Figure 1.20b**), which further aggregation impact significantly on the additional absorption as well as emission at longer wavelengths [49]. Therefore, the thermal synthesis of carbon dots from amine precursors at various time allow to adjust in a controlled manner the type and optical properties of the intrinsic emitters via a simple modification of the synthetic conditions [22, 49].

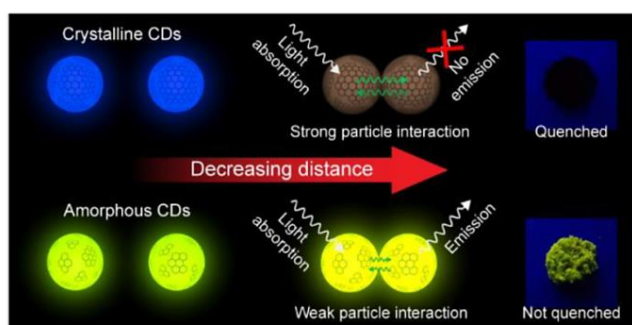


**Figure 1.20** Schematic representation of the emission characteristics of different photoactive aromatic species produced through the pyrolytic treatment of CA and EA mixture (a) and hydrothermal treatment of CA and EN (b) which demonstrate the consumption of organic fluorophores (blue colours) during the synthesis step for the build-up of the carbogenic cores (black and red colours) (Adapted from Ref. 61 and Ref. 49).

### 1.2.3.3 Rationale for research work

The motivation behind the work presented in this thesis was associated with exceptional properties of carbon dots as well as the current trends in development of novel environmentally benign nanosystems for demanding biomedical applications, such as cellular labelling and bioimaging, optical sensing and traceable drug delivery. In order to fulfil this goal, various novel strategies were used to fabricate a large galleries of CA/urea and CA/EA derived carbon dots, Fe/CAEA derived magnetic C-dots and chitosan/C-dots based nanocomposites. In brief, although many researchers reported the fabrication of carbon dots from binary CA/urea precursors mixture in either open

or closed reaction vessel, majority of the reports correspond to the physicochemical characterisation of their PL suspensions with either blue or green emission associated with the dominant content of CA and urea, respectively. Thus, this work demonstrates a novel strategy to generate a large gallery of PL suspensions and powders from the CA/urea precursors via facile synthesis in an open reaction vessel, whereas the use of different purification strategies, either filtration or dialysis, efficiently separated the blue and green emissive fractions from all materials. Besides that, the pioneering use of the filtration strategy together with an excessive amount of urea precursor allowed to generate C-dots based powders with strong luminescent properties in a solid-state form as well as novel types of C-dots based suspensions. In addition, the transformation of carbogenuous residue from the filtration step into another type of fluorescent C-dots proved the environmentally benign nature of presented approach, which is in line with current environmental trends and overcome more complex strategies for the synthesis of toxic semiconductor quantum dots. In similar, the modification of post-synthesis oxidative treatment for CA/EA derived C-dots allowed to generate another type of novel fluorescent nanopowder, which comprise of a smaller content of conjugated carbogenic nanodomains in aggregated powder form, as schematically demonstrated in **Figure 1.21** [62]. Thus, presented two pioneering strategies for development of a bright yellow C-dots nanopowders from either CA/urea or CA/EA precursors mixture open the doors for a large scale modification of fluorophore-rich C-dots nanopowders that may be expanded even in different range of applications (i.e. optical devices).



**Figure 1.21** The graphical representation of luminescence quenching schematics of amorphous and crystalline C-dots with varied content of  $sp^2$ -hybridized carbon domains (Adapted from Ref. 62).

In reference to the quenching effect, there is also a need to develop highly fluorescent hybrid NPs that can combine the multifunctional properties in a single platform for applications in biosensing, multimodal imaging or advanced theranostics. Although several types of magneto-fluorescent NPs have been developed, the significantly diminished optical features after conjugation of C-dots with Fe-NPs constitute a limitation for their efficient use in biomedical applications. Thus, in this work magnetic C-dots were derived from highly luminescent precursor of C-dots (PL-CAEA180), which in contrast to other magneto-fluorescent NPs have superior optical properties. In addition, the presented one-step and one-pot approach overcome tedious multistep synthetic procedures, while the strategies leading to enhancement of both fluorescent and magnetic properties through C-dots or gadolinium doping could be used as a guidelines for other researchers to optimise their synthetic protocols, accordingly to desired properties. It is important to mention that the literature lacks in the compressive and systematic guidelines for nanomaterials fabrication. At least, the generation of novel chitosan/C-dots based nanocomposites with antimicrobial finish contributes towards the current need to both combat the bacterial infections as well as to cure common diseases (e.g. cancer), thereby give a promise to be utilised in clinical settings for traceable drug delivery application.

#### **1.2.3.4 Limitations**

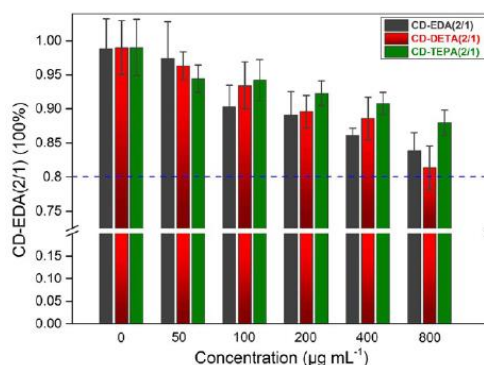
Besides superior optical properties, the preparation of C-dots holds some limitations. First, in order to fabricate nanoparticles with uniform properties, the batch-to-batch variations should be tested and the synthesis conditions should be kept the same each time. Second, the purification strategy that has a significant impact on the complete removal of fluorescent impurities as well as unreacted molecules should be design in a way to facilitate a large scale production of C-dots. Third, the synthesis of carbon dots from natural resources is limited to availability of specific biomass resources in particular regions of the world, thus complicate the reproducibility of the results. Fourth, the detailed stability studies should be undertaken with emphasis given to evaluation of their properties after long-term exposure to the UV light or pH variations, in order to estimate the extent of NPs aggregation in liquid dispersions over

a specific periods of time (e.g. 3-12 months). Fifth, the synthetic strategies should be optimised for desired application and comply with the rules of green chemistry, while limiting the environmental wastes, improving the yields at minimal costs and neglecting the use of harmful organic solvents. Sixth, the insufficient surface functionalisation of C-dots based nanosystems can facilitate both the agglomeration as well as the uptake by the reticuloendothelial system, thereby impact on the decrement of circulation half-life in the biological fluids. At least, the detailed studies related to testing the cytotoxicity, biodistribution and metabolism of C-dots based materials should be conducted prior their implementation for *in vivo* applications.

#### **1.2.4 Toxicity**

The toxicity of nanomaterials in living organisms can be assessed through *in vivo* or *in vitro* experiments [63]. After introducing nanoparticles into a living matter they could be metabolized via two major routes: in the kidneys into the urine as well as in the liver into a bile. The key factor to minimize the toxic effect of NPs is to optimize their synthesis protocols, thereby assure a complete removal from the body within a reasonable period of time [64]. In general, the toxicity studies against the cells (known as cytotoxicity) undertaken by several research groups proved that carbon-based nanomaterials possess a negligible toxicity against numerous cell lines as well as advantageous biocompatible elemental composition [23, 64-66]. In the recent studies, Janus et al. concluded that chitosan-based C-dots possess a non-toxic effect towards human dermal fibroblasts. After 48 hours of incubation period, the investigation of fibroblasts microphotographs confirmed their flattered and standard morphology without the occurrence of granules in the cytoplasm [65]. On the other side, Zhang et al. reported that after incubation of gC-dots (100µg/mL) with the stem cells, the cells viability reached above 80%. Thus, these results demonstrated both excellent low-cytotoxicity of gC-dots with bright yellow emission as well as their biocompatible nature for labelling of the steam cells [66]. In another study undertaken by Huang et al., the toxicity of nitrogen doped C-dots was evaluated after 24 hours with the use of HeLa cell line and colorimetric MTT assay. The results indicated a low cytotoxicity of N-

rich carbon nanoemitters with concentrations up to 800  $\mu\text{g/mL}$  and overall cell viability above 80% (**Figure 1.22**) [64].



**Figure 1.22** MTT assay results for *in vitro* cytotoxicity testing of various concentrations of nitrogen doped C-dots against HeLa cells after 24h (Adapted from Ref. 64).

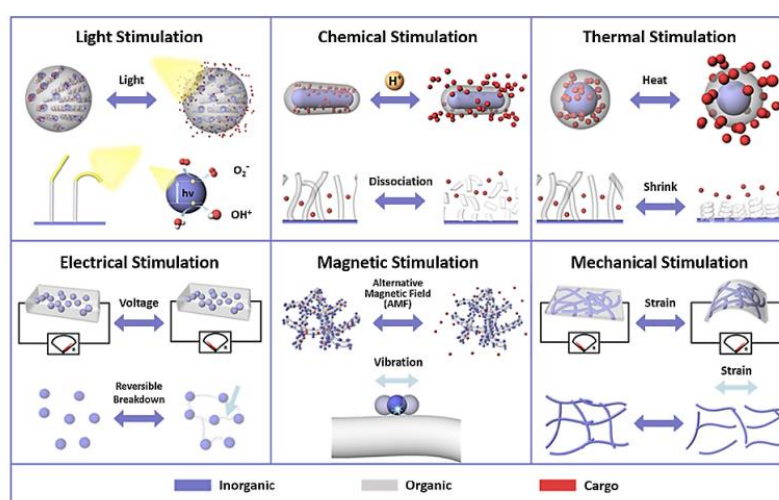
In addition, the group of Wang et al. reported that the cytotoxicity of carbon dots depend on the selection of various surface passivation molecules. Their results proved that PEGylated C-dots in all available configurations have a non-toxic nature up to concentrations higher than acquired for optical cellular imaging as well as closely related biomedical applications [67]. In another study, Chandraet et al. investigated the hemolysis rate with the use of C-dots and healthy human blood cells. This research confirmed some toxic effect of C-dots enriched with  $-\text{COOH}$  surface groups as well as reduced cytotoxicity of carbon dots linked with various organic molecules via amide bonds [68]. In addition, several studies have been performed to also test the *in vivo* toxicity of nanomaterials with the use of mice as a test subjects. The first systematic *in vivo* studies were conducted by Nurunnabi et al. and confirmed that after 12 hours post-injection, the GQDs were detected in the tumor site under the skin, while in the deep organs the fluorescence signal was detected after 24 hours. In contrast, the *ex vivo* imaging of extracted organs revealed the distribution of GQDs throughout the whole animal body within first 12 hours, whereas after 2 hours the highest accumulation of NPs was detected in the heart and liver plus after 12 hours in the kidneys. Generally, the results collected by Nurunnabi et al. confirmed the equal biodistribution of GQDs in the mouse body and implied their promising application for skin cancer detection [66]. In general, a relatively non-toxic nature of carbon-based

nanomaterials prove that there is an urgent need to further investigate the safety of novel C-dots based nanostructures, which hold an enormous potential to be applied as nanoprobes for cellular optical imaging [64, 66, 67].

### **1.3 Nanocomposites**

Nanocomposites (NCs) are solid materials composed of several phases, in which at least one of the phases demonstrate dimensions in the nanometre range [69, 70]. In regard to synthesis methods, the nanocomposite materials are mainly prepared via wet blending (random mixing of liquid with solid particles), thermal evaporation (vaporization of target material onto the sample), sol-gel process (conversion of small monomers into integrated network), electrochemical deposition (reduction of metal ions from electrolytes for growth), casting (liquid is poured and spread onto the mold), hydrothermal method (chemical reaction in aqueous solution under specific pressure and temperature), electrospinning method (the composite fibres are drawn via electrical force) as well as wet spinning method (drawing the composite fibres through precipitation force) [71]. However, depending on the desired properties of nanocomposite material and promising applications, the above mentioned processes are implemented or combined as well as can be modified in order to discover a new strategies [71]. Nowadays, a special attention is attributed to organic-inorganic nanocomposites combining unique features of organic components enriched in reactive functional groups (eg. hydroxyl groups, aldehyde groups, amino groups, carboxyl groups) that allow their linkage with an active biomolecules (eg. protein, enzyme, antibody, DNA) as well as inorganic components, which can adjust the nanocomposites properties towards desired biomedical applications [72-74]. The several structures can constitute a part of organic-inorganic nanocomposites, such as core-shell nanoparticles or nanorods, porous or hollow particles, nanofibers, multilayer components as well as crystal structures [3]. Owing to a unique physical and chemical attributives arising from particular components, nanocomposites are becoming materials of the future [74, 75]. Especially, organic-inorganic nanocomposites can display changes in their characteristic properties while being exposed to different stimuli, which originate from both organic and inorganic components. In detail, two

main types of stimuli can be distinguished, such as physical stimuli (eg. light, mechanical force, electric or magnetic field, heat) which detect the changes in the external environment as well as chemical stimuli (eg. pH, enzymes, changes in ions concentration) which are categorized as an internal stimuli (**Figure 1.23**). In comparison, the external stimuli are transmitted through the material and can modulate its properties, whereas the internal stimuli impact slowly on the internal changes [3].



**Figure 1.23** The graphical illustration of switching phenomena of organic-inorganic nanocomposites induced by different stimuli (Adapted from Ref. 3).

In general, nanocomposite materials can be divided into three main groups based on the type of inner matrix material, which could be either metal (metal matrix nanocomposites) or polymer (polymer matrix nanocomposites) or ceramic (ceramic matrix nanocomposites) [71, 75]. However, the greatest attention is attributed especially to polymer matrix nanocomposites, which are commonly utilized in multifarious biomedical applications, such as drug delivery, tissue engineering, electrochemical sensors, and stem cell therapy [3, 71, 73]. In polymer nanocomposites at least one evenly dispersed phase with nanometric dimensions (eg. carbon nanoparticles) is dispersed within a polymer matrix [76]. In contrast to pure polymeric counterparts or polymers modified with conventional additives, nanocomposites may possess enhanced mechanical, thermal as well as optical properties [71, 76]. The properties of polymer nanocomposites are dependent on the

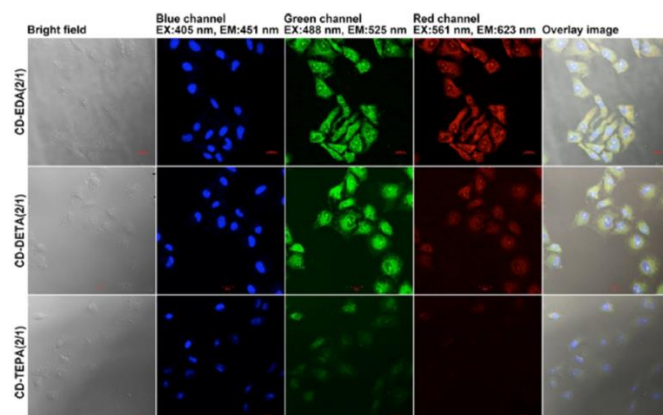
type of polymer matrix, size, nature, composition, dispersion level of incorporated nanoparticles as well as interactions at the interphase region between nanoparticles and polymeric material [77]. A good dispersion of nanoscopic particles inside the polymeric matrix may be achieved through physical methods (eg. ultrasonic treatment, high-energy ball-milling process) or chemical surface modifications [71, 77]. Owing to the nature of polymer materials, they can be classified into natural (e.g. chitosan, alginate, dextran, gelatin, starch) or synthetic (poly(vinyl alcohol), poly(ethylene glycol), poly(lactic acid), poly(acrylic acid), poly(glycolic acid), poly( $\epsilon$ -caprolactone)) [74, 77]. Importantly, the use of both natural and synthetic polymers play a crucial role in controllable degradation of polymer matrix NCs as well as significantly increase the biocompatibility of as-prepared nanocarriers [77].

## 1.4 Biomedical applications

### 1.4.1 Bioimaging

On the basis of low toxicity and notable PL properties, C-dots are an excellent candidates to be used for bioimaging applications. In this regard, Huang et al. investigated the application of N-rich C-dots for *in vitro* cellular imaging. The fluorescent images of HeLa cells incubated with carbon dots (200  $\mu\text{g/mL}$ ) for 4 hours revealed their multicolour nature with strong green luminescence at  $\lambda_{\text{ex}}=488\text{nm}$  and weakened red fluorescence at  $\lambda_{\text{ex}}=561\text{nm}$  (**Figure 1.24**). The examination of the images collected with the green channel proved the major C-dots distribution in the cytoplasm region while the red channel displayed a significantly diminished optical properties of C-dots. The collected results led to conclusion that the cellular uptake of N-rich C-dots by HeLa cells could be similar to the pathway of some GQDs, which penetrate the cell membrane through damaging the structure and conformation of lipid bilayer [64, 66]. Besides that, other literature reports noted that C-dots were successfully used to label various bacterial or cancer cells, such as HepG2, HeLa, U87, A549, L929, MCF-7 [78-83].

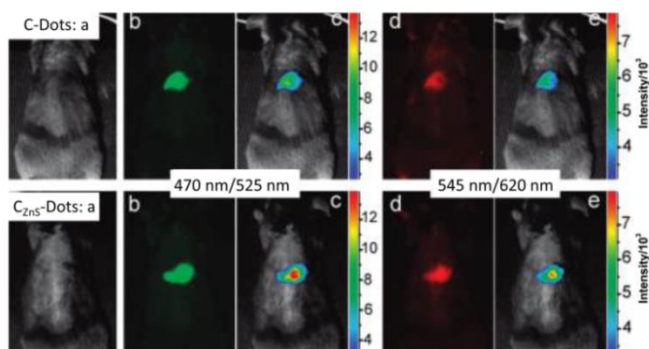




**Figure 1.24** Confocal fluorescence microscopy images of HeLa cells incubated with 200 $\mu$ g/mL of C-dots for 4 hours. The images were captured in the bright field as well as with the use of blue, green, red and merged channels. The cell nuclei were stained with DAPI dye as presented in blue channel (Adapted from Ref. 23).

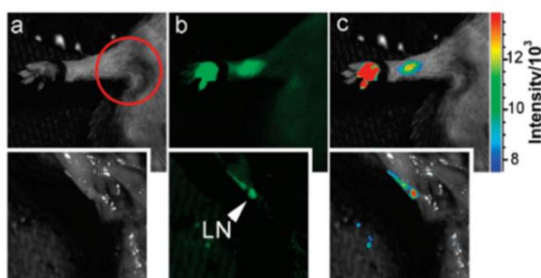
### 1.4.2 *In vivo* fluorescence imaging

The *in vivo* cytotoxicity evaluation of various C-dots for optical imaging has been extensively studied in recent years. Sun et al. were the first to investigate the feasibility of carbon-based nanoemitters as a fluorescence contrast agents in mice. They examined *in vivo* safety and optical imaging performance of C-Dots and C<sub>ZnS</sub>-Dots functionalized with PEG<sub>1500N</sub> molecules, in reference to cadmium-based semiconductor quantum dots that possess a significant toxicity. Upon subcutaneous injection of C-Dots (30 $\mu$ g in 30 $\mu$ L) and C<sub>ZnS</sub>-Dots (65 $\mu$ g in 30 $\mu$ L) solutions the mice were imaged using an *in vivo* imaging system/facility and displayed either bright green ( $\lambda_{ex}$ = 470nm,  $\lambda_{em}$ = 525nm) or red ( $\lambda_{ex}$ = 545nm,  $\lambda_{em}$ = 620nm) fluorescence (**Figure 1.25**), fading after 24 hours of post injection [84].



**Figure 1.25** Subcutaneous injection of C-Dots (images on the top) and C<sub>ZnS</sub>-Dots (images at the bottom) in the bright field (a), as-detected fluorescence (b,d) along with color-coded images (c,e) (Adapted from Ref. 84).

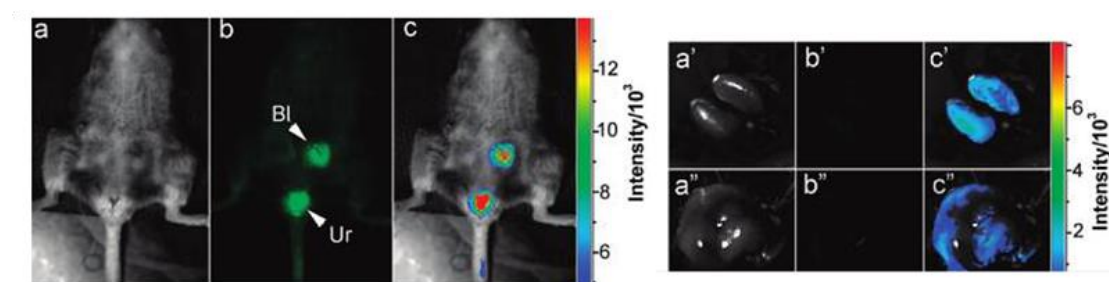
Furthermore, the same research group used C<sub>ZnS</sub>-Dots solutions (10 $\mu$ g in 10 $\mu$ L) with brighter green fluorescence for intradermal injection. The migration of C<sub>ZnS</sub>-Dots through the lymph vessels of mice confirmed both the instant fluorescence properties of carbon dots which gave a sufficient contrast for imaging in the front extremity as well as in dissected axillary lymph nodes at 24h post injection (**Figure 1.26**).



**Figure 1.26** Intradermal injection of C<sub>ZnS</sub> salt doped C-dots in the bright field (a), as-detected fluorescence (b) and color-coded images. The images inserted below represent the dissected axillary lymph node (LN) of the mouse (Adapted from Ref. 23).

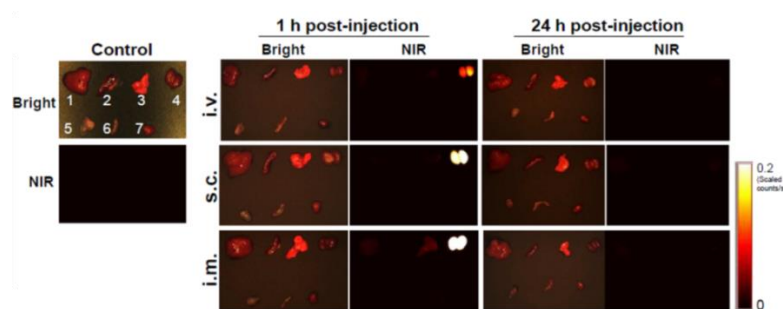
Additionally, Yang et al. intravenously injected into mice the aqueous dispersion of C-Dots (440 $\mu$ g in 200 $\mu$ L) for whole-body circulation. The *in vivo* optical imaging confirmed the excretion of highly fluorescent nanoparticles via urine after approximately 3 hours post-injection and their accumulation in the bladder at about 1 hour post-injection (**Figure 1.27b,c**). The dissection of organs from abdomen after 4 hours post-injection revealed the *ex vivo* fluorescence features of liver and kidneys, which are actively involved in the urine excretion pathway (**Figure 1.27c',c''**). The significantly reduced fluorescence in dissected liver confirmed a low accumulation of

C-dots in this organ, as a result of PEGylation process. To this point, it has been widely reported that PEGylation process reduce the affinity of nanoparticles towards proteins and make them stealthy with respect to hepatic uptake [84]. Nevertheless, for efficient renal excretion the hydrodynamic diameter of PEGylated QDs has to be less than 5.5 nm due to gradual decreasing clearance efficiency above this value [64].



**Figure 1.27** Intravenous injection of C-dots in the bright field (a), as-detected fluorescence (b) and color-coded images (c). The dissected kidneys (a'-c') and liver (a''-c'') are in the same order and Bl represents bladded while Ur - urine (Adapted from Ref. 84).

In addition, Chen et al. investigated the effect of C-dots injection routes on their biodistribution in major organs and tissues, tumor uptake over time as well as the specific rate of blood and urine clearance. They discovered that C-dots are rapidly and efficiently excreted from the mice body and the fastest clearance rate was attributed to intravenous injection while slower for intramuscular and subcutaneous injection, accordingly. The *ex vivo* imaging displayed the highest accumulation of C-dots in the kidneys after 1 hour post-injection with only tiny amount of carbon dots accumulated in the liver (**Figure 1.28**). In contrast, no signal was detected in any organ after 24 hours, thereby proving the complete removal of NPs from the mice body regardless the injection route [64].



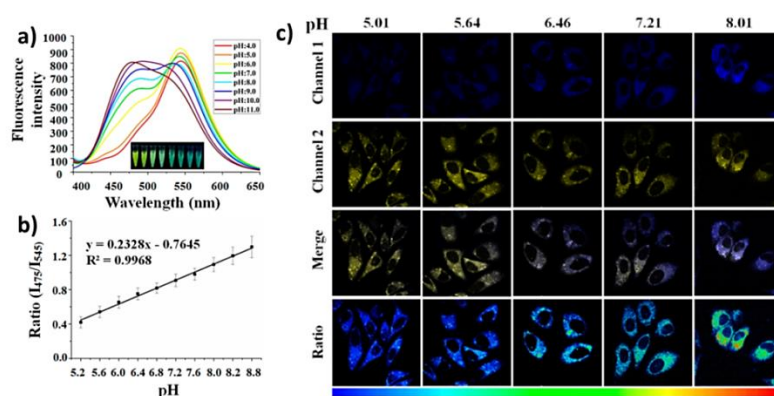
**Figure 1.28** *Ex vivo* imaging of C-dots biodistribution in harvested liver (1), spleen (2), lung (3), kidneys (4), muscle (5), intestine (6) and heart (7) after three injection routes: intravenous (top), subcutaneous (middle), intramuscular (bottom) (Adapted from Ref. 64).

Collectively, the evidences from *in vivo* studies after intravenous injections of C-dots have demonstrated that their uptake is mainly undertaken by reticuloendothelial system (RES) organs, in particular spleen or liver while the elimination is followed via renal excretion pathway [64, 84]. Moreover, the results reported by several research groups demonstrated that intravenous injection of carbon dots solutions into mice retain their *in vivo* strong fluorescence characteristic, which along with good biocompatibility and low cytotoxicity suggest an enormous potential for both optical bioimaging as well as related biomedical applications [23, 84].

### 1.4.3 Optical sensors

The intercellular pH has a crucial role in various physiological and pathological processes, including ion transport, cell cycle and apoptosis, muscle contraction, receptor-mediated signal transduction, tumor growth and inflammation. Thus, the measurement of pH variations and distribution in living cells play a crucial role in early diagnosis of several diseases as well as help to understand the general cellular functions [85, 86]. To this point, the first report regarding the C-dots based ratiometric pH sensors used to measure the intercellular pH was delivered by Shi and co-workers [87]. In detail, they developed a nanosystem based on C-dots labelled with fluorescein isothiocyanate and rhodamine B isothiocyanate fluorescent dyes, which endowed the carbon dots with two emission bands centered at 515 nm and 575 nm ( $\lambda_{ex}=488$  nm), respectively. The changes in the pH ranging from 5 to 9 influenced on the significant increment of the PL intensity at  $\lambda_{em}=515$  nm and negligible enhancement at  $\lambda_{em}=575$

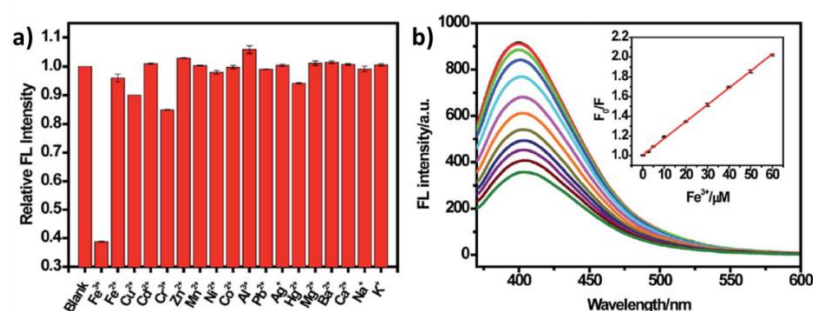
nm, thereby impacted on the overall linear ratiometric response of carbon dots to pH input [87, 88]. To overcome issues associated with the leaching of a small molecules from C-dots, the Shangguan et al. developed a label free carbon dots ratiometric pH sensor via hydrothermal treatment of fuchsin and citric acid [85]. Similarly, these C-dots exhibited two emission peaks centered at 475 nm and 545 nm ( $\lambda_{\text{ex}}$ =380 nm), which intensities manifested different performance in pH ranging from 4 to 11 (**Figure 1.29a**). The linear relationship of the intensities ratios ( $I_{475}/I_{545}$ ) towards varied pH values between 5.1 and 8.8 (**Figure 1.29b**) confirmed that these nanoemitters could be utilized as the ratiometric pH sensors for bioimaging of HeLa cells with internalized C-dots (**Figure 1.29c**), which stronger blue emission ( $\lambda_{\text{em}}$ =465-495 nm) at higher pH led to notable colour change [85].



**Figure 1.29** PL spectra of carbon dots in PBS buffer with various pH values under  $\lambda_{\text{ex}}$ = 380nm while inserted images show the colour change under UV light exposure (a), linear relationship between the PL intensity ratio and pH values (b), confocal fluorescence images of carbon dots incubated with HeLa cells in buffered solutions with nigericin at different pH (c) (Adapted from Ref. 85).

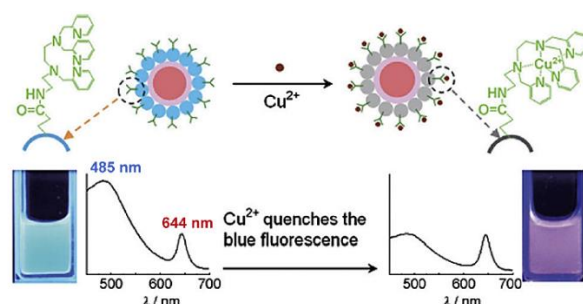
Besides detecting the pH changes, carbon dots have been fabricated as a direct fluorescence sensors for detecting metal ions, anions and molecules [89, 90]. Among all metal ions, the  $\text{Fe}^{3+}$  is the most widely detected by C-dots (**Figure 1.30**). To this point, the group of Song et al. synthesized BCDs from black tea via hydrothermal method, which demonstrated the fluorescence quenching of these C-dots derived from biomass in the presence of  $\text{Fe(III)}$ . Similarly, Zhang et al. prepared a blue luminescent carbon dots with quantum yield of 31%, which surface functional oxygen-rich groups were strongly coordinating the  $\text{Fe}^{3+}$  ions, thereby induced the PL quenching

by non-radiative electron transfer [89, 90]. In general, the mechanisms responsible for the fluorescence changes in C-dots include resonance energy transfer, inner filter effect, photo-induced electron transfer as well as photo-induced charge transfer [89, 90].



**Figure 1.30** The fluorescence response of BCDs in the presence of various metal ions with concentration 100 mM (a) together with the fluorescence emission spectra of BCDs after addition of different concentrations of Fe<sup>3+</sup> and the linear calibration plot for F<sub>0</sub>/F versus different concentrations of Fe<sup>3+</sup> (b) (Adapted from Ref. 91).

In other report, Dong et al. developed a highly fluorescent C-dots via multistep thermal pyrolysis of citric acid and branched poly(ethylenimine). In this system, a multiple surface functional amine groups had affinity to coordinate the Cu<sup>2+</sup> ions. Then, the as-formed formed strong complex quenched the emissive mode of C-dots due to possible inner filter effect [92]. In similar case, Tian and co-workers manufactured a dual-emission nanohybrid system of CdSe/ZnS-Cdots for ratiometric PL detection of Cu<sup>2+</sup> ions in the cells. They reported that the primarily higher PL emission attributed to C-dots ( $\lambda_{em}=485$  nm) with blue luminescence was more intense than that corresponding to quantum dots ( $\lambda_{em}=644$  nm) (**Figure 1.31**). However, after the addition of Cu<sup>2+</sup> the molecular receptors on the surface of Cdots linked with them and quenched the blue PL, while the emission at 644 nm stayed constant [93]. Overall, the optical sensing constitute one of the most promising biomedical applications of C-dots based nanosystems [90].



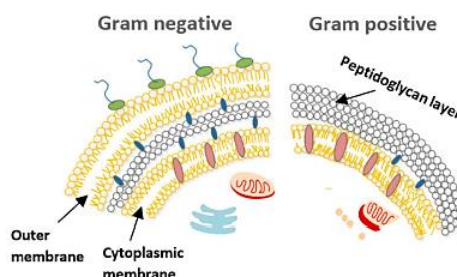
**Figure 1.31** The schematic illustration of the dual-emission fluorescent sensing of  $\text{Cu}^{2+}$  ions based on CdSe/ZnS-Cdots hybrid nanosystem (Adapted from Ref. 93).

#### 1.4.4 Antimicrobial agents

Nowadays, antimicrobial resistance against wide range of antibiotics (i.e. penicillin, tetracycline, methicillin, vancomycin) constitute a considerable health issue and arise as a global thread [94]. Therefore, there is an urgent need to generate innovative strategies in antimicrobial therapies to overcome a commonly used antibiotic-based treatment. In the group of strategies that have been examined for antimicrobial therapies are antimicrobial nanoparticles, which increase the efficacy of the treatment as well as reduced a side effects due to precisely targeted action [95]. In reference to NPs antimicrobial action, it is believed that after crossing the bacterial cell membrane they inhibit the enzymes inside the cell, induce the oxidative stress and electrolyte imbalance, deactivate proteins as well as modify the gene expression levels [96]. In regard to literature reports, the first drug delivery nanosystem for antimicrobial therapy was fabricated by Bonventre et al. in 1978 and was based on dihydrostreptomycin antibiotic entrapped within liposomes molecules [97]. To date, different types of nanoparticles are used for antibiotic drug delivery, including polymer-based NPs, carbon dots as well as magnetic NPs [98]. Among all, especially the use of carbon dots provide not only enhanced antimicrobial activity but also enable an additional fluorescent labelling of bacterial cells [78]. Moreover, the response of Gram-negative as well as Gram-positive bacterial species towards antibacterial nanoparticles may be diversified, due to the structural differences of their membranes. In detail, Gram-positive bacteria possess a thick cell wall with many layers (**Figure 1.32**), which consist of peptidoglycan and teichoic acids. On the other side,



Gram-negative bacteria have rather a thin few-layer but more complex cell wall (**Figure 1.32**) [99, 100]. Therefore, the development of antimicrobial nanoparticles which are effective against both Gram-positive and Gram-negative bacteria have currently a significant importance in biomedical fields [100].



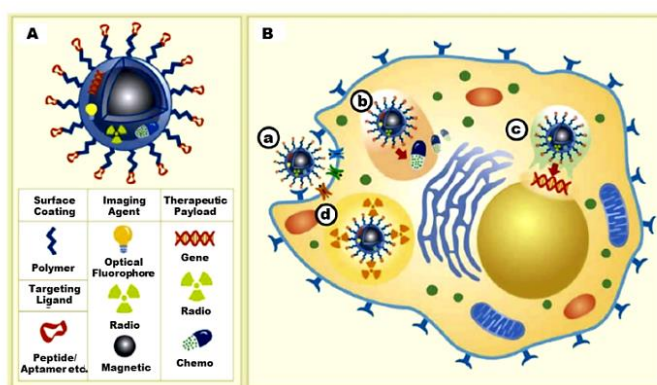
**Figure 1.32** The schematic representation of the cell walls of Gram-positive and Gram-negative bacteria (Adapted from Ref. 101).

#### 1.4.5 Drug delivery nanosystems

Nanotechnology offers a promising prospects for designing a multifunctional drug delivery systems, which could overcome the limitations of conventional drug delivery approaches. Nanocarriers are colloidal systems based on various nanomaterials (i.e. natural or synthetic polymeric NPs, lipid NPs, carbon dots) and carry an active therapeutic agent (e.g. vaccine, gene, protein, drug), which may be encapsulated, dissolved, adsorbed, covalently attached or electrostatically bound to the particles surface [102]. In general, the engineering of nanoparticles for drug delivery applications enable to develop a multifunctional targeted nanocarriers, which could be combined with various imaging reporters (magnetic, optical, radio), chemotherapeutics, biotherapeutics (gene-DNA, siRNA) or radiotherapeutics (radionucleotides) via surface modifications of bare NPs with biomolecules or polymers (**Figure 1.33**). At the cellular level, the therapeutic payload integrated onto nanoparticles impact on different internalization mechanisms, among which are differentiated the receptor-mediated internalization (**Figure 1.33a**), internalization and slow intracellular release of chemotherapeutic agents (**Figure 1.33b**), cellular uptake followed by release from endosomal compartments in the perinuclear region or nucleus (**Figure 1.33c**) as well as internalization of radiotherapeutics (**Figure 1.33d**).



Overall, the size of nanoparticles is a key parameter for development of drug delivery systems and should be large enough to prevent rapid permeability and renal filtration (>10 nm) as well as kept below 200 nm to avoid the reticular endothelial system phagocytosis by the liver and spleen. Thus, NPs with the size in the range of 10 nm to 200 nm demonstrate prolonged circulation in the blood and enable an efficient accumulation in the tumor sites, where subsequently undergo a biodegradation [74, 103].



**Figure 1.33** The design of multifunctional nanocarrier for targeted delivery applications (A) with possible routes of action (B), including inactivation of the cell surface receptors (a), intercellular release of therapeutic substance (b), controlled release of gene therapeutic materials (c) or intracellular decay of radioactive materials (d) (Adapted from Ref. 103).

## 1.5 Study aims

The overall research aim of this study was to develop novel types of fluorescent carbogenic nanoparticles, hybrid magneto-fluorescent NPs as well as chitosan-based nanocomposites for various biomedical applications, including the optical sensors for detection of heavy metals or pH variations, nanotracers for the cellular labelling and imaging as well as traceable drug delivery nanosystems. In consequence, the following objectives were articulated:

- To separate blue and green emissive species from the post-synthesized carbogeneous mixture and develop an efficient purification procedures for fabrication of fluorescent C-dots nanopowders

- To produce a large gallery of environmentally benign photoluminescent suspensions for bioimaging and optical pH-sensing applications
- To demonstrate how incorporation of iron into C-dots matrix impact on the structural, optical and magnetic features of hybrid magneto-fluorescent NPs
- To develop a novel family of magnetic C-dots as well as various hybrid magneto-fluorescent nanocomposites for labelling of the cancer cells as well as ion sensing applications
- To improve magnetic properties of C/Fe-NPs through incorporating Gd-dopant into previously designed synthetic approach
- To estimate how the modulation of surface characteristics impact on the structural, optical and biological properties of various C-dots and test their suitability for bioimaging applications
- To develop highly fluorescent chitosan@C-dots nanocomposites as efficient nanocarriers for traceable drug delivery applications
- To fabricate chitosan-based nanocomposites with strong fluorescence properties in a solid-state
- To test the vancomycin release from a model chitosan@C-dots drug nanocarrier that was design for drug delivery and cellular imaging applications

## 1.6 References

1. Khan, I., K. Saeed, and I. Khan, *Nanoparticles: Properties, applications and toxicities*. Arabian Journal of Chemistry, 2019. **12**: p. 908–931.
2. Shirazi, H., et al., *Synthesis, characterization and in vitro biocompatibility study of Au/TMC/Fe<sub>3</sub>O<sub>4</sub> nanocomposites as a promising, nontoxic system for biomedical applications*. Beilstein J. Nanotechnol., 2015. **6**: p. 1677–1689.
3. Lee, W., et al., *Stimuli-responsive switchable organic-inorganic nanocomposite materials*. Nano Today, 2018. **23**: p. 97-123.
4. Pokropivny, V.V. and V.V. Skorokhod, *Classification of nanostructures by dimensionality and concept of surface forms engineering in nanomaterial science*. Materials Science and Engineering C, 2007. **27**: p. 990–993.
5. Jeevanandam, J., et al., *Review on nanoparticles and nanostructured materials: history, sources, toxicity and regulations*. Beilstein J. Nanotechnol., 2018. **9**: p. 1050–1074.
6. Panneerselvam, S. and S. Choi, *Nanoinformatics: Emerging Databases and Available Tools*. Int. J. Mol. Sci., 2014. **15**: p. 7158-7181.
7. Wichlab. 2017 [cited 2020 15March].
8. Kroto, H.W., et al., *C60: Buckminsterfullerene*. Nature, 1985. **318**: p. 162–163.
9. Namdari, P., B. Negahdari, and A. Eatemadi, *Synthesis, properties and biomedical applications of carbon-based quantum dots: An updated review*. Biomedicine & Pharmacotherapy, 2017. **87**: p. 209–222.
10. Iijima, S., *Helical microtubules of graphitic carbon*. Nature, 1991. **354**: p. 56-58.
11. Iijima, S. and T. Ichihashi, *Single-shell carbon nanotubes of 1-nm diameter*. Nature, 1993. **363**: p. 603-605.
12. Terrones, M., et al., *Graphene and graphite nanoribbons: Morphology, properties, synthesis, defects and applications*. Nano Today, 2010. **5**: p. 351–372.
13. Xu, X., et al., *Electrophoretic Analysis and Purification of Fluorescent Single-Walled Carbon Nanotube Fragments*. J. Am. Chem. Soc. , 2004. **126**: p. 12736-12737.
14. Sun, Y.P., et al., *Quantum-Sized Carbon Dots for Bright and Colorful Photoluminescence*. J. Am. Chem. Soc. , 2006. **128**: p. 7756-7757.
15. Wang, X., et al., *A Mini Review on Carbon Quantum Dots: Preparation, Properties, and Electrocatalytic Application*. Frontiers in Chemistry, 2019. **7**: p. 1-9.
16. Farshbaf, M., et al., *Carbon quantum dots: recent progresses on synthesis, surface modification and applications*. Artificial Cells, Nanomedicine, and Biotechnology, 2017. **46**(7): p. 1331-1348.

17. Sciortino, A., A. Cannizzo, and F. Messina, *Carbon Nanodots: A Review—From the Current Understanding of the Fundamental Photophysics to the Full Control of the Optical Response*. Journal of Carbon Research, 2018. **4**(67): p. 1-35.
18. Zhou, J., et al., *An Electrochemical Avenue to Blue Luminescent Nanocrystals from Multiwalled Carbon Nanotubes (MWCNTs)*. J. Am. Chem. Soc. , 2007. **129**: p. 744-745.
19. Baker, S.N. and G.A. Baker, *Luminescent Carbon Nanodots: Emergent Nanolights*. Angew. Chem. Int. Ed. , 2010. **49**: p. 6726–6744.
20. Liu, M., et al., *Carbon quantum dots directly generated from electrochemical oxidation of graphite electrode in alkaline alcohols and the applications for specific ferric ion detection and cell imaging*. Analyst, 2016. **141**: p. 2657-2664.
21. Liu, M.L., et al., *Carbon dots: synthesis, formation mechanism, fluorescence origin and sensing applications*. Green Chem., 2019. **21**: p. 449–471.
22. Krysmann, M.J., A. Kelarakis, and E.P. Giannelis, *Photoluminescent carbogenic nanoparticles directly derived from crude biomass*. Green Chem., 2012. **14**(11): p. 3141-3145.
23. Wang, J., et al., *Opportunities and Challenges of Fluorescent Carbon Dots in Translational Optical Imaging*. Curr Pharm Des., 2015. **21**(37): p. 5401-5416.
24. Bourlinos, A.B., et al., *Surface Functionalized Carbogenic Quantum Dots*. small, 2008. **4**: p. 455-458.
25. Wang, H., et al., *Fluorescently tuned nitrogen-doped carbon dots from carbon source with different content of carboxyl groups*. APL Materials 2015. **3**(8): p. 1-7.
26. Chatzimitakos, T., et al., *Two of a kind but different: Luminescent Carbon Quantum Dots from Citrus Peels for Iron and Tartrazine Sensing and Cell Imaging*. Talanta, 2017. **175**: p. 305-312.
27. Gu, J., et al., *Synthesis of fluorescent carbon nanoparticles from polyacrylamide for fast cellular endocytosis*. RSC Advances, 2013. **3**: p. 15589-15591.
28. Xia, C., et al., *Evolution and Synthesis of Carbon Dots: From Carbon Dots to Carbonized Polymer Dots*. Adv. Sci., 2019. **6**: p. 1901316.
29. Song, Z., et al., *Multifunctional N,S co-doped carbon quantum dots with pH- and thermo-dependent switchable fluorescent properties and highly selective detection of glutathione*. Carbon, 2016. **104**: p. 169-178.
30. Zhu, S., et al., *Highly Photoluminescent Carbon Dots for Multicolor Patterning, Sensors, and Bioimaging*. Angew. Chem. Int. Ed., 2013. **52**: p. 1-6.
31. Sharma, A., et al., *Interaction of Carbon Dots with Endothelial Cells: Implications for Biomedical Applications*. ACS Appl. Nano Mater. , 2019. **2**: p. 5483–5491.

32. Zhu, H., et al., *Microwave synthesis of fluorescent carbon nanoparticles with electrochemiluminescence properties*. Chem. Commun., 2009(34): p. 5118-5120.
33. Liu, Y., et al., *One-step microwave-assisted polyol synthesis of green luminescent carbon dots as optical nanoprobe*s. Carbon, 2014. **68**: p. 258-264.
34. Kasprzyk, W., et al., *Luminescence phenomena of carbon dots derived from citric acid and urea - a molecular insight*. Nanoscale, 2018. **10**(29): p. 13889-13894.
35. Wang, T., et al., *Highly Fluorescent Green Carbon Dots as a Fluorescent Probe for Detecting Mineral Water pH*. Sensors, 2019. **19**: p. 3801-3811.
36. Chen, B.B., et al., *Fluorescent carbon dots functionalization*. Advances in Colloid and Interface Science, 2019. **270**: p. 165–190.
37. Zhu, S., et al., *The photoluminescence mechanism in carbon dots (graphene quantum dots, carbon nanodots, and polymer dots): Current state and future perspective*. Nano Res., 2015. **8**(2): p. 355–381.
38. Suvarnaphaet, P. and S. Pechprasarn, *Graphene-Based Materials for Biosensors: A Review*. Sensors, 2017. **17**: p. 2161-2185.
39. Kelarakis, A., *From highly graphitic to amorphous carbon dots: A critical review*. . MRS Energy & Sustainability, 2014. **1**(2): p. 1-15.
40. Li, X., et al., *Engineering surface states of carbon dots to achieve controllable luminescence for solid-luminescent composites and sensitive Be<sup>2+</sup> detection*. Sci Rep. , 2014. **4**: p. 4976-4984.
41. Zhang, X., et al., *Review of natural product derived carbon dots: from natural products to functional materials*. ChemSusChem, 2018. **11**(1): p. 11-24.
42. Hu, L., et al., *Metal-based quantum dots: synthesis, surface modification, transport and fate in aquatic environments and toxicity to microorganisms*. RSC Adv., 2016. **6**: p. 78595-78611.
43. Zhou, L., B. He, and J. Huang, *Amphibious fluorescent carbon dots: one-step green synthesis and application for light-emitting polymer nanocomposites*. Chem. Commun., 2013. **49**: p. 8078-8080.
44. Abbas, A., L.T. Mariana, and A.N. Phan, *Biomass-waste derived graphene quantum dots and their applications*. Carbon, 2018. **140**: p. 77-99.
45. Ding, Z., et al., *Gram-scale synthesis of single-crystalline graphene quantum dots derived from lignin biomass*. Green Chem., 2018. **20**: p. 1383-1390.
46. Peng, J., et al., *Graphene Quantum Dots Derived from Carbon Fibers*. Nano Lett. , 2012. **12**: p. 844–849.
47. Yan, F., et al., *The fluorescence mechanism of carbon dots, and methods for tuning their emission color: a review*. Microchimica Acta, 2019. **186**(583): p. 1-37.

48. Li, L. and T. Dong, *Photoluminescence Tuning in Carbon Dots: Surface Passivation or/and Functionalization, Heteroatom Doping*. J. Mater. Chem. C, 2018. **6**(30): p. 7944-7970.
49. Ehrat, F., et al., *Tracking the Source of Carbon Dot Photoluminescence: Aromatic Domains versus Molecular Fluorophores*. Nano Lett., 2017. **17**(12): p. 7710–7716.
50. Ding, H., et al., *Full-Color Light-Emitting Carbon Dots with a Surface-State-Controlled Luminescence Mechanism*. ACS Nano, 2016. **10**: p. 484–491.
51. Zhang, Y., et al., *Multicolour nitrogen-doped carbon: tuneable photoluminescence and sandwich fluorescent glass-based light-emitting diodes*. Nanoscale, 2017. **9**: p. 17849-17858.
52. Zhu, S., et al., *Photoluminescence mechanism in graphene quantum dots: Quantum confinement effect and surface/edge state*. Nano Today, 2017. **13**: p. 10-14.
53. Eda, G., et al., *Blue Photoluminescence from Chemically Derived Graphene Oxide*. Adv. Mater., 2010. **22**: p. 505–509.
54. Li, H., et al., *Water-Soluble Fluorescent Carbon Quantum Dots and Photocatalyst Design*. Angew. Chem. Int. Ed., 2010. **49**: p. 4430 –4434.
55. Bao, L., et al., *Photoluminescence-Tunable Carbon Nanodots: Surface-State Energy-Gap Tuning*. Adv. Mater., 2015. **27**(10): p. 1663-1667.
56. Liu, Z., et al., *Photoluminescence of carbon quantum dots: coarsely adjusted by quantum confinement effects and finely by surface trap states*. Sci. China Chem., 2018. **61**: p. 490-496.
57. Xiong, Y., et al., *Influence of molecular fluorophores on the research field of chemically synthesized carbon dots*. Nano Today 2018. **23**: p. 124–139.
58. Zholobak, N.M., et al., *Facile fabrication of luminescent organic dots by thermolysis of citric acid in urea melt, and their use for cell staining and polyelectrolyte microcapsule labelling*. Beilstein J Nanotechnol, 2016. **7**: p. 1905-1917.
59. Song, Y., et al., *Investigation from chemical structure to photoluminescent mechanism: a type of carbon dots from the pyrolysis of citric acid and an amine*. J. Mater. Chem. C, 2015. **3**: p. 5976-5984.
60. Schneider, J., et al., *Molecular Fluorescence in Citric Acid-Based Carbon Dots*. J. Phys. Chem. C 2017. **121**: p. 2014-2022.
61. Krysmann, M.J., et al., *Formation mechanism of carbogenic nanoparticles with dual photoluminescence emission*. J Am Chem Soc, 2012. **134**(2): p. 747-50.
62. Yoo, H.J., B.E. Kwak, and D.H. Kim, *The Self-Quenching Origin of Carbon Dots and the Guideline for Its Solid-State Luminescence*. The Journal of Physical Chemistry, 2019. **123**(44): p. 27124-27131.

63. Wang, S., I.S. Cole, and Q. Qin Li, *The toxicity of graphene quantum dots*. RSC Adv., 2016. **6**: p. 89867-89878.
64. Huang, X., et al., *Effect of Injection Routes on the Biodistribution, Clearance, and Tumor Uptake of Carbon Dots*. ACS Nano, 2013. **7**(7): p. 5684-5693.
65. Janus, Ł., et al., *Chitosan-Based Carbon Quantum Dots for Biomedical Applications: Synthesis and Characterization*. Nanomaterials 2019. **9**(274): p. 1-13.
66. Wang, S., I.S. Cole, and Q. Li, *The toxicity of graphene quantum dots*. RSC Adv., 2016. **6**: p. 89867-89878.
67. Wang, Y., et al., *Carbon dots of different composition and surface functionalization: cytotoxicity issues relevant to fluorescence cell imaging*. Experimental Biology and Medicine, 2011. **236**: p. 1231-1238.
68. Chandra, S., et al., *Synthesis, functionalization and bioimaging applications of highly fluorescent carbon nanoparticles*. Nanoscale, 2011. **3**: p. 1533-1540.
69. Camargo, P.H.C., K.G. Satyanarayana, and F. Wypych, *Nanocomposites: Synthesis, Structure, Properties and New Application Opportunities*. Materials Research, 2009. **12**(1): p. 1-39.
70. Mishra, D.K., et al., *Nanocomposite for cancer targeted drug delivery*, in *Applications of Nanocomposite Materials in Drug Delivery*, L.M. Inamuddin, A. Asiri, and A. Mohammad, Editors. 2018, Woodhead Publishing. p. 323-337.
71. Kumar, S., et al., *Recent advances and remaining challenges for polymericnanocomposites in healthcare applications*. Progress in Polymer Science, 2018. **80**: p. 1-38.
72. Kalia, S., et al., *Magnetic polymer nanocomposites for environmental and biomedical applications*. Colloid Polym Sci 2014. **292**: p. 2025-2052.
73. Yiu, H.P.H., et al., *Designed Multifunctional Nanocomposites for Biomedical Applications*. Adv. Funct. Mater. , 2010. **20**: p. 1599-1609.
74. Wu, W., Q. He, and C. Jiang, *Magnetic Iron Oxide Nanoparticles: Synthesis and Surface Functionalization Strategies*. Nanoscale Res Lett 2008. **3**: p. 397-415.
75. Omanović-Miklićanin, E., et al., *Nanocomposites: a brief review*. Health and Technology, 2020. **10**: p. 51-59.
76. Passador, F.R., A. Ruvoilo-Filho, and L.A. Pessan, *Nanocomposites of Polymer Matrices and Lamellar Clays*, in *Nanostructures*, A.L. Da Róz, et al., Editors. 2017, Elsevier. p. 187-207.
77. Zare, Y. and I. Shabani, *Polymer/metal nanocomposites for biomedical applications*. Materials Science and Engineering C, 2016. **60**: p. 195-203.
78. Lin, F., Y.W. Bao, and F.G. Wu, *Carbon Dots for Sensing and Killing Microorganisms*. Journal of Carbon Research, 2019. **5**(2): p. 1-21.

79. Zheng, M., et al., *Preparation of highly luminescent and color tunable carbon nanodots under visible light excitation for in vitro and in vivo bio-imaging*. Journal of Materials Research, 2015. **30**(22): p. 3386-3393.
80. Zheng, X., et al., *Single and repeated dose toxicity of citric acidbased carbon dots and a derivative in mice*. RSC Adv., 2015. **5**: p. 91398-91406.
81. Li, L.S., et al., *Highly fluorescent carbon dots synthesized with binary dopants for "turn off" and "turn off-on" sensing and cell imaging*. Sensors and Actuators B, 2018. **268**: p. 84–92.
82. Sarkar, S., et al., *Amino acid functionalized blue and phosphorous-doped green fluorescent carbon dots as bioimaging probe*. RSC Adv., 2015. **5**: p. 65913-65921.
83. Wang, J., S. Su, and J. Qiu, *Biocompatible Carbon Dots with Diverse Surface Modification*. MRS Advances, 2016. **1**(19): p. 1333-1338.
84. Yang, S.T., et al., *Carbon Dots for Optical Imaging in Vivo*. J. Am. Chem. Soc. , 2009. **131**: p. 11308–11309.
85. Shangguan, J., et al., *Label-Free Carbon-Dots-Based Ratiometric Fluorescence pH Nanoprobes for Intracellular pH Sensing*. Anal. Chem., 2016. **88**: p. 7837–7843.
86. Huang, M., et al., *Carbon Dots for Intracellular pH Sensing with Fluorescence Lifetime Imaging Microscopy*. Nanomaterials, 2020. **10**: p. 1-17.
87. Shi, W., X. Li, and H. Ma, *A Tunable Ratiometric pH Sensor Based on Carbon Nanodots for the Quantitative Measurement of the Intracellular pH of Whole Cells*. Angew. Chem. Int. Ed. , 2012. **51**: p. 6432 –6435.
88. Xiao, L. and H. Sun, *Novel Properties and Applications of Carbon Nano-dots*. Nanoscale Horiz., 2018. **3**(6): p. 565-597.
89. Zhang, J. and S.H. Yu, *Carbon dots: large-scale synthesis, sensing and bioimaging*. Materials Today, 2016. **19**(7): p. 382-393.
90. Meng, W., et al., *Biomass-Derived Carbon Dots and Their Applications*. Energy Environ. Mater., 2019. **2**(3): p. 172-192.
91. Song, P., et al., *A multianalyte fluorescent carbon dots sensing system constructed based on specific recognition of Fe(III) ions*. RSC Adv., 2017. **7**: p. 28637-28646.
92. Dong, Y., et al., *Polyamine-functionalized Carbon Quantum Dots as Fluorescent Probes for Selective and Sensitive Detection of Copper Ions*. 2012. **84**(14): p. 6220-6224.
93. Zhu, A., et al., *Carbon-Dot-Based Dual-Emission Nanohybrid Produces a Ratiometric Fluorescent Sensor for In Vivo Imaging of Cellular Copper Ions*. Angew. Chem. Int. Ed., 2012. **51**: p. 1-6.



94. Tran, N., et al., *Bactericidal effect of iron oxide nanoparticles on Staphylococcus aureus*. International Journal of Nanomedicine, 2010. **5**: p. 277–283.
95. Rodrigues, G.R., et al., *Antimicrobial Magnetic Nanoparticles Based-Therapies for Controlling Infectious Diseases*. Int J Pharm, 2019. **555**: p. 356-367.
96. Shaikh, S., et al., *Mechanistic Insights into the Antimicrobial Actions of Metallic Nanoparticles and Their Implications for Multidrug Resistance*. Int J Mol Sci., 2019. **20**(10): p. 2468-2483.
97. Bonventre, P.F. and G. Gregoriadis, *Killing of Intraphagocytic Staphylococcus Aureus by Dihydrostreptomycin Entrapped Within Liposomes*. Antimicrob Agents Chemother., 1978. **13**(6): p. 1049-1051.
98. Wang, L., C. Hu, and L. Shao, *The antimicrobial activity of nanoparticles: present situation and prospects for the future*. International Journal of Nanomedicine, 2017. **12**: p. 1227–1249.
99. Kousheh, S.A., et al., *Preparation of antimicrobial/ultraviolet protective bacterial nanocellulose film with carbon dots synthesized from lactic acid bacteria*. International Journal of Biological Macromolecules, 2020. **155**: p. 216–225.
100. Shahshahanipour, M., et al., *An ancient plant for the synthesis of a novel carbon dot and its applications as an antibacterial agent and probe for sensing of an anti-cancer drug*. Materials Science & Engineering C, 2019. **98**: p. 826–833.
101. Kravanja, G., et al., *Chitosan-Based (Nano)Materials for Novel Biomedical Applications*. Molecules, 2019. **24**: p. 1-23.
102. Mc Carthy, D.J., et al., *Nanoparticles and the Blood-Brain Barrier: Advancing from In-Vitro Models Towards Therapeutic Significance*. Pharm Res., 2014. **32**(4): p. 1161-1185.
103. Shen, L., B. Li, and Y. Qiao, *Fe<sub>3</sub>O<sub>4</sub> Nanoparticles in Targeted Drug/Gene Delivery Systems*. Materials, 2018. **11**: p. 324-353.

# **CHAPTER 2:**

## **Experimental section**

*“A scientist in his laboratory is not a mere technician:  
he is also a child confronting natural phenomena that  
impress him as though they were fairy tales”*

*Maria Skłodowska-Curie*

## 2.1 Materials

Citric acid monohydrate 99.5%, fluorescein, rhodamine 6G and rhodamine B, disodium hydrogen orthophosphate 99%, potassium dihydrogen orthophosphate 99%, sodium chloride 99%, 4-(dimethylamino)pyridine  $\geq 99\%$  and N,N'-dicyclohexylcarbodiimide  $\geq 99\%$ , polyethylene glycol 400 ( $M_w = 400$  g/mol), diphenyl ether 99.5% and vancomycin hydrochloride were purchased from Alfa Aesar. Urea, anthracene 99%, ethanolamine  $\geq 98\%$ , ethylenediamine  $\geq 99\%$ , deuterium oxide ( $D_2O$ , 99.9%), iron (III) acetylacetonate  $\geq 99.9\%$  trace metal basis ( $Fe(acac)_3$ ), gadolinium (III) acetylacetonate hydrate 99.9% trace metal basis ( $Gd(acac)_3$ ), diethylenetriaminepentaacetic acid gadolinium (III) dihydrogen salt hydrate (Gd-DTPA), branched polyethylenimine, trypan blue solution, 3-(4,5-dimethylthiazolyl-2)-2,5-diphenyltetrazolium bromide (MTT) and LUDOX HS-30 colloidal silica 30 wt% suspension in water were ordered from Sigma Aldrich. Dimethyl sulfoxide-D6 (d-DMSO, 99.9%) was ordered from Cambridge Isotopes Laboratories. Nitric acid 70%, Propan-2-ol, ethanol absolute 99%, HPLC grade water, acetic acid glacial 99% and tetrahydrofuran 99% were bought from Fischer Chemical. Polyetheramine JEFFAMINE® D-230 was supplied from HUNTSMAN. The Cellulose Nitrate Membrane Filters (0.1  $\mu m$  pore size) were supplied by Whatman® (GE Healthcare Life Sciences). The SnakeSkin Dialysis Tubing membrane 3.5K MWCO (35 mm), Dulbecco's Modified Eagle Medium (DMEM), Trypsin 10%, Penicilin-Streptomycin (10,000 U/mL), Fetal Bovine Serum (FBS) and Sodium Dodecyl Sulphate 95% were purchased from Thermo Fisher Scientific.

## 2.2 Synthesis protocols

### 2.2.1 Urea-based carbon dots

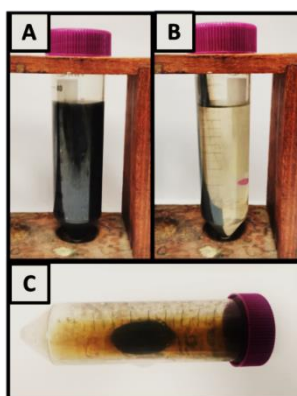
To synthesize the CU-dots used for this investigation, citric acid (CA) and urea (U) were mixed in four different molar ratios 1:3, 1:25, 1:50 and 1:100, respectively. Herein, as prepared materials were abbreviated CU03, CU25, CU50 and CU100, correspondingly to the applied urea ratio. In the initial step, both reactants were weighed and transferred into a porcelain crucible. Subsequently, these open vessels were placed in

a furnace and heated to 230 °C at the rate of 1°C/min for 1 hour. After completed synthesis, the brown solids were left overnight in the furnace to cool down to room temperature. The final products were transferred into a mortar with pestle and ground to fine powders. Afterwards, powders were dispersed in water, giving a dark brown solutions and either filtered (**F-series**) through Cellulose Nitrate Membrane Filters with 0.1 µm pore size or extensively dialysed against the water (**D-series**) using SnakeSkin Dialysis Tubing membrane (with a molecular cut-off of 3500 Da). The dialysis of the aqueous dispersions of CU-dots last for 10 weeks, in order to remove all impurities as well as undesirable by-products. The run-off substances were further collected during the first four weeks of dialysis and formed the D1-series. At the end, filtered and dialyzed aqueous solutions of carbon dots were initially frozen at temperature -20°C for 24 hours and then freeze-dried for 5 days at the temperature -110°C. The as prepared CU powders had either dark brown (**D-series**) or bright yellow (**F-series**) colour. Additionally, the leftover insoluble carbogenuous residue from the filtration step (**preF1-series**) was further utilized and heated for 18 hours with 100 mL of 3M HNO<sub>3</sub>. The as prepared highly water-dispersible CU-dots had light brown colour (**F1-series**).

### 2.2.2 Magnetic C-dots

The C/Fe-NPs were synthesized from iron and carbon precursors through one-step thermal decomposition method, in the presence of diphenyl ether as a high boiling point solvent. At first, highly photoluminescent carbon dots precursor (CAEA180) was prepared from citric acid and ethanolamine, using previously reported method [1]. In brief, EA and CA were mixed in the round bottom flask with molar ration 3:1 and heated under reflux at 180°C for 30 minutes, under the air atmosphere. Subsequently, diversified molar ratio of iron (III) acetylacetonate varied from 2.1 mmol to 1.1 mmol was added into the yellowish carbon dots precursor along with 7.5 mmol of polyethylene glycol 400 and 20 mL of diphenyl ether. Ultimately, the mixture was thoroughly mixed and heated under reflux at 230°C for 3 hours, in the air atmosphere with constant stirring. Afterwards, the product was purified from the organic solvent by adding 40 mL of propan-2-ol (**Figure 2.1A**) and centrifuged at 8000 rpm for 10

minutes (**Figure 2.1B**). The purification procedure was repeated four times in order to completely remove organic solvent and unreacted chemicals. Pure C/Fe-NPs were dispersed in a small amount of distilled water and left overnight with attached magnet (**Figure 2.1C**). Next day, attracted to the magnet hybrid C/Fe-NPs were collected and non-magnetic solution was discarded. The pure nanoparticles were freeze-dried and stored at room temperature.



**Figure 2.1** Picture of the sample of C/Fe-NPs prior (A) and during (B) and after (C) finished purification procedure.

In another approach, Gd-doped C/Fe-NPs were prepared from the same protocol as magnetic C-dots (230°C, 3h), while additionally 0.25 mmol of either Gd-DTPA (referred hereafter as Gd1) or Gd(acac)<sub>3</sub> (referred hereafter as Gd2) were added to the Fe(acac)<sub>3</sub> and PL-CAEA180 precursors mixture.

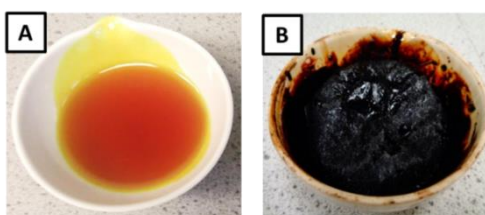
### 2.2.3 Hybrid magnetic nanoparticles

The C@Fe-NPs were synthesized through thermal decomposition method with the use of different carbon precursors. Briefly, the chosen carbon-rich reagent, either the ethanolamine (16.4 mmol, EA), ethylenediamine (16.7 mmol, EN), branched polyethylenimine (0.16 mmol, BPEI), polyethylene glycol 400 (20 mmol, PEG) or polyetheramine JEFFAMINE® D-230 (15.6 mmol, PEA), was mixed with 2 mmol of iron (III) acetylacetonate, 7.5 mmol of polyethylene glycol 400 and 20 mL of diphenyl ether. Subsequently, the reaction mixture was entirely mixed and subjected to thermal treatment under the reflux at 230°C for 3 hours with constant stirring, in the air atmosphere. Afterwards, the as-prepared magnetic nanocomposites were purified from diphenyl ether by adding 40 mL of propan-2-ol and centrifuged at 8000 rpm for

10 minutes. The purification procedure was repeated four times in order to completely remove the remaining DPE and unreacted chemicals. Finally, the pure C@Fe-NPs were dispersed in a small amount of distilled water and separated from weakly magnetic domains by using strong neodymium magnet while non-magnetic solution was discarded. In the final step, the pure nanoparticles were freeze-dried and stored at room temperature.

#### 2.2.4 Carbogenic nanoparticles

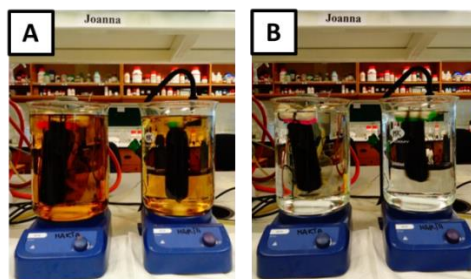
Synthesis of fluorescent carbogenic nanoparticles from citric acid (CA) and ethanolamine (EA) has already been reported by Krysmann et al. At the first step, citric acid (CA) and ethanolamine (EA) were added to the round bottomed flask and mixed in a molar ratio 1:3. Then, the mixture of CAEA was constantly stirred and initially heated at 180°C for 30 minutes with a reflux, in order to promote the formation of highly fluorescent precursor of carbogenic nanoparticles (CAEA180). Then, the temperature was increased up to 230°C and heating continued for next 30 minutes without the reflux, which facilitated the formation of carbogenic cores (CNP230). Afterwards, the orange viscous liquid of CAEA230 was immediately transferred into porcelain crucible (**Figure 2.2A**) and calcine in the oven for 1 hour at 300°C in air (CNP300). After pyrolysis step (**Figure 2.2B**), the carbonaceous material was crushed into smaller particles with the use of mortar and pestle.



**Figure 2.2** Pictures showing the transformation of a partially carbonized viscous dark orange material CAEA230 (A) to a black powder of CNP300 (B).

The as obtained powder was either dispersed in distilled water or nitric acid (1.5M or 5M) and heated at 100°C for 16 hours with reflux. The purification procedures were based on removal of carbogeous agglomerates with the use of cellulose nitrate membrane filters (0.1  $\mu\text{m}$ ) for filtration step as well as Snake Skin dialysis membrane

with a molecular weight cut-off 3500 Da for elimination of unreacted nitric acid and impurities (**Figure 2.3A**) through dialysis against distilled water (**Figure 2.3B**).



**Figure 2.3** Photos of the samples suggesting the presence (A) and absence (B) of low molecular weight particles in the dialysis water.

The as prepared nanomaterials were named CNP300non-ox, CNP300oxB and CNP300oxG, respectively. The similar surface functionalization approach was undertaken for the preparation of B-dots from the grass as a carbon source. Briefly, 100 grams of fresh grass was mixed with the minimum quantity of distilled water was thoroughly shredded in a blender. The as prepared mixture was transferred into porcelain crucibles and heated at 300°C for 4h. Afterwards, the oxidation of B-dots with 5M nitric acid was undertaken at 100°C for 16 h. The carbon product was then thoroughly filtered through cellulose nitrate membrane filter (0.1  $\mu\text{m}$ ) and purified from the residue of nitric acid with the use of Snake Skin dialysis membrane (MWCO = 3500 Da). The purified carbon dots solutions were subsequently placed in the freezer and then freeze-dried for 5 days. The final nanomaterials due to the hygroscopic nature were stored in a closed container at room temperature. Afterwards, all samples were stored in a closed container at room temperature, due to their hygroscopic nature.

### 2.2.5 Chitosan-carbon dots based nanocomposites

Synthesis of biodegradable chitosan-based nanocomposites with embedded carbon dots into their polymeric networks were based on a novel protocol at room temperature. At the first step, 0.2 g of low molecular weight chitosan was mixed in round bottom flask with 80 mL of 0.1 M acetic acid (AA) and further sonicated for 60 minutes. Afterwards, a small crystal of 4-(dimethylamino)pyridine (DMAP) was added

to 25 mL of tetrahydrofuran and that basic solution was transferred to previously ultrasonicated mixture. At the last step, previously freeze-dried C-dots powder (molar ratio 1:2 with chitosan) was added along with 3 mmol of N,N'-dicyclohexylcarbodiimide (DCC). The reaction took place at room temperature for 24 hours in the air atmosphere. Subsequently, the white crystals of a dicyclohexylurea (DCU) by-product were separated from the reaction mixture with the use of centrifuge (10000 rpm for 5 minutes). The supernatant was transferred to another conical flask and subsequently centrifuged again (10000 rpm for 5 minutes) while the white co-product was discarded. Finally, the nanocomposite aqueous dispersion without DCU residue was transferred into the round-bottom flask and connected to rotary evaporator for complete evaporation of organic solvents. The concentrated solution was centrifuged once again (10000 rpm for 5 minutes) and subsequently poured into the SnakeSkin dialysis membrane (with a molecular weight cut-off 3500 Da). The samples were dialyzed against distilled water to remove unreacted DCC and DMAP for 2 weeks with regular replacement of water. The final pure CS-CNP solutions were transferred into plastic bottles and put to the freezer for 24 hours. In the last step, samples were freeze dried for 5 days and then stored at room temperature.

#### **2.2.6 CS-CNP@Vancomycin drug delivery nanosystem**

Synthesis of CS-CNP nanocomposite conjugated with the antibiotic vancomycin hydrochloride was similarly based on the use of DCC coupling method. Thus, as described above 0.2 g of LMW chitosan was mixed with 80 mL of 0.1 M AA and sonicated for 60 minutes. Afterwards, 0.1 g of carbon dots powder and 0. g of vancomycin hydrochloride were added to the chitosan solution and properly mixed. Subsequently, a small crystal of DMAP was added to 25 mL of tetrahydrofuran and that basic solution was transferred into nanocomposite-drug mixture, followed by addition of 8mmol of DCC reagent into the reaction mixture. The reaction took place at room temperature for 24 hours in the air atmosphere. Subsequently, identical to abovementioned purification procedure was applied for the removal of reaction by-product. The collected supernatant was transferred into the SnakeSkin membrane



(MWCO= 3,5 kDa). The dialysis last for 2 hours in order to remove uncovalently bounded drug molecules as well as unreacted DMAP and DCC traces. Final product were freeze-dried for 5 days and then stored at ambient temperature.

## **2.3 Characterization methods**

### **Chemical analysis**

#### **2.3.1 X-Ray Photoelectron Spectroscopy (XPS)**

X-ray photoelectron spectroscopy (XPS) constitute the most common analytical technique for surface chemical analysis as well as general characterization of nanoscale materials. As a quantitative technique is often utilized to elucidate the elemental composition, electronic structure as well as oxidation states of elements in examined material. Additionally, the XPS analysis constitute a useful tool to study ligand exchange interactions, core-shell structures and generally surface functionalization of nanomaterials [2].

XPS analysis was carried out with the use of ESCA2SR spectrometer (Scienta Omicron GmbH) equipped with a monochromatic Al K $\alpha$  X-ray radiation source (1486 eV) with 15 mA emission at 300 W. Any differential charging effects were removed using a charge neutralising low-energy electron gun (FS40A, PREVAC) under X-ray illumination. High resolution core level scans were measured with a pass energy of 20 eV, and overview surveys with 80 eV pass energy. Gaussian-Lorentzian peak shapes were used in CASAXPS for spectral deconvolution.

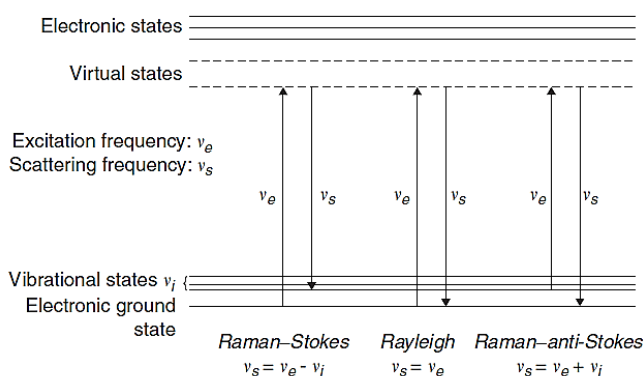
#### **2.3.2 Fourier-transform Infrared Spectroscopy (FTIR)**

Fourier-transform Infrared spectroscopy constitute an analytical technique which measures the absorption of an electromagnetic radiation with wavelengths within the mid-infrared region (4000-400 cm<sup>-1</sup>). The collected spectrum gives information about the position of bands, which correspond to the strength and nature of particular bonds. The determination of specific functional groups provide useful information about molecular structures of analysed materials as well as molecular interactions [2].

Fourier Transform Infra-Red (FT-IR) spectra were recorded using NICOLET IS5 spectrometer (Thermo Scientific, USA), in the absorbance mode. Samples were scanned 128 times at a resolution of  $2\text{ cm}^{-1}$ , in the range of  $3750\text{--}650\text{ cm}^{-1}$ .

### 2.3.3 Raman Spectroscopy

Raman spectroscopy constitute a complementary technique to infrared absorption spectroscopy and probe the molecular vibrations. The main principle grant that during the scattering process of the light a molecule is getting excited to a virtual state and returns instantly to the ground state while re-emitting the light. The energy of the light define the type of scattering process. In detail, the energy of the scattered light can be higher than the energy of incident light (Raman–anti-Stokes scattering) or lower than that of incident light (Raman–Stokes scattering) as well as photons can diffuse without any changes in energy (Rayleigh scattering). These changes are related to the energy of characteristic vibrations of the molecule or crystal (**Figure 2.4**) [4].



**Figure 2.4** The energy-level diagram representing the states involved in Raman spectra  
(Adapted from Ref. 4).

Raman spectra were collected using a HR800 Raman spectrometer equipped with microscope state (Horiba Jobin-Yvon) and the laser operating at  $\lambda = 532\text{ nm}$ . Sample was scanned 256 times in the range of  $1000\text{--}2000\text{ cm}^{-1}$  at room temperature. The LabSpec6 software was used for further analysis of the results.

### 2.3.4 Nuclear Magnetic Resonance Spectroscopy (NMR)

Nuclear magnetic resonance spectroscopy is a non-destructive technique which can reveal the number of protons and carbon atoms along with their connectivities, relative and absolute stoichiometries as well as the conformations of the organic molecules from the analysis of the chemical shifts of nuclei. The determination of the molecular structure of several organic compounds can be done with the use of  $^{13}\text{C}$ -NMR as well as  $^1\text{H}$ -NMR, which analyse the spin-spin couplings and the chemical shifts of protons. The carbon NMR spectra provides the information regarding the number and types of carbon atoms as well as indicate the presence of functional groups with at least one carbon atom (e.g. ketone, alkanes, ester, imines, alkenes, amide carbonyls) [5].

Hydrogen-1 ( $^1\text{H}$ ) and Carbon-13 ( $^{13}\text{C}$ ) NMR spectra were recorded using Bruker Advance-III spectrometer operating at 300 MHz for  $^1\text{H}$  and 75 MHz for  $^{13}\text{C}$ , with tetramethylsilane (TMS) as an internal standard. The samples were dissolved in deuteriodimethylsulfoxide (d-DMSO) and scanned 128 times ( $^1\text{H}$ -NMR) or 1024 times ( $^{13}\text{C}$ -NMR) at ambient temperature, using a 5mm NMR tube (Wilmad LabGlass, USA).

### 2.3.5 UV-Visible Spectroscopy (UV-VIS)

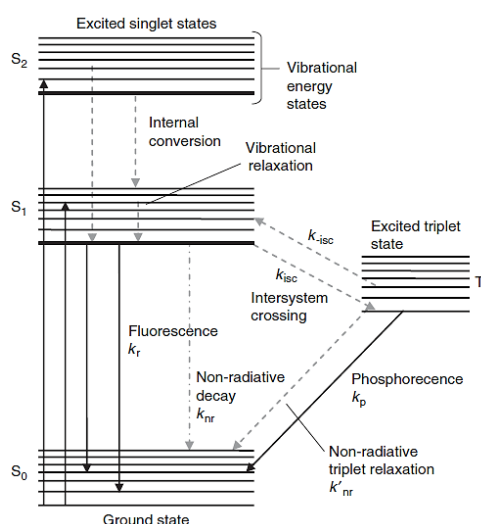
The Ultraviolet-visible spectroscopy is a quantitative analytical technique which investigate the absorption of near-ultraviolet (180-390 nm) or visible (390-780 nm) radiation by various materials in the solution. Generally, the organic compounds which contain chromophores possess an ability to absorb energy in the near-UV region owing to  $n \rightarrow \pi^*$ ,  $\pi \rightarrow \pi^*$ ,  $n \rightarrow \sigma^*$  and  $\sigma \rightarrow \sigma^*$  transitions. Usually, the majority of transitions involve the promotion of  $n$  or  $\pi$  electrons towards the  $\pi^*$  excited state and therefore benefit the molecule with delocalized  $\pi$  electrons. Nevertheless, the nature of the substituents in the conjugated system determines the maximum absorption wavelength of an examined material [6].

The absorption spectra were recorded using UV-3600 spectrophotometer (SHIMADZU, USA). Diluted aqueous solutions with concentration 0.1 mg/mL were placed in Hellma Analytics quartz cuvette (1.0 cm pathlength). Deionized water with a

resistivity of 15.6 MΩ cm was used for majority of experiments and phosphate buffer saline 7.4 was applied for drug release studies. The measurements were collected at room temperature.

### 2.3.6 Fluorescence Spectroscopy (PL)

Fluorescence spectroscopy is a very sensitive tool for biophysical and biochemical studies. Generally, the electron in the ground molecular orbital state absorb the energy and transfer upon the higher unoccupied molecular orbital which is called an excited state of the electron. The photoluminescence phenomena refers to the emission of light from the fluorescent materials which excited electrons returns to the ground-state orbitals and emit photons with various emission intensities. The variety of the molecular transitions of electrons are illustrated by the Jablonski diagram, depicted in **Figure 2.5**.



**Figure 2.5** The schematic presentation of the Jablonski diagram (Adapted from Ref. 7).

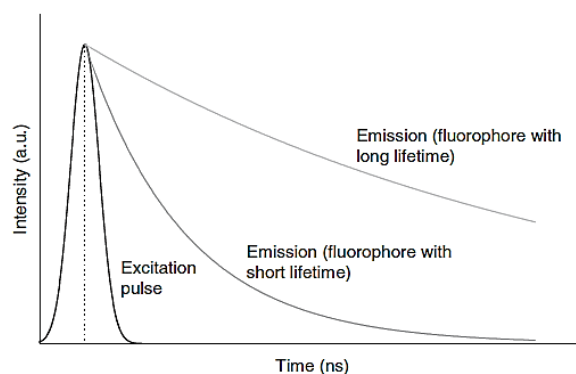
The emission spectra recorded by spectrofluorometer demonstrates the wavelength distribution of a measured emission at a chosen excitation wavelength. Depending on the emission pathway and the electronic configuration of the excited state, the sample could reveal phosphorescence or fluorescence. The molecules which are undergoing an electronic transitions resulting in fluorescence are named fluorophores or fluorochromes [7].

The liquid-state photoluminescence (PL) spectra were recorded at room temperature using FluoroMax-4 spectrofluorometer (HORIBA Scientific). The excitation wavelengths were varied from 275 nm to 500 nm, with the fixed increment of 25 nm, unless otherwise stated. The emission spectra were recorded in the range of 300-650 nm. The aqueous dispersions of the samples with concentration 0.01 mg/mL were transferred into Hellma Analytics quartz cuvette (1.0 cm pathlength). Deionized water with a resistivity of 15.6 MΩ cm was used in all the experiments. On the contrary the solid-state photoluminescence (PL) measurements were conducted for the excitation wavelengths varied from 300 nm to 580 nm, with the fixed increment of 40 nm. The emission spectra were recorded in the range of 320-750 nm. Importantly, for the collection of solid-state PL spectra, a sample holder was positioned at 30 degree angle from incident beam, in order to protect detector from a potential damage [8].

### **2.3.7 Fluorescence lifetime**

The PL lifetime constitute a complementary analysis to the emission spectra and determines the time available for the fluorophore to interact or diffuse in its environment. Thus, the evaluation of this characteristic time enable to estimate how long the fluorophore stays in the excited state before returning to the ground state. For the measurements of a fluorescence lifetime two different methods could be used: the time-domain and the frequency-domain. The time-domain method relies on the measurement of the fluorophore time-dependent emission intensity while following the excitation. In detail, after the exposition of luminescent material to a pulse of light, the fluorophores move to the excited state and create an initial population of a fluorophores. Subsequently, the initial population of fluorophores decay exponentially with time, owing to the non-radiative processes and fluorescence emission. In result, the PL lifetimes of fluorophore are deducted from the slope of the decays represented as a logarithm of emission intensity versus time.

The fluorescence decay following pulsed excitation is schematically presented in **Figure 2.6** [7, 8].



**Figure 2.6** The scheme presenting the possible fluorescence decays upon pulsed excitation while emitted fluorescence is measured in a time-resolved manner (Adapted from Ref. 7).

The decay of fluorescence intensity as a function of time in a uniform population of excited fluorophores is described by an exponential function. The monoexponential nature of decay indicates only the presence of fluorophores population with longer PL lifetimes while the multiexponential decay suggest the presence of several time components displaying a short lifetimes [7].

In this research, the photoluminescence lifetime decays were recorded by Edinburgh Instruments LifeSpec-II time-resolved fluorescence spectrometer, equipped with two high-repetition rate picosecond pulsed diode lasers (EPL-375 and EPL-450) with a 5 MHz repetition pulse rate, operating at 375 nm and 450 nm (Edinburgh, UK). The detector signals were transformed by using time-correlated single photon counting (TCSPC) data acquisition unit (Edinburgh Instruments, UK). The PL lifetime decays for aqueous dispersions of analysed samples were measured in quartz cuvette Hellma Analytics (10 mm light path) at room temperature, over 200 ns time range and 10 000 peak counts. Deionized water was used in all experiments. The solid-state PL lifetime decays of fluorescent nanopowders were collected by using a solid-state samples holder (Edinburgh Instruments, UK). The instrument response function (IRF) was measured at the same experimental parameters with the use of either quartz cuvette filled of aqueous dispersion of colloidal silica (LUDOX HS-30) or empty quartz slides (0.5 mm pathlength), while samples were in liquid or solid state, respectively. The PL lifetime values of  $\tau_1$  and  $\tau_2$ , were generated through following non-linear deconvolution algorithm:

$$R(t) = A_1 e^{(-\frac{t}{\tau_1})} + A_2 e^{(-\frac{t}{\tau_2})}$$

Where:  $\tau_1, \tau_2$  – lifetime components from time-resolved photoluminescence decays,  $A_1, A_2$  – fractional contributions of time-resolved decay lifetimes of  $\tau_1$  and  $\tau_2$  [9].

The quality of as calculated bi-exponential deconvolution fitting was further estimated by comparison of chi-square values ( $\chi^2$ ) and distribution of residuals, approximate to 1. The amplitude-weighted average PL lifetimes ( $\tau_{avg}$ ) were calculated using subsequent equation:

$$\tau_{avg} = \frac{\sum \alpha_i \tau_i^2}{\sum \alpha_i \tau_i}$$

Where: where  $\tau_i$  is the time component of multiexponential decay fitting and  $\alpha_i$  is the fractional weight for each lifetime component [9] .

On the contrary to steady-state data, time-resolved measurements give more information about the PL behaviour and are especially useful for the investigation of the interaction of examined phosphors with other biomolecules as well as help to determine the static and dynamic quenching.

### 2.3.8 Quantum yield measurements (QY)

The quantum yield (QY) is defined as a number of emitted photons relative to the number of absorbed photons and together with the fluorescence lifetime is one of the most significant characteristics of the fluorophore. The estimation of QY for a studied fluorophore is carried out by its comparison with highly fluorescent dyes, which constitute a group of reference standards with well-known quantum yield. Determination of the quantum yield could be accomplished by comparison of the wavelength integrated intensities of examined samples to those of reference dyes, which were excited by light source at the same wavelength. In general, the higher value of quantum yield define the ability of the sample to display the brighter emission [8]. Quantum yield measurements of liquid dispersions of carbon-based nanomaterials were calculated using following equation:

$$\Phi = \Phi_R \times \left( \frac{m}{m_R} \right) \times \left( \frac{\eta^2}{\eta_R^2} \right)$$

Where:  $\Phi_R$  - the quantum yield of a reference dye,  $m$  - the slope calculated from linear regression of tested material,  $m_R$  - the slope calculated from linear regression of reference dye,  $\eta^2$  - the refractive index of water and  $\eta_R^2$  - the refractive index of ethanol [10, 11]. The anthracene ( $\Phi = 0.27$ ), fluorescein ( $\Phi = 0.79$ ), rhodamine 6G ( $\Phi = 0.95$ ) and rhodamine B ( $\Phi = 0.70$ ) were dissolved in ethanol and used as standard reference dyes with excitation wavelengths 365 nm, 425 nm, 480 nm and 510 nm, respectively [12-14]. The HPLC grade water was used for preparation of extra pure aqueous solutions of examined nanomaterials. All the measurements of absorbance (UV-3600 spectrophotometer, SHIMADZU) as well as integrated PL intensity (FluoroMax-4 spectrofluorometer, HORIBA Scientific) were done using Hellma Analytics quartz cuvette with 1.0 cm pathlength. The absorbance values were kept below 0.1, in order to minimize the re-absorption effects.

### 2.3.9 Elemental Analysis

Elemental analysis was used both as qualitative as well as quantitative technique and allowed to determine the presence of main organic components, such as carbon, hydrogen, nitrogen and oxygen. In this technique, an organic material has undergone oxidative decomposition, which lead to the formation of carbon dioxide, water and nitric oxide. The masses of combustion products are subsequently used for the calculation of the unknown samples [24].

In this research, elemental analysis was performed using Flash 2000 CHNS-O Analyzer (Thermo Scientific, UK). Prior the analysis, the equipment was calibrated using a non-measurable pan (called bypass) and followed by the 3 runs of a minor amount of the standard 2,5-(Bis(5-tert-butyl-2-benzo-oxazol-2-yl)thiophene, known as a BBOT (Themro Scientific, UK). The CHN-analysis was carried out in the aluminium pans (CE INSTRUMENTS, UK) while for O-analysis silver pans (CE INSTRUMENTS, UK) were used. The analysis was performed in duplicates for each sample.



## Morphological analysis

### 2.3.10 Powder X-ray Diffraction (PXRD)

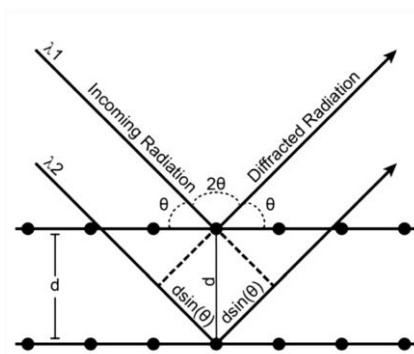
The powder X-ray diffraction is a non-destructive technique used to determine the phase identification of various materials. In case of nanoparticles, XRD is one of the most extensively used techniques which provides information about their crystalline structure, crystalline grain size, lattice parameters and nature of the phase [2].

The crystalline material coherently diffract while the interval between crystal lattice planes implement the Bragg's law. This law implies that the integer value of the wavelength corresponds to the distance between the parallel atomic planes and the angle of the diffracted beam, as described by the following formula:

$$n\lambda = 2d_{hkl} \sin\theta_{hkl}$$

Where:  $\theta$  - the angle of the diffracted beam comparative to the crystal lattice plane,  $\lambda$  - the wavelength of an incident beam,  $n$  - positive integer and  $d_{hkl}$  - the interplanar distance of plane hkl [3]

The schematic visualization of a set of parallel atomic planes separated by the distance ( $d$ ) within the crystal lattice is depicted in **Figure 2.7**.



**Figure 2.7** Schematic explanation of the Bragg's law conditions (Adapted from Ref. 3).

PXRD patterns were collected using the X-Ray diffractometer D2 Phaser (Bruker, Germany) coupled with a LYNXEYE 1-dimensional detector which suppresses the fluorescence of a sample. The wavelength of the X-rays was equal to  $1.54\text{\AA}$  using a Cu source at a voltage of 30 kV. All samples were scanned in the range of 2Theta from  $5^\circ$

to 80° with the use of 0.01 step width as well as a 1 second time count. The divergence slit was equal to 1 mm while the scatter slit was 0.6 mm. The examined materials were exposed to X-ray radiation for 60 minutes, unless otherwise stated.

### **2.3.11 Dynamic Light Scattering (DLS)**

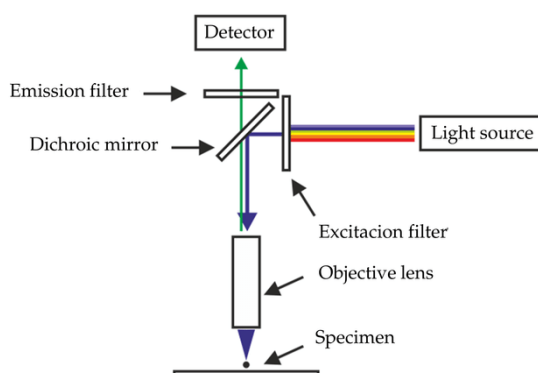
Dynamic Light Scattering is a very powerful technique used for studying the diffusion behaviour of the macromolecules in the solution. The random movement of the particles in the solution - known as Brownian motion - results from their collision with solvent molecules and is relevant to the size of particles. The particles movement in the solution depends on the solvent viscosity, temperature as well as the size of analysed macromolecules. The small particles move faster without a specific position while the large particles diffuse slowly, resulting a similar positions at different time points [18]. The DLS technique also enable to estimate the stability of colloidal dispersions through the zeta potential ( $\zeta$ -potential) measurements. The value for  $\zeta$ -potential of a colloidal NPs dispersion in the range of  $\pm 20$ –30 mV or higher suggest that particles tend to repel each other and form stable colloidal dispersions with minor tendency to agglomerate. This property can be tuned by modification of the surface chemistry of nanoparticles while the stabilisation of colloidal suspensions is made through electrostatic repulsions. The composition of the solvent, presence of other additives or concentration of the suspension influence on the zeta potential values [2].

The DLS measurements were performed using Malvern Zetasizer Nano-ZS (Malvern Instruments, UK) equipment with a He-Ne laser operating at  $\lambda = 633\text{nm}$ . The examined solutions were filtered through membrane filters with a pore size 0.2-0.45  $\mu\text{m}$  (Sartorius Minisart) in order to remove residue of dust and subsequently diluted several times.

### **2.3.12 Fluorescence Microscopy**

Fluorescence microscopy is a highly sensitive imaging technique which enable the visual detection of fluorescence signal from illumined fluorophore-rich sample. As demonstrated in **Figure 2.8**, the specimen is illuminated with a light of particular wavelengths which is absorbed by fluorophore molecules and emitted back of longer

wavelengths, revealing a different colours than absorbed light. The entire filtering of the exciting light without blocking the emitted fluorescence enable to capture the signal only from the fluorescent molecules. The use of a spectral emission filter enables the separation of illuminated light from significantly weaker emitted fluorescence. The dichroic beam splitter and filters are selected accordingly to the emission characteristics of a particular fluorophore which is used for labelling the specimen. In this manner, a multi-colour images of several types of fluorophores have to be composed from the distribution of a single fluorophore at a time [15].



**Figure 2.8** The schematic illustration of the fluorescence microscope (Adapted from Ref. 16).

Fluorescence Microscopy images of fluorescent powders or HeLa cancer cells with internalized fluorescent nanoparticles were obtained via Zeiss Axio Scope A1 microscope equipped with band-pass filters of different excitation wavelengths: 366 nm (UV excitation), 488 nm (blue excitation) and 512 nm (green excitation), which corresponded to DAPI, GFP and Texas Red dyes, respectively.

### **2.3.13 Scanning / Transmission Electron Microscopy (SEM, STEM, TEM)**

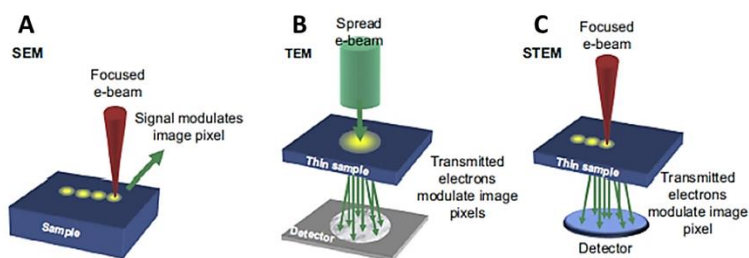
Both TEM and SEM generate a highly focused beam of electrons which have an impact on the analysed specimen inside the vacuum chamber. However, the TEM microscopes are primarily designed to study the internal structure of specimens while SEM microscopes are utilized to examine the materials surface.

In **Scanning Electron Microscopy (SEM)** the electron beam is focused on a particular spot and sequentially scanned across the sample (**Figure 2.9A**). Signals are emitted from analysed material at each spot and collected by detector, which synchronize the

received signal with location of the beam on the specimen. The collected in series signals are combined and create the SEM image. In this case, the typical applied electron energies are in the range 1 to 30 eV.

In **Transmission Electron Microscopy (TEM)** the electron beam is incident onto a defined area of the analysed sample, as displayed in **Figure 2.9B**. The transmitted through the specimen electrons are focused by lenses and accumulated by a parallel detector to form an image. Electron energies are much higher in TEM, usually within the range of 80 to 300 kV accelerating voltage, in order to penetrate through the analysed material.

In **Scanning Transmission Electron Microscopy (STEM)** the electron beam is focused at the fine spot, which is scanned over the sample in a raster, in contrast to conventional TEM, as demonstrated in **Figure 2.9C** [17] .



**Figure 2.9** Scheme of SEM (A), TEM (B) and STEM (C) imaging techniques (Adapted from Ref. 17).

The SEM images were obtained by JCM-6000PLUS benchtop SEM at 10 kV. Thin layer of nanocomposites powders were deposited on a carbon coated copper grid (Agar Scientific, USA) and blown with compressed air to remove detached powder.

The STEM images were captured by performed by using JEOL-JSM-7001F at 20-30 kV accelerating voltages. A droplet of sample was deposited on a carbon coated copper grid and left to dry in the air. The initial concentration of aqueous dispersion of analysed nanomaterials was about 1mg/mL and diluted several times to prevent nanoparticles aggregation.

The TEM images were obtained by A FEI T12 Spirit microscope operated at 120 kV accelerating voltage. A droplet of sample (0.05 mg / 1 mL in water or ethanol) was deposited on a carbon coated copper grid (Agar Scientific, USA) and dried under air.

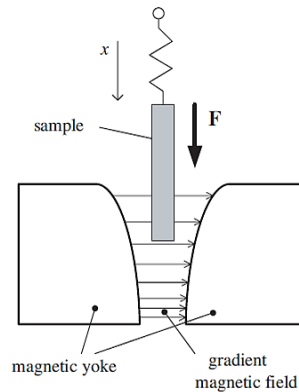
## Magnetic analysis

### 2.3.14 Faraday force magnetometry

Faraday force magnetometry is one of the techniques used to measure the magnetic susceptibility of nanomaterials, thus defining their magnetic properties. The magnetic susceptibility is usually examined over a range of temperatures and indicates whether analysed material is repelled out or attracted into magnetic field. Therefore, these measurements are a key in order to establish the possible implications of magnetic nanoparticles for practical applications [2]. By definition, the magnetic susceptibility is described as a ratio between magnetization ( $M$ ) of the material in the magnetic field and the field intensity ( $H$ ), as presented by the following formula:

$$M = \chi_m H$$

The calculated values of  $\chi_m$  allow to classify the magnetic materials into one of three groups: paramagnetic ( $0 < \chi_m < 1$ ), diamagnetic ( $-1 < \chi_m < 0$ ) or ferromagnetic ( $\chi_m > 1$ ) [19]. The estimation of magnetic susceptibility using a Faraday method rely on measuring the change of sample weight by sensitive microbalance after applied magnetic field, as presented in **Figure 2.10**.



**Figure 2.10** The scheme presenting the principle of Faraday balance utilized for magnetic susceptibility measurements (Adapted from Ref. 19).

The magnetic force acting on the examined sample in magnetic field with gradient in direction  $x$  can be further calculated using the following formula:

$$F = \Delta mg$$

Where:  $\Delta m$  – mass change,  $g$  – gravitational constant

The calculated  $F$  value can be further used to indicate the magnetic susceptibility of examined material accordingly from the following formula:

$$F = \mu_0 \chi_m V H \frac{dH}{dz}$$

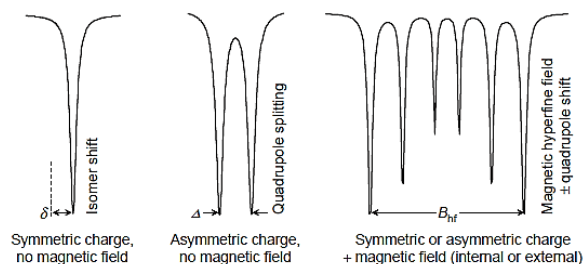
Where:  $\mu_0$  – magnetic permeability,  $\chi_m$  - magnetic susceptibility,  $V$  – volume of the sample,  $H$  – magnetic field strength,  $\frac{dH}{dz}$  – the magnetic field gradient along the  $z$ -direction [19]

The significant advantage over the susceptibility measurements is that the magnetic signal is usually independent on the size of particles and can be determined only by their total weight. On the other side, among disadvantages is the necessity of measuring the magnetic signal only in the presence of excitation field [2]. Additionally, during magnetization measurements the estimation of the blocking temperature can be done by employing the zero-field-cooled/field-cooled procedure, in which the sample is cooled from room temperature in a magnetic field (FC) as well as zero magnetic field (ZFC). At first, magnetization is recorded on warming and a small magnetic field is applied ( $\sim 100$  Oe). The rise of temperature disturbs the system while more moments acquire the thermal energy to be aligned with the external field direction. Then, the number of unblocked and aligned moments reach a maximum at blocking temperature. Nevertheless, above blocking temperature the thermal energy is sufficient to randomize the magnetic moments, which impact on diminished magnetization [20, 21].

Magnetization curves of the solid samples were obtained by using a low temperature Faraday balance magnetometer with a continuous flow cryostat. The additional magnetic measurements for the most magnetic samples were carried out at the VSM option of the Quantum Design PPMS apparatus in the temperature range 4 – 300 K.

### 2.3.15 Mössbauer spectroscopy

Mössbauer spectroscopy is based on the Mössbauer effect consisting on recoil-free absorption and emission of gamma rays in solid samples. Similarly to NMR spectroscopy, this technique probes very small changes in the energy levels of an atomic nucleus in response to its environment. The  $^{57}\text{Fe}$  Mössbauer spectroscopy is especially used to estimate the composition of the magnetic nanoparticles based on magnetite and maghemite mixtures as well as the stoichiometry between both iron oxides. In the Mössbauer spectra Fe(III) and Fe(II) can be readily differentiated due to their distinct isomer shifts, which correspond to various types of nuclear interactions, such as an isomeric split, quadrupole splitting, as well as magnetic or hyperfine splitting (**Figure 2.11**). The  $^{57}\text{Fe}$  Mössbauer spectra can provide details about the local structural and chemical environments around the iron nuclei, thereby allowing the determination of Fe-containing phases and quantitative analysis of their relative proportions [2, 22].



**Figure 2.11** The representative shapes of  $^{57}\text{Fe}$  Mössbauer spectra of iron-bearing materials (Adapted from Ref. 22).

$^{57}\text{Fe}$  Mössbauer measurements have been carried out in the transmission mode at a constant acceleration spectrometer. A source of 50 mCi  $^{57}\text{Co}$  in rhodium matrix has been used. External magnetic field of induction of 0.5 Tesla was produced by a set of neodymium permanent magnets.

## **Thermal analysis**

### **2.3.16 Thermogravimetric Analysis (TGA)**

Thermogravimetric analysis is a thermal analysis method which investigate the change of sample weight over time while being subjected to increasing temperature. With this technique, the thermal treatment of nanomaterials leads to the decomposition and vaporisation of its components, which possess various degradation temperatures. The temperature and the change of weight are monitored by the TGA device and used for calculation of mass loss while taking into account the weight of starting material. Thus, the final results could be used to estimate the oxidation and thermal stability of nanomaterials. The analysis of TGA curves of various materials allows to determine the loss of volatile or gaseous products executed during several thermal events, such as desorption, decomposition, vaporisation or reduction [2, 23].

The thermal stability of several nanomaterials was carried out using TGA Q500 (TA Instruments, UK). Samples were heated over the range of 25-500°C at a heating rate of 10°C/min, under a continuous flow of nitrogen.

## **Biological analysis**

### **2.3.17 Bacterial culture techniques**

#### **2.3.17.1 *Escherichia coli* and *Staphylococcus aureus* bacterial strains**

Two different kinds of bacterial species can be distinguished: Gram-positive bacteria as well as Gram-negative bacteria. In detail, Gram-positive bacteria possess a thick cell wall with many layers, which consist of peptidoglycan and teichoic acids, whereas Gram-negative bacteria have rather a thin few-layer but more complex cell wall [68, 69]. Thus, in this research the antimicrobial activity was estimated against Gram-negative *Escherichia coli* and Gram-positive *Staphylococcus aureus* bacterial species.

#### **2.3.17.2 Sterilisation procedure**

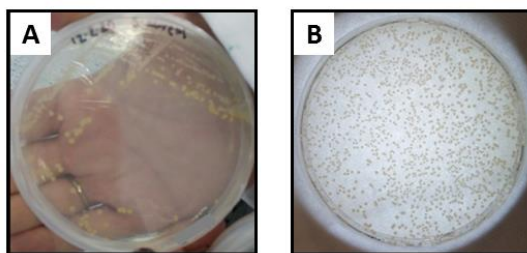
Prior conducting any cell culture work with either bacterial or mammalian cells, C-dots solutions were autoclaved at 121°C for 20 minutes. The implementation of sterilisation



process assured the absence of viable microorganisms in tested C-dots dispersions, which presence could lead to false results [24]. Nevertheless, the use of elevated temperatures for decontamination of nanoparticles solutions may have a negative impact on their morphological, structural and optical properties [24, 25]. It was observed that the colour of autoclaved solutions became more clear after sterilisation, thereby confirming nanoparticles degradation. These changes were further linked with negligibly diminished fluorescence intensity at higher temperatures, thus in agreement with previous reports [26]. In regard to literature reports, polymer-based nanoparticles have tendency to form larger aggregates with broad size distribution, after autoclaving their solutions at 100°C [25]. On the other side, another studies investigated the effect of autoclaving at 134°C for 40 minutes on the physicochemical properties of PEGylated nanoparticles. In detail, the analysis of TEM images prior and after autoclaving confirmed minor aggregation of nanoparticles, whereas additional FTIR spectra showed no changes in the poly(ethylene glycol) coating [27].

#### **2.3.17.3 Culturing method**

The culturing method was based on the inoculation of 25 mL of nutrient broth with a single loop of each bacteria from a streak plate (**Figure 2.12A**) and followed by 24 hours incubation at 37°C in a SciQuip Incu-Shake MIDI orbital shaker (SciQuip Ltd, UK) set to 200 rpm. Afterwards, the cultures were centrifuged at 4000 rpm for 10 minutes followed by removal of supernatant and addition of 20 mL of ¼ strength Ringer's solution. The tubes were vortexed and centrifuged again for further 10 minutes at 4000 rpm. Subsequently, the supernatant was discarded and the tubes and vortexed final time after addition of 2 mL of ¼ strength Ringer's solution. Then, re-suspended cultures were diluted in nutrient broth to give an absorbance reading equivalent to a 0.5 MacFarlane standard as recorded by Biochrom WPA S800 visible spectrophotometer (Biochrom Ltd, Cambridge, UK).



**Figure 2.12** The photos of a streak (A) and control (B) plates with the cultures of *Staphylococcus aureus*.

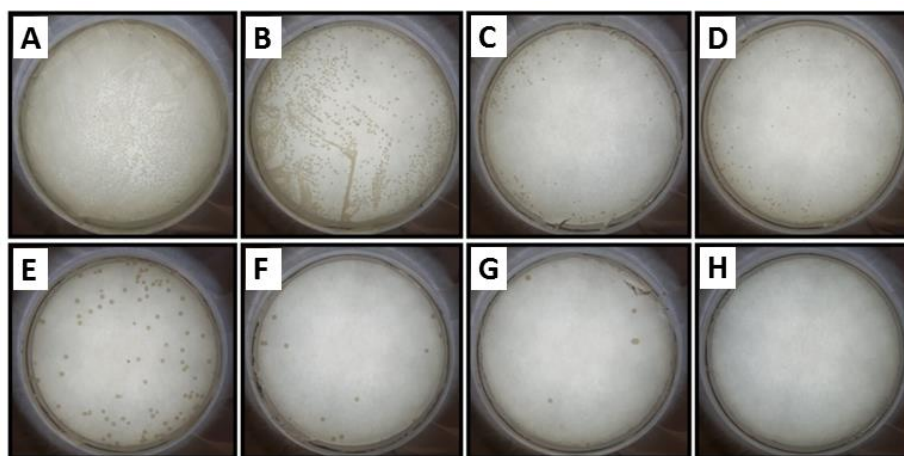
#### 2.3.17.4 Antimicrobial testing

Prior antimicrobial testing, the C-dots solutions as well as pure nutrient broth solution were autoclaved. For preparing C-dots solution,  $0.1\text{g}\pm 0.01\text{g}$  of tested nanoparticles were dissolved in 1 mL nutrient broth. Subsequently, 8mL sterile nutrient broth and 1mL of either *E.coli* or *S.aureus* were added into C-dots dispersions and as-prepared samples were further placed into a shaking incubator set to 200 rpm at  $37^{\circ}\text{C}$ . Separately, 1mL of *E.coli* and *S.aureus* was added separately to each of 8mL sterile nutrient broth and afterwards put into shaking incubator (200 rpm,  $37^{\circ}\text{C}$ ). After incubation intervals equal to 2 and 24 hours, 1 mL aliquot was removed from each sample and serially diluted by adding 100 $\mu\text{L}$  sample into 900 $\mu\text{L}$   $\frac{1}{4}$  strength Ringer's solution. Then, 100 $\mu\text{L}$  of respective dilution was spread onto agar-gelled nutrient plates with the use of sterile plastic spreader. In order to confirm the reproducibility of the results, each dilution was plated in triplicate. Finally, plates were incubated for 24h at  $37^{\circ}\text{C}$  and afterwards used for calculation of bacterial cultures decrease. The agar plates with only bacterial colonies were used as control plates (**Figure 2.12B**). The percentage decrease compared to the control plate was calculated for each test sample using the following formula:

$$\text{Bacterial colony decrease [\%]} = \frac{\text{Control} - \text{Test}}{\text{Control}} \times 100$$

Estimation of colony forming units (CFU) through serial dilution plating on a nutrient agar plates consist the most applied method for monitoring cultivable bacteria. Typically, 30-300 bacterial colonies per agar plate (100 mL sample) constitute acceptable CFU for an accurate counting. Therefore, due to unclear indication of dilution level which leads to the above mentioned colony forming units range, several

nutrient agar plates with different dilutions were prepared, as presented in **Figure 2.13** [28].



**Figure 2.13** The photos of agar spread plates containing different concentrations of *S. aureus* cultures, prepared by ten-fold serial dilution ranging from  $10^{-1}$  (A) up to  $10^{-8}$  (H).

## 2.3.18 Mammalian cell culture techniques

### 2.3.18.1 HeLa cervix cancer cell line

The HeLa cancer cell line was derived from 30-year-old woman named Henrietta Lacks who died in 1951 because of an aggressive adenocarcinoma of the cervix. The cells obtained from her biopsy specimen were placed into culture by applying the roller-tube technique. Subsequently, the cells grew robustly in contrast to previous specimens and became the first human cancer cell line immortalized in tissue culture. Since then, the HeLa cells were used by researchers around the world [29]. In this research, HeLa cells as a well characterised model cell line with fully sequenced genome were used for the evaluation of *in vitro* nanoparticles toxicity, which suitability has been accepted by regulatory bodies (i.e. OECD) [30].

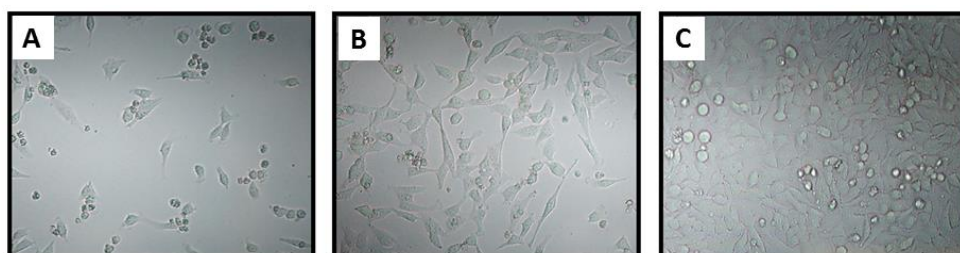
### 2.3.18.2 Recovery of the cells from the cell bank

Frozen HeLa cells were received in a cryogenic vial (1 mL) and were kept in liquid nitrogen before defrosting. The thawing of the frozen cells was carried out by placing the cryogenic vial in a water bath set up to 37°C for approximately 1 minute. Subsequently, thawed cell suspension was transferred to T75 flask with 15 mL DMEM

media in order to further dilute the dimethyl sulfoxide cryoprotectant used for the freezing down procedure. The flask with the cell suspension was incubated for further 24 hours at 37°C and under 5% CO<sub>2</sub>. Afterwards, the attachment of the cells to the wall of T75 flask was investigated under the optical microscope. For the flasks with successfully attached HeLa cells the media with DMSO was discarded and replaced with 10 mL of fresh DMEM media supplemented with high glucose, L-glutamine, 10% Fetal Bovine Serum and 1% Penicillin-Streptomycin antibiotic.

### 2.3.18.3 Subculturing / passaging of adherent cells

The adherent HeLa cells were grown until covered 80-95% of the surface of T75 culture flask (known as confluency), as presented in **Figure 2.14C**. Meanwhile, the confluency of the cells was routinely investigated with the use of optical microscope. The ready to split cells were passaged by aspirating the media from the T75 flask and washing the cells from the media residue by using PBS with the pH = 7.2. Subsequently, 3 mL of 1% trypsin-PBS solution were added into T75 flask and further incubated for 2 minutes at 37°C (trypsinization step). The use of trypsin enzyme effect on detachment of the cells from the wall of the flask, which usually was supported by a gentle tapping of the flask with adhered cells after the short incubation step. The effect of trypsin enzyme was further neutralized by addition of 6 mL of DMEM media. In the last step, the cell suspension was agitated and equally passaged to T75 culture flasks containing 10 mL of DMEM media.

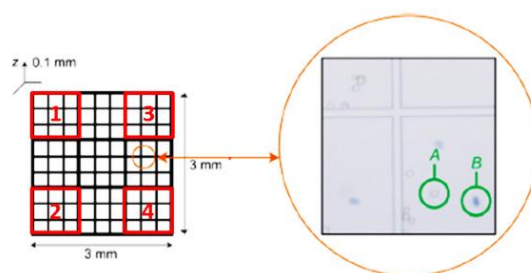


**Figure 2.14** The photos of the cells under the optical microscope after reaching approximately 20% confluency (A), 50% confluency (B) and 95% confluency (C).

### 2.3.18.4 Cell counting using haemocytometer

Neutralized with the media cell suspension after trypsinization step was carefully agitated before transferring a 10 µL aliquot into Eppendorf tube. Secondly, 40 µL of

trypan blue solution (Sigma Aldrich, UK) was added to the collected cell suspension and the Eppendorf tube was vortexed for a few seconds. The 10  $\mu\text{L}$  of trypan blue-treated cell suspension was applied into disposable haemocytometer counting-chamber (C-Chip, NanoEnTek) and evenly redistributed through the capillary action. The haemocytometer consist of two counting chambers while each of them is defined by 9 squares with 1 mm length. The alive and dead cells were counted in four different squares of haemocytometer, as highlighted in **Figure 2.15**. The average of alive cells was further multiplied by 5 (the dilution factor after adding Trypan Blue solution) and next multiplied by  $10^4$ . From the chemical point of view, trypan blue is defined as toluidine-derived dye and consist of a membrane-impermeable molecule which only enters the cells with compromised membranes. Upon entry to the cell, the trypan blue binds to intercellular proteins, resulting in blue colour of the dead cells in the brightfield, On the contrary, the colour of living cells remains unchanged. The cell viability using this dye is estimated indirectly by detecting cell membrane integrity [31].



**Figure 2.15** The schematic representation of the grid of a haemocytometer along with magnified a living cells (A) as well as a blue coloured dead cells (B) (Adapted from Ref. 31).

### 2.3.18.5 Freezing down the cells

In order to have sufficient stock of the HeLa cells for further experiments, the freeze down of the cells was obligatory. After trypsinization step, the trypsin-PBS based cell suspension was neutralized with DMEM media, as described in section 2.2. The cell suspension was further centrifuged for 5 minutes at 1000 rpm and the supernatant removed. The cells were re-suspended in 1 mL of freezing media, which consisted of 90% DMEM culture media and 10% DMSO. After careful agitation the re-suspended cells were added into cryogenic vial and placed into freezing container (Mr Frosty™),

which allowed to keep the optimal cooling rate of -1°C/min for cell preservation. Finally, Mr Frosty™ container was placed for 24 hours in the freezer with temperature -80°C before transferring cells into the liquid nitrogen (-196°C) for long term storage.

### **2.3.18.6 Cell viability determined by MTT assay**

In order to evaluate the cytotoxicity of synthesized nanomaterials against the cancer HeLa cell line, the MTT (3-(4,5-dimethylthiazol-2-yl)-2,5-diphenyltetrazolium bromide) reduction assay was applied. For determination of the cytotoxicity of the nanoparticles, 50µL of HeLa cells with density  $5 \times 10^4$  were seeded in 96-well plates, followed by incubation for 24 hours at 37°C and under 5% CO<sub>2</sub>. Subsequently, 50µL of nanoparticles solutions at various concentrations were added and again incubated for 24 hours 37°C, 5% CO<sub>2</sub>). Afterwards, 20 µL of MTT solution (Sigma Aldrich, UK) with concentration 5 mg/mL were added to each well of 96-well plates and placed in the incubator for 2 hours (37°C, 5% CO<sub>2</sub>). Viable cells with active metabolism possess an ability to convert the MTT tetrazolium into a purple coloured formazan crystals while dead cells lose this ability. The formazan product accumulates inside the cells in the form of insoluble precipitate as well as in the culture medium and around cells surfaces. Prior recording the absorbance readings the formazan product must be solubilized by acidified solubilizing solution which additionally change the colour of phenol red to yellow, resulting in less interference with the absorbance readings [32]. Therefore, in the next step 150 µL of lysis buffer as solubilizing solution was added to each well of 96-well plates and incubated for 3 hours. The final absorbance readings were taken using a plate reading spectrophotometer (Thermo Scientific, UK) at 595 nm wavelength. The cell viability was calculated according to the following equation:

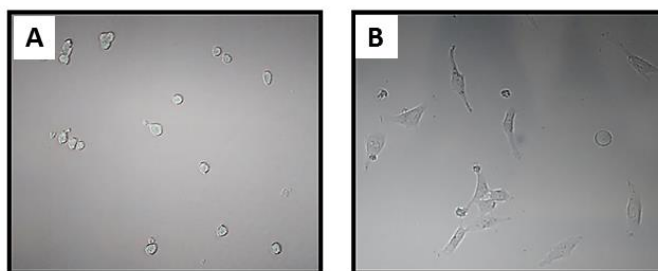
$$\text{Cell viability [\%]} = \frac{\text{OD treated}}{\text{OD control}} \times 100$$

OD treated and controls were obtained in the presence and the absence of fluorescent nanomaterials, respectively. The optical density is closely correlated with the cells viability, assuming the 100% viability for the control sample without addition of any nanoparticles. For the graphs preparation, the percentage viability based on the

received absorbance values were plotted against nanoparticles concentrations. All assays were performed minimum in triplicates.

### 2.3.18.7 Bioimaging

The HeLa cells which reached 80-90% confluency underwent the above mentioned trypsinization procedure. The detached cells were further counted using trypan blue solution on disposable haemocytometer (C-Chip, NanoEnTek). The dispersed in DMEM media HeLa cells with overall density  $0.5 \times 10^4$  were seeded in 6-well plate, equipped with the glass cover slips at the bottom of each well (**Figure 2.16A**). The 6-well plate with the HeLa cells was incubated for 24 hours at 37°C and under 5% CO<sub>2</sub> (**Figure 2.16B**). Subsequently, the NPs solutions with various concentrations were added to each well of 6-well plate and further incubated for 24 hours at 37°C with 5% CO<sub>2</sub>. In the final step, the media was aspirated and the cover slips were washed three times with the phosphate buffer saline 7.2 solution, in order to eliminate the auto fluorescence of the media in the background. The cells samples were placed on microscopy glass slides and examined with the use of Zeiss Axio Scope A1 Fluorescence Microscope at excitation wavelengths: 366nm (UV excitation), 488nm (blue excitation) and 512 nm (green excitation).



**Figure 2.16** The photos of the immature cells adhered to the cover slip (A) and after 24 hours incubation at 37°C (B).

The limitation of bioimaging experiments constitute the autofluorescence of the HeLa cells, which arise from the abundant content of aromatic structures such as NADPH or cellular organelles. In order to overcome this limitation, the HeLa cells were investigated under the fluorescence microscope (results not included here) prior addition of NPs dispersions and the comparison of the PL intensity of control sample (only cells) was significantly diminished, in contrast to the cells with internalized NPs.

In addition, another limitation constitute also the residue of the cell culture media, which due to the content of phenol red can interfere with recorded fluorescence signal. Therefore, careful sample preparation step is crucial prior bioimaging experiments.

### **2.3.19 Collaborators contribution**

The main part of physicochemical characterisation as well as *in vitro* toxicity studies on HeLa cancer cell line were completed by myself, unless otherwise stated in this paragraph. Nonetheless, the contributions of external collaborators were as the following:

- STEM – the images presented in Chapter 3 were collected by Prof. Engin Burgaz at Ondokuz Mayıs University (Turkey), whereas the uniform scale in all images was adjusted by myself.
- TEM – the image presented in Chapter 4 was collected by Dr Marta Krysmann at Cornell University (USA), whereas the data visualisation and calculations of NPs size distribution was done by myself.
- XPS – the spectra presented in Chapter 3 were collected by Dr Joshua Moore and Professor Stephen Yates at University of Manchester (UK), while the analysis, interpretation and graphical presentation of the data were done by myself. In addition, the spectra demonstrated in Chapter 4 were collected by Dr Anna Szwajca at Adam Mickiewicz University (Poland), whilst the final results were interpreted and described by myself.
- Faraday-type Magnetometer – the measurements and calculations were done under the supervision of Dr Monika Gamża at the University of Central Lancashire (UK), while the graphical visualisation and interpretation of the results were exclusively my own work.
- Vibrating Sample Magnetometer / Mössbauer spectroscopy – the results were conducted and visualized by MSc Elżbieta Gumieniczek-Chłopek, MEng Tomasz Strączek and Professor Czesław Kapusta at AGH University of Science and Technology (Poland). These results constituted only comparative analysis to



magnetisation data collected at UCLan and strengthen the overall conclusion related to magnetic properties of selected samples.

- Antimicrobial studies – in major part the results were collected by BSc Ella Gibbons at University of Central Lancashire (UK), due to the limited access to biological laboratories.

## 2.4 References

1. Krysmann, M.J., et al., *Formation mechanism of carbogenic nanoparticles with dual photoluminescence emission*. J Am Chem Soc, 2012. **134**(2): p. 747-50.
2. Mourdikoudis, S., R.M. Pallares, and N.T.K. Thanh, *Characterization techniques for nanoparticles: comparison and complementarity upon studying nanoparticle properties*. Nanoscale, 2018. **10**: p. 12871-12934.
3. Stan, C.V., et al., *X-Ray Diffraction under Extreme Conditions at the Advanced Light Source*. Quantum Beam Sci., 2018. **2**(4): p. 1-33.
4. Inkson, B.J., *Scanning electron microscopy (SEM) and transmission electron microscopy (TEM) for materials characterization*, in *Materials Characterization Using Nondestructive Evaluation (NDE) Methods*, G. Hübschen, et al., Editors. 2016, Elsevier Ltd. . p. 17-43.
5. Lichtman, J.W. and J.A. Conchello, *Fluorescence microscopy*. Nature Methods 2005. **2**(12): p. 910-919.
6. Lewandowska, R., *Raman Microscopy: Analysis of Nanomaterials*, in *Encyclopedia of Materials: Science and Technology* K.H. Jürgen Buschow, Editor 2001, Elsevier Ltd. p. 1-6.
7. McClure, C.K., *Structural Chemistry Using NMR Spectroscopy, Organic Molecules*, in *Encyclopedia of Spectroscopy and Spectrometry* J.C. Lindon, G.E. Tranter, and D.W. Koppenaal, Editors. 2017, Elsevier Ltd. p. 281-292.
8. Worsfold, P.J. and E.A.G. Zagatto, *Spectrophotometry: Overview*, in *Encyclopedia of Analytical Science* P. Worsfold, et al., Editors. 2019, Elsevier. p. 244-248.
9. Jain, A., C. Blum, and V. Subramaniam, *Fluorescence Lifetime Spectroscopy and Imaging of Visible Fluorescent Proteins*, in *Advances in Biomedical Engineering*, P. Verdonck, Editor 2009, Elsevier. p. 147-176.
10. Lakowicz, J.R., *Principles of Fluorescence Spectroscopy*. Third Edition ed2006, United States: Springer. 960.
11. Fan, R.J., et al., *Photoluminescent carbon dots directly derived from polyethylene glycol and their application for cellular imaging*. Carbon, 2014. **71**: p. 87-93.
12. Eaton, D.F., *Reference Materials for Fluorescence Measurement*. Pure & Appl. Chem., 1988. **60**(7): p. 1107-1114.
13. J. Wang, P.Z., C. Huang, G. Liu, K.C.-F. Leung, Y.X.J. Wáng, *High Performance Photoluminescent Carbon Dots for In Vitro and In Vivo Bioimaging: Effect of Nitrogen Doping Ratios*. Langmuir 2015. **31**: p. 8063–8073.
14. Arbeloa, F.L., P.R. Ojeda, and I.L. Arbeloa, *Fluorescence self-quenching of the molecular forms of rhodamine B in aqueous and ethanolic solutions*. Journal of Luminescence 1989. **44**: p. 105-112.

15. Brouwer, A.M., *Standards for photoluminescence quantum yield measurements in solution*. Pure Appl. Chem., 2011. **83**(12): p. 2213–2228.
16. Kellogg, R.G. and R.G. Bennett, *Radiationless Intermolecular Energy Transfer. III. Determination of Phosphorescence Efficiencies*. J. Chem. Phys., 1964. **41**: p. 3042-3045.
17. Stetefeld, J., S.A. McKenna, and T.R. Patel, *Dynamic light scattering: a practical guide and applications in biomedical sciences*. Biophys Rev, 2016. **8**: p. 409–427.
18. Marcon, P. and K. Ostanina. *Overview of Methods for Magnetic Susceptibility Measurement*. in *Progress in Electromagnetics Research Symposium*. 2012. Kuala Lumpur: The Electromagnetics Academy.
19. Lu, A.H., E.L. Salabas, and F. Schuth, *Magnetic Nanoparticles: Synthesis, Protection, Functionalization, and Application*. Angew. Chem. Int. Ed. , 2007. **46**: p. 1222 – 1244.
20. Barrera, G., et al., *Magnetic Properties of Nanocomposites*. Appl. Sci., 2019. **9**.
21. Murad, E., *Mössbauer Spectroscopy*, in *Handbook of Clay Science*, G.L. Faïza Bergaya, Editor 2013, Elsevier. p. 11-24.
22. Loganathan, S., et al., *Thermogravimetry Analysis for Characterization of Nanomaterials*, in *Thermal and Rheological Measurement Techniques for Nanomaterials Characterization*, S. Thomas, et al., Editors. 2017, Elsevier.
23. Fadeeva, V.P., V.D. Tikhova, and O.N. Nikulicheva, *Elemental Analysis of Organic Compounds with the Use of Automated CHNS Analyzers*. Journal of Analytical Chemistry, 2008. **63**(11): p. 1094–1106.
24. Vetten, M.A., et al., *Challenges facing sterilization and depyrogenation of nanoparticles: Effects on structural stability and biomedical applications*. Nanomedicine, 2014. **10**: p. 1391-1399.
25. Galante, R., et al., *About the Sterilization of Chitosan Hydrogel Nanoparticles*. PLoS ONE, 2016. **11**: p. 1-18.
26. Mohammed, L.J. and K.M. Omer, *Carbon Dots as New Generation Materials for Nanothermometer: Review*. Nanoscale Research Letters, 2020. **15**: p. 182.
27. França, Á., et al., *Sterilization Matters: Consequences of Different Sterilization Techniques on Gold Nanoparticles*. Small, 2010. **6**: p. 89-95.
28. Thomas, P., et al., *Optimization of single plate-serial dilution spotting (SP-SDS) with sample anchoring as an assured method for bacterial and yeast cfu enumeration and single colony isolation from diverse samples*. Biotechnology Reports, 2015. **8**: p. 45-55.
29. Lucey, B.P., W.A. Nelson-Rees, and G.M. Hutchins, *HeLa Cells and Cell Culture Contamination*. Arch Pathol Lab Med, 2009. **133**: p. 1463-1467.

30. Landry, J.J.M., et al., *The genomic and transcriptomic landscape of a HeLa cell line*. G3 (Bethesda). 2013. **3**: p. 1213-1224.
31. Piccinini, F., et al., *Cell Counting and Viability Assessment of 2D and 3D Cell Cultures: Expected Reliability of the Trypan Blue Assay*. Biological Procedures Online, 2017. **19**(8): p. 1-12.
32. Riss, T.L., et al., *Cell Viability Assays*, in *Assay Guidance Manual* A. Grossman and K.e.a. Brimacombe, Editors. 2013, Eli Lilly & Company and the National Center for Advancing Translational Sciences: Bethesda (MD).

# **Chapter 3:**

## **Novel photoactive carbon dots with dual optical properties for bioimaging and pH-sensing applications**

*“One never notices what has been done;  
one can only see what remains to be done”*

*Maria Skłodowska-Curie*

### 3.1 Introduction

To date, various protocols have been developed to prepare highly graphitic carbon dots (gC-dots) with remarkable optical properties, which in similar to C-dots with amorphous carbogenic cores (aC-dots) are based on the top-down and bottom-up methods [1]. Among both, the bottom-up approaches enable to adjust the physical and chemical properties of C-dots in a controlled manner, while utilising diverse small organic molecules as well as carbonization conditions [2]. To that end, an extensive body of literature is centered around the synthesis of gC-dots via the carbonization of simple organic precursors like citric acid (CA) and urea (referred hereafter as CU-dots), owing to their biocompatible character and non-toxic nature [2-11]. So far, CU-dots have been synthesized via the hydrothermal [6-12], solvothermal [13-16], pyrolytic [3, 5, 17] or microwave-assisted [18-24] methods, while using a molar ratio of CA to urea ( $f_{\text{CA/urea}}$ ) as low as 1:3. Besides that, only some reports noted the preparation of CU-dots with  $f_{\text{CA/urea}} \geq 1:10$  [4, 25-32]. Although, the excess of CA in the precursors mixture impacts on the blue colour emission under the ultraviolet light [33], the addition of significant urea content impact on the red-shifting of the maximum fluorescence emission peak towards a green-emissive region [19]. Nonetheless, the optical properties of post-synthesized CU-dots can be also dependent on the applied purification method, among which the most popular are either centrifugation [6-8, 10, 14-16, 19, 20, 23, 26-30, 33-35] or dialysis [2, 4, 11, 21, 32, 36-39]. Besides commonly used citric acid, other carbon-rich sources include the calcium citrate [40] or trisodium citrate [36, 38], whereas dicyandiamide can be used as effective replacement for the urea reagent [39]. To date, CU-dots have been applied as a probe to assay the concentration of  $\text{Hg}^{2+}$  [16], nanotracers for imaging of cancer cells [22, 38], photothermal and *in vivo* theranostic agents [28, 31], antitumor agents that suppress the metabolism of malignant cells [3], biolabelling probes with binding affinity towards the RNA [29], cytocompatible and hemocompatible agents in wound healing applications [15], selective sensors for detecting the dopamine [9] as well as nanoprobe for the detection of metal ions [41] or intracellular pH sensing [39]. Therefore, the enormous potential of CU-dots in biomedical applications constituted

an inspiration for this project that focused on the development of a large gallery of novel materials derived from the CA/urea precursors mixture, which have a potential to be applied as nanotracers for imaging of cancer cells as well as nanoprobe for detection of pH variations.

### **3.2 Novelty and predominance over existing materials**

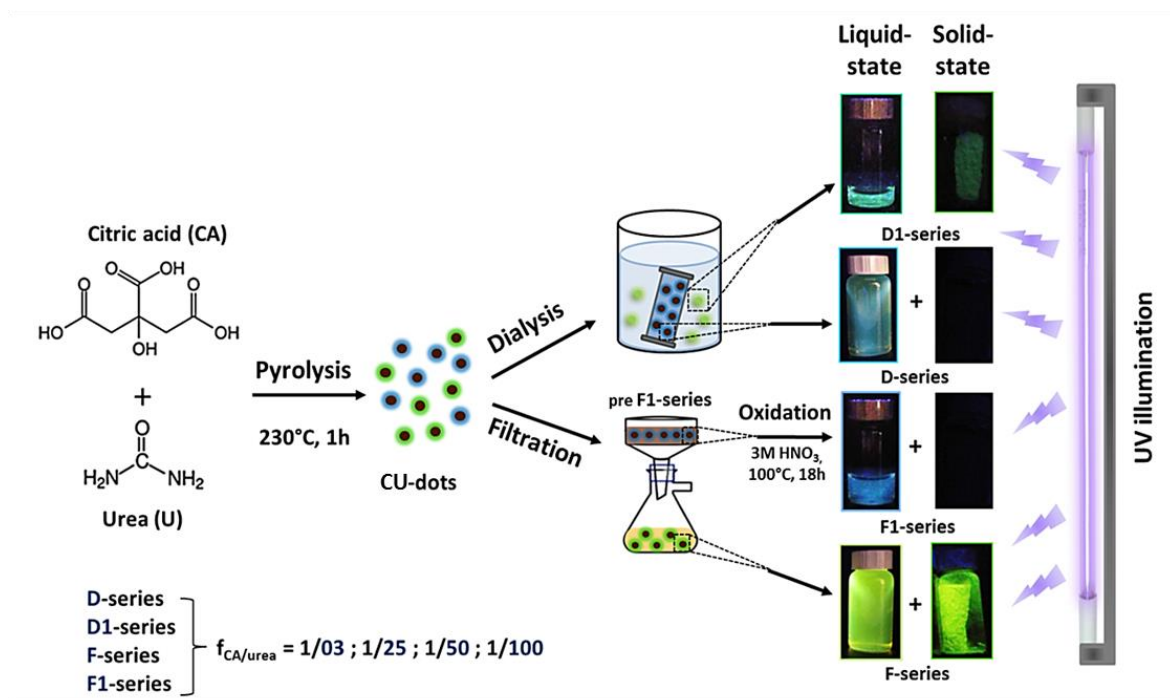
Within the considerable body of literature focused on the fabrication of CU-dots from the CA/urea precursors mixtures [2-24], the present work constitute novel insights into three specific directions. First, the utilisation of versatile pyrolytic approaches led to fabrication of a large gallery of PL materials, while the detailed morphological, structural and optical properties of CU-dots derived from  $f_{\text{CA/urea}} \geq 1:25$  has not been explored yet [42, 43]. Second, the detailed and comparative analysis of optical efficiencies between D-series and F-series facilitated a quantitative assessment of the impact of each molecular fluorophore on the fluorescent properties of CU-dots suspensions. Third, the presented filtration strategy discloses an effective way to produce novel PL powders by using an excessive amount of urea that simultaneously serves as the precursor for the synthesis of molecular fluorophores, the nitrogen and carbon source used for the build-up of carbogenic cores as well as the diluent matrix which suppresses an undesired self-quenching effect [44].

On the contrary to reported materials, the superior advantage of as-prepared CU-dots constitute their fabrication method that utilise only the pyrolytic treatment of precursors mixture in an open reaction vessel [32], thus enable a large scale synthesis as well as give a promise for future commercialization. Besides that, the use of two different purification strategies, either filtration or dialysis, allow to efficiently separate various molecular fluorophores, thereby opens the door for the replacement of tedious column chromatography method. Nevertheless, in the midst of disadvantages are diminished optical efficiencies of D-series CU-dots, that were affected by significantly prolonged dialysis step (12 weeks) in contrast to previous reports (e.g. 1 day) [24].

### 3.3 Results and discussion

The summary of the synthetic and purification strategies that were used for the fabrication of a large gallery of photoluminescent suspensions and powders from the CA/urea precursor mixtures is highlighted in the **Figure 3.1**. After pyrolytic treatment at 230°C, the final products with the  $f_{\text{CA/urea}}$  equal to 1:3, 1:25, 1:50 and 1:100 were purified via dialysis (D-series) and filtration (F-series), in order to separate two distinct molecular fluorophores with either blue or green luminescence, respectively. The collection of the run-off substances (D1-series) from dialysis step led to generation of another type of luminescent CU-dots that display a greenish-blue emission under the ultraviolet (UV) illumination at  $\lambda_{\text{ex}} = 365$  nm. Nevertheless, in order to confirm a waste-free approach of proposed strategy, the carbogenuous leftover from the filtration step (preF1-series) was further oxidized with 3M  $\text{HNO}_3$ , thus generated another photoactive type of CU-dots (F1-series) with blue emissive signal under the UV light. Besides that, the freeze-dried powders corresponding to D1-series and F-series also exhibit strong luminescence properties in a solid-state form. Overall, the emissive signal in as-prepared nanomaterials predominantly arise from the CU-dots with embedded fluorophores (D-series), a blend of two molecular fluorophores (D1-series), the mixture of CU-dots with unbound molecular fluorophores (F-series) as well as cyanuric acid-rich CU-dots (F1-series).



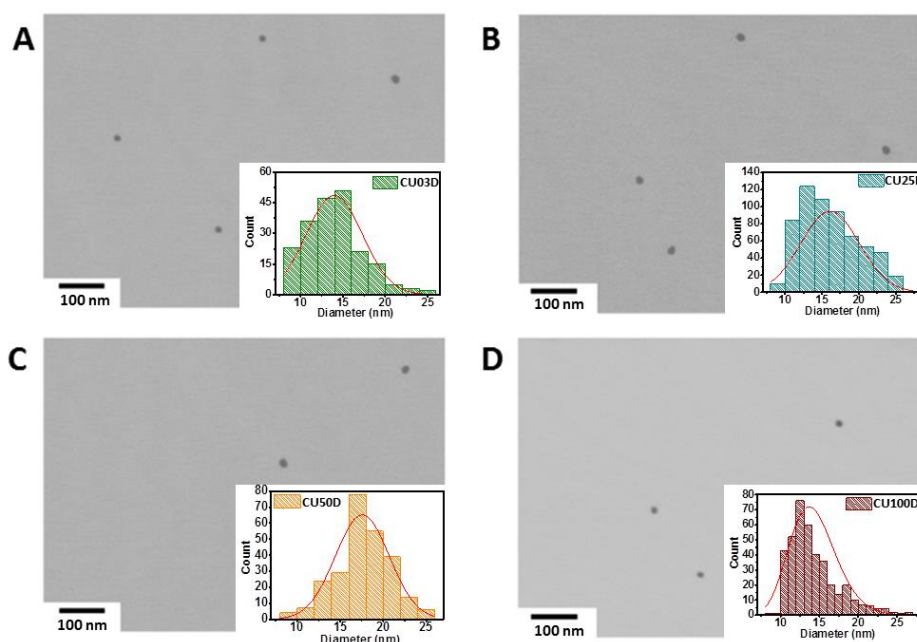


**Figure 3.1** Scheme presenting the synthetic and purification strategies leading to the formation of four distinct series of fluorescent suspensions and powders derived via pyrolytic treatment of CA/urea precursors mixture.

### 3.2.1 Characterization

#### D-series

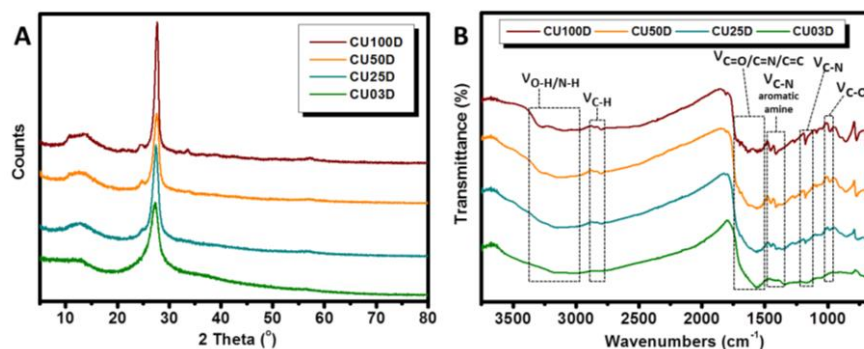
As presented in **Figure 3.2**, the Scanning Transmission Electron Microscopy (STEM) images display the spherical nature of CU03D, CU25D, CU50D and CU100D with mean diameters equal to 14.0, 16.1, 17.6 and 13.7 nm, respectively. The collected results are in agreement with previous studies, which noted that the average size of CU-dots varies from 2 up to 16 nanometres [5, 6, 9, 10, 13, 15, 19, 22, 30, 35, 42, 43, 45].



**Figure 3.2** STEM images of CU03D (A), CU25D (B), CU50D (C) and CU100D (D).

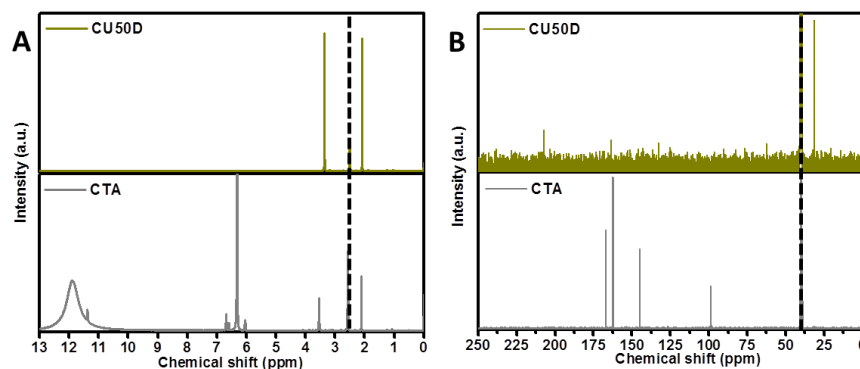
The structural insight into the crystalline nature of D-series nanopowders was gained by the X-Ray Powder Diffraction (XRD) analysis. Thus, the XRD patterns of CU03D, CU25D, CU50D and CU100D reveal the presence of a sharp diffraction peak at  $2\theta = 27.6^\circ$  (**Figure 3.3A**) that corresponds to the (002) lattice spacing of graphite-type materials and confirm the complete carbonization of CA into highly graphitic carbogenic cores [4, 14, 46]. Additionally, the increment of its intensity along with descending  $f_{\text{CA/urea}}$  imply that higher N-doping enhance the crystallinity of CU-dots [34]. Additionally, the graphitic character of D-series CU-dots was further confirmed by the presence of the peak around  $1600\text{cm}^{-1}$  in the Fourier Transform Infrared (FTIR) spectra (**Figure 3.3B**), which specifically confirms the presence of isolated  $\text{sp}^2$  clusters arising from the benzene skeleton vibrations [4]. Besides that, the vibration peaks of  $=\text{C-H}$  ( $2810\text{-}2197\text{ cm}^{-1}$ ),  $\text{C=O}$  or  $\text{C=N}$  ( $1653\text{-}1556\text{ cm}^{-1}$ ),  $\text{C-N}$  from aromatic amine ( $1462\text{-}1340\text{ cm}^{-1}$ ),  $\text{C-N}$  ( $1178\text{ cm}^{-1}$ ) and  $\text{C-O}$  ( $1090\text{-}1060\text{ cm}^{-1}$ ) were detected in all four materials, whereas the broad bands attributed to amine ( $\text{N-H}$ ) and hydroxyl ( $\text{O-H}$ ) groups ( $3028\text{-}3250\text{ cm}^{-1}$ ) further ensure a good solubility of CU-dots in polar solvents [14, 22, 27, 46]. In this regard, elemental analysis (Appendix, **Table A1**) further revealed that the nitrogen content for CU03D, CU25D, CU50D and CU100D is equal to 21%, 25%, 28% and 33%, respectively and this trend is followed by a systematic decrease in the carbon

content from 47% for CU03D to 40% for CU100D. At the same time, CU-dots belonging to D-series maintain the hydrogen content between 3 to 4% and the oxygen content between 24% to 28%. Overall, lower  $f_{\text{CA/urea}}$  leads to CU-dots with enhanced N content [13, 27, 47].



**Figure 3.3** XRD patterns (A) and FTIR spectra (B) for CU03D, CU25D, CU50D and CU100D.

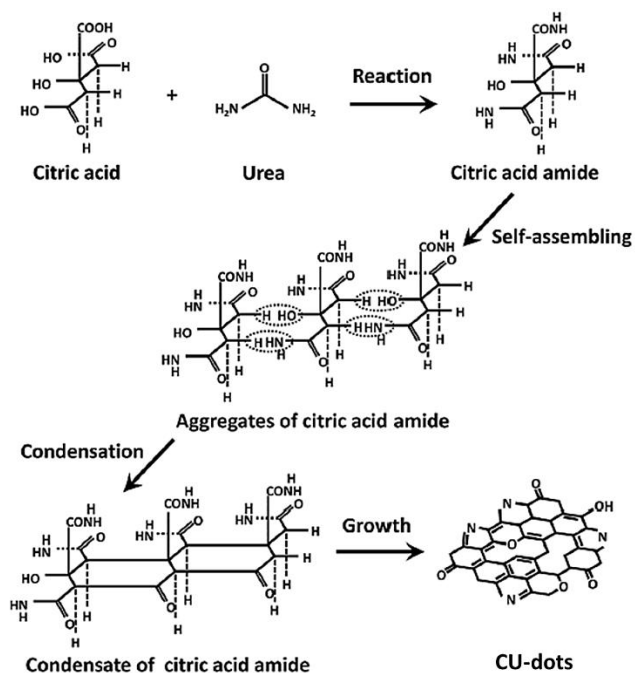
The  $^1\text{H}$ -NMR spectra of CU50D (**Figure 3.4A**) and other CU-dots from the D-series (Appendix, **Figure A1**) reveal two main peaks in the aliphatic region at 2.1 ppm and 3.4 ppm, which are attributed to the  $\text{sp}^3$  protons. On the other hand, the  $^{13}\text{C}$ -NMR spectra of CU50D (**Figure 3.4B**) as well as CU03D, CU25D and CU100D (Appendix, **Figure A1**) display one similar peak at 169.3 ppm, which suggest the presence of citrazinic acid fluorophore as a building block of carbogenic cores.



**Figure 3.4** The  $^1\text{H}$ -NMR (A) and  $^{13}\text{C}$ -NMR (B) spectrum of CU50D and citrazinic acid. The d-DMSO solvent peaks are marked as a dashed black line.

In regard to the formation mechanism of CU-dots, it has been reported that CA undergo reaction with urea in a molar ratio of 1:1 and initially form the citrazinic acid amide [48], as depicted in **Figure 3.5**. Subsequently, further thermal treatment facilitate the self-assembly of citrazinic acid amide into graphitic nanosheets through

the dehydration and deammoniation of  $\text{-COOH}$ ,  $\text{-OH}$  and  $\text{-NH}_2$  groups of aggregated intermolecular compounds [43]. Overall, the PL properties of as-prepared CU-dots could arise from both the condensates of citrazinic acid amide as well as the final graphitic nanosheets with diverse C-N configurations, such as graphitic-N, pyridinic-N and pyrrolic-N [2, 25, 43].


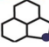



**Figure 3.5** The mechanism depicting the formation of CU-dots derived from CA/urea precursors mixture (Adapted from Ref. 43).

In order to gain structural insight into the elements binding configurations at the surface of CU-dots, the full scan of X-Ray photoelectron spectroscopy (XPS) survey spectra was recorded (Appendix, **Figure A2**) and confirmed the presence of three characteristic peaks at 286 eV, 400 eV and 532 eV that correspond to C1s, N1s and O1s, accordingly [5, 6, 13, 17, 22, 39, 42, 43]. Furthermore, the deconvolution of C1s (Appendix, **Figure A3**), N1s (Appendix, **Figure A4**) and O1s (Appendix, **Figure A5**) XPS spectra of CU03D, CU25D, CU50D and CU100D gave detailed insight into correlation between the PL properties of CU-dots and the presence of particular functional groups on their surface, as summarized in **Table 3.1**. In particular, the analysis of an input of each peak from the C1s spectra (Appendix, **Figure A3**) reveal an increase in contributions arising from C-O and C=O (285.4 eV) and C-N and C=N (286.9 eV) (lowest

for CU03D) as well as a systematic decrease in the contributions arising from C-C and C=C (284.0 eV) (highest for CU03D), which refer to graphene hexagonal structure [25, 33]. Besides that, the deconvolution of N1s spectra (Appendix, **Figure A4**) shows the dominant population of pyrrolic nitrogen (400.1 eV), whereas the pyridinic nitrogen (399.1 eV) systematically decreases from 29% for CU03D to 11% for CU100D and the graphitic nitrogen (401.5 eV) increases considerably from 9% for CU03D to 43% for CU100D [22, 47]. Likewise, the deconvolution of O1s spectra (Appendix, **Figure A5**) exhibit that C-O (531.5eV) decreases from 22% for CU03D to 11% for CU100D, whereas C=O (533.3eV) increases from 78% for CU03D to 89% for CU100D. Importantly, the presence of oxygenated surface functional groups, such as epoxide (C-O-C) and carbonyl (C=O) suggest an excellent stability of CU-dots in aqueous solutions [8, 17, 39, 49].

**Table 3.1** Deconvolution results for C1s, O1s and N1s spectra

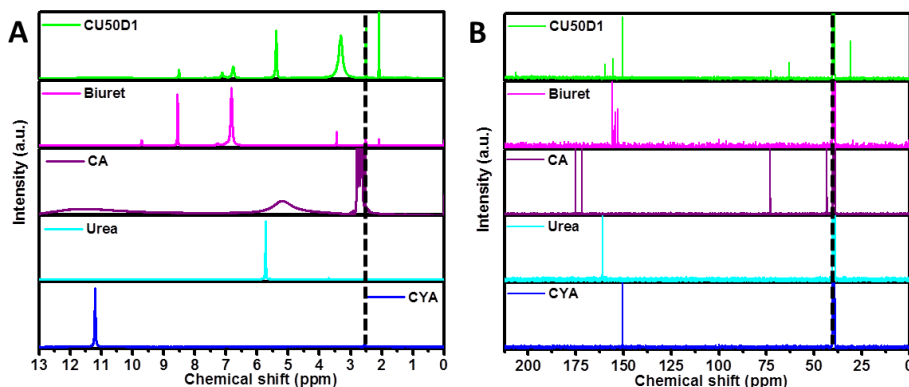
Material	C1s				O1s		N1s		
	C-C C=C	C-O C=O	C-N C=N	O-C-O	C=O	C-O	Graphitic-N 	Pyrrolic-N 	Pyridinic-N 
CU03D	51%	18%	25%	6%	78%	22%	9%	62%	29%
CU25D	45%	18%	30%	7%	85%	15%	18%	61%	21%
CU50D	44%	19%	31%	6%	87%	13%	25%	59%	16%
CU100D	34%	21%	38%	7%	89%	11%	43%	46%	11%

Overall, the evidence discussed above confirmed that nanoparticles belonging to D-series are composed of spherical gC-dots with abundant nitrogen content and possess a dense population of hydrophilic groups on their surface. Besides that, it is believed that molecular fluorophores are embedded within carbogenic cores or may be strongly adsorbed on their surface, while taking into account their extensive dialysis against water over a prolonged period of time [50].

### **D1-series**

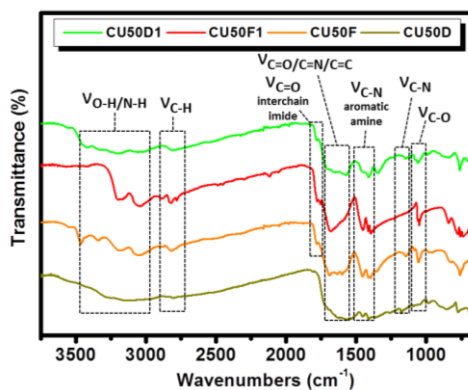
The CU50D1 was selected as a representative member of D1-series and used for further characterisation. It has been previously reported that the use of cellulose dialysis membrane constitute an efficient method for the elimination of unreacted molecules during synthesis step as well as unbounded fluorophores [51]. Thus, the  $^1\text{H}$ -NMR (**Figure 3.6A**) and  $^{13}\text{C}$ -NMR (**Figure 3.6B**) spectra of CU50D1 along with co-

products provide the evidence for successful removal of biuret (155.9 ppm  $^{13}\text{C}$ -NMR and 6.8 ppm, 7.1 ppm, 8.5 ppm  $^1\text{H}$ -NMR), citric acid (72.9 ppm  $^{13}\text{C}$ -NMR), urea (160.0 ppm  $^{13}\text{C}$ -NMR, 5.4 ppm  $^1\text{H}$ -NMR) and cyanuric acid (150.7 ppm  $^{13}\text{C}$ -NMR) molecules from the post-synthesis carbogeous material.



**Figure 3.6** The  $^1\text{H}$ -NMR (A) and  $^{13}\text{C}$ -NMR (B) spectrum of CU50D1 along with the side products which diffuse through the dialysis membrane. The d-DMSO solvent peaks are marked as a dashed black line.

The FTIR spectrum of CU50D1 (**Figure 3.7**) shows the vibration peaks of N-H and O-H ( $3418\text{--}3060\text{ cm}^{-1}$ ), C-H ( $2810\text{ cm}^{-1}$ ), C=O or C=N ( $1655\text{--}1571\text{ cm}^{-1}$ ), C-N from aromatic amine ( $1412\text{--}1346\text{ cm}^{-1}$ ), C-N ( $1147\text{ cm}^{-1}$ ) and C-O ( $1059\text{ cm}^{-1}$ ) [14, 21, 27, 46]. Moreover, the vibration peak ca.  $1655\text{--}1571\text{ cm}^{-1}$  is also related to C=C stretching, that corresponds to the benzene skeleton rings [4, 45]. In summary, the CU50D1 material is composed of a blend of CYA, CA, urea, biuret and molecular fluorophores.

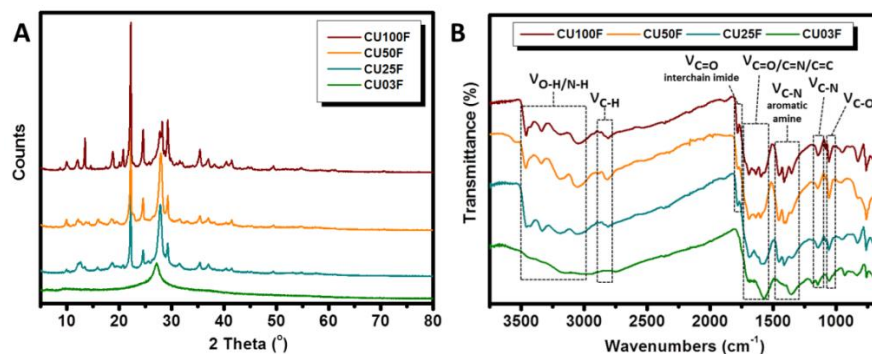


**Figure 3.7** FTIR spectra of CU50D1, CU50F1, CU50F and CU50D.

## **F-series**

The XRD patterns of F-series CU-dots (**Figure 3.8A**) reveal a characteristic diffraction peak at  $2\theta = 27.9^\circ$  attributed to the (002) plane of graphite [4, 15, 39], which along with further N-doping split into two twin peaks. This constitutes a confirmation of two distinct types of layered graphitic structure within the crystalline configuration and may imply the N-induced shrinkage within the graphene sheets, arising from the presence of amino functionalities at the edge of gC-dots or different structural defects [19]. Furthermore, the XRD patterns of CU25F, CU50F and CU100F (Appendix, **Figure A6A**) demonstrate the presence of the main diffraction peaks centered at  $22.2^\circ$ ,  $24.6^\circ$ ,  $29.3^\circ$  and  $35.4^\circ$ , which correspond to the (112), (221), (003) and (330) crystal planes of urea. In contrast, the crystal nature of CU03 nanomaterial remains unchanged despite different purification strategy (D-series and F-series), thereby only shows a single graphitic peak at  $2\theta = 27.1^\circ$  (Appendix, **Figure A6B**). This phenomenon imply that low nitrogen content leads to similar extent of graphitization in CU-dots [14], whereas the absence of additional crystalline peaks suggests the presence of structural defects [4, 46]. On the other hand, the FTIR spectra of F-series CU-dots (**Figure 3.8B**) reveals the peaks at around  $3490\text{ cm}^{-1}$ ,  $3370\text{ cm}^{-1}$  together with  $3028\text{ cm}^{-1}$  as well as  $3270\text{ cm}^{-1}$ , which are assigned to N-H stretching of aromatic amines, O-H stretching of alcohol or carboxyl groups as well as to N-H stretching of amides [21]. Likewise D-series, the peaks at  $2963\text{--}2810\text{ cm}^{-1}$ ,  $1690\text{--}1653\text{ cm}^{-1}$ ,  $1354\text{--}1085\text{ cm}^{-1}$  and  $1058\text{--}1052\text{ cm}^{-1}$  can be ascribed to the stretching vibrations of C-H, C=O/C=N, C-N and C-O bonds, respectively [4, 27, 46]. In addition, the transmittance peak occurring at ca.  $1602\text{--}1596\text{ cm}^{-1}$  is related to C=C stretching, which habitually occur in the nitrogen-doped gC-dots [34]. The enhancement of the stretching vibrations in the region  $1000\text{--}1600\text{ cm}^{-1}$  suggest the increment of O-rich and N-rich surface functional groups along with the further nitrogen doping [14, 22]. In analogy to D-series, the elemental analysis of F-series CU-dots (Appendix, **Table A2**) confirms that the nitrogen content for CU03F, CU25F, CU50F and CU100F is equal to 31%, 35%, 37% and 38%, accordingly and this trend is followed by a systematic decrease in carbon content from 36% for CU03F to 29% for CU100F. At

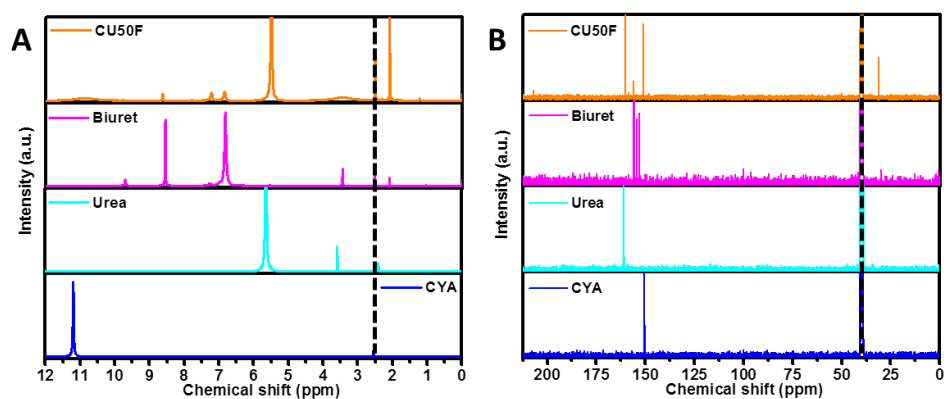
the same time, the hydrogen content in F-series CU-dots remains within 4 to 5% and the oxygen content between 28 to 30%.



**Figure 3.8** XRD patterns (A) and FTIR spectra (B) for CU03F, CU25F, CU50F and CU100F.

The  $^1\text{H}$ -NMR spectra of CU50F (**Figure 3.9A**) and other members of F-series (Appendix, **Figure A7A**) are dominated by the peaks at 2.1 ppm, 7.2 ppm, 7.8 ppm and 8.6 ppm, which arise from biuret content. On the other side, the prominent peak at 5.6 ppm is stemming from urea, while the peaks below 3.5 ppm and within the range 6.5-8.5 ppm are attributed to the  $\text{sp}^3$  and  $\text{sp}^2$  carbons, respectively [40]. Likewise, the  $^{13}\text{C}$ -NMR spectra for CU50F (**Figure 3.9B**) and other members of F-series (Appendix, **Figure A7B**) reveal the peaks at 160.2 ppm and 155.9 ppm, which correspond to the presence of urea and biuret, accordingly. In general, the presence of the peaks in the range 25-35 ppm as well as 150-210 ppm in the  $^{13}\text{C}$ -NMR spectra of F-series CU-dots (Appendix, **Figure A7B**) confirm the presence of both  $\text{sp}^3$ - and  $\text{sp}^2$ -hybridized carbon atoms [23]. The additional peak at the chemical shift 151.1 ppm suggest the presence of cyanuric acid, which is one of the main components after citric acid-urea melt decomposition [45, 52].



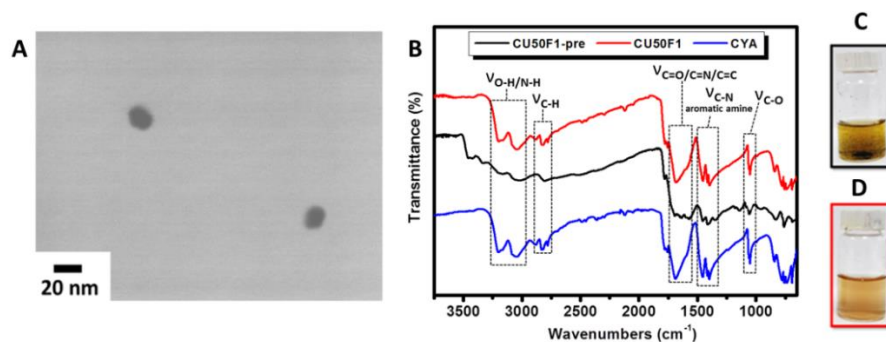


**Figure 3.9** The  $^1\text{H}$ -NMR (A) and  $^{13}\text{C}$ -NMR (B) spectra of CU50F, biuret, urea and cyanuric acid (CYA). The d-DMSO solvent peaks are marked as a dashed black line.

In general, the materials from F-series represent a multicomponent system that besides carbon dots comprise of CYA, urea, biuret and molecular fluorophores.

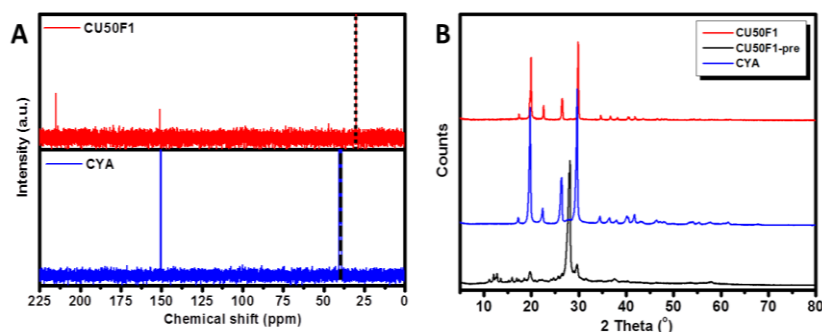
### **F1-series**

The CU50F1 was selected as a representative member of the F1-series for further characterization. The STEM image presented in **Figure 3.10A** displays that CU50F1 are spherical nanoparticles with an average diameter of 15 nm. The FTIR spectrum of CU50F1 (**Figure 3.10B**) clearly resembles the one of cyanuric acid (CYA), while both are governed by the vibrational peaks at  $3199\text{ cm}^{-1}$ ,  $3046\text{ cm}^{-1}$ ,  $1685\text{ cm}^{-1}$  and  $1452\text{ cm}^{-1}$ , assigned to O-H band of hydroxyl group, N-H band, C=O and C=N bands, C-N band of aromatic amine and C-O band, accordingly. Importantly, the abundant presence of hydrophilic moieties facilitate the dispersion of CU50F1 in polar solvents (**Figure 3.10D**), while the pre-CU50F1 material demonstrates poor solubility in water (**Figure 3.10C**). This behaviour may be related to the oxygen content (Appendix, **Table A3**) that is equal to 34% for CU50F1 and 28% for its pre-CU50F1 counterpart.



**Figure 3.10** STEM image of CU50F1 (A) together with the FTIR spectra (B) and photos of aqueous dispersions of pre-CU50F1 (C) and CU50F1 (D).

In addition, the  $^{13}\text{C}$ -NMR spectrum of CU50F1 (**Figure 3.11A**) shows a characteristic peak at 151.1 ppm, which corresponds to the main peak seen for the CYA. Likewise, the XRD pattern of CU50F1 with the main diffraction peaks at  $2\theta = 19.7^\circ$ ,  $22.4^\circ$ ,  $26.3^\circ$  and  $29.6^\circ$  (**Figure 3.21B**) provides matching evidence about the CYA-rich nature of CU50F1, that incorporates an abundant content of CYA crystals into their carbogenic cores. In regard to literature reports, alike system comprising of CYA-rich CU-dots has been previously synthesized through infrared-assisted pyrolysis of the same precursors mixture with  $f_{\text{CA/urea}} = 1:3$  [45].



**Figure 3.11** The  $^{13}\text{C}$ -NMR spectrum (A) and the XRD patterns (B) of CU50F1 compared to CYA. The d-DMSO and  $\text{D}_2\text{O}$  solvent peaks are marked as dashed and dotted black lines in  $^{13}\text{C}$ -NMR spectrum.

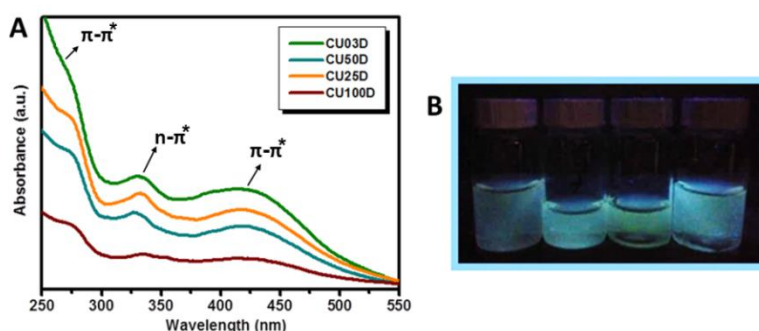
### 3.2.2 Liquid-state fluorescent properties

It has been previously reported that CU-dots synthesized from the binary systems of CA and urea may exhibit either blue or green fluorescence, depending on the synthesis conditions [19, 32]. In this study, the selected separation strategies favoured the predominance of different molecular fluorophores in post-purified materials, such as

citrazinic acid (CTA) or (4-hydroxy-1H-pyrrolo(3,4-c)pyridine-1,3,6(2H,5H)-trione (HPPT) [32].

### **D-series**

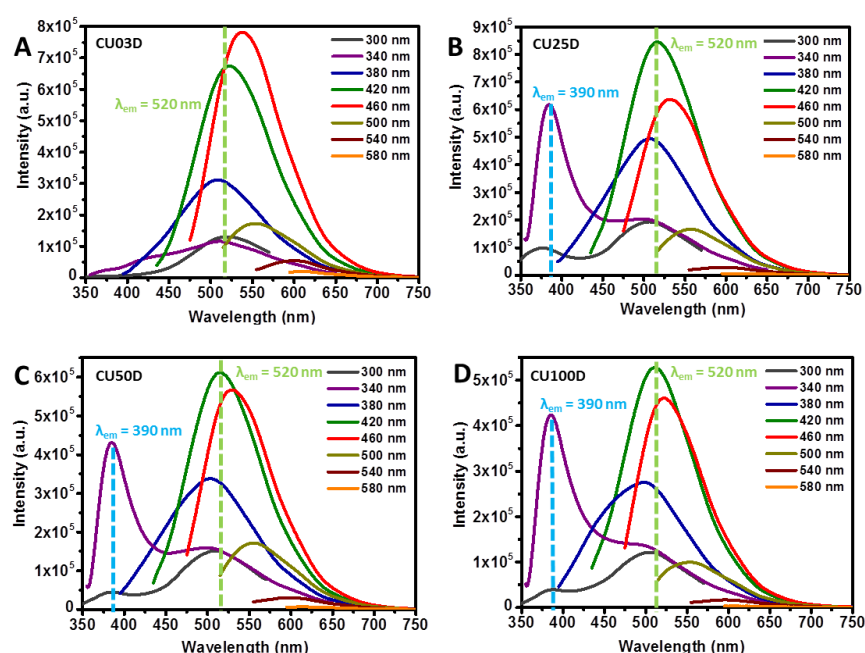
The absorption spectra of D-series CU-dots (**Figure 3.12A**) exhibit a characteristic bands at 330 nm and notably broaden at around 420 nm, which indicate the formation of citrazinic acid aggregates [44, 53]. In addition, a weakly pronounced absorption band around 270 nm for CU25D, CU50D and CU100D imply the negligible presence of HPPT fluorophore, which impact on the greenish-blue luminescence of their aqueous dispersions under the UV illumination at  $\lambda_{\text{ex}} = 365\text{nm}$  (**Figure 3.12B**). On the contrary, a raw citric acid and urea do not show any predominant absorbance peaks in the UV-Vis region, thus confirming the predominant presence of CTA as a molecular fluorophore that is adsorbed on the surface of D-series CU-dots [21, 23, 37, 40].



**Figure 3.12** UV-Vis spectra (A) and photos under the UV light (B) of aqueous dispersions of CU03D, CU25D, CU50D and CU100D. The concentration of the solutions was equal to 0.1 mg/mL.

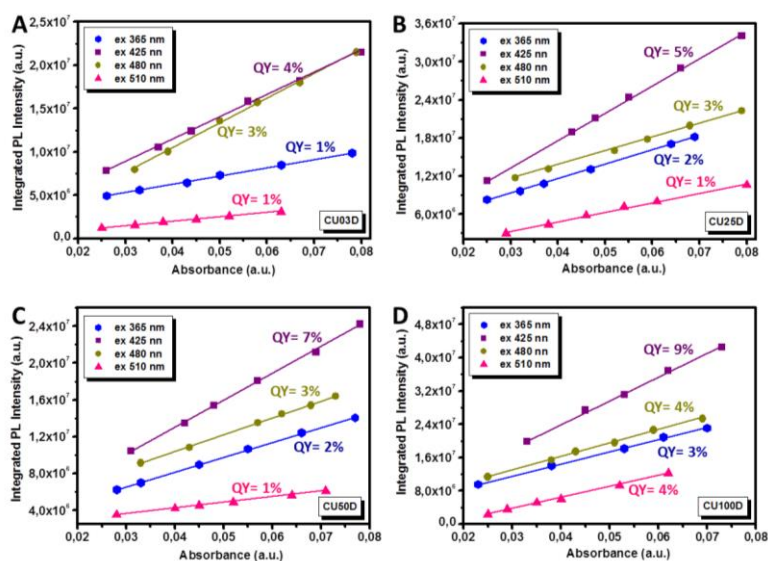
The PL spectra of D-series CU-dots (**Figure 3.13**) demonstrate a characteristic excitation wavelength-dependent luminescence behaviour with the emission peaks shifting from 390 nm (blue-light region) up to 625 nm (red-light region), when  $300 < \lambda_{\text{ex}} < 580\text{ nm}$ . For all samples a contribution stemming from HPPT fluorophore can be observed at  $\lambda_{\text{em}} = 525\text{ nm}$ , while for CU25D, CU50D and CU100D an additional contribution arising from CTA units at  $\lambda_{\text{em}} = 390\text{ nm}$  is also present [32]. The maximum PL emission for CU03D (**Figure 3.13A**) was recorded at  $\lambda_{\text{ex}} = 460\text{ nm}$ , whereas the PL spectra for CU25D, CU50D and CU100D (**Figure 3.13B-D**) show the highest emission peaks at  $\lambda_{\text{ex}} = 420\text{ nm}$ . In regard to previous reports, a similar excitation-dependent PL phenomena was noted for CU03D, proving that N-doping enhance the PL intensity

without further red-shifting [33]. Additionally, the characteristic blue-shifting was observed for the emission peaks recorded at  $\lambda_{\text{ex}}=460$  nm (Appendix, **Figure A8**), related to even hybridization of frontier orbitals between edge N atoms and gC-dots [54]. Overall, the emission mechanism of CU-dots may be related to three emissive modes, such as the presence of isolated  $\text{sp}^2$  carbogenic cores with  $\text{sp}^3$  domains, surface defects or crosslink-enhanced emission originating from the simultaneous presence of different molecular fluorophores [32, 55, 56].



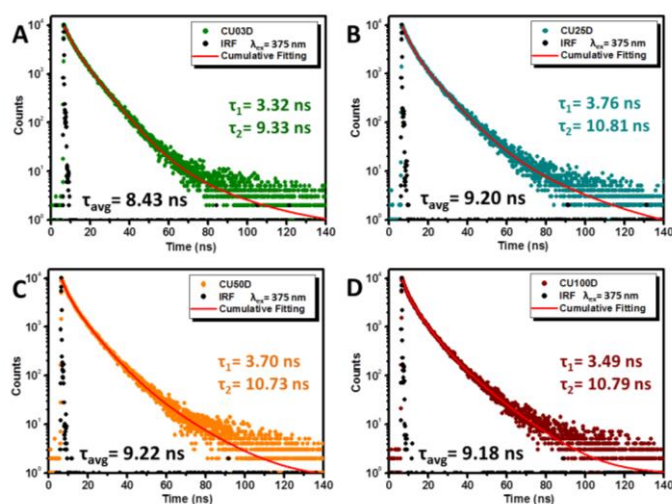
**Figure 3.13** Liquid-state photoluminescent spectra of aqueous dispersion of CU03D (A), CU25D (B), CU50D (C) and CU100D (D). The concentration of the solutions was equal to 0.1 mg/mL.

Furthermore, the quantum yield (QY) values were calculated in regard to several reference dyes, such as anthracene ( $\lambda_{\text{ex}}= 365$  nm), fluorescein ( $\lambda_{\text{ex}}= 425$  nm), rhodamine 6G ( $\lambda_{\text{ex}}= 480$  nm) and rhodamine B ( $\lambda_{\text{ex}}= 510$  nm) with the well-known optical efficiencies (Appendix, **Figure A9**). In detail, the QY falls within 1-4% for CU03D, 1-5% for CU25D, 2-7% for CU50D and 3-9% for CU100D (**Figure 3.14**), thereby showing a trend of a systematic enhancement along with increment of nitrogen content. Besides that, the collected results revealed that the optical efficiencies at  $\lambda_{\text{ex}}=365$  nm (QY=1-3%) are lower than previously reported for CA-based C-dots with QY $\approx$ 10% [37] or CU-dots with QY $\approx$ 6-9% that were synthesized from the  $f_{\text{CA/urea}}=1/3$  [3, 27, 32, 40].



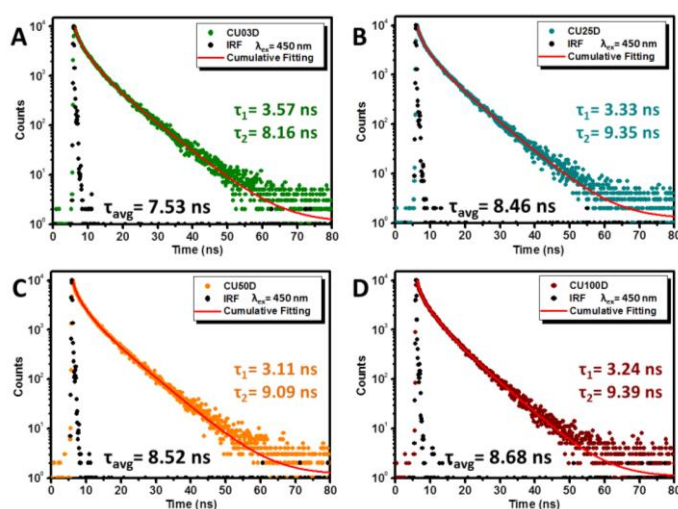
**Figure 3.14** The plots demonstrating the integrated PL intensity of CU03D (A), CU25D (B), CU50D (C) and CU100D (D) materials dissolved in extra pure water as a function of optical absorbance. The results were collected at 365 nm, 425nm, 480nm and 510 nm excitation wavelengths.

The time-resolved PL lifetime decays of D-series CU-dots were further recorded at  $\lambda_{\text{ex}} = 375$  nm (**Figure 3.15**) and  $\lambda_{\text{ex}} = 450$  nm (**Figure 3.16**). The average fluorescence lifetimes ( $\tau_{\text{avg}}$ ) were found to be between 8.4 ns (CU03D) to 9.2 ns (CU25D, CU50D, CU100D) at  $\lambda_{\text{ex}} = 375$  nm (**Figure 3.15**). Knowing that the CTA molecular fluorophore has a single exponential PL decay with lifetime of 6.4 ns, the multi-exponential decay of CU-dots may arise from a larger C-dots ensemble or a heterogeneous emitting states in a single carbon nanodomain [57, 58].



**Figure 3.15** Liquid-state PL lifetime decays of aqueous dispersions of CU03D (A), CU25D (B), CU50D (C) and CU100D (D) recorded at  $\lambda_{\text{ex}} = 375$  nm.

The similar trend in the PL lifetime characteristics was found at  $\lambda_{\text{ex}} = 450$  nm with the  $\tau_{\text{avg}}$  varied from 7.5 ns (CU03D) up to 8.5 ns (CU25D, CU50D, CU100D), as demonstrated in **Figure 3.16**. In regard to previous protocols, the  $\tau_{\text{avg}}$  of CU-dots derived via pyrolytic treatment (250°C, 1h) of CA/urea mixture with  $f_{\text{CA/urea}} = 1/3$  was equal to 6.7 ns, while the hydrothermal treatment (110°C, 3h) of the same reactants mixture resulted in the  $\tau_{\text{avg}}$  ranging from 7.4 ns to 8.1 ns [2, 5, 11]. Interestingly, it has been reported that the selection of dialysis as a separation procedure impact on prolonged PL lifetimes ( $\tau_{\text{avg}} = 7.8$  ns), in contrast to the filtration strategy ( $\tau_{\text{avg}} = 7.40$  ns) [2].



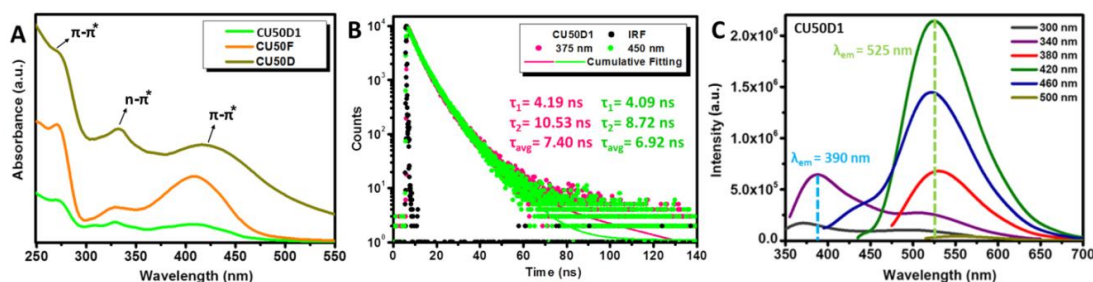
**Figure 3.16** Liquid-state fluorescence lifetime decays of aqueous dispersions of CU03D (A), CU25D (B), CU50D (C) and CU100D (D) at  $\lambda_{\text{ex}} = 450$  nm.

### D1-series

The UV-Vis spectrum of CU50D1 (**Figure 3.17A**) reveal the presence of absorption bands around 270 nm and 410 nm that are attributed to the  $\pi$ - $\pi^*$  transitions of the HPPT pyridone ring as well as less pronounced absorption band around 330 nm, corresponding to the  $n$ - $\pi^*$  transitions of citrazinic acid aggregates [32]. In addition, the average PL lifetimes of CU50D1 (**Figure 3.17B**) equal to either 7.4 ns ( $\lambda_{\text{ex}} = 375$  nm) or 6.9 ns ( $\lambda_{\text{ex}} = 450$  nm) are significantly lower than for the CU50D counterpart, thereby suggesting the interference from other run-off substances or the dominant content of HPPT molecular fluorophore. The PL spectra of CU50D1 (**Figure 3.17C**) is dominated by



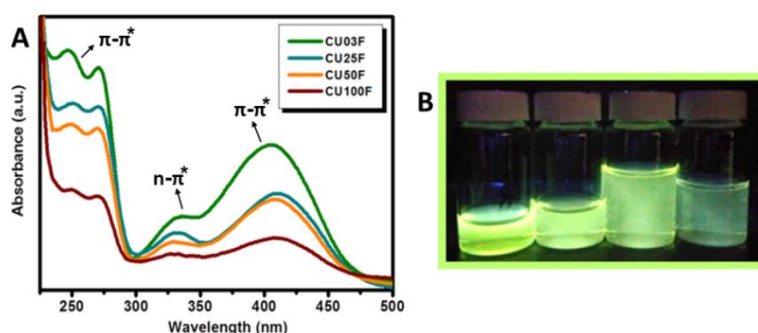
two excitation wavelength independent contributions stemming from CTA ( $\lambda_{em}$  = 390 nm) and HPPT ( $\lambda_{em}$  = 525 nm) fluorophores, accordingly.



**Figure 3.17** The UV-Vis spectra (A), PL lifetime decays measured at  $\lambda_{ex}$  = 375 nm and  $\lambda_{ex}$  = 450 nm (B) and the PL spectra (C) of aqueous dispersions of CU50D1. The concentration of the solutions was equal to 0.01 mg/mL.

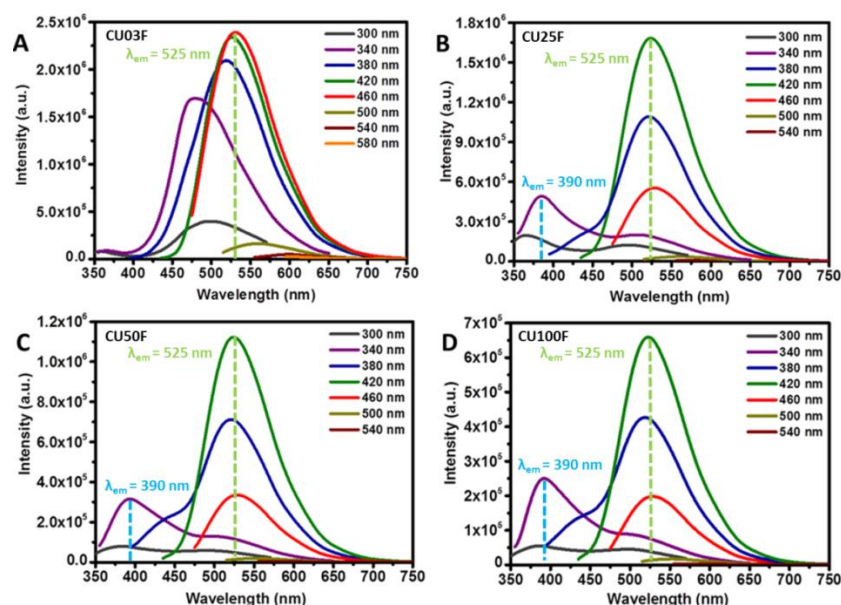
### F-series

The UV-Vis spectra of F-series CU-dots (**Figure 3.18A**) display a strong absorption bands around 250 nm and 330 nm, which corresponds to the  $\pi-\pi^*$  transitions emerging from conjugated electrons in the aromatic unit of the HPPT fluorophore as well as the  $n-\pi^*$  transitions originated from the presence of citrazinic acid derivatives, respectively. The additional long-wave band around 405 nm is attributed to the  $\pi-\pi^*$  transition of the HPPT pyridone ring [24, 32, 53]. Importantly, descending intensity of the absorption bands characteristic for the HPPT fluorophore is correlated with its diminished contribution in the CU100F, which aqueous dispersion displays a greenish-blue luminescence under the UV light (**Figure 3.18B**).



**Figure 3.18** UV-Vis spectra of aqueous dispersions of F-series CU-dots (A) along with the photo revealing their blue luminescence after UV illumination (B). The concentration of the solution was equal to 0.1 mg/mL.

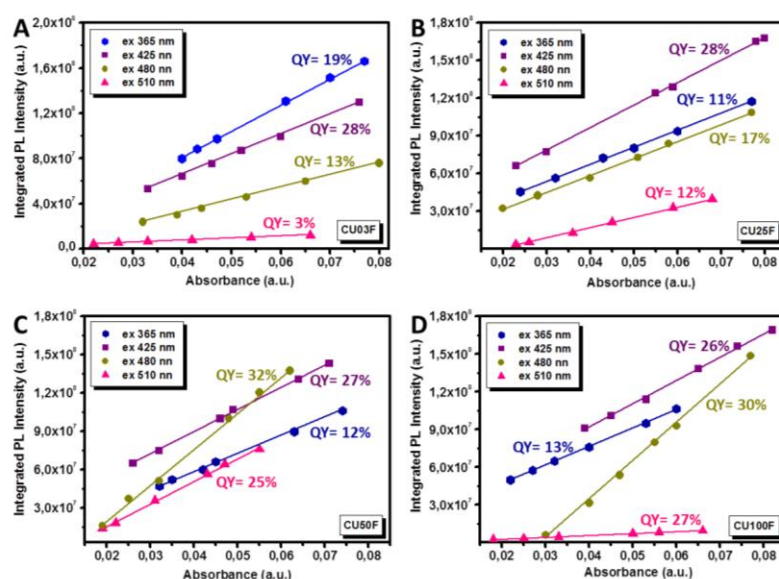
The liquid-state PL spectra of F-series CU-dots (**Figure 3.19**) display a characteristic signals at  $\lambda_{em}$ = 390nm and  $\lambda_{em}$ = 525nm, which arise from CTA and HPPT, respectively [32]. The PL mechanism of CU25F, CU50F and CU100F predominantly exhibit the excitation wavelength dependent emission at  $300 < \lambda_{ex} < 340$  nm, while from  $380 < \lambda_{ex} < 540$  nm the excitation wavelength-independent phenomena is clearly observed (**Figure 3.19B-D**). The gradual shifting of the emission peaks towards the higher wavelengths and the independent PL mechanism after reaching the maximum emission ( $\lambda_{em}$ = 525 nm) was previously reported by other researchers, without the consideration of an impact caused by the higher N-doping [4, 13, 16, 40]. On the other side, the signals stemming from CTA and HPPT are relatively weaker for CU03F nanomaterial, which demonstrates only the excitation wavelength-dependent emission at  $300 < \lambda_{ex} < 580$  nm (**Figure 3.19A**). Moreover, the presence of a broad emission peaks with double maxima at  $300 < \lambda_{ex} < 340$  nm (**Figure 3.19B-D**), highlight the presence of both HPPT chromophore ( $\lambda_{em} \approx 520$  nm) as well as aggregated aromatic units of citrazinic acid fluorophore ( $\lambda_{em} \approx 390$  nm) [13, 53]. Overall, the wide emissive range of the presented PL spectra confirm the multicolour nature of F-series CU-dots, whereas the excitation wavelength-independent emission feature implies that the size of nanodomains and surface states should be uniform [23, 37].



**Figure 3.19** Liquid-state photoluminescent spectra of aqueous dispersion of CU03F (A), CU25F (B), CU50F (C) and CU100F (D) powders. The concentration of the solutions was equal to 0.1 mg/mL.

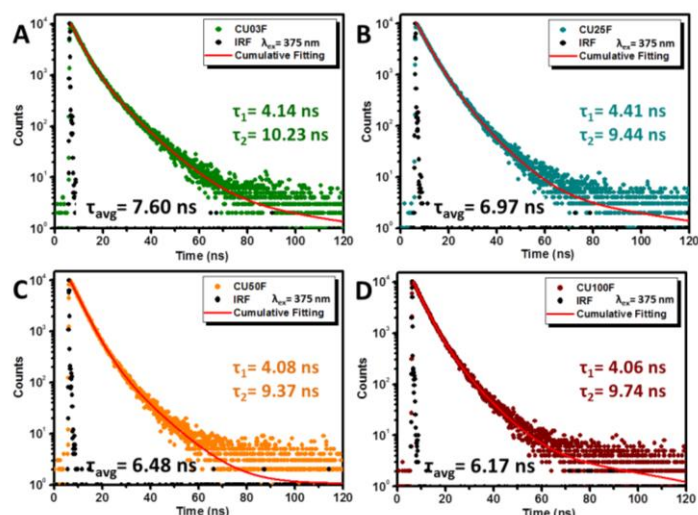


The calculated quantum yield values for F-series CU-dots (**Figure 3.20**) fall within 3-28% for CU03F, 11-28% for CU25F, 12-32% for CU50F and 13-30% for CU100F, thus are significantly higher than for D-series with diminished content of fluorophores molecules. In reference to previous reports, the QY values of CU-dots derived from the  $f_{\text{CA/urea}} = 1/3$  considerably vary from 9% to 27%, and up to 73% at  $\lambda_{\text{ex}} = 410 \pm 10$  nm [3, 16, 23, 24]. On the other side, the QY=11-19% at  $\lambda_{\text{ex}} = 365$  nm surpass the previous reports for similar systems (QY $\approx$ 10%) [23, 27, 36, 38, 40], although cyanuric acid may quench the PL intensity of CU-dots [45].



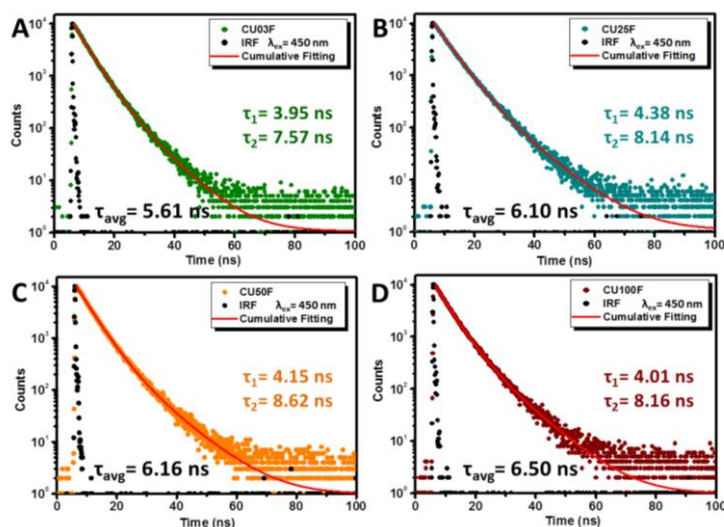
**Figure 3.20** The plots demonstrating the integrated PL intensity of CU03F (A), CU25F (B), CU50F (C) and CU100F (D) samples dissolved in ultra-pure water as a function of optical absorbance. The results were collected at 365 nm, 425 nm, 480 nm and 510 nm excitation wavelength.

The PL lifetime decays of F-series CU-dots recorded at  $\lambda_{\text{ex}} = 375$  nm (**Figure 3.21**) revealed that the longest  $\tau_{\text{avg}}$  equal to 7.6 ns corresponds to the CU03F (**Figure 3.21A**), which presumably contain the highest content of CTA. On the contrary to D-series, the  $\tau_{\text{avg}}$  of F-series are shorter, thereby implying that the excess of fluorophore molecules may initiate their interactions in the excited states.



**Figure 3.21** Liquid-state fluorescence lifetime decays of aqueous dispersions of CU03F (A), CU25F (B), CU50F (C) and CU100F (D) at  $\lambda_{\text{ex}} = 375$  nm.

On the other side, the change of the excitation wavelength ( $\lambda_{\text{ex}} = 450$  nm) do not impact significantly on the average PL lifetimes of CU-dots with higher urea content (**Figure 3.22**), thus suggest the presence of similar luminescence centres in these materials.

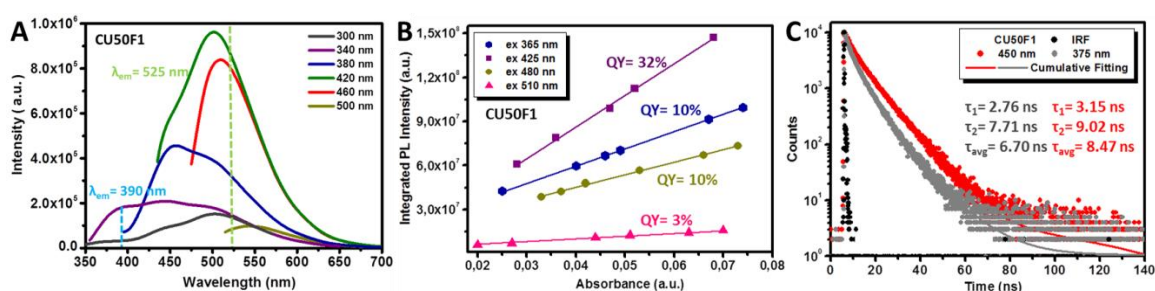


**Figure 3.22** Liquid-state fluorescence lifetime decays of aqueous dispersions of CU03F (A), CU25F (B), CU50F (C) and CU100F (D) at  $\lambda_{\text{ex}} = 450$  nm.

### **F1-series**

The CU50F1 displays an excitation wavelength dependent PL emission behaviour (**Figure 3.23A**), whereas the characteristic asymmetric lamps centered around 460 nm

( $\lambda_{\text{ex}}$  = 380 nm) and 520 nm ( $\lambda_{\text{ex}}$  = 460 nm) resemble the emissive characteristics of previously reported CYA-based C-dots [45]. Importantly, the PL spectra of CU50F1 confirms that unique luminescence features of F1-series arise from the carbogenic cores enriched with CYA crystals rather than the presence of molecular fluorophores. The calculated QY values of CU50F1 are in the range of 3% up to 32% (**Figure 3.23B**), alike to previously reported values of 8-16% ( $\lambda_{\text{ex}}$  = 360 nm) for CYA-rich gC-dots [45]. In addition, the QY = 32% ( $\lambda_{\text{ex}}$  = 425 nm) suggest that the luminescence origin of F1-series probably arise from the oxidation of the graphitic cores rather than the surface traps. The prolonged average PL lifetime of CU50F1 at  $\lambda_{\text{ex}}$  = 450 nm (**Figure 3.23C**) may be associated with a large content of C=N and C-N configurations in the binary crystal structure of CYA-based CU-dots [34].

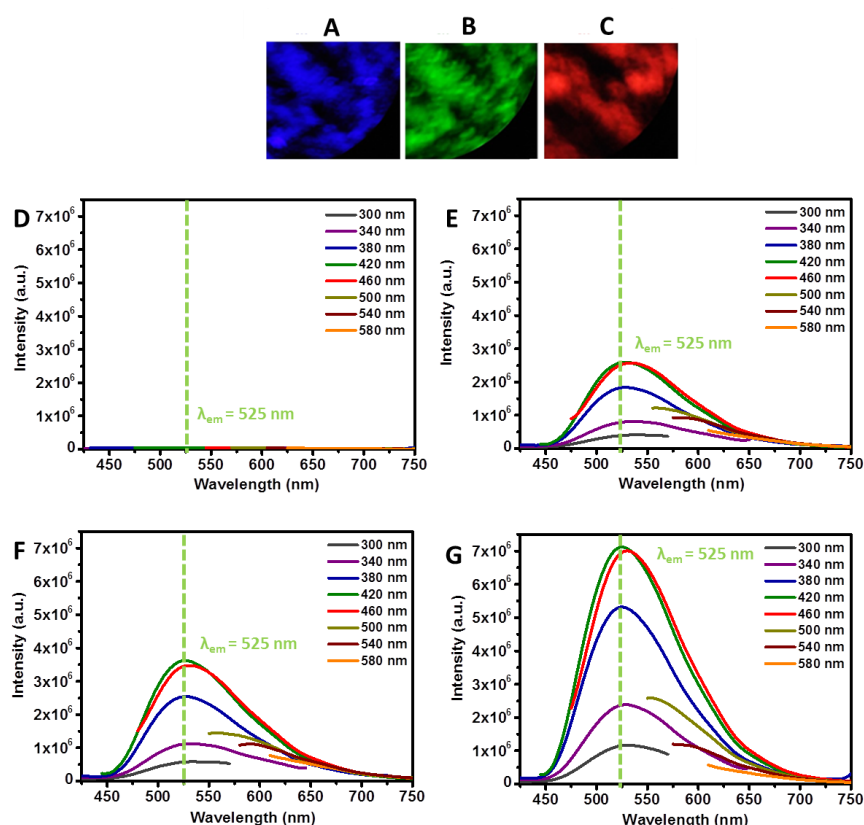


**Figure 3.23** The PL spectra (A), plots of integrated PL intensity as a function of optical absorbance ( $\lambda_{\text{ex}}$  = 365, 425, 480 and 510 nm) (B) and PL lifetime decays recorded at  $\lambda_{\text{ex}}$  = 375 and 450 nm (C) for aqueous dispersion of CU50F1.

### 3.2.3 Solid-state optical properties

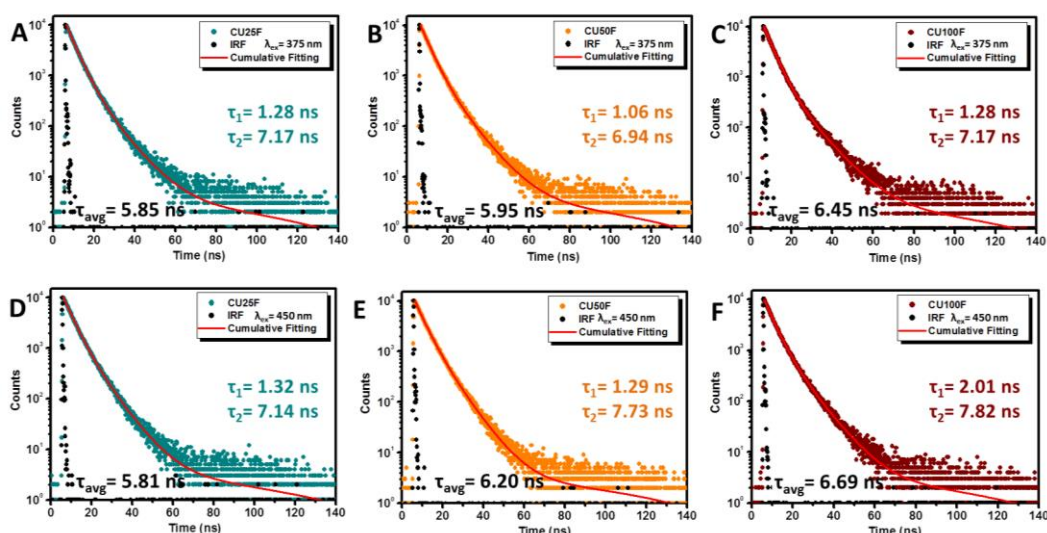
All powders from D-series as well as CU03F (**Figure 3.24D**) are not photoactive in a solid-state, presumably due to the quenching effect between conjugated carbogenic domains with  $\text{sp}^2$ -hybridization in aggregated form [44]. On the contrary, CU25F, CU50F and CU100F powders demonstrate a colour tunable optical features, while adopting a blue, green and red colours during illumination by the ultraviolet, blue and green radiation, accordingly (**Figure 3.24A-C**). Although the corresponding image is not presented here, the PL phenomenon of F-series powders originates from the content of CU-dots, while the fluorescent microscopy images of the CA/urea blend do not reveal any luminescence under identical conditions. In addition, the broad emissive peaks of CU25F, CU50F and 100F powders show a maximum at  $\lambda_{\text{em}}$  = 525 nm and their

intensities increase in a controlled manner along with further N-doping (**Figure 3.24E-G**). Early reports recognised the challenges to generate the fluorescent powders from the CA/urea precursors mixture [23], whilst only one report that utilised the  $f_{\text{CA/urea}}=1/26$  and tedious purification strategies shows any resemblance to presented work [44]. Overall, the excess of urea within CA/urea precursors system plays a triple role: as a building block of the carbogenic cores, reactant for the generation of molecular fluorophores as well as diluent matrix that suppress the undesired self-quenching effects [44].



**Figure 3.24** Fluorescent microscopy images of CU100F powder on a glass slide illuminated by ultraviolet (A), blue (B) and green (C) excitation wavelength and the fluorescence emission spectra of CU03F (D), CU25F (E), CU50F (F) and CU100F (G) powders recorded at  $\lambda_{\text{ex}}=300\text{-}580\text{nm}$ .

The values of the  $\tau_{\text{avg}}$  close to 5.8 ns for CU25F, 5.9 ns for CU50F and 6.4 ns for CU100F (**Figure 3.25A-C**) surpass the  $\tau_{\text{avg}}$  ranging from 1ns to 5ns for more toxic organic dyes [59], while being even prolonged at  $\lambda_{\text{ex}}=450 \text{ nm}$ .



**Figure 3.25** Solid-state PL lifetime decays of CU25F, CU50F and CU100F recorded at 375 nm (A-C) and 450 nm (D-F).

For further clarity, **Table 3.2** summarises the composition and optical characteristics for a large gallery of above mentioned photoluminescent suspensions and powders.

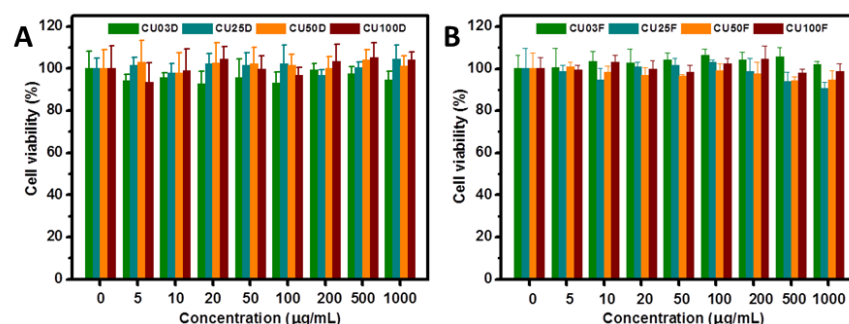
**Table 3.2** Composition and PL behaviour of D-, D1-, F- and F1-series

Type of material	Composition	Liquid state, QY	Solid state PL
<b>D-series</b>	C-dots, CTA and HPPT entrapped in C-dots	CU03D, 1-4%	No
		CU25D, 1-5%	No
		CU50D, 2-7%	No
		CU100D, 3-9%	No
<b>D1-series</b>	CYA, CA, urea, biuret, HPPT	Yes	Yes
<b>F-series</b>	C-dots, CYA, CTA, urea, biuret, HPPT	CU03F, 3-19%	No
		CU25F, 11-28%	Yes
		CU50F, 12-32%	Yes
		CU100F, 13-30%	Yes
<b>F1-series</b>	CYA-rich C-dots	CU50F1, 3-32%	No

### 3.2.4 Biological applications

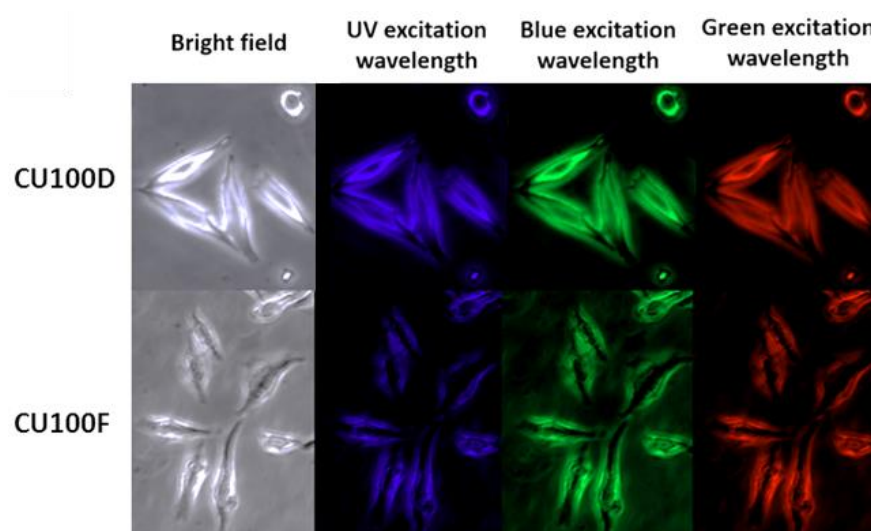
In order to assess the suitability of CU-dots for potential biomedical applications, the MTT assay was used to test their cytotoxicity against HeLa cancer cell line. The results demonstrated that the mortality of HeLa cells incubated for 24 hours with D-series (**Figure 3.26A**) or F-series (**Figure 3.26B**) CU-dots at concentrations up to 1000  $\mu\text{g/mL}$  was lower than 10%, thus showing a negligible toxicity even at high concentrations [15, 28, 31, 39]. Importantly, such low toxicity values presumably related to the abundant

content of surface functional groups are highly desirable for *in vivo* and *in vitro* biomedical applications and have been rarely reported for other classes of photoactive materials [3, 28].



**Figure 3.26** The cell viability of human cancer cervix HeLa cell line calculated from MTT assay after their incubation with D-series (A) and F-series (B) of CU-dots for 24 hours. The data is expressed as mean  $\pm$  SD of triple experiments while percentage of cytotoxicity is represented comparatively to untreated controls.

Moreover, the fluorescent images (**Figure 3.27**) revealed that CU-dots become internalised by HeLa cells upon incubation and illuminate both their cytoplasm as well as the cell membranes. Importantly, those findings demonstrate that both D-series as well as F-series of CU-dots are ideal candidates for cell labelling and multicolour imaging, while having an ability to emit a strong fluorescence signals under a broad range of excitation wavelengths [5, 29, 38, 39].



**Figure 3.27** Fluorescent microscope images of HeLa cell line incubated with 50  $\mu\text{g/mL}$  of CU100D and CU100F nanoparticles presenting their multicolour emission at various excitation wavelengths.



Additionally, the assessment of antimicrobial activity of D-series and F-series CU-dots was evaluated with the use of *Escherichia coli* and *Staphylococcus aureus* bacterial species. In detail, the F-series demonstrates remarkable antimicrobial properties against *E.coli* and *S.aureus* strains, while causing the reduction of their bacterial colonies between 99.5% to 99.9% and 99.2% to 99.9%, respectively. In like manner, the D-series shows notable antimicrobial properties against *E.coli* and *S.aureus*, which are more pronounced for CU03D, CU25D and CU50D but falls to 79% against *E.coli* for CU100D. Overall, it has been reported that the derivatives of CTA as well as molecules with similar structures to HPPT or CA have a significant antimicrobial properties [60-62].

**Table 3.3** The results from antimicrobial studies presenting the reduction in *E.coli* or *S.aureus* bacterial colonies incubated with D-series and F-series CU-dots for 24 hours at 37°C

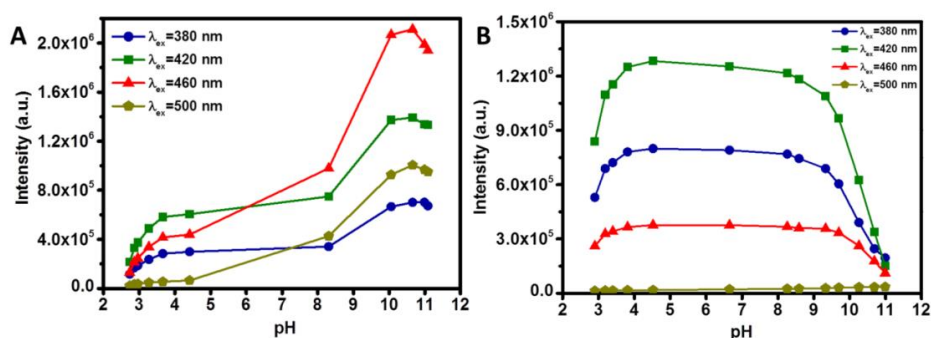
Material	<i>Escherichia coli</i>		<i>Staphylococcus aureus</i>	
	% decrease		% decrease	
	D-series	F-series	D-series	F-series
CU03	99.0	99.9	99.9	99.9
CU25	98.2	99.9	99.9	99.9
CU50	98.6	99.6	99.7	99.9
CU100	79.0	99.5	97.2	99.2

### 3.2.5 Photoluminescent properties at various pH

Prior deliberating about potential application of CU-dots as pH sensors, the examination of their PL properties in a liquid-state (**Figure 3.30**) as well as solid-state (**Figure 3.33**) forms was investigated in detail. The pH of photoluminescent suspensions and powders were modulated with the use of 1M hydrochloric acid (HCl) and 1M sodium hydroxide (NaOH) solutions, while for the preparation of the powders with the pH $\approx$ 2 and pH $\approx$ 11 the required amount of HCl or NaOH was added into filtered solutions of CU25F, CU50F, CU100F and after recording their pH the freeze drying step was carried out.

### 3.2.5.1 Liquid-state solutions

In recent decades, pH sensing in liquid media has attracted a significant interest due to the important role of pH in biomedical and environmental applications [63]. It has been previously reported that the photoluminescent properties of carbon dots in a liquid-state are sensitive towards the external parameters, including alkalinity and acidity of their aqueous solutions [41, 49, 64, 65]. In detail, the remarkable pH sensitivity of C-dots is related to the protonation and deprotonation of carbogenic cores that possess an abundant content of the surface functional groups [41, 64]. To this end, the analysis of the changes in the PL intensity of D-series (**Figure 3.30A**) and F-series (**Figure 3.30B**) CU-dots at various pH confirmed an increment of their deprotonation degree, while changing the pH from 2 up to 11. Overall, the pH-sensitive optical feature pave a way for promising use of D-series CU-dots as fluorescent probes for monitoring the intercellular pH variations as well as detecting the alerting changes in an early stage diseases [49, 65].

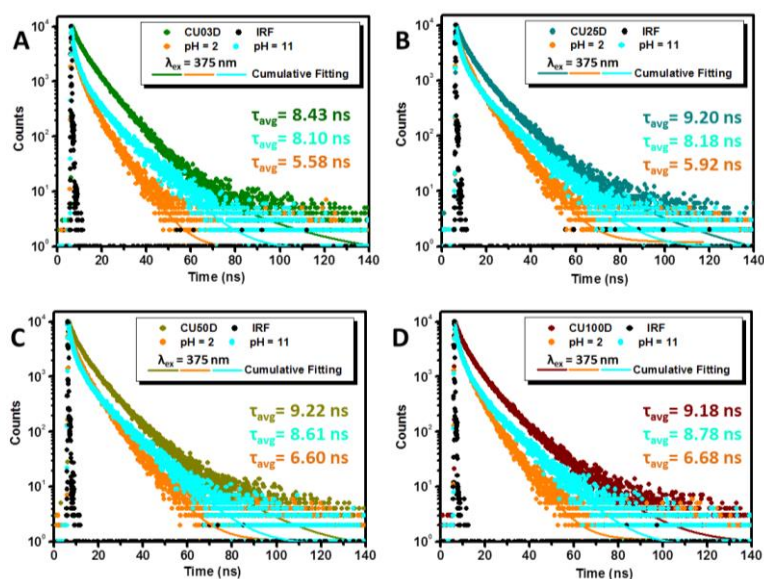


**Figure 3.28** pH dependence of the PL intensity of aqueous dispersions of CU50D (A) and CU50F (B) recorded at varied excitation wavelengths: 380 nm (blue circles), 420 nm (red triangles), 460 nm (green squares) and 500 nm (dark yellow pentagons).

The analysis of the PL lifetime decays of D-series CU-dots recorded at  $\lambda_{ex} = 375\text{nm}$  (**Figure 3.29**) confirmed that at  $\text{pH} \approx 2$  the protonation of fluorophore molecules occur with a decrement of  $\tau_{avg}$  from around 9.2 ns to 5.9 ns (CU25D) and 6.6 ns (CU50D, CU100D). To this point, it has been reported that the reduction of the citrazinic acid lifetime at acidic pH was caused by the formation of dimeric compounds that form

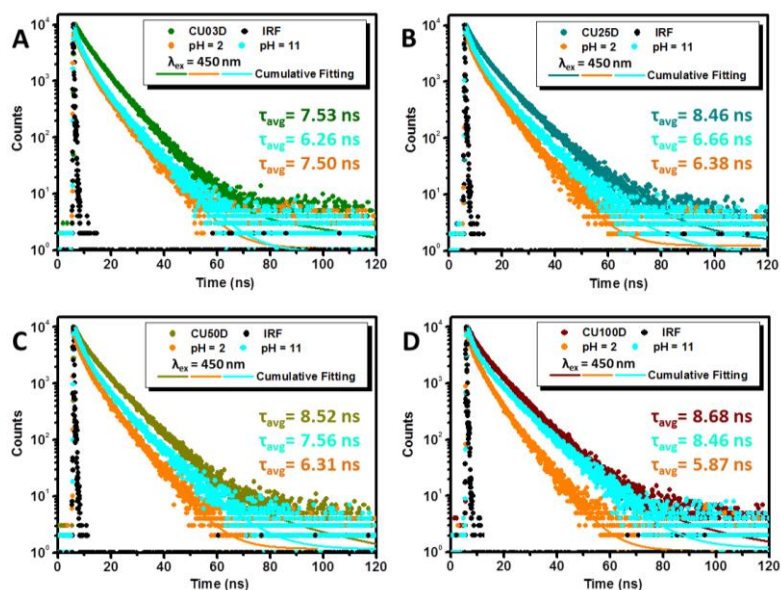


weakly fluorescent aggregates. On the other side, the insignificantly diminished PL lifetime at pH $\approx$ 11 suggest the deprotonation of citrazinic acid molecules [66].



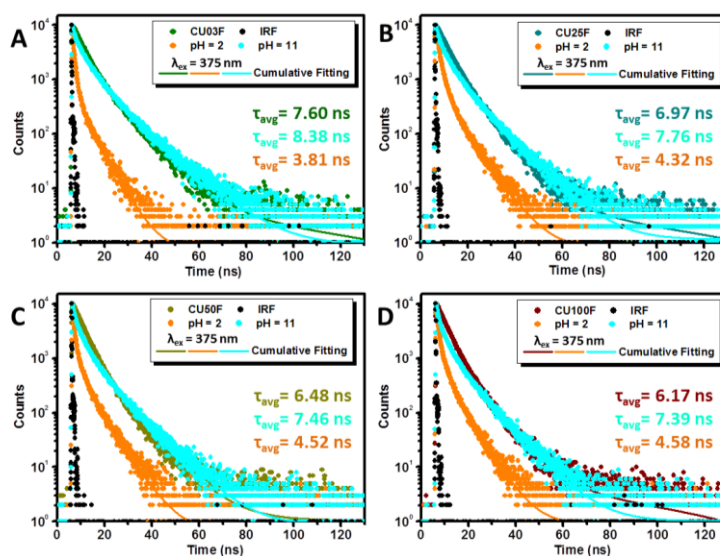
**Figure 3.29** Liquid-state fluorescence lifetime decays of aqueous dispersions of CU03D (A), CU25D (B), CU50D (C), CU100D (D) with neutral pH, pH=2 (orange colour) and pH=11 (cyan colour) at  $\lambda_{ex}$  = 375 nm.

In contrast, the PL lifetime decays recorded at  $\lambda_{ex}$  = 450nm (**Figure 3.30**) show an opposite trend to above described results, with the  $\tau_{avg}$  decreasing at acidic pH along with further N-doping. Interestingly, even though the PL intensity of CU03D nanomaterial is in similar quenched at pH $\approx$ 2 ( $\tau_{avg}$ = 7.50 ns) and pH $\approx$ 11 ( $\tau_{avg}$ = 6.26 ns), the average PL lifetimes reveal a change in the fluorophores environment.



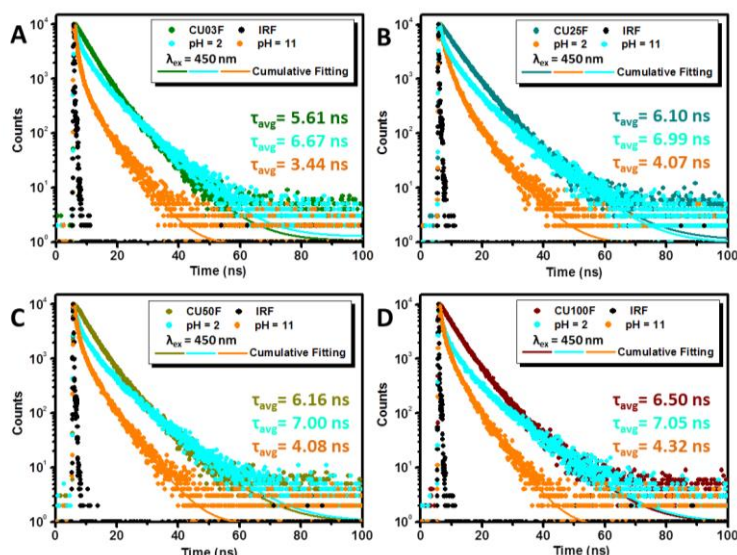
**Figure 3.30** Liquid-state fluorescence lifetime decays of aqueous dispersions of CU03D (A), CU25D (B), CU50D (C), CU100D (D) with neutral pH, pH = 2 (orange colour) and pH = 11 (cyan colour) at  $\lambda_{ex}$  = 450 nm

The fluorescence decay curves of F-series CU-dots demonstrate that the  $\tau_{avg}$  are significantly shorter at acidic pH and remain unchanged under both excitation wavelengths with  $\tau_{avg} \approx 3.6$  ns for CU03F and  $\tau_{avg} \approx 4.3$  ns for CU25F, CU50F, CU100F (**Figure 3.31**). On the other hand, the changes in the  $\tau_{avg}$  in alkaline environment may be related to creation of protective shell via the passivation of adsorbed  $OH^-$  on the original acidic defects on CU-dots surface. Thus, this phenomenon makes CU-dots non-isolated as well as increases the non-radiative recombination rate [67].



**Figure 3.31** Liquid-state fluorescence lifetime decays of aqueous dispersions of CU03F (A), CU25F (B), CU50F (C), CU100F (D) with neutral pH, pH=2 (orange colour) and pH=11 (cyan colour) at  $\lambda_{ex}$  = 375 nm.

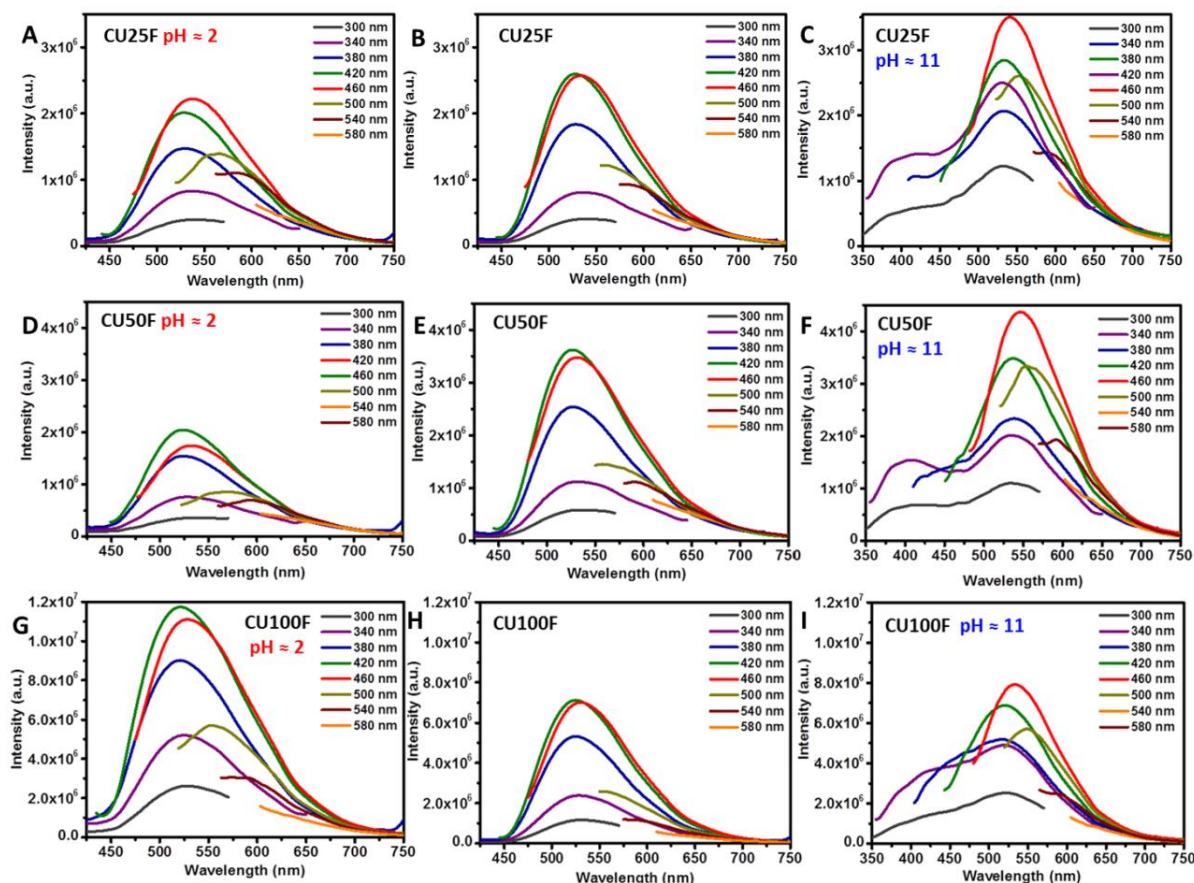
Overall, the analysis of the fluorescence decays of F-series CU-dots (**Figure 3.32**) revealed that these fluorophore-rich materials demonstrate sensitivity towards acidic pH, presumably due to the aggregation of CTA and HPPT fluorophore molecules [66].



**Figure 3.32** Liquid-state fluorescence lifetime decays of aqueous dispersions of CU03F (A), CU25F (B), CU50F (C), CU100F (D) with neutral pH, pH=2 (orange colour) and pH=11 (cyan colour) at  $\lambda_{ex}$ = 450 nm.

### 3.2.5.2 Solid-state powders

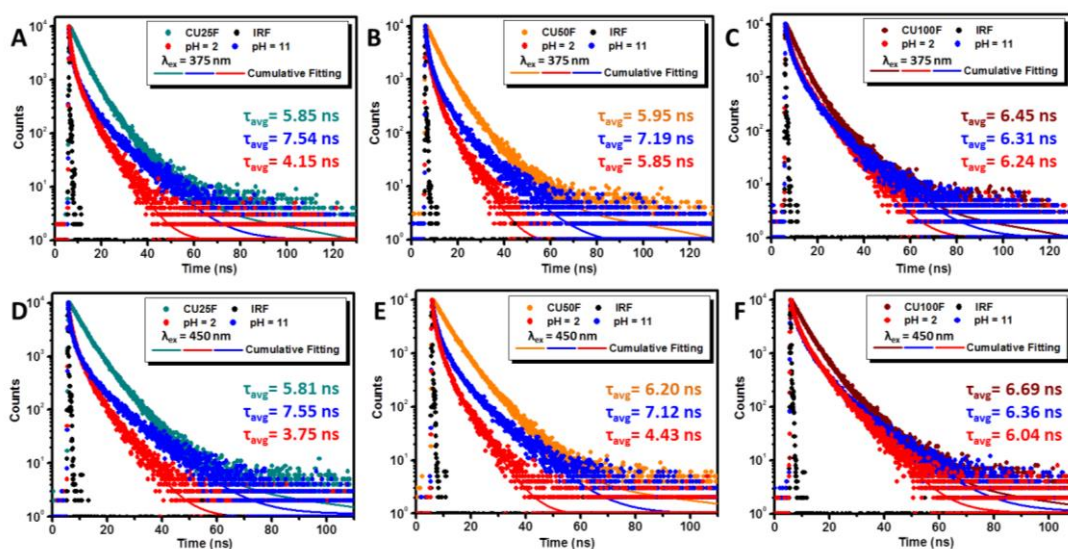
The PL spectra of CU25F (**Figure 3.33A-C**) and CU50F (**Figure 3.33D-F**) powders with modulated pH demonstrate that the PL emission become significantly diminished at pH $\approx$ 2, while otherwise the PL intensities increase at pH $\approx$ 11. This phenomenon could be attributed to the abundant content of CTA molecular fluorophore that due to the higher content of sp<sup>2</sup> domains is prone to aggregate [44], as proved by the presence of additional contributions stemming from the CTA units at  $\lambda_{em}\approx$  390nm (**Figure 3.33C,F**). In contrast, the CU100F powder (**Figure 3.33G-I**) displays an opposite behaviour with increased PL at acidic pH (**Figure 3.33G**) and alike luminescence at basic pH (**Figure 3.33I**), presumably due to significant content of HPPT as a molecular fluorophore as well as abundant content of urea that works as a diluent and suppress the aggregation of conjugated sp<sup>2</sup>-hybridized nanodomains [44].



**Figure 3.33** Solid-state PL spectra of CU25F (A-C), CU50F (D-F) and CU100F (G-I) nanopowders with pH $\approx$ 2 (left), neutral pH (middle) and pH $\approx$ 11 (right).

The PL lifetime decays of the powders with modulated pH (**Figure 3.34**) further proved the sensitivity of CU25F (**Figure 3.34A,D**) and CU50F (**Figure 3.34B,E**) powders towards acidic and basic pH, which was more pronounced for the CU25F powder, derived from the higher CA content. On the other side, negligible variations in the  $\tau_{avg}$  of CU100F powder being close to 6.3 ns at pH $\approx$ 2 as well as 6.1 ns at pH $\approx$ 11 implied that the excess of urea diminish the contribution of the molecular fluorophores towards the PL phenomena. In general, the collected results demonstrated that CU25F and CU50F powders hold a great potential to be applied as solid-state pH sensors.





**Figure 3.34** Solid-state PL lifetime decays of CU25F, CU50F and CU100F nanopowders with various pH recorded at 375 nm (A-C) and 450 nm (D-F).

### 3.3 Conclusion

In conclusion, a large gallery of photoactive suspensions and powders was derived from the CA/urea precursors mixture. The chemical composition as well as the optical properties of each member of particular family were fine-tuned by adjusting the molar ratio of the precursors. The novel approach based on the utilization of a different molar ratios between CA and urea precursors as well as two standard size separation strategies, either filtration or dialysis, led to fabrication of four distinct families (D-,D1-F-,F1-series) of photoluminescent CU-dots suspensions, in which the emissive signal predominantly arises from C-dots with embedded fluorophores (D-series), a blend of molecular fluorophores (D1-series), a mixture of C-dots with unbound molecular fluorophores (F-series) as well as cyanuric acid-rich C-dots (F1-series). The versatile separation strategies favoured the predominance of different molecular fluorophores, either citrazinic acid (CTA) or (4-hydroxy-1H-pyrrolo(3,4-c)pyridine-1,3,6(2H,5H)-trione (HPPT), as confirmed by the detailed spectroscopic studies. The excellent photoluminescent properties under a broad range of excitation wavelengths proved that these nanoscopic emitters are ideal candidates for the cell labelling and multicolour imaging applications, while the evaluation of their optical sensitivity towards pH variations proved their potential to be use as optical nanoprobes for

monitoring of the intercellular pH variations or detecting the alerting changes in the early stage of disease. Besides that, the use of abundant urea content in the precursors mixture together with filtration as a purification strategy facilitated the generation of fluorescent powders that hold the potential to be used as a solid-state pH sensors. In the midst of additional advantages, presented methodology led the generation of fluorescent nanoparticles from both the filtrate as well as the residue, thereby constitute an eco-friendly synthetic approach that generate a minimal waste. Conclusively, both an easy-to-follow waste-free approaches as well as the utilization of a cost efficient precursors mixture opens a door for commercialization of these environmentally benign nanoemitters. Moreover, the modulated luminescent features, non-toxic nature, antimicrobial properties as well as pH-responsive behaviour pave a way for their promising applications in the biomedical fields.

### 3.4 References

1. Kelarakis, A., *From highly graphitic to amorphous carbon dots: A critical review*. MRS Energy & Sustainability, 2014. **1**(2): p. 1-15.
2. Hao, Y.N., et al., *Enhanced photoluminescence of pyrrolic-nitrogen enriched graphene quantum dots*. RSC Advances, 2015. **5**(54): p. 43750-43755.
3. Zholobak, N.M., et al., *Facile fabrication of luminescent organic dots by thermolysis of citric acid in urea melt, and their use for cell staining and polyelectrolyte microcapsule labelling*. Beilstein J Nanotechnol, 2016. **7**: p. 1905-1917.
4. Wang, T., et al., *Carbon dots with molecular fluorescence and their application as a "turn-off" fluorescent probe for ferricyanide detection*. Scientific Reports, 2019. **9**(10723): p. 1-9.
5. Wang, H., et al., *Fluorescently tuned nitrogen-doped carbon dots from carbon source with different content of carboxyl groups*. APL Materials 2015. **3**(8): p. 1-7.
6. Qu, D., et al., *Formation mechanism and optimization of highly luminescent N-doped graphene quantum dots*. Sci. Rep., 2014. **4**: p. 5294-5303.
7. Fan, X. and Z. Fan, *Determination of Thiourea by On–Off Fluorescence Using Nitrogen-Doped Graphene Quantum Dots*. Analytical Letters, 2019. **52**(13): p. 2028–2040.
8. Shen, S., et al., *Advanced Synthesis of Carbon Dots: Novel Insights into Temperature Effect on Fluorescent Performance*. Thermal Science, 2019. **23**(4): p. 2453-2459.
9. Ma, Y., et al., *Doping effect and fluorescence quenching mechanism of N-doped graphene quantum dots in the detection of dopamine*. Talanta, 2019. **196**: p. 563–571.
10. Qu, D., et al., *Highly luminescent S, N co-doped graphene quantum dots with broad visible absorption bands for visible light photocatalysts*. Nanoscale, 2013. **5**: p. 12272–12277.
11. Jin, L., et al., *The Synthesis and Application of Nitrogen-Doped Graphene Quantum Dots on Brilliant Blue Detection*. Journal of Nanomaterials, 2019: p. 1-9.
12. Yang, C., et al., *Biodegradable Polymer-Coated Multifunctional Graphene Quantum Dots for Light-Triggered Synergetic Therapy of Pancreatic Cancer*. ACS Appl. Mater. Interfaces 2019. **11**: p. 2768–2781.
13. Xue, Z., H. Gao, and X. Li, *A Green and lower-temperature synthesis of two-color fluorescent nitrogen doped graphene quantum dots*. Dyes and Pigments, 2018. **156**: p. 379-385.

14. Miao, X., et al., *Synthesis of Carbon Dots with Multiple Color Emission by Controlled Graphitization and Surface Functionalization*. Adv. Mater., 2017: p. 1-8.
15. Sharma, A., et al., *Interaction of Carbon Dots with Endothelial Cells: Implications for Biomedical Applications*. ACS Appl. Nano Mater. , 2019. **2**: p. 5483–5491.
16. Cao, X., et al., *A facile microwave-assisted fabrication of fluorescent carbon nitride quantum dots and their application in the detection of mercury ions*. Spectrochimica Acta Part A: Molecular and Biomolecular Spectroscopy, 2015. **151**: p. 875-880.
17. Wang, J., et al., *Simply synthesized nitrogen-doped graphene quantum dot (NGQD)-modified electrode for the ultrasensitive photoelectrochemical detection of dopamine*. Nanophotonics, 2019: p. 1-9.
18. Li, X., et al., *Using N-doped Carbon Dots Prepared Rapidly by Microwave Digestion as Nanoprobes and Nanocatalysts for Fluorescence Determination of Ultratrace Isocarbophos with Label-Free Aptamers*. Nanomaterials, 2019. **9**(223-237).
19. Gu, S., et al., *Microwave Growth and Tunable Photoluminescence of Nitrogen-doped Graphene and Carbon Nitride Quantum Dots*. Journal of Materials Chemistry C, 2019. **7**(18): p. 5468-5476.
20. Tsai, H., et al., *Fluorescence studies of the interaction between chloramphenicol and nitrogen-doped graphene quantum dots and determination of chloramphenicol in chicken feed*. J Chin Chem Soc. , 2019: p. 1-8.
21. Devi, J.S.A., et al., *Understanding the Citric Acid–Urea Co–Directed Microwave Assisted Synthesis and Ferric Ion Modulation of Fluorescent Nitrogen Doped Carbon Dots: A Turn On Assay for Ascorbic Acid*. Chemistry Select 2019. **4**: p. 816-824.
22. Permatasari, F.A., et al., *Design of Pyrrolic-N-rich Carbon Dots with Absorption in the First Near-Infrared Window for Photothermal Therapy*. ACS Appl. Nano Mater., 2018. **1**(5): p. 2368-2375.
23. Qu, S., et al., *A Biocompatible Fluorescent Ink Based on Water-Soluble Luminescent Carbon Nanodots*. Angew. Chem. Int. Ed. , 2012. **51**: p. 12215 – 12218.
24. Sciortino, A., et al.,  *$\beta$ -C<sub>3</sub>N<sub>4</sub> nanocrystals: Carbon dots with extraordinary Morphological, Structural and Optical Homogeneity*. Chem. Mater., 2018. **30**: p. 1695–1700.
25. Permatasari, F.A., et al., *Role of C–N Configurations in the Photoluminescence of Graphene Quantum Dots Synthesized by a Hydrothermal Route*. Sci. Rep. , 2016. **6**: p. 21042-21050.



26. Zhu, J., et al., *Modulation of the photoluminescence in carbon dots through surface modification: from mechanism to white light-emitting diodes*. Nanotechnology, 2018. **29**: p. 245702-245711.
27. Simões, E.F.C., J.M.M. Leitão, and J.C.G. Esteves da Silva, *Carbon dots prepared from citric acid and urea as fluorescent probes for hypochlorite and peroxyxynitrite*. Microchim Acta, 2016. **183**: p. 1769–1777.
28. Bao, X., et al., *In vivo theranostics with near-infraredemitting carbon dots—highly efficient photothermal therapy based on passive targeting after intravenous administration*. Light: Science & Applications, 2018. **7**(91).
29. Khan, S., et al., *Carbon Dots for Single-Molecule Imaging of the Nucleolus*. ACS Appl. Nano Mater. , 2018. **1**(2): p. 483-487.
30. Qu, S., et al., *Toward Efficient Orange Emissive Carbon Nanodots through Conjugated sp<sup>2</sup>-Domain Controlling and Surface Charges Engineering*. Adv. Mater. , 2016. **28**: p. 3516–3521.
31. Li, D., et al., *Supra-(carbon nanodots) with a strong visible to near-infrared absorption band and efficient photothermal conversion*. Light: Science & Applications, 2016. **5**: p. 1-8.
32. Kasprzyk, W., et al., *Luminescence phenomena of carbon dots derived from citric acid and urea - a molecular insight*. Nanoscale, 2018. **10**(29): p. 13889-13894.
33. Qu, S., et al., *Amplified Spontaneous Green Emission and Lasing Emission From Carbon Nanoparticles*. Adv. Funct. Mater., 2014. **24**: p. 2689–2695.
34. Gu, S., et al., *Fluorescence of functionalized graphene quantum dots prepared from infrared-assisted pyrolysis of citric acid and urea*. Journal of Luminescence, 2020. **217**: p. 1-10.
35. Tian, Z., et al., *Full-Color Inorganic Carbon Dot Phosphors for White-Light-Emitting Diodes*. Adv. Optical Mater., 2017. **5**: p. 1-9.
36. Hou, Y., et al., *One-pot electrochemical synthesis of functionalized fluorescent carbon dots and their selective sensing for mercury ion*. Analytica Chimica Acta, 2015. **866**: p. 69-74.
37. Wang, W., et al., *Photobleaching and stabilization of carbon nanodots produced by solvothermal synthesis*. Phys. Chem. Chem. Phys., 2016. **18**: p. 466-475.
38. Stefanakis, D., et al., *Synthesis of fluorescent carbon dots by a microwave heating process: structural characterization and cell imaging applications*. J Nanopart Res, 2014. **16**: p. 2646-2656.
39. Wu, Z.L., et al., *A general quantitative pH sensor developed with dicyandiamide N-doped high quantum yield graphene quantum dots*. Nanoscale, 2014. **6**: p. 3868-3874.

40. Xu, M., et al., *A green heterogeneous synthesis of N-doped carbon dots and their photoluminescence applications in solid and aqueous states*. *Nanoscale*, 2014. **6**: p. 10307-10316.
41. Kong, W., et al., *Optical properties of pH-sensitive carbon-dots with different modifications*. *Journal of Luminescence*, 2014. **148**: p. 238–242.
42. Ogi, T., et al., *Kinetics of nitrogen-doped carbon dot formation via hydrothermal synthesis*. *NewJ.Chem.* , 2016. **40**: p. 5555-5561.
43. Ogi, T., et al., *Transient nature of graphene quantum dot formation via a hydrothermal reaction*. *RSC Adv.*, 2014. **4**(99): p. 55709-55715.
44. Yoo, H.J., B.E. Kwak, and D.H. Kim, *The Self-Quenching Origin of Carbon Dots and the Guideline for Its Solid-State Luminescence*. *The Journal of Physical Chemistry*, 2019. **123**(44): p. 27124-27131.
45. Gu, S., et al., *Fluorescence of functionalized graphene quantum dots prepared from infrared-assisted pyrolysis of citric acid and urea*. *Journal of Luminescence* 2020. **217**: p. 116774.
46. Liu, W., et al., *Highly crystalline carbon dots from fresh tomato: UV emission and quantum confinement*. *Nanotechnology*, 2017. **28**(48): p. 485705.
47. Santiago, S.R.M., et al., *Effect of nitrogen doping on the photoluminescence intensity of graphene quantum dots*. *Optics Letters*, 2017. **42**(18): p. 3642-3645.
48. Sell, W.J. and T.H. Easterfield, *LXXIII.—Studies on citrazinic acid. Part I*. *Journal of the Chemical Society, Transactions*, 1893. **63**: p. 1035-1051.
49. Hu, Y., et al., *Waste frying oil as a precursor for one-step synthesis of sulfur-doped carbon dots with pH-sensitive photoluminescence*. *Carbon*, 2014. **77**: p. 775-782.
50. Ehrat, F., et al., *Tracking the Source of Carbon Dot Photoluminescence: Aromatic Domains versus Molecular Fluorophores* *Nano Lett*, 2017. **17**(12): p. 7710-7716.
51. Yarur, F., J.R. Macairan, and N. R., *Ratiometric Detection of Heavy Metal Ions Using Fluorescent Carbon Dots*. *Environmental Science: Nano*, 2019(4): p. 1-11.
52. Schaber, P.M., et al., *Thermal decomposition (pyrolysis) of urea in an open reaction vessel*. *Thermochimica Acta*, 2004. **424**: p. 131–142.
53. Reckmeier, C.J., et al., *Aggregated Molecular Fluorophores in the Ammonothermal Synthesis of Carbon Dots*. *Chem. Mater.*, 2017. **29**: p. 10352-10361.
54. Niu, X., et al., *Revealing the underlying absorption and emission mechanism of nitrogen doping graphene quantum dots*. *Nanoscale*, 2016. **8**: p. 19376-19382
55. Xiong, Y., et al., *Carbonization conditions influence the emission characteristics and the stability against photobleaching of nitrogen doped carbon dots*. *Nanoscale*, 2017. **9**: p. 11730-11738.

56. Sharma, A., et al., *Origin of Excitation Dependent Fluorescence in Carbon Nanodots*. J. Phys. Chem. Lett. , 2016. **7**: p. 3695–3702.
57. Xiong, Y., et al., *Influence of molecular fluorophores on the research field of chemically synthesized carbon dots*. Nano Today, 2018. **23**: p. 124–139.
58. Schneider, J., et al., *Molecular Fluorescence in Citric Acid-Based Carbon Dots*. J. Phys. Chem. C 2017. **121**: p. 2014–2022.
59. Zheng, C., X. An, and J. Gong, *Novel pH sensitive N-doped carbon dots with both long fluorescence lifetime and high quantum yield*. RSC Adv., 2015. **5**: p. 32319–32322.
60. Hossan, A.S.M., et al., *Synthesis and Antimicrobial Activity of Some New Pyrimidinone and Oxazinone Derivatives Fused with Thiophene Rings Using 2-Chloro-6-ethoxy-4-acetylpyridine as Starting Material*. Molecules, 2012. **17**: p. 13642–13655.
61. Westhuyzen, R., et al., *Pyrrolo[3,4-c]pyridine-1,3(2H)-diones: A Novel Antimycobacterial Class Targeting Mycobacterial Respiration*. J. Med. Chem. , 2015. **58**(23): p. 9371–9381.
62. Burel, C., A. Kala, and L. Purevdorj-Gage, *Impact of pH on citric acid antimicrobial activity against Gram-negative bacteria*. Lett Appl Microbiol. , 2020.
63. Yu, T., et al., *A rapid microwave synthesis of green-emissive carbon dots with solid-state fluorescence and pH-sensitive properties*. R. Soc. open sci. 5: 180245., 2018. **5**: p. 180245–180256.
64. Choudhury, S.D., et al., *pH Elicited Luminescence Functionalities of Carbon Dots: Mechanistic Insights*. J. Phys. Chem. Lett., 2017. **8**(7): p. 1389–1395.
65. Ehtesabi, H., et al., *Carbon dots with pH-responsive fluorescence: a review on synthesis and cell biological applications*. Microchimica Acta, 2020. **187**(150).
66. Stagi, L., et al., *Anomalous Optical Properties of Citrazinic Acid under Extreme pH Conditions*. ACS Omega, 2020. **5**: p. 10958–10964.
67. Guo, X., et al., *A facile and green approach to prepare carbon dots with pH-dependent fluorescence for patterning and bioimaging*. RSC Adv., 2018. **8**: p. 38091–38099.

**Chapter 4:**  
**Iron based carbogenic  
nanoparticles with  
exceptional optical,  
magnetic and antimicrobial  
properties**

*“Creativity is seeing what everyone else has seen,  
and thinking what no one else has thought”*

*Albert Einstein*

## 4.1 Introduction

Among various types of nanoparticles used in biomedical applications, a special attention is given to superparamagnetic Fe<sub>3</sub>O<sub>4</sub> NPs (Fe-NPs) with sizes below 20 nm that have been used for bioseparation of cells [1], magnetically controlled gene and drug delivery [2, 3], magnetic hyperthermia treatment [4], magnetic resonance imaging (MRI) contrast agents [5], biosensors development [6], stem cell tracking and tissue repair [2] as well as the diagnosis and treatment of bacterial infections [7]. To date, Fe-NPs have been synthesized via bottom-up strategies, such as thermal decomposition [8], coprecipitation [9], hydrothermal or solvothermal methods [5] as well as sol-gel method [10]. Nonetheless, the as-prepared bare Fe-NPs have tendency to oxidise in the air, which further impact on the loss of their characteristic magnetic features, aggregation *in vivo* as well as rapid detection by the immune system [2]. Therefore, the generation of protective coating constitute a crucial approach to improve the dispersion of Fe-NPs in biological media, facilitate their compatibility with the blood, delay the degradation by macrophages as well as adsorption by plasma proteins [2, 11]. To this direction, small hydrophilic molecules and biocompatible polymers have been used as protective shells for Fe-NPs cores, including polyethylene glycol (PEG), chitosan, dextran, polyvinyl alcohol (PVA), citric acid as well as organic (i.e. C-dots) or inorganic (i.e. SiO<sub>2</sub>) components [2, 11]. Among all, the build-up of C-dots shell around the Fe-NPs cores constitute a promising strategy for development of multifunctional platforms (C/Fe-NPs) for *in vivo* fluorescence imaging [12], photodynamic therapy [13] or traceable drug and gene delivery [14]. Besides that, C/Fe-NPs have been also applied as dual-modal imaging agents used for detection of breast cancer cells [15], single nanoplatforms in magnetic hyperthermia treatment for cancer theranostics [16], highly sensitive sensors of dopamine for diagnosing the neurological diseases [17], portable biosensors used for on-site tests [18] as well as magneto/photothermally responsive drug nanocarriers for chemotherapy or photothermal therapy [19, 20]. In regard to preparation methods, carbogenically-coated Fe-NPs with shape-controlled morphology have been widely synthesized via coprecipitation [18, 21-24], thermal decomposition [15, 25, 26], microwave-assisted

[27], hydrothermal [17, 28-32] and solvothermal [16, 20, 32-35] strategies, whereas the ultrasonication has been rarely used to promote the self-assembly of C-dots on the pre-synthesized Fe-NPs [36, 37]. Importantly, the presence of multifarious surface functional moieties on C-dots pavement facilitate further conjugation of C/Fe-NPs with cellular components and biomolecules, thus making them also an ideal platforms for sensitive biosensing [38] or selective detection of pathogens [14]. Overall, carbogenically-coated Fe-NPs possess desired features for promising biomedical applications, such as cytocompatibility, biodegradability, antimicrobial activity, low toxicity, superior colloidal stability as well as a high relaxation values [2, 11, 39]. Thus, in this project the suitability of magnetic C-dots to be used as a magnetically-guided optical nanoprobe for the labelling of cancer cells was investigated in detail.

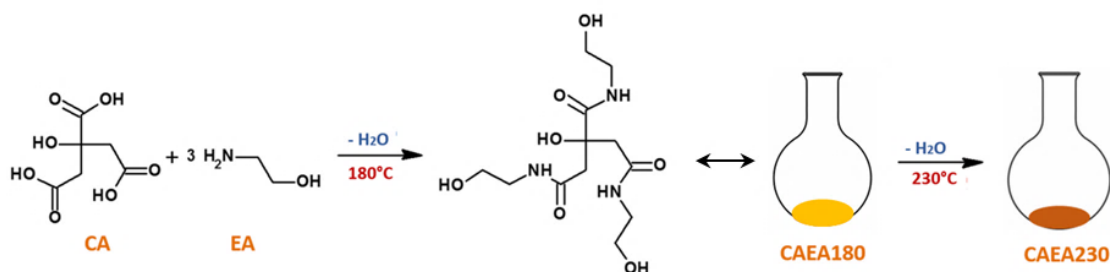
## **4.2 Novelty and predominance over existing materials**

The present work constitute novel insights into three specific directions. First, the impact of Fe-doping on the morphological, structural and optical properties of CNP230, derived from PL-CAEA180 via thermal treatment at 230°C, was compressively investigated for the first time. In detail, the systematic incorporation of iron into the C-dots matrix led to generation of a novel family of magnetic C-dots, which optical and magnetic properties can be modified in a controlled manner by adjusting the C/Fe ratios. Second, the versatility of carbon sources (i.e. amines, polymers, polyetheramine) used for the synthesis of hybrid magneto-fluorescent NPs proved that the proposed fabrication method can be applied in a different settings, thereby giving a promise for a large scale commercialisation of diverse magneto-fluorescent NPs. Importantly, the presented synthetic approach is not only convenient due to the one-pot reaction and single-step synthesis but also can be performed without the use of inert gases, which has been neglected in previous literature reports. Third, although significant carbon content diminish the magnetic features of magnetic C-dots, the incorporation of  $Gd^{3+}$  ions into C/Fe-NPs matrix via novel approach overcame this limitation as well as broaden their potential use in the application as Magnetic Resonance Imaging (MRI) contrast agents.

Among superior advantages of developed procedure for the fabrication of magnetic C-dots are facile one-pot and single-step fabrication process as well as the versatility of precursors mixtures that lead to a large gallery of magneto-fluorescent NPs, which could be easily implemented in the industrial setting. In contrast, many literature reports noted tedious multistep synthetic procedures of C/Fe-NPs, which limit their large scale synthesis as well as potential commercialisation [21, 23, 28-30, 32, 36, 37, 40, 41]. Besides advantages, significant carbogenic content in the structure of magnetic C-dots have a negative impact on their magnetisation values, which are significantly diminished in contrast to several literature reports [33, 37]. Nevertheless, further incorporation of gadolinium into the structure of C/Fe-NPs overcame this limitation and proved that their magnetic features, without compensation of fluorescence properties, can be further improved for specific biomedical applications [42-46].

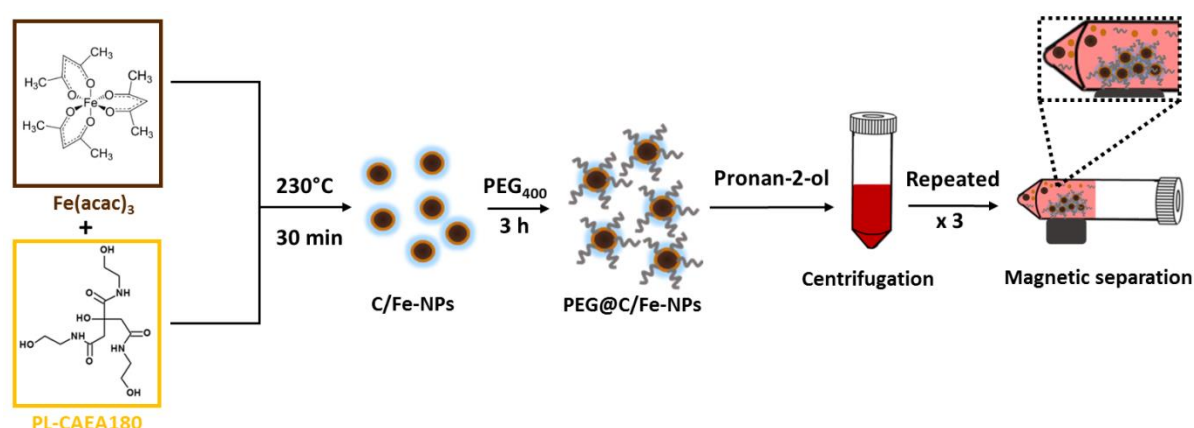
#### 4.3 Results and discussion

The syntheses of magnetic C-dots (abbreviated hereafter as C/Fe-NPs) with modulated fluorescent properties were based on a novel approach utilizing highly photoluminescent (PL) carbon dots precursor (PL-CAEA180) as a carbon source. As presented in **Figure 4.1**, the PL-CAEA180 is formed from citric acid and ethanolamine (molar ratio 3:1) as starting reagents, after being subjected to heating under the reflux at 180°C for 30 minutes. Subsequently, continuous heating at 230°C without reflux results in the evaporation of water molecules arising from the condensation reaction, thus the formation of C-dots (known as CNP230) with well-defined shape is completed [42].



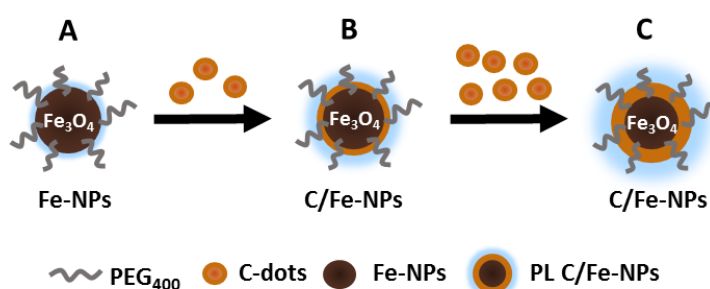
**Figure 4.1** Scheme presenting the formation of PL-CAEA180 and CNP230 derived from the mixture of citric acid (CA) and ethanolamine (EA).

In the next step, C/Fe-NPs were synthesized from the carbon and iron precursors mixture based on the pre-formed PL-CAEA180 and iron (III) acetylacetonate ( $\text{Fe}(\text{acac})_3$ ), respectively. In regard to the formation mechanism, it is believed that the heating of the reaction mixture at  $230^\circ\text{C}$  influence on the generation of protective carbogenic shell with blue luminescence on the Fe-NPs cores, whereas addition of polyethylene glycol suppress the aggregation of magnetic domains and enhance dispersibility of as-prepared C/Fe-NPs in biological media. The schematic presentation of the synthesis approach for C/Fe-NPs is depicted in **Figure 4.2**.



**Figure 4.2** Scheme presenting the formation and purification of magnetic C-dots via thermal treatment of  $\text{Fe}(\text{acac})_3$  and PL-CAEA180 precursors mixtures.

Nevertheless, the adjustment of PL-CAEA180 content during the synthesis step play a crucial role in the formation of protective carbogenic shell on the magnetite-based cores (**Figure 4.3A**), which thickness can modulated by increment of C-dots content (**Figure 4.3B,C**).

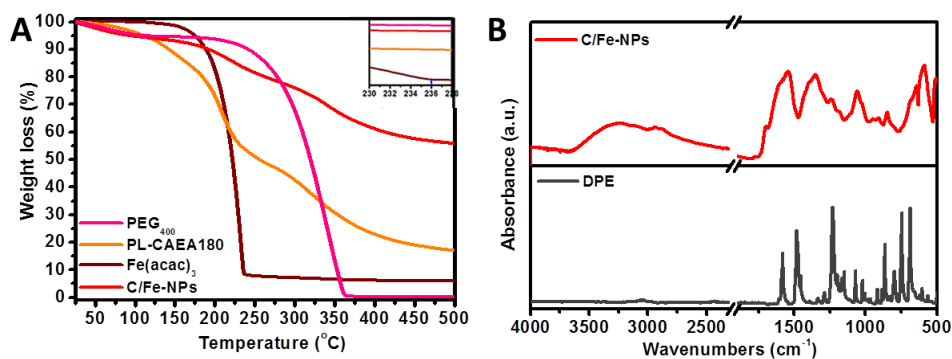


**Figure 4.3** Scheme presenting the controlled self-assembly of C-dots (B,C) on the surface of Fe-NPs (A).



### 4.3.1 Optimization of magnetic C-dots synthesis parameters

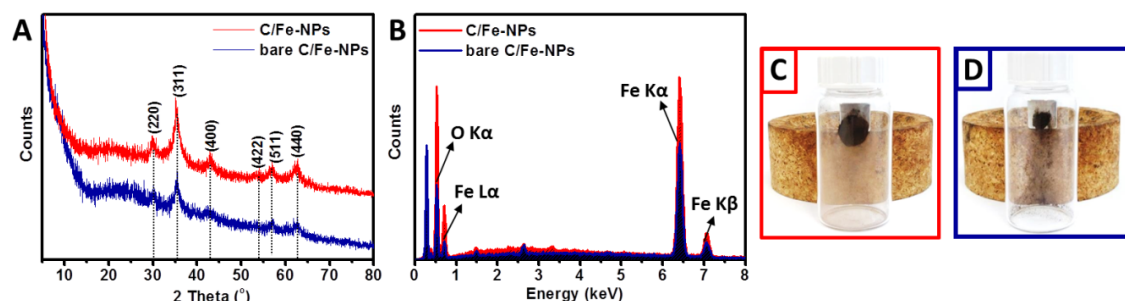
The development of synthesis protocol was associated with the adjustment of crucial parameters, such as temperature, time of heating as well as selection of iron precursor, reaction solvent and capping agent. In order to adjust the optimal synthesis temperature, thermal analysis was conducted for the precursors mixture. It has been previously reported by Krysmann et al., that pyrolysis of PL-CAEA180 at 230°C leads to the formation of CNP230 with well-defined carbogenic cores and an average nanoparticle size of 19 nm [42]. Therefore, a temperature for the synthesis of hybrid C/Fe-NPs was kept the same and iron (III) acetylacetonate was chosen as Fe precursor, while undergo thermal decomposition with a total weight loss equal to 91,04% at 236°C (**Figure 4.4A**). Importantly, previous report highlighted that the supplementary presence of diphenyl ether (DPE) as a high boiling point solvent decreases the decomposition temperature of  $\text{Fe}(\text{acac})_3$  to 200°C, thereby suggested its use as a reaction medium [29, 43]. The high purity of synthesized C/Fe-NPs is confirmed by the FTIR spectra and displayed as a lack of characteristic for diphenyl ether absorption bands (**Figure 4.4B**).



**Figure 4.4** TGA curves of magnetic C-dots and synthesis precursors (A) together with their FTIR spectra depicting the purity of post-synthesized C/Fe-NPs (B).

To enhance biocompatibility and dispersibility of magnetic C-dots in biological fluids, polyethylene glycol (PEG<sub>400</sub>) was selected as a non-toxic surface capping agent, which also prevents agglomeration of magnetic domains through repulsive interactions between polymeric chains [35, 44]. Importantly, PEGylation process further prolong the circulation of C/Fe-NPs in the body [35] and impact on the formation of well-

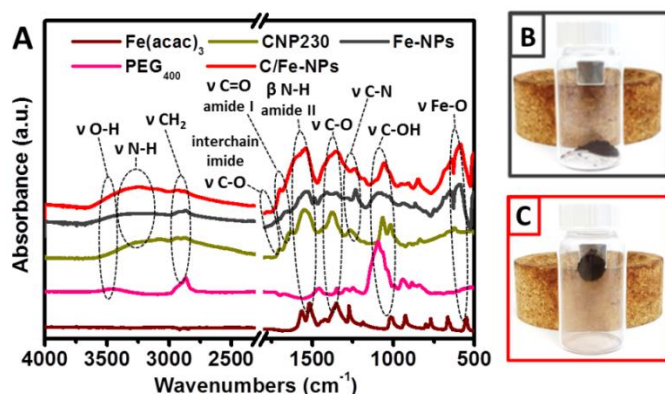
defined hybrid nanocrystals with enhanced magnetic properties, as further confirmed by the chemical analysis (**Figure 4.5A,B**) or response towards an external magnet of C/Fe-NPs (**Figure 4.5C**) as well as bare C/Fe-NPs (**Figure 4.5D**) that were prepared without addition of PEG<sub>400</sub>.



**Figure 4.5** The XRD patterns (A), EDS spectra (B) and photos of C/Fe-NPs (C) and bare C/Fe-NPs (D) with attached external magnets.

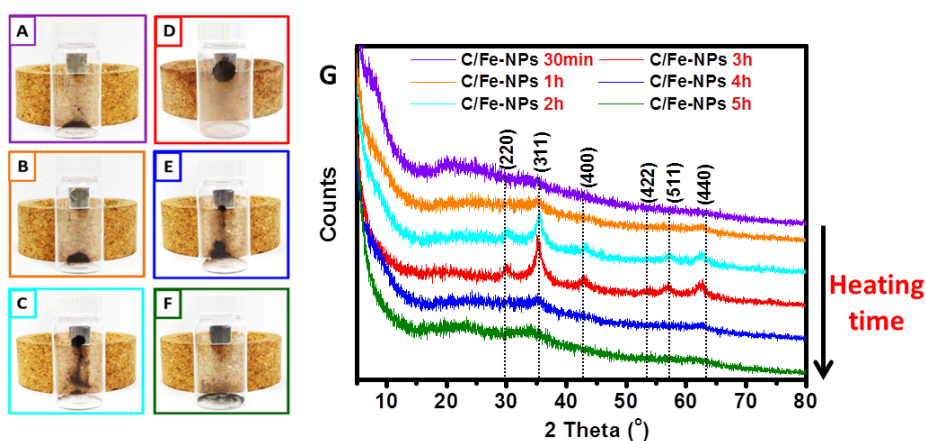
The structural insight into chemical composition of magnetic C-dots and their corresponding precursors was gained by the FTIR analysis, as presented in **Figure 4.6A**. In detail, the FTIR spectrum of CNP230 displays the presence of stretching vibrations at  $1067\text{ cm}^{-1}$  (O-H bond of hydroxyl group),  $1270\text{ cm}^{-1}$  (C-N bond),  $1386\text{ cm}^{-1}$  (C-O bond of carboxylic group),  $1557\text{ cm}^{-1}$  (N-H in-plane bending and C-N bond),  $1634\text{ cm}^{-1}$  (C=O bond),  $1750\text{ cm}^{-1}$  (C=O and C=N imide bonds as a result of extensive crosslinking reactions),  $2879\text{ cm}^{-1}$  and  $2935\text{ cm}^{-1}$  (symmetric and asymmetric C-H bonds) and  $3262\text{ cm}^{-1}$  (N-H bond of amine functional group), which occurrence can facilitate the interactions of C-dots with cellular components [30, 42]. On the other hand, the FTIR spectra of magnetic C-dots further confirmed the presence of above mentioned functional groups, while the shifting of C=O stretching vibration of carboxylic moieties ( $1697\text{ cm}^{-1}$ ) as well as Fe-O-Fe band of magnetite ( $588\text{ cm}^{-1}$ ) indicated changes in the coordination environment of C-dots as well as Fe-NPs, respectively [27, 30, 41, 45]. In particular, these changes have a significant impact on the overall magnetic properties of C/Fe-NPs (**Figure 4.6C**), whereas Fe-NPs with the Fe-O-Fe band centered at  $566\text{ cm}^{-1}$  demonstrate lack of magnetic response in the presence of an external magnet (**Figure 4.6B**). Therefore, the collected results suggest that CA component originating from PL-CAEA180 plays a role as coordinating ligand, which hardly immobilise C-dots on the

pavement of pre-formed Fe-NPs and stabilise the magnetic domains [27, 30, 31, 45, 46].



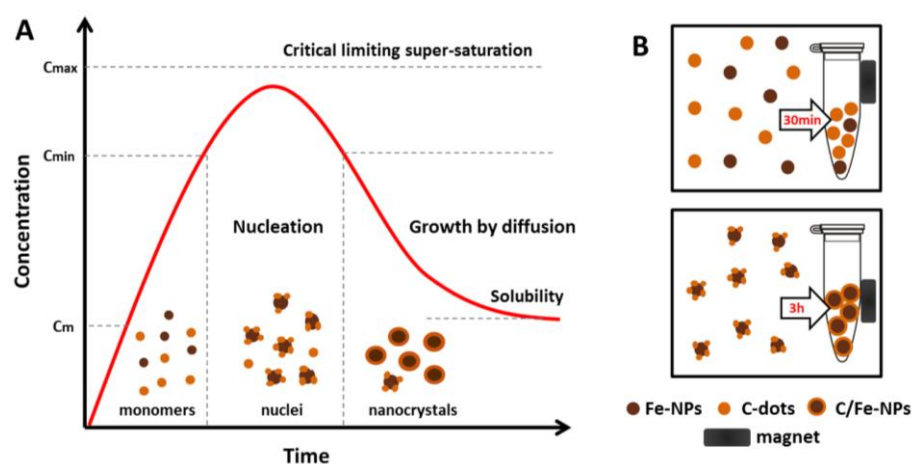
**Figure 4.6** FTIR spectra of C/Fe-NPs, Fe-NPs, CNP230, PEG400 and Fe(acac)<sub>3</sub> (A) together with the photos of Fe-NPs (B) and C/Fe-NPs (C) with external magnet.

The evaluation of optimum synthesis conditions was undertaken to select the synthesis protocol that leads to C/Fe-NPs with superior both fluorescent and magnetic properties. For this reason, the synthesis was carried out from 30 minutes up to 5 hours and the products were purified and characterised after specific time intervals. The XRD analysis performed for the powders of C/Fe-NPs revealed the presence of well-defined diffraction peaks for the C/Fe-NPs 2h and C/Fe-NPs 3h (**Figure 4.7G**), thereby concluded that favourable time for the formation of nanocrystals with the intrinsic structure of magnetite as well as superior magnetic properties (**Figure 4.7C-D**) is between 2 to 3 hours.



**Figure 4.7** Photos of C/Fe-NPs with external magnet synthesized by 30 minutes up to 5 hours (A-F) along with their XRD patterns (G).

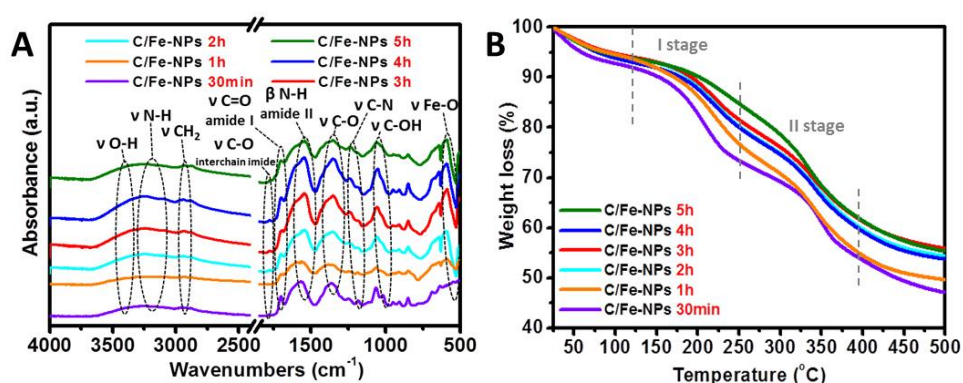
In regard to the formation mechanism of C/Fe-NPs, it is believed that during the thermal treatment of precursors mixture the nucleation and growth phases take place separately, as demonstrated in **Figure 4.8A**. Initially, the concentration of iron in the reaction mixture rise rapidly up to critical point of super-saturation and CNP230 are formed from PL-CAEA180 precursor [47, 48]. Afterwards, the concentration of free monomers in the precursors mixture decreases and burst nucleation process facilitate the formation of magnetite nanocrystals (Fe-NPs). In the same time, CNP230 starts to self-assembly on the pre-formed magnetite cores, thereby constitute an explanation for notable magnetic properties of C/Fe-NPs 2h [49]. In the last growth stage, CNP230 continue to self-assembly on the pre-formed C/Fe-NPs, thereby through stabilisation of magnetic nanodomains enhance magnetic properties of C/Fe-NPs 3h (**Figure 4.8B**) [50].



**Figure 4.8** Schematic mechanism presenting the formation of magnetic C-dots over a specific period of time (A) (Adapted and changed from Ref. 51) together with an illustration depicting the differences in their morphology and magnetic properties after 30 minutes or 3 hours of synthesis (B).

Further insight into proposed mechanism of C/Fe-NPs formation was gained by the FTIR analysis of corresponding nanomaterials. Thus, the results presented in **Figure 4.9A** imply that no reaction occur between precursors up to 30 minutes (C/Fe-NPs 30min) and fast synthesis is not sufficient for the formation of Fe-NPs and CNP230. After 60 minutes of synthesis, the intensities of C-O stretching vibration at  $1352\text{ cm}^{-1}$ , N-H bending vibration at  $1543\text{ cm}^{-1}$  as well as C=O band at  $1634\text{ cm}^{-1}$  decrease rapidly, thereby confirming the initial interactions between magnetite nanodomains and C-

dots (C/Fe-NPs 1h). Subsequently, it is believed that CNP230 self-assembly on the magnetite cores (C/Fe-NPs 2h-4h), which is demonstrated by intensification of the bands attributed to diverse surface functional groups of CNP230 [35]. Nevertheless, the reduction of absorption intensities for all the bands in C/Fe-NPs 5h suggest the decomposition of organic content from the C-dots structure. Besides that, the analysis of thermal degradation patterns of all samples provide an additional confirmation about interactions between Fe-NPs and CNP230 (**Figure 4.9B**). While first decomposition stage (up to around 250°C) corresponds to the chemical bonding between Fe-NPs and CNP230, the results further confirm that C/Fe-NPs 30min constitute only a physical mixture of both precursors [9]. Although the formation of covalent bonds between C-dots and Fe-NPs begin after 1 hour of reaction, the higher weight loss for C/Fe-NPs 1h (16.84%) in associated with residual content of carbogenic nanodomains, which form covalent bonds with Fe-NPs in C/Fe-NPs 2h (13.86%), C/Fe-NPs 3h (9.80%), C/Fe-NPs 4h (12.93%). On the other side, significant weight loss in C/Fe-NPs 5h (15.08%) indicates that CNP230 become detached from the surface of Fe-NPs and further decompose in the form of carbon dioxide [9]. The lack of obvious weight loss above 400°C suggest further decomposition of carbogenic residue as well as conversion of magnetite into hematite [33].



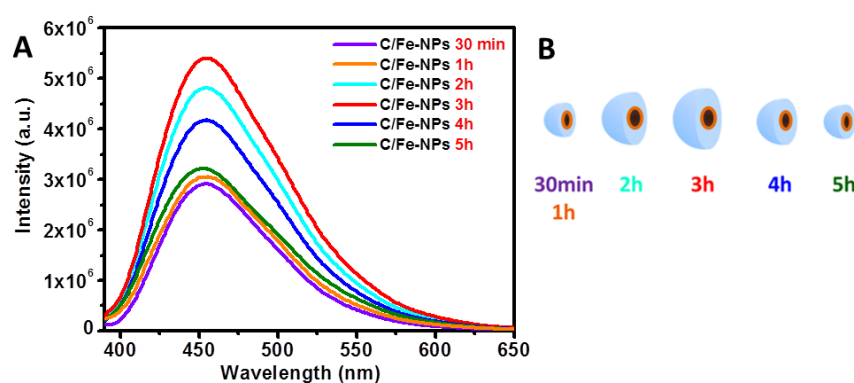
**Figure 4.9** FTIR spectra (A) and TGA curves (B) of C/Fe-NPs synthesized from 30 minutes up to 5 hours.

In addition to above discussed results, the elemental analysis (**Table 4.1**) further confirm that the highest Fe content is attributed to C/Fe-NPs 3h.

**Table 4.1** Elemental analysis results for magnetic C-dots synthesized at different time intervals

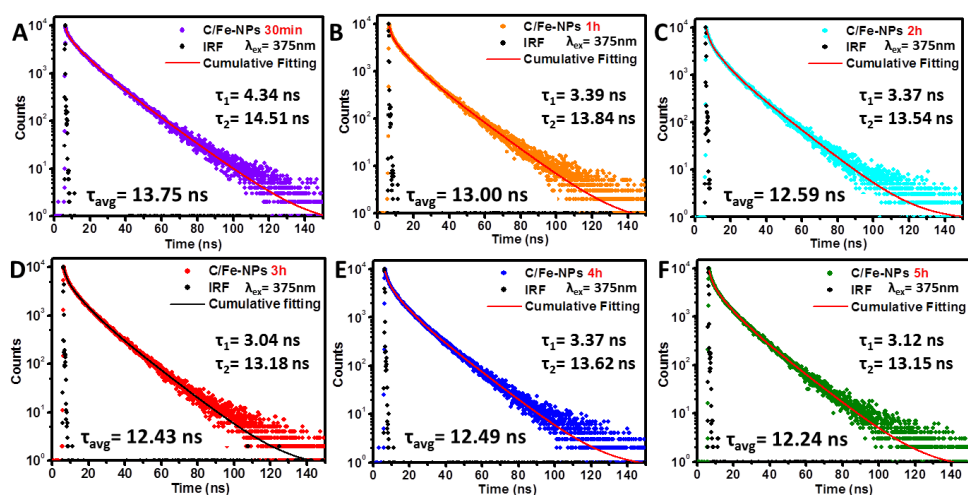
	C	H	N	O	Fe
C/Fe-NPs 1h	27.60	3.98	4.25	36.79	27.38
C/Fe-NPs 2h	28.65	3.89	4.19	35.54	27.73
C/Fe-NPs 3h	26.85	3.62	3.85	34.68	31.00
C/Fe-NPs 4h	28.57	3.89	3.86	35.70	27.98
C/Fe-NPs 5h	35.71	4.00	4.01	32.48	23.80

On the other hand, the PL analysis was conducted in order to evaluate the impact of synthesis time on the optical features of magnetic C-dots. As displayed in **Figure 4.10A**, the highest PL intensity is observed for the emission peak of C/Fe-NPs 3h, which demonstrates that this nanomaterial has predominant fluorescence properties, while for C/Fe-NPs 2h recorded PL intensity was negligibly diminished. In addition, the enhancement of fluorescence properties in C/Fe-NPs 2h, C/Fe-NPs 3h and C/Fe-NPs 4h constitute a further confirmation that at these time intervals C-dots are strongly immobilised on Fe-NPs (**Figure 4.10B**), while for CNP230 the increment of the synthesis time influence on the formation of larger content of molecular fluorophores that enhance the overall optical properties (Appendix, **Figure A10**). Besides the fact that C/Fe-NPs 5h have the highest carbon content among all samples (**Table 4.1**), the reduction of their PL intensity may be related to the agglomeration of magnetic nanodomains during the purification step, thereby result in lower iron content (**Table 4.1**) [23].



**Figure 4.10** PL spectra recorded at  $\lambda_{\text{ex}} = 375$  nm for exemplary C/Fe-NPs synthesized by various time (A) along with the scheme presenting the thickness of the fluorophore outer layer at various synthesis stages (B).

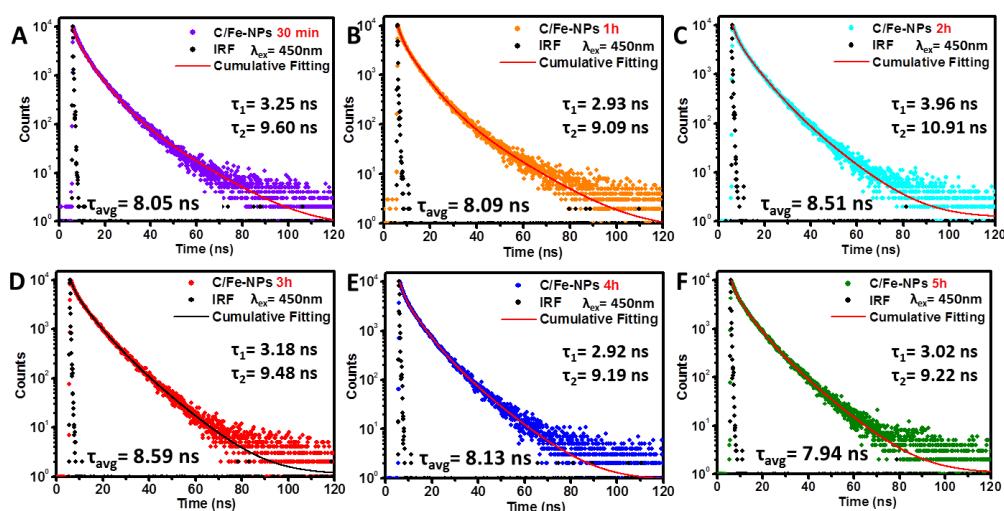
Furthermore, the PL lifetime decays were recorded at  $\lambda_{\text{ex}} = 375$  nm (**Figure 4.11**) and  $\lambda_{\text{ex}} = 450$  nm (**Figure 4.12**), in order to collect complementary information about fluorophores interactions with magnetite cores. The detailed analysis of the average PL lifetimes ( $\tau_{\text{avg}}$ ) confirmed that CNP230 with abundant molecular fluorophores are formed after 30 minutes of reaction ( $\tau_{\text{avg}} = 13.75$  ns), whereas the controlled decrement of PL lifetimes for C/Fe-NPs 1h ( $\tau_{\text{avg}} = 13.00$  ns), C/Fe-NPs 2h ( $\tau_{\text{avg}} = 12.59$  ns) and C/Fe-NPs 3h ( $\tau_{\text{avg}} = 12.43$  ns) indicates the occurrence of fluorescence quenching. This phenomenon clearly confirms that the formation of covalent bonds between Fe-NPs and weakly bounded to C-dots pavement molecular fluorophores is accomplished after 3 hours of synthesis.



**Figure 4.11** Fluorescence lifetime decays of C/Fe-NPs 30 min and C/Fe-NPs 1-5h aqueous dispersions measured at  $\lambda_{\text{ex}} = 375$  nm.

On the contrary, the average PL lifetimes of C/Fe-NP at  $\lambda_{\text{ex}} = 450$  nm (**Figure 4.12**) gradually increase and reach the maximum for C/Fe-NPs 3h ( $\tau_{\text{avg}} = 8.59$  ns), thus indicating the highest content of photoluminescence centres in this nanomaterial. Subsequent decrement of  $\tau_{\text{avg}}$  for C/Fe-NPs 4h ( $\tau_{\text{avg}} = 8.13$  ns) and C/Fe-NPs 5h ( $\tau_{\text{avg}} = 7.94$  ns) could suggest the consumption of molecular fluorophores for the build-up of carbogenic cores with reduced PL properties.





**Figure 4.12** Fluorescence lifetime decays of C/Fe-NPs 30 min and C/Fe-NPs 1-5h aqueous solutions recorded at  $\lambda_{ex}$  = 450 nm.

In summary, detailed chemical analysis of C/Fe-NPs synthesized at different time intervals confirmed that the 3 hours constitute an optimal time for the synthesis of a large family of magnetic C-dots, as C/Fe-NPs 3h demonstrate the most tempting optical features for desired biomedical application.

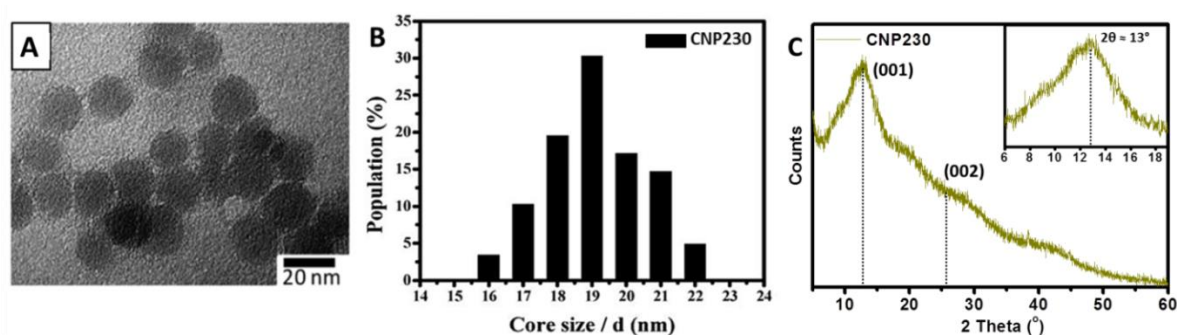
### 4.3.2 Systematic study of iron incorporation into carbogenic nanoparticles

After optimising the synthesis conditions for development of magneto-fluorescent C/Fe-NPs, the impact of Fe doping on the amorphous CNP230 matrix was investigated in a controlled manner, which resulted in generation of a large family of magnetic C-dots. Prior performing biological analysis, the structural, optical and magnetic features were carefully evaluated for all C/Fe-NPs, in order to select samples with distinguished properties for further application as multifunctional probes for labelling of cancer cells.

At first, CNP230 were synthesized as a reference sample with well-established morphological, structural and optical properties. It has been reported that as-prepared C-dots have a spherical shape (**Figure 4.13A**) and an average size of 19 nm (**Figure 4.13B**). Furthermore, the structural insight gained by the X-Ray Diffraction analysis confirmed the graphitic nature of CNP230, as displayed in **Figure 4.13C**. Thus, the presence of well-pronounced diffraction peak at  $2\theta \approx 13^\circ$  corresponds to the graphitic

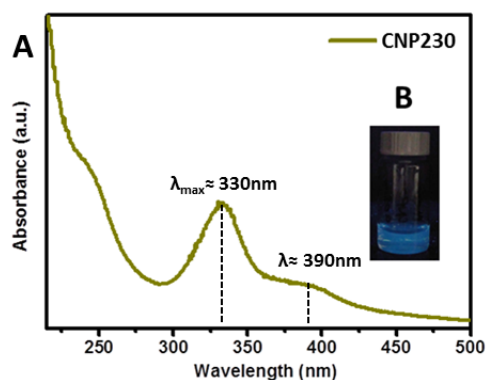


carbon (001) plane, while a broad reflection at  $2\theta \approx 25^\circ$  confirms an ultra small size of carbon domains [52].



**Figure 4.13** TEM image (A), size histogram plotted on the basis of 150 fields (B) and the XRD pattern (C) of CNP230 (A,B - Adapted from Ref. 42).

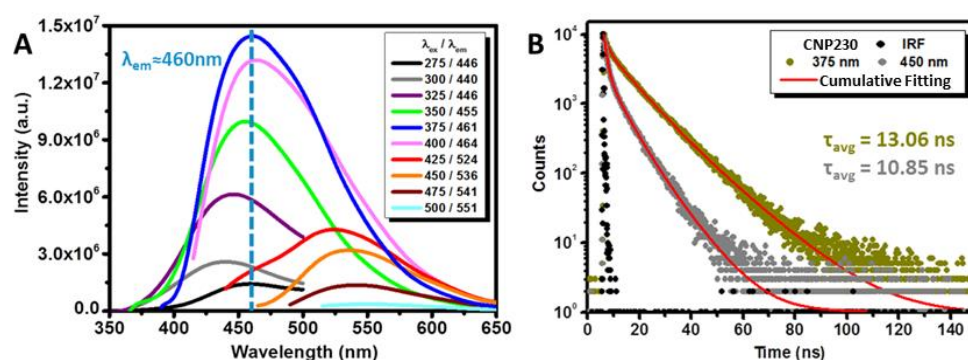
The exceptional optical properties of CNP230 are arising from abundant content of molecular fluorophores as well as carbogenic cores [42]. In this regard, the absorption spectra of CNP230 (**Figure 4.14A**) display a characteristic band around 330 nm, which is attributed to the presence of citrazinic acid (CTA) fluorophore (Appendix, **Figure A11**), impacting on their strong blue luminescence under the UV light (**Figure 4.14B**) [34, 53, 54]. In addition, the main absorption peak displays a characteristic tail extending up to 500 nm with a clear hump around 390 nm, thus confirming the formation of citrazinic acid aggregates [54].



**Figure 4.14** The UV-Vis spectra of aqueous dispersion of CNP230 (A) together with its photo under the UV lamp (B). The sample concentration was equal to 0.01 mg/mL.

The photoluminescence spectra (**Figure 4.15A**) unveiled the excitation-wavelength independent luminescence behaviour of CNP230 in the range of  $400 < \lambda_{ex} < 275\text{ nm}$  along with the excitation-wavelength dependent fluorescence at  $500 < \lambda_{ex} < 425\text{ nm}$ ,

attributed to the presence of aromatic organic fluorophores as well as carbogenic cores, respectively [42]. The maximum emission peak centered around 460 nm reveal the dominant contribution of blue-emissive citrazinic acid fluorophore (Appendix, **Figure A11**). Moreover, the bimodal exponential fitting of PL lifetime decays revealed the average PL lifetimes ( $\tau_{avg}$ ) of CNP230 being equal to 13.06 ns ( $\lambda_{ex}$ =375nm) and 10.85 ns ( $\lambda_{ex}$ =450nm) (**Figure 4.15B**).



**Figure 4.15** The PL spectra (A) and fluorescence lifetime decays recorded at excitation wavelength 375 nm and 450 nm (B) of CNP230. The sample concentration was equal to 0.01 mg/mL.

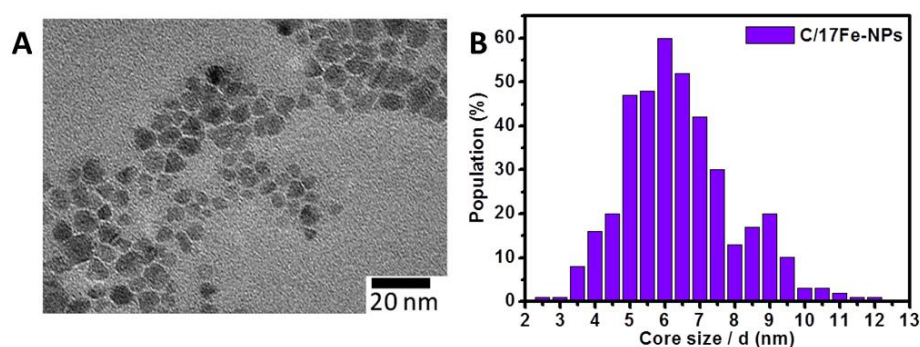
In regard to magnetic C-dots, the increasing Fe doping led to fabrication of eight types of C/Fe-NPs with iron content ranging from 17% (C/17Fe-NPs) up to 31% (C/31Fe-NPs), as determined from the elemental analysis (**Table 4.2**). Therefore, the calculated values of Fe content were used to distinguish the samples in this chapter.

**Table 4.2** Elemental analysis results for magnetic C-dots, Fe-NPs and CNP230

	C	H	N	O	Fe
Fe-NPs	27.77	3.44	----	35.83	32.96
C/26Fe-NPs	31.31	4.07	2.77	35.84	26.69
C/28Fe-NPs	28.03	3.87	3.64	36.15	28.31
C/31Fe-NPs	26.85	3.62	3.85	34.68	31.00
C/27Fe-NPs	28.90	3.97	4.33	35.87	26.93
C/24Fe-NPs	31.03	4.16	4.86	36.16	23.79
C/23Fe-NPs	31.45	4.29	5.38	36.11	22.77
C/19Fe-NPs	35.34	4.40	5.81	34.98	19.47
C/17Fe-NPs	36.30	4.66	6.50	35.16	17.38
CNP230	43.30	5.39	9.03	42.28	----

The TEM image of exemplary C/17Fe-NPs (**Figure 4.16A**) shows their nanoscopic nature as well as roughly spherical shape, while the data presented in a size histogram

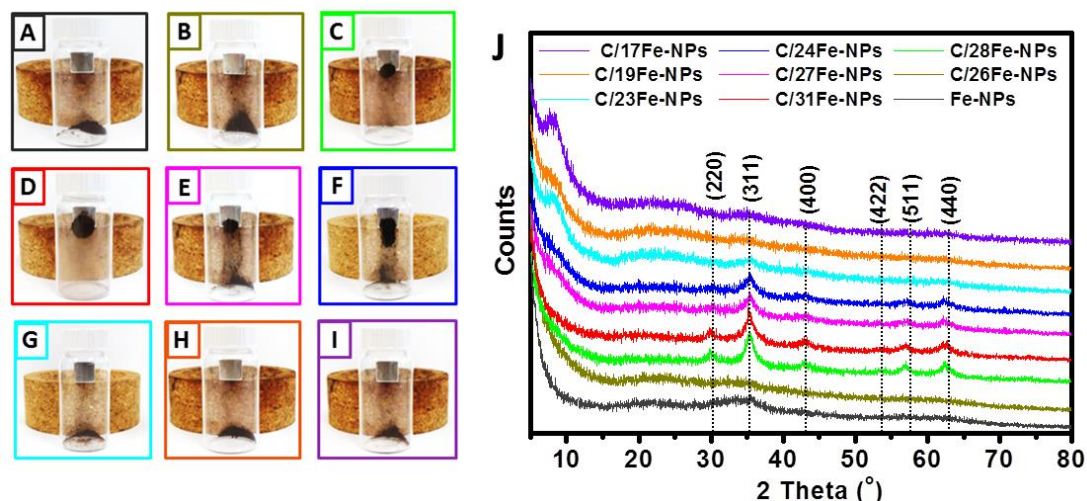
confirms an average particle size equal to 6.45 nm (**Figure 4.16B**). The well-defined and homogeneous shape of magnetic C-dots could be attributed to the addition of PEG<sub>400</sub> during the synthesis step, which plays a role as dispersing agent and stabilizer [24]. According to the literature, it has been reported that the spherical shape of nanoparticles is generated when the nucleation rate per unit area is isotropic at the interface between nanoparticles [24] and overall the growth of nanoparticles into spherical shape minimize their surface energy [22].



**Figure 4.16** TEM image (A) and size histogram plotted on the basis of 395 fields (B) of C/17Fe-NPs.

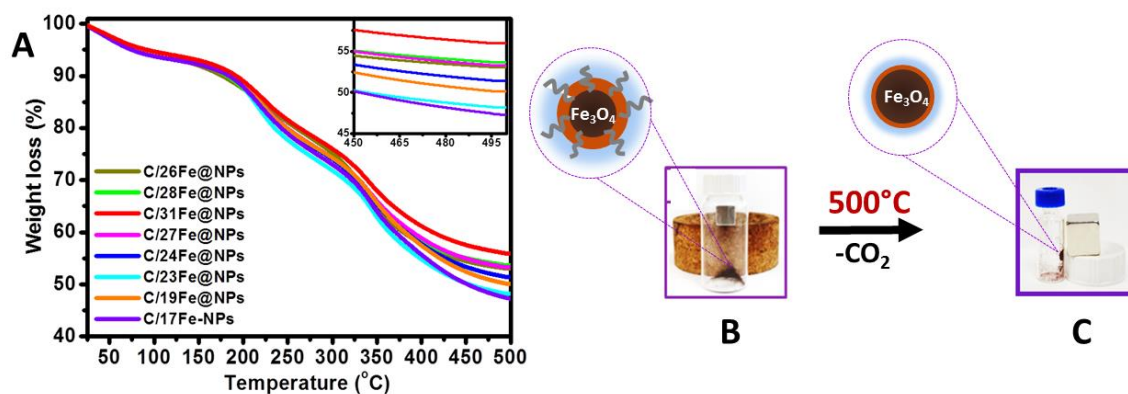
The crystallinity and phase purity of magnetic C-dots and Fe-NPs were examined by X-ray powder diffraction analysis [23, 34]. As presented in **Figure 4.17J**, the characteristic diffraction peaks arising from an iron oxide component are well-pronounced only for C/28Fe-NPs, C/31Fe-NPs, C/27Fe-NPs and C/24Fe-NPs, which also demonstrated a positive response towards an external magnet (**Figure 4.17C-F**). In detail, the diffraction peaks at  $2\theta = 30.02^\circ$ ,  $35.14^\circ$ ,  $42.96^\circ$ ,  $53.50^\circ$ ,  $56.93^\circ$  and  $62.63^\circ$  are attributed to the (220), (311), (400), (422), (511) and (440) crystal planes of magnetite with cubic structure [20, 23, 27, 30, 31, 36, 40, 41]. Importantly, the presence of magnetite is highly desired for biomedical applications and the match of reflection planes with the standard Fe<sub>3</sub>O<sub>4</sub> XRD pattern constitute an agreement with previous reports [18, 26, 29, 31, 36, 37, 55-57]. On the other side, the XRD patterns of C/23Fe-NPs, C/19Fe-NPs and C/17Fe-NPs display minor crystalline phase with broad amorphous peaks around  $2\theta = 20-30^\circ$ , which are attributed to significant carbon content in their structure [16, 26, 29, 31, 36, 37, 41, 55]. In contrast, the lack of characteristic amorphous peaks in the XRD patterns of strongly magnetic samples

suggest that the crystalline phase of magnetite is not destroyed by a relatively poor content of CNP230 [26, 29, 31]. Overall, the magnetic properties of C/Fe-NPs strongly depend on the applied molar ration between both precursors and significant broadening of diffraction peaks attributed to magnetite content is affected by nanoscopic nature of C/Fe-NPs [23, 27, 36, 58].



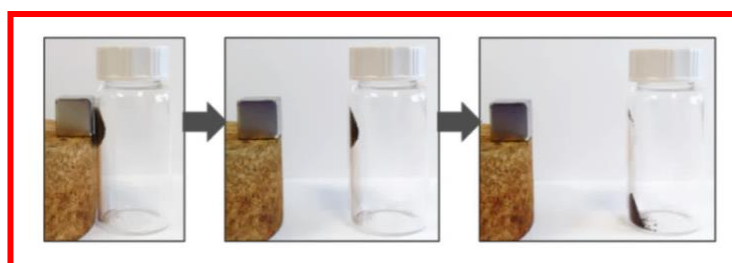
**Figure 4.17** Photos of Fe-NPs (A) and C/Fe-NPs (B-I) with an external magnet together with the X-Ray diffraction patterns of all sample (J).

Thermogravimetric analysis further confirmed abundant organic content in magnetic C-dots, as presented in **Figure 4.18A**. The weight loss ranging from 12.41% (C/31Fe-NPs) up to 15.53% (C/17Fe-NPs) in the first decomposition step ( $T = 120-255^{\circ}\text{C}$ ) refers to the breakage of chemical bonds between C-dots and Fe-NPs, thus suggest an increment of C-dots content in outer protective shell [9]. On the other side, the analysis of C/17Fe-NPs residue after TGA analysis (**Figure 4.18C**) further proved the concept about core-shell structure. Owing to restored magnetic nature of C/17Fe-NPs after thermal treatment, it is believed that at high temperature the thickness of carbogenic shell significantly shrink (**Figure 4.18B-C**) through decomposition of carbonyl groups in the form of carbon dioxide [9].



**Figure 4.18** TGA curves of magnetic C-dots (A) along with the scheme illustrating the thermal induced shrinkage of outer carbon shell in C/17Fe-NPs (B).

Among all, the strongest magnetic features are attributed to C/31Fe-NPs with the highest iron content, as demonstrated in **Figure 4.19**. Importantly, preserved magnetic features in a weak magnetic field hold a promise for utilising this material in magnetically-guided biomedical applications, as demonstrated by photos with distant external magnet. On top of that, another experiment demonstrated that C/31Fe-NPs can be easily separated by an external magnet from the liquid phase, thereby suggesting both their promising behaviour in biological fluids as well as an ability to be recycled and reused again (Appendix, **Figure A12**) [36].

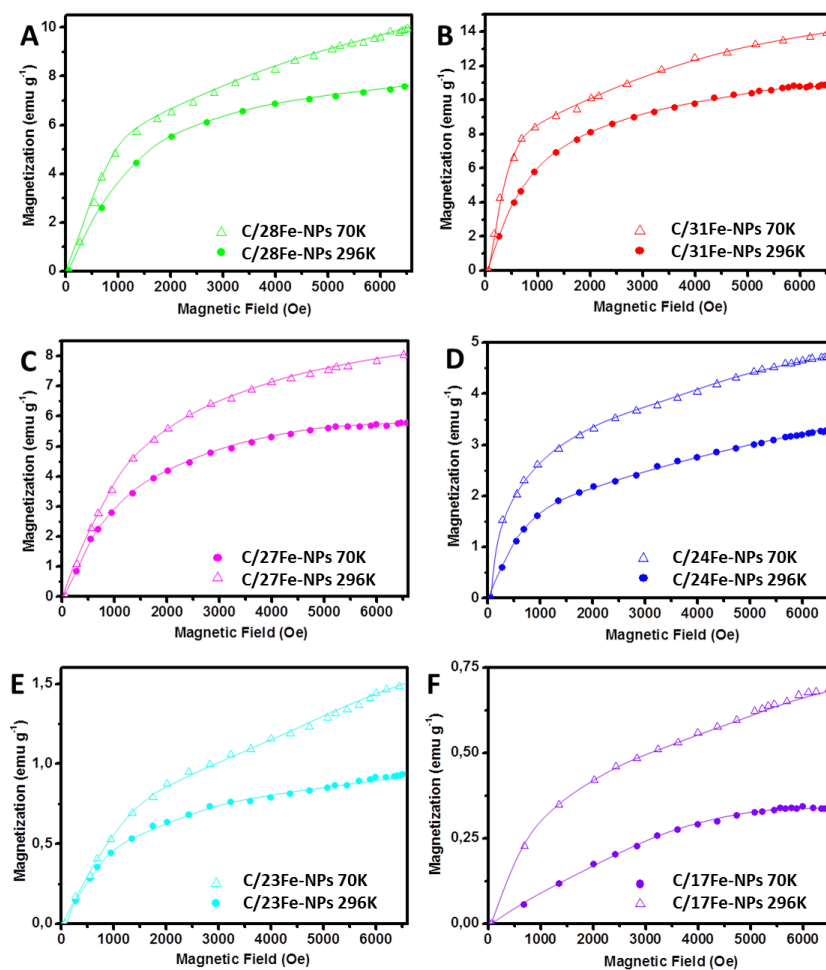


**Figure 4.19** Photos of C/31Fe-NPs with an external magnet in a close or far distance.

Further evaluation of detailed magnetic properties for selected C/Fe-NPs was based on the analysis of magnetization results (**Figure 4.20**) as well as the Mössbauer spectra (**Figure 4.21**). The magnetization results recorded at room temperature (296K) by the Faraday type balance (**Figure 4.20**) revealed that the highest saturation magnetization ( $M_s$ ) values are attributed to the samples with predominant iron content, thus C/31Fe-NPs ( $M_s = 11.07$  emu/g), C/28Fe-NPs ( $M_s = 7.58$  emu/g) and C/27Fe-NPs ( $M_s = 6.09$  emu/g). Overall, it has been reported that the saturation magnetization above 6 emu/g

is sufficient for utilisation of C/Fe-NPs in biomedical applications (i.e. magnetic separation, hyperthermia treatment, targeted drug delivery) [24, 59]. Nevertheless, the presence of carbogenic shell significantly reduces the overall magnetic properties of C/Fe-NPs [24, 28, 41, 55-57], due to the fact that C/24Fe-NPs ( $M_s = 3.28$  emu/g), C/23Fe-NPs ( $M_s = 0.93$  emu/g) and C/17Fe-NPs ( $M_s = 0.33$  emu/g) have a smaller magnetic moment per unit mass than pristine Fe-NPs ( $M_s = 20-40$  emu/g) [33, 37]. Besides reduced magnetization, the presence of carbon coating on the magnetite nanocrystals play an important role in prevention of aggregation [33]. Furthermore, the superparamagnetic behaviour of C/31Fe-NPs, C/28Fe-NPs and C/27Fe-NPs was confirmed by complementary analysis with the use of Vibrating Sample Magnetometer (Appendix, **Figure A13**). The measurements collected at room temperature confirmed that superparamagnetic nature of C/Fe-NPs originates from the absence of a hysteresis loops as well as zero coercivity and zero remanence [21, 23, 26]. In regard to this, zero coercivity impose that magnetic nanodomains do not retain a residual magnetism in the absence of external magnetic field, thus exclude the possibility of their aggregation and precipitation in liquid media [21, 24]. In addition, the absence of hysteresis loops suggest an ease in their redispersion in biological fluids after removal an external magnetic field, thereby being crucial for selected biomedical applications as magnetically-guided nanotracers for cell labelling [21]. On the other side, the appearance of a symmetric hysteresis loops in magnetization curves at lower temperatures indicates enhanced magnetization of aggregates, that transit from superparamagnetic to ferromagnetic behaviour [21, 22].

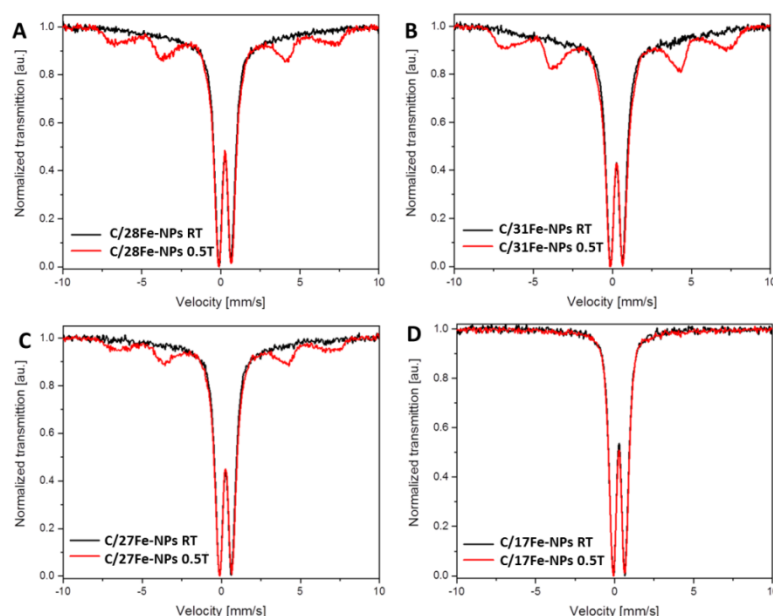




**Figure 4.20** Magnetization results recorded at room temperature (296K) and at temperature around - 200°C (70K) for selected C/Fe-NPs.

The Mössbauer spectra were collected for C/31Fe-NPs, C/28Fe-NPs, C/27Fe-NPs and C/17Fe-NPs (**Figure 4.21**), in order to differentiate the iron oxide phase purity in their structure [25]. It has been reported that both maghemite ( $\gamma\text{-Fe}_2\text{O}_3$ ) and magnetite ( $\text{Fe}_3\text{O}_4$ ) can be present as magnetic components in Fe-NPs, due to the similar spinel crystal structure of both iron oxides [26, 28]. As presented in **Figure 4.21**, the Mössbauer spectra reveals a broad doublets that are characteristic for superparamagnetic state of Fe-NPs [9]. The comparison of the tails at outer sides of these characteristic doublets indicated the slowest relaxation behaviour for C/31Fe-NPs (**Figure 4.21B**) and the fastest relaxation behaviour for C/17Fe-NPs (**Figure 4.21D**). Besides that, the main isomer shifts equal to 0.35 mm/s (C/31Fe-NPs) and 0.40 mm/s (C/17Fe-NPs) correspond to the highest and the lowers mean Fe (III) oxidation degree,

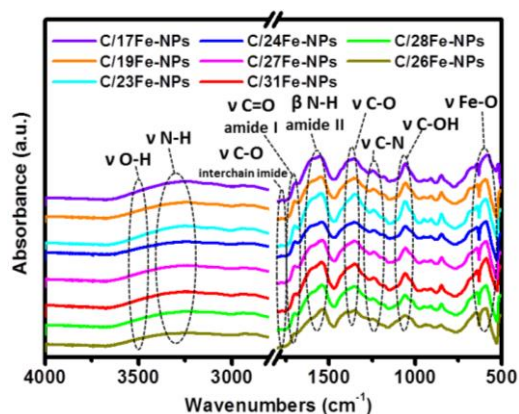
respectively. Further analysis at 0.5T magnetic field demonstrates the appearance of additional lines correlated to slow relaxing fractions of C/Fe-NPs. The slowest relaxation phenomenon is attributed to C/31Fe-NPs (14%), while C/17Fe-NPs possess only fast relaxing particles originating from the maghemite phase, as demonstrated by negligible changes in their Mössbauer spectrum (**Figure 4.20D**).



**Figure 4.21** Normalized Mössbauer spectra of C/28Fe-NPs (A), C/31Fe-NPs (B), C/27Fe-NPs (C), C/17Fe-NPs (D) at room temperature and with an external 0.5T magnetic field.

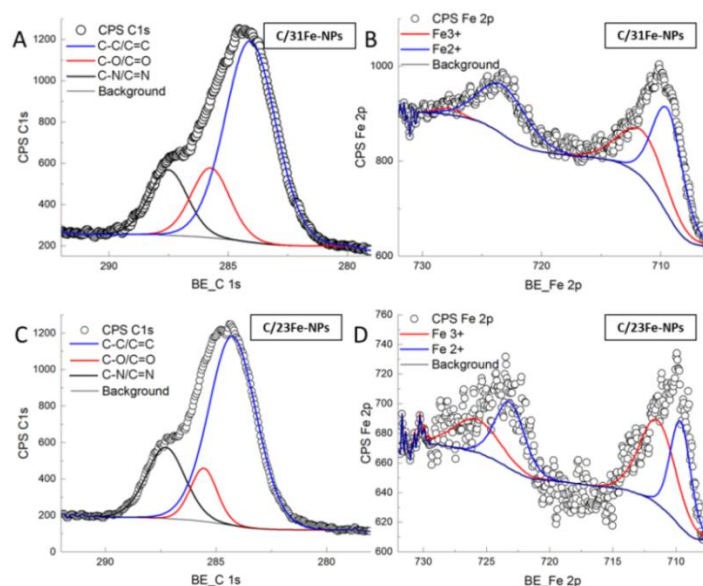
The FTIR spectra collected for all magnetic C-dots revealed the presence of abundant surface functional groups, as displayed in **Figure 4.22**. The main vibrational fingerprints of magnetic C-dots are centred around  $588\text{ cm}^{-1}$  (Fe-O stretching vibration),  $1054\text{ cm}^{-1}$  (C-OH stretching vibration),  $1232\text{--}1352\text{ cm}^{-1}$  (C-O and C-N stretching vibrations),  $1750\text{ cm}^{-1}$  (C=O stretching vibration),  $2900\text{ cm}^{-1}$  (C-H symmetric and asymmetric stretching vibrations) and  $3240\text{ cm}^{-1}$  (N-H and O-H stretching vibrations) [17, 30, 31, 35, 36, 40]. The band centered in the range of  $1540\text{ to }1697\text{ cm}^{-1}$  reflect to the C=O stretching vibration as well as N-H in-plane bending vibration of amide I and amide II, respectively [15, 23, 26, 30, 31]. Accordingly to previous reports, the presence of N-H in-plane bending vibrations further confirm the presence of polycyclic aromatic hydrocarbons in the structure of C/Fe-NPs [30].





**Figure 4.22** FTIR spectra of magnetic C-dots with diversified iron content.

Complementary, the full-scan XPS spectra for particular C/Fe-NPs confirmed the existence of carbon, nitrogen, oxygen and iron elements in their structure (Appendix, **Figure A14**), whereas the characteristic peaks at 290 eV, 400 eV, 530 eV and 710 eV corresponded to the binding energies of C1s, N1s, O1s and Fe2p, respectively [15, 30]. In detail, the high-resolution C1s spectra of C/31Fe-NPs (**Figure 4.23A**) and C/23Fe-NPs (**Figure 4.23C**) was deconvoluted into four peaks located at 284.1eV, 285.7eV and 287.5eV, which correspond to C-C or C=C, C-N or C=N as well as C-O or C=O bonds in CNP230-based shell, respectively [17, 31, 36]. On the other side, the high-resolution Fe2p spectra demonstrated the occurrence of Fe2p<sub>3/2</sub> and Fe2p<sub>1/2</sub> peaks centered around 722eV and 711eV, which confirm the presence of Fe<sup>3+</sup> and Fe<sup>2+</sup> oxidation states and dominant magnetite phase in C/31Fe-NPs (**Figure 4.23B**) and C/23Fe-NPs (**Figure 4.23D**) [15, 16, 31, 36]. Furthermore, the lack of satellite peak around 718eV assigned to the +III oxidation state of Fe (**Figure 4.23B,D**) implies that the cores composed of Fe-NPs are fully coated with CNP230 and no oxidation of bare Fe-NPs occurred [17, 31].

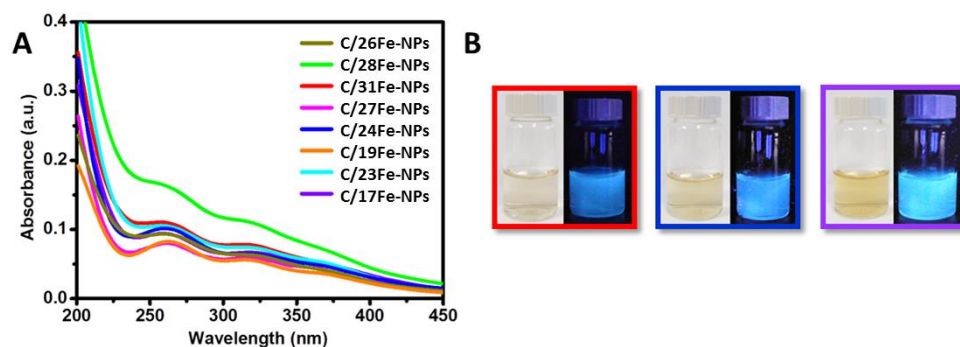


**Figure 4.23** High-resolution C1s and Fe2p XPS spectra of C/31Fe-NPs (A-B) and C/23Fe-NPs (C-D).

Overall, the results from the FTIR and XPS analysis confirmed the existence of abundant oxygen-rich groups on the surface of C/Fe-NPs, which endow them with excellent dispersibility in aqueous media, hence suggest further dispersibility in biological fluids [15, 17, 28, 29, 33, 34]. Besides that, the surface functional groups have a strong affinity towards other biomolecules or cellular components (e.g. proteins), thereby imply that magnetic C-dots have potential to be applied for both *in vitro* as well as *in vivo* applications [33].

After establishing the samples with prominent magnetic properties, the detailed fluorescence analysis was conducted to assess their optical properties in a liquid-state. The UV-Vis spectra of magnetic C-dots presented in **Figure 4.24A** reveals the absorption peak at 270 nm and a hump around 320 nm, which are attributed to  $\pi$ - $\pi^*$  electron transitions of aromatic  $sp^2$  bonds as well as  $n$ - $\pi^*$  electron transitions of the amine (C-N) and carbonyl (C=O) functional groups [15, 30]. In addition, the absorption peak ca. 270 nm confirms the existence of multiple polyaromatic chromophores in magnetic C-dots [20, 28]. Despite the coloured nature and a strong blue luminescence under the UV light (**Figure 4.24B**), the absorptivities of magnetic C-dots aqueous solutions are usually very low due to the contribution of iron oxide [27, 30, 31, 60]. In general, majority of previous reports correspond to the bright blue emission of

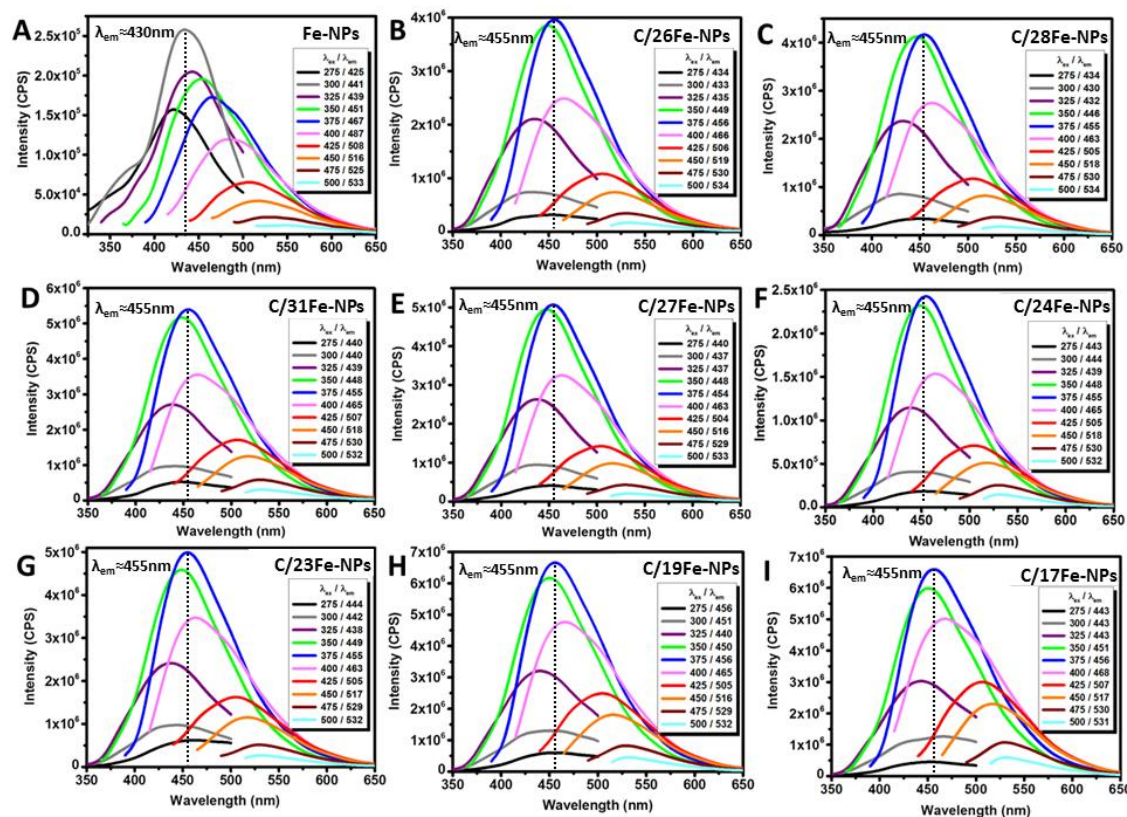
aqueous dispersions of C/Fe-NPs upon their irradiation with the ultraviolet light [15, 17].



**Figure 4.24** The UV-Vis spectra of aqueous dispersions of C/Fe-NPs (A) together with the photos of C/31Fe-NPs, C/24Fe-NPs, C/17Fe-NPs under the daily (left) and ultraviolet (right) light (B).

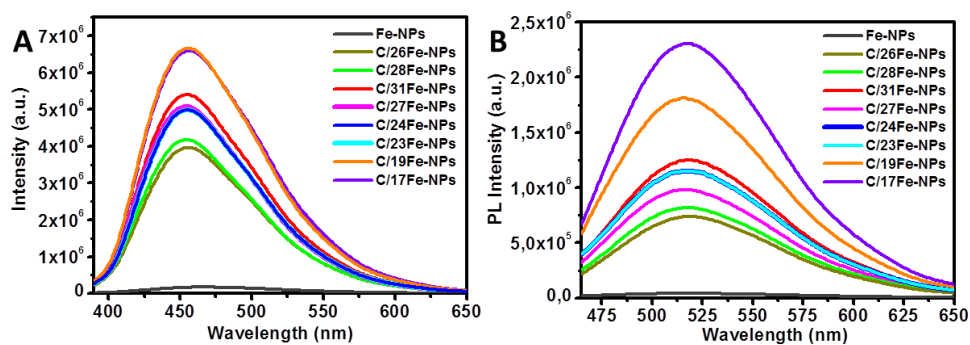
The fluorescence spectra of Fe-NPs (**Figure 4.25A**) and C/Fe-NPs (**Figure 4.25B-I**) were recorded and compared with the PL spectra of pure CNP230 (**Figure 4.15A**). In general, the fluorescence mechanism of magnetic C-dots is associated with dual photoluminescence emission, which can be distinguished as the excitation wavelength-independent ( $275 < \lambda_{\text{ex}} < 325$  nm) or excitation wavelength-dependent ( $325 < \lambda_{\text{ex}} < 500$  nm). In contrast, the PL spectra of pure Fe-NPs (**Figure 4.25A**) demonstrates only the  $\lambda_{\text{ex}}$ -dependent luminescence behaviour at  $275 < \lambda_{\text{ex}} < 500$  nm, with the highest emission peak centered at  $\lambda_{\text{em}} \approx 430$  nm. Overall, the excitation-dependent emission plays an important role in multicolour imaging applications and may be related to various sizes of carbogenic nanodomains, different surface states distributions or multi-photon active processes [15-17, 30, 40]. In addition, the inherent photoluminescence may additionally arise from electronic transitions of aromatic hydrocarbons (C=C) that are present in the carbogenic shell of C/Fe-NPs [16]. The fluorophores efficiency in converting the excitation light into fluorescence was further evaluated by calculating the quantum yields (QY) of C/Fe-NPs, with the use of anthracene ( $\lambda_{\text{ex}} = 365$  nm) as a reference dye (Appendix, **Figure A15**). Although previous reports stated that CNP230 possess the  $\text{QY} \approx 15\%$  at  $\lambda_{\text{ex}} = 365$  nm [42], a significantly diminished values of  $\text{QY} \approx 5-9\%$  for C/Fe-NPs are related to dynamic and static fluorescence quenching of C-dots emissive excited states by an iron oxide component [27, 31, 61]. Nonetheless, similar

values of absolute QY ranging from 4.6% up to 8% were reported before for C/Fe-NPs [16, 20, 31].



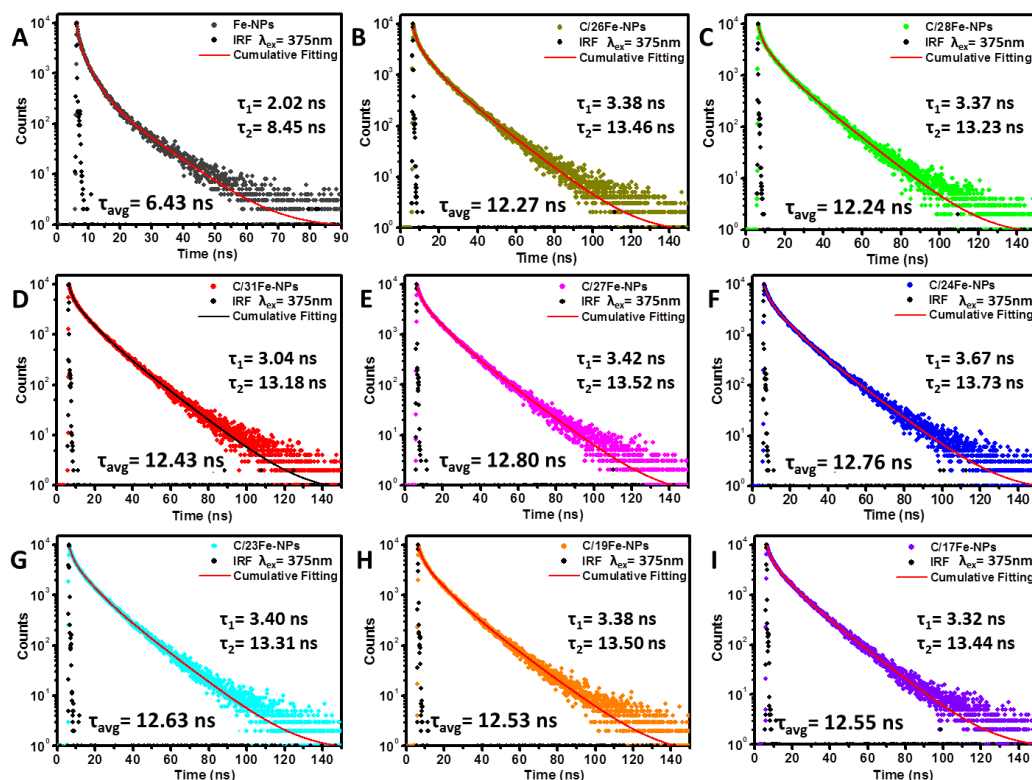
**Figure 4.25** PL spectra of aqueous solutions of iron oxide-based nanoparticles (A) and magnetic C-dots with varied iron content (B-I). The samples concentration was 0.01 mg/mL.

Furthermore, the analysis of individual fluorescence emission peaks recorded at  $\lambda_{\text{ex}} = 375$  nm (**Figure 4.26A**) and  $\lambda_{\text{ex}} = 450$  nm (**Figure 4.26B**) was carried out in order to evaluate the interactions between C-dots and Fe-NPs. Besides the fluorescence quenching phenomenon related to systematic decrement of PL intensities along with substantial Fe doping, these results further suggest the occurrence of an ultrafast electron transfer processes [36].



**Figure 4.26** PL spectra of magnetic C-dots aqueous dispersions recorded for the maximum emission peak at  $\lambda_{ex} = 375$  nm (A) and higher wavelength peak at  $\lambda_{ex} = 450$  nm (B).

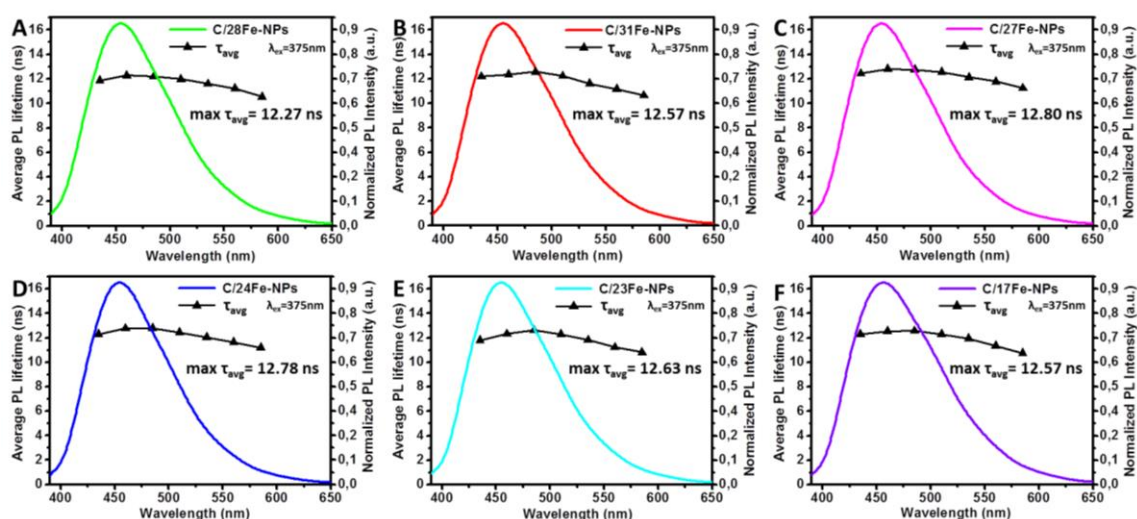
To further support the results from the liquid-state fluorescence measurements, the time-resolved PL lifetime decays were recorded at  $\lambda_{ex} = 375$  nm (**Figure 4.27**) or  $\lambda_{ex} = 450$  nm (**Figure 4.29**) for aqueous dispersion of magnetic C-dots and Fe-NPs. Overall, the average PL lifetimes ( $\tau_{avg}$ ) of C/Fe-NPs ranging from 12.24 ns up to 12.80 ns (**Figure 4.27B-I**) are negligibly shorter than the  $\tau_{avg} = 13.06$  ns for pure CNP230 (**Figure 4.15B**), thus confirming the presence of abundant emissive trap sites in the carbogenic shell or suggesting variations in particles sizes [31]. In contrast, bare Fe-NPs (**Figure 4.27A**) have significantly lower value of the  $\tau_{avg} = 6.43$  ns, owing to the lack of carbogenic shell with plentiful amide bonds that correspond to  $n-\pi^*$  transitions [62]. Overall, the presented results are in agreement with previous reports describing the multiexponential nature of C/Fe-NPs [30].



**Figure 4.27** Time-resolved PL decay curves for aqueous dispersions of magnetic C-dots at  $\lambda_{ex}$  = 375 nm.

In addition, complementary experiment was performed to assess the variations in the average PL lifetime of C/28Fe-NPs, C/31Fe-NPs, C/27Fe-NPs, C/24Fe-NPs, C/23Fe-NPs and C/17Fe-NPs, over a broad emission detection ranges (**Figure 4.28**). To this point, the increment of the  $\tau_{avg}$  within the emission range of CTA ( $\lambda_{ex}$  = 375 nm) was observed for all C/Fe-NPs, thereby confirming the changes in the local environment of CTA molecules ( $\tau_{avg}$  = 6.4 ns) that are bonded with carbogenic cores. On the other side, the decrement of the  $\tau_{avg}$  trend at longer  $\lambda_{em}$  imply the arising contribution of carbogenic cores towards the fluorescence phenomena [53].

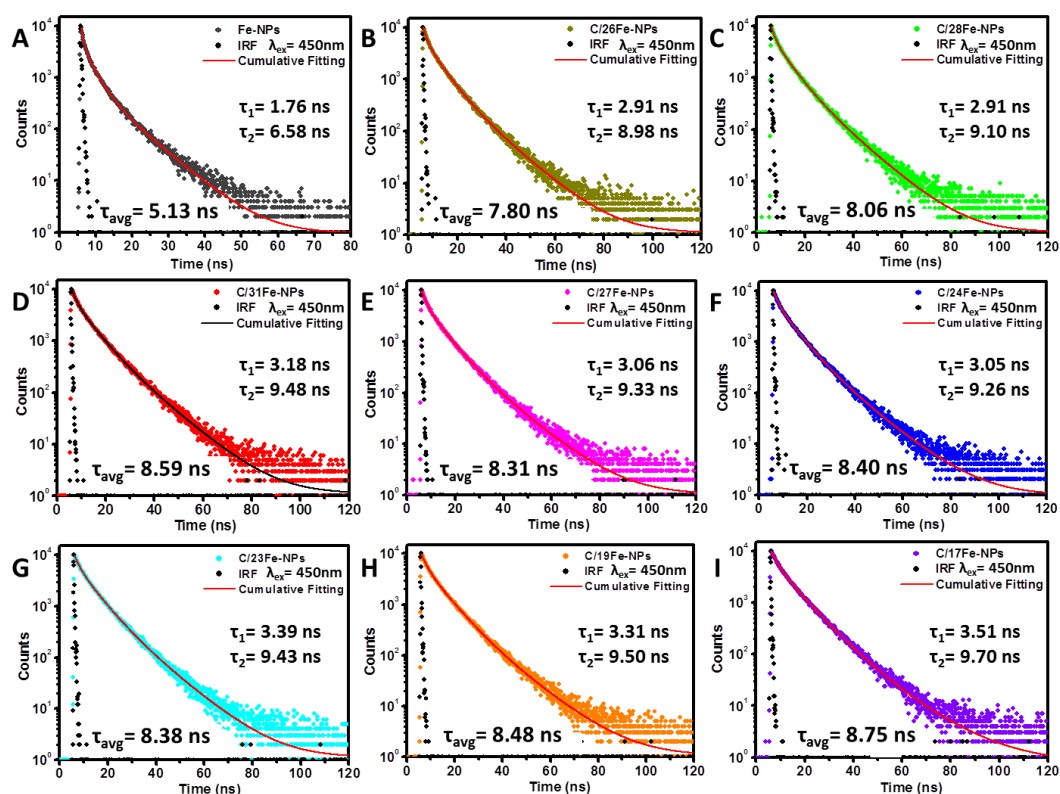




**Figure 4.28** The range of average PL lifetimes of selected magnetic C-dots as a detection function at  $435 \leq \lambda_{em} \leq 585$  nm. The relevant PL emission peaks were measured at  $\lambda_{ex} = 375$  nm.

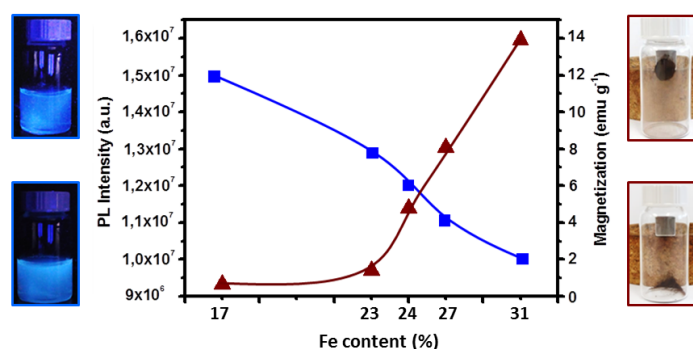
The time-resolved PL lifetime decays recorded at  $\lambda_{ex} = 450$  nm further confirm the general decrease in the radiative decay along with higher Fe-doping [16], as demonstrated in **Figure 4.29**. Nevertheless, a random increment and decrement of  $\tau_{avg}$  for particular C/Fe-NPs suggest either not evenly distributed photoluminescence centres on their surface or non-specific PL quenching mechanism caused by magnetite component [31].

Overall, the calculated average fluorescence lifetimes of C/Fe-NPs are significantly longer than the values recorded for either the auto fluorescence of the cells ( $\tau_{avg} = 1.5$ -4 ns) or majority of organic dyes ( $\tau_{avg} = 1$ -5 ns), therefore pave the way for promising utilization of magnetic C-dots for long-term cellular labelling of cancer cells [15, 16, 30].



**Figure 4.29** Time-resolved PL decay profiles for aqueous solutions of magnetic C-dots at  $\lambda_{ex}$  = 450 nm.

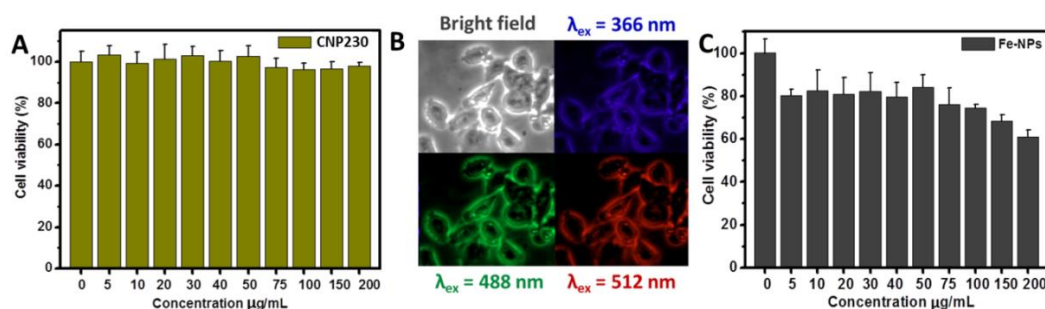
The conclusive summary of the results corresponding to magnetization as well as fluorescence intensity of C/Fe-NPs with iron content ranging from 17% (C/17Fe-NPs) up to 31% (C/31Fe-NPs) is exhibited in **Figure 4.30**. Importantly, presented data could be potentially used by other researchers as a guidance for predicting the optimum C/Fe ratios during the synthesis step, thereby generating nanomaterials with desired properties for particular applications.



**Figure 4.30** Plots showing the impact of Fe content on both magnetic (brown line) as well as fluorescent (blue line) properties of selected magnetic C-dots.



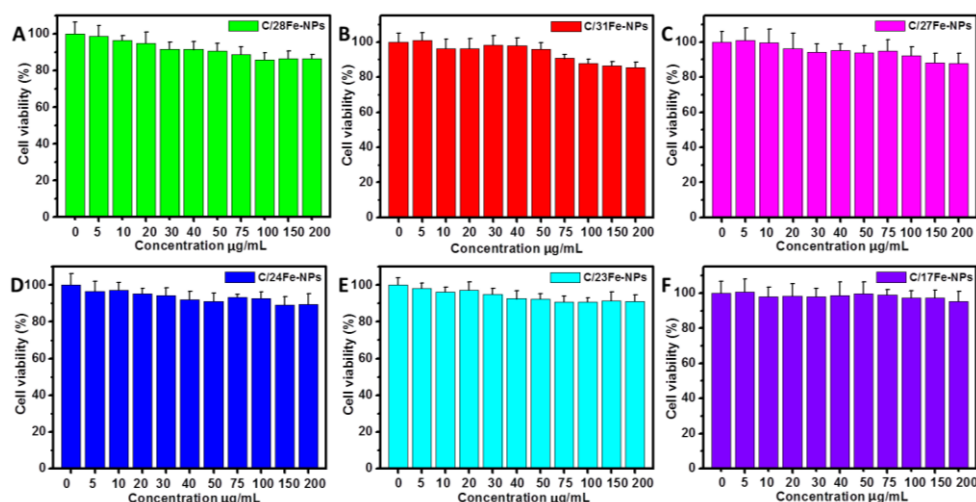
In regard to biological studies, the cytotoxicity of CNP230, Fe-NPs and C/Fe-NPs was examined with the use of 3-(4,5-dimethylthiazol-2-yl)-2,5-diphenyltetrazolium bromide (MTT) assay against HeLa cancer cell line, in order to estimate their potential to be utilised in biological applications [20, 21]. In detail, the HeLa cells were incubated with diversified concentrations (5, 10, 20, 30, 40, 50, 75, 100, 150, 200  $\mu\text{g/mL}$ ) of sterile aqueous dispersions of CNP230, Fe-NPs and C/Fe-NPs for 24 hours. Afterwards, the analysis of the absorbance values for CNP230 indicated that the cells viability remained as high as 97% at concentrations up to 200  $\mu\text{g/mL}$  (**Figure 4.31A**), thereby confirming an excellent cytocompatibility of C-dots derived from CA and EA, in a given concentration range [30]. Additionally, the use of fluorescence microscope further revealed a bright blue, green and red luminescence capabilities of HeLa cells with internalised CNP230, under the UV ( $\lambda_{\text{ex}} = 366 \text{ nm}$ ), blue ( $\lambda_{\text{ex}} = 488 \text{ nm}$ ) and green ( $\lambda_{\text{ex}} = 512 \text{ nm}$ ) excitation wavelengths (**Figure 4.31B**). This phenomenon further confirmed the multicolour nature of CNP230, which originates from the excitation wavelength-dependent fluorescence behaviour [15]. In contrast, the incubation of the HeLa cells with Fe-NPs resulted in significant decrease of the cells viability from 80% at concentration as low as 5  $\mu\text{g/mL}$  up to 61% at concentration of 200  $\mu\text{g/mL}$  (**Figure 4.31C**). Although the cytotoxic effect of uncoated Fe-NPs may be cell-type specific, many reports suggest that C-dots are biocompatible with biological tissues [63, 64].



**Figure 4.31** The MTT assay results for HeLa cells incubated with CNP230 (A) and Fe-NPs (C) for 24 h together with the fluorescence microscope images of HeLa cells with internalised CNP230 (B).

As presented in **Figure 4.32**, the cytotoxicity results for C/Fe-NPs with varied Fe content show that the presence of protective carbogenic shell impact on the gradual increment of cells viability, which at concentration of 200  $\mu\text{g/mL}$  were equal to 87%, 86%, 88%, 90%, 91% and 95% for C/28Fe-NPs, C/31Fe-NPs, C/27Fe-NPs, C/24Fe-NPs,

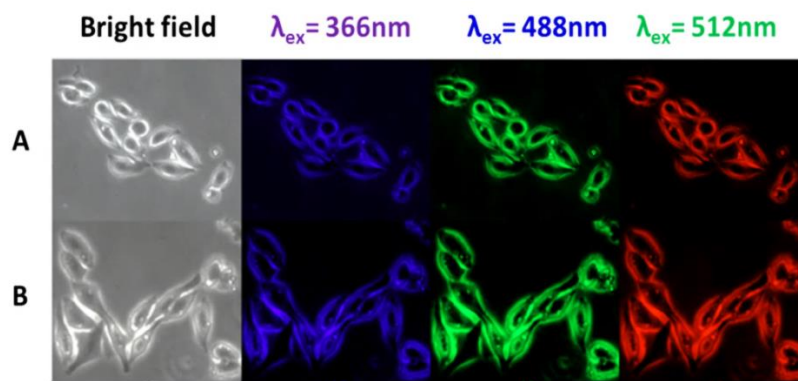
C/23Fe-NPs and C/17Fe-NPs, respectively. Besides the fact that above discussed results suggest the presence of carbogenic shell in C/Fe-NPs, it is believed that lower cell viability could be also related to aggregation of strongly magnetic nanodomains inside the cells. In addition, previous reports stated that 24 hours incubation of HeLa cells with C/Fe-NPs at concentrations up to 500  $\mu\text{g/mL}$  led to the cells viability exceeding 90% [17, 23, 30].



**Figure 4.32** The MTT assay results presenting the *in vitro* cytotoxicity of magnetic C-dots against the HeLa cell line after incubation for 24h. The data is expressed as mean  $\pm$  SD of triple experiments while percentage of cytotoxicity is represented comparatively to untreated controls.

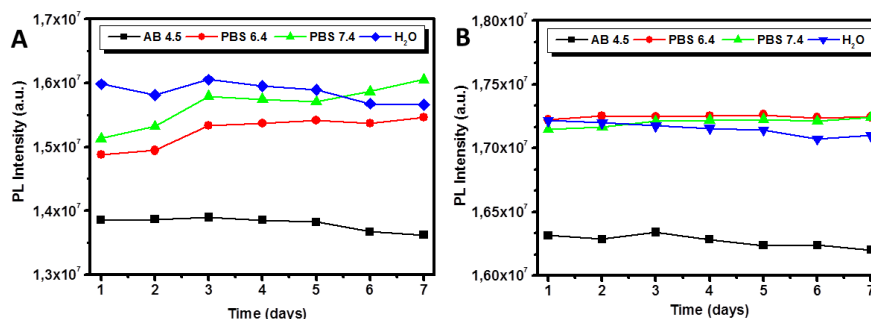
Prior performing *in vitro* cellular imaging with the use of fluorescence microscope for the investigation of magnetic C-dots cellular uptake, the HeLa cells were incubated with sterile dispersions of C/31Fe-NPs and C/17Fe-NPs at concentrations of 50  $\mu\text{g/mL}$  for 24 hours [23]. Afterwards, the images collected in the bright field displayed the morphological integrity of HeLa cells (**Figure 4.33**), which further confirms a non-toxic nature of magnetic C-dots at examined concentrations. Otherwise, the exposure of the HeLa cells towards the UV, blue and green excitation wavelengths (**Figure 4.33**) displayed that after internalisation magnetic C-dots were accumulated mainly in the cytoplasm of HeLa cells, thus illuminated them with blue, green and red fluorescence. Importantly, presented results further confirm that C/Fe-NPs are ideal candidates to be applied as magneto-fluorescent probes for the labelling of cancer cells, whereas an

additional magnetic feature could further facilitate their accumulation in preferred locations by using the external magnetic field [15].



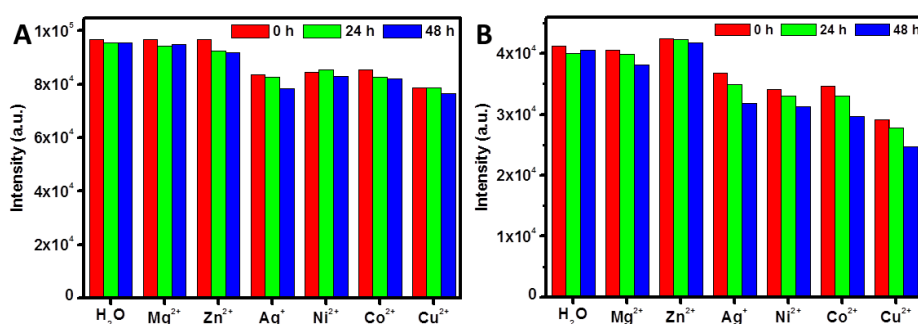
**Figure 4.33** Fluorescent microscope images of HeLa cells with internalized C/31Fe-NPs (A) and C/17Fe-NPs (B) showing their multicolour imaging capabilities at UV ( $\lambda_{ex}=366\text{ nm}$ ), blue ( $\lambda_{ex}=488\text{ nm}$ ) and green ( $\lambda_{ex}=512\text{ nm}$ ) excitation wavelengths.

In additional experiment, C/31Fe-NPs (**Figure 4.34A**) and C/17Fe-NPs (**Figure 4.34B**) were dispersed in buffer solutions that imitate the environment of the cells and the PL intensity of as-prepared dispersions was investigated in detail for 7 days. As presented in **Figure 4.34A**, a slight variations in the fluorescence intensities of C/31Fe-NPs suggested the formation of aggregates, due to the  $\pi$ - $\pi$  interactions between highly magnetic nanodomains [58]. Besides that, collected results clearly indicated that the optical properties of magnetic C-dots are preserved in a wide range of pH (Appendix, **Figure A16**), thus have potential to be utilised for *in vivo* and *in vitro* biomedical applications [15]. In regard to literature reports, it has been noted that the optical properties of C/Fe-NPs remains stable up to a few months [15, 21, 30].



**Figure 4.34** Plots showing the variations of the PL intensity recorded at  $\lambda_{ex}=365\text{ nm}$  for C/31Fe-NPs (A) and C/17Fe-NPs (B) dispersions over 7 days. The concentration of the samples was equal to 0.1 mg/mL.

In addition, the presence of fluorophore-rich carbogenic shell in the structure of C/Fe-NPs endow them in metal complexation ability for particular metal ions, such as Ag(I), Cu(II), Co(II) and Ni(II), as shown in **Figure 4.35** [42]. In detail, a high selectivity and specificity towards specific metal ions is related to the presence of amine groups ( $-NH_2$ ), from which the nitrogen atom donates electron to selected ion and makes surface complexation that impact on the decrement of photoluminescence intensity [23]. Thus, these results imply that besides proposed application in bioimaging, C/Fe-NPs can be also used as chemosensors for the detection of poisonous metal ions (i.e.  $Ni^{2+}$ ) in the cells or biological fluids [65].



**Figure 4.35** The plots representing an impact of selected metal ions in aqueous solutions of C/31Fe-NPs on the maximum PL intensity recorded at  $\lambda_{ex} = 375$  nm (A) and  $\lambda_{ex} = 450$  nm (B).

In addition, the antimicrobial activities of CNP230, Fe-NPs and selected C/Fe-NPs were tested against Gram-positive *Staphylococcus aureus* as well as Gram-negative *Escherichia coli* bacterial species. As summarised in **Table 4.5**, magnetic C-dots demonstrate excellent antimicrobial effect after incubation with bacterial species for 24 hours at  $37^\circ C$  and caused the reduction in either *E.coli* colonies between 99.0% to 99.9% or in *S.aureus* colonies between 99.5% to 99.9%. Although it has been reported that both C-dots as well as iron oxide-based NPs demonstrate antimicrobial effect, the Fe-NPs displayed only 91.4% decrease in *E.coli* colonies that could be related to poor colloidal stability of uncoated Fe-NPs in the nutrient medium [66, 67]. On the other side, CNP230 caused the reduction in both *E.coli* and *S.aureus* colonies up to 99.9% while being well-known as photo-activated antimicrobial agents that are environmentally benign and intrinsically non-toxic both *in vivo* as well as *in vitro* [66].

Overall, the presented results suggest that magnetic C-dots could be applied as an effective antimicrobial agents for fighting the infectious diseases [68].

**Table 4.3** The results from antimicrobial studies presenting the number of colony forming units (CFU) for agar plates incubated with selected C/Fe-NPs and either *E.coli* or *S.aureus* for 24 hours at 37°C

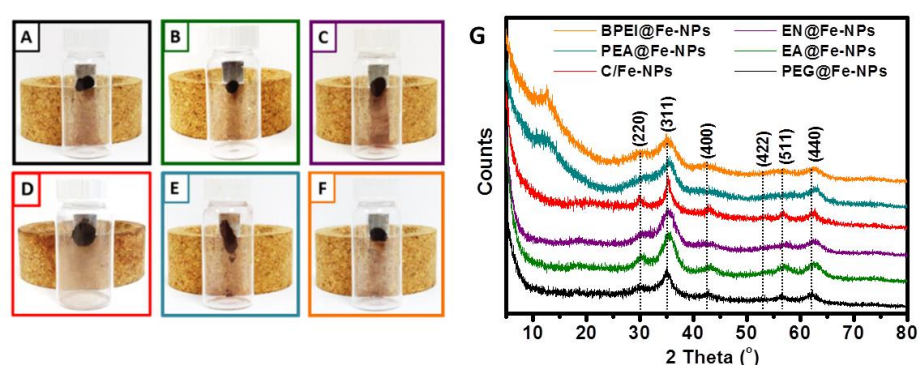
Material	<i>Escherichia coli</i>	<i>Staphylococcus aureus</i>
	% decrease	% decrease
	24h	24h
CNP230	99.9	99.9
C/Fe17-NPs	99.9	99.9
C/Fe23-NPs	99.9	99.9
C/Fe24-NPs	99.9	99.9
C/Fe27-NPs	99.0	99.5
C/Fe31-NPs	99.5	99.9
Fe-NPs	91.4	99.9

#### 4.3.3 Comparison of magnetic C-dots with other carbon-rich magnetic NPs

In order to evaluate the extent of predominant optical and magnetic properties of above characterized C/Fe-NPs, more hybrid magneto-fluorescent nanoparticles (C@Fe-NPs) were synthesized with the use of iron (III) acetylacetonate as Fe precursor and via the same thermal decomposition approach. On the contrary, previously used PL-CAEA180 was replaced by exemplary amines (ethanolamine-EA and ethylenediamine-EN), polymers (polyethylene glycol-PEG, branched polyethyleneimine-BPEI) or polyetheramine (Jeffamine® D-230) as carbon sources, thereby led to fabrication of EA@Fe-NPs, EN@Fe-NPs, PEG@Fe-NPs, BPEI@Fe-NPs and PEA@Fe-NPs, respectively.

The X-Ray diffraction patterns of C@Fe-NPs (**Figure 4.36G**) reveal the presence of a crystalline phase with various broaden diffraction peaks at  $2\theta$  of 30.02°, 35.14°, 42.96°, 53.50°, 56.93° and 62,63°, which correspond to the (220), (311), (400), (422), (511) and (440) crystal planes of magnetite [18, 31, 36, 37, 41, 56, 57]. Nonetheless, significantly broaden diffraction peaks in the XRD patterns of EA@Fe-NPs, EN@Fe-NPs, BPEI@Fe-NPs and PEA@Fe-NPs suggest an abundant content of covalently bounded to their surface polymeric organic chains, which arise from insufficient carbonization process

[24, 27]. On the other side, the broad diffraction peaks at  $2\theta \approx 14^\circ$  for BPEI@Fe-NPs and PEA@Fe-NPs confirm the presence of amorphous phase attributed to carbogenic nanodomains as well as suggest that C-dots may not be completely redistributed within the Fe-NPs matrix [29, 31]. Overall, the results confirmed the presence of magnetite in EA@Fe-NPs, EN@Fe-NPs, PEG@Fe-NPs, BPEI@Fe-NPs and PEA@Fe-NPs, as anticipated from their ability to respond firmly towards an external magnet (**Figure 4.36A-F**). Besides that, the insignificantly reduced magnetic properties of PEA@Fe-NPs may be attributed to diverse magnetic ordering in Fe-NPs or insufficient content of carbogenic domains [16, 23, 29, 37].



**Figure 4.36** Photos of PEG@Fe-NPs (A), EA@Fe-NPs (B), EN@Fe-NPs (C), C/31Fe-NPs (D), PEA@Fe-NPs (E) and BPEI@Fe-NPs (F) along with their X-Ray diffraction patterns (G).

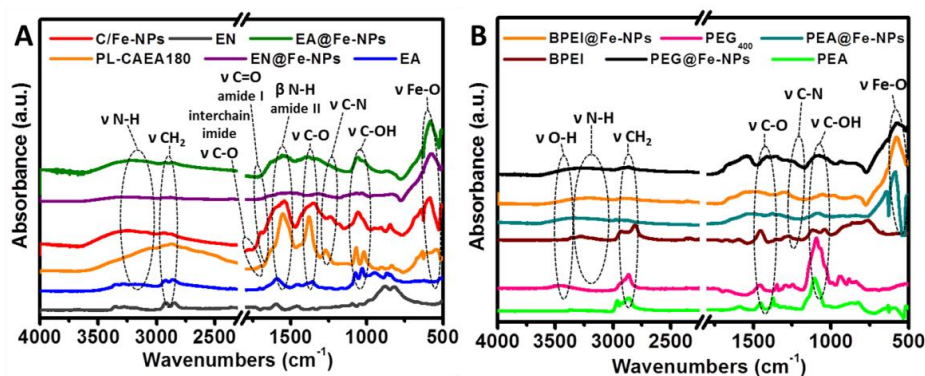
Furthermore, the results obtained from the elemental analysis revealed that all C@Fe-NPs possess higher Fe content than C/31Fe-NPs, as summarised in **Table 4.4**. Although the highest iron content corresponds to PEA@Fe-NPs (71.35%), their reduced magnetic properties (**Figure 4.36E**) probably arise from insufficient carbon doping (7.73%) that do not stabilise the magnetite component.

**Table 4.4** Elemental analysis results for various C@Fe-NPs and C/31Fe-NPs

	C	H	N	O	Fe
C/Fe-NPs	26.85	3.62	3.85	34.68	31.00
PEG@Fe-NPs	15.53	2.34	----	32.60	49.53
BPEI@Fe-NPs	13.18	2.67	5.55	25.00	53.60
PEA@Fe-NPs	7.73	1.70	1.34	17.88	71.35
EA@Fe-NPs	12.85	2.06	3.36	28.96	52.77
EN@Fe-NPs	7.19	1.63	2.53	18.71	69.94

From the structural point of view, synthesized C@Fe-NPs may be considered as carbogenically doped Fe-NPs with several organic species bounded to their surface.

The presence of additional organic molecules (either polymers or amine chains) on the surface of hybrid nanoparticles results from insufficient carbonization process and leads to the formation of specific linkages between passivating reagents and the C-dots surface [27, 69]. Thus, the structural insight into various amine, polyetheramine or polymer functionalized C@Fe-NPs was gained by the analysis of their FTIR spectra (**Figure 4.37A,B**). The comparison of the intensities of the symmetric and asymmetric C-H bands in C@Fe-NPs as well as the neat EN, EA, BPEI, PEG<sub>400</sub> and PEA imply that a large amount of carbon-rich precursors have been consumed for the formation of C-dots during the carbonization process, whereas the presence of –COOH groups in the PEG@Fe-NPs arise from the partial oxidation of the terminal –OH groups of PEG<sub>400</sub> molecules during the synthesis process [26, 27, 31]. Additionally, plentiful functional moieties represented by C-OH stretching at 1034-1086 cm<sup>-1</sup>, C-N stretching around 1285 cm<sup>-1</sup>, C-O stretching at 1302-1386 cm<sup>-1</sup>, N-H in-plane bending at 1412-1577 cm<sup>-1</sup>, C=O stretching at 1634-1654 cm<sup>-1</sup>, C-H symmetric and asymmetric stretching at 2867-2972 cm<sup>-1</sup> and N-H or O-H stretching at around 3217-3262 cm<sup>-1</sup> could facilitate the linkage between C@Fe-NPs and other biomolecules or biological components, while the Fe-O absorption band around 580 cm<sup>-1</sup> confirms the presence of iron oxide component [22, 26, 30, 31, 42].

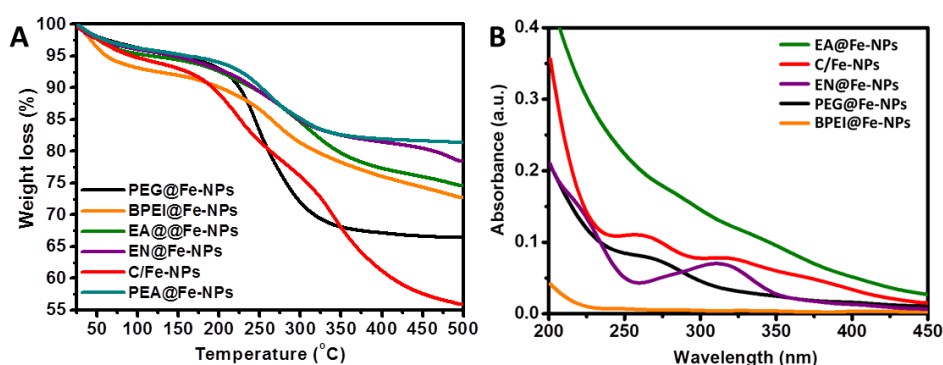


**Figure 4.37** FTIR spectra of amine (A) and polymer (B) functionalized magnetic nanoparticles.

The comparison of the results from the thermogravimetric analysis (**Figure 4.38A**) further displayed that among all C@Fe-NPs the highest cumulative weight loss was attributed to C/31Fe-NPs (45.22%) with predominant organic content. Besides that, the first degradation step ( $T \approx 125\text{--}350^\circ\text{C}$ ) in the TGA curves of C@Fe-NPs refer to the



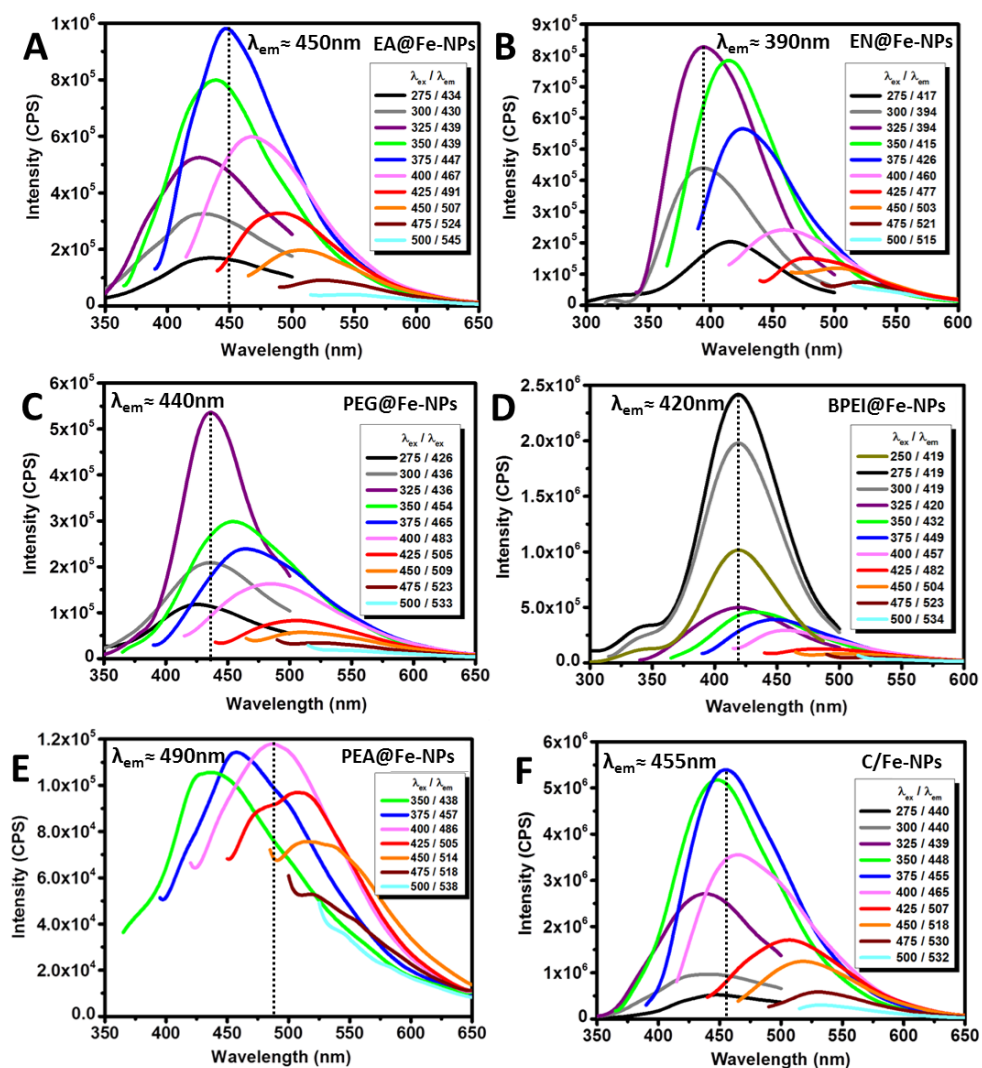
conjugation of carbon dots with magnetite cores [9]. Furthermore, the optical properties of C/31Fe-NPs were compared with other C@Fe-NPs and their UV-Vis spectra (**Figure 4.38B**), PL spectra (**Figure 4.39**) and PL lifetime decays (**Figure 4.40** and **Figure 4.41**) were analysed in detail. The UV-Vis absorbance spectra of both PEG@Fe-NPs and C/31Fe-NPs reveal an absorption band around 250 nm (**Figure 4.38B**), which is attributed to the presence of  $\pi$ - $\pi^*$  electron transition of multiple aromatic chromophores [20, 28]. On the other side, the presence of the absorption peaks around 320 nm suggest the carbonyl and amine n- $\pi^*$  electron transitions [15, 30]. In contrast, the EA@Fe-NPs and BPEI@Fe-NPs show no absorption in the presented energy range [31].



**Figure 4.38** UV-Visible absorption spectra of aqueous dispersion of C@Fe-NPs. The concentration of the samples was equal to 0.1 mg/mL.

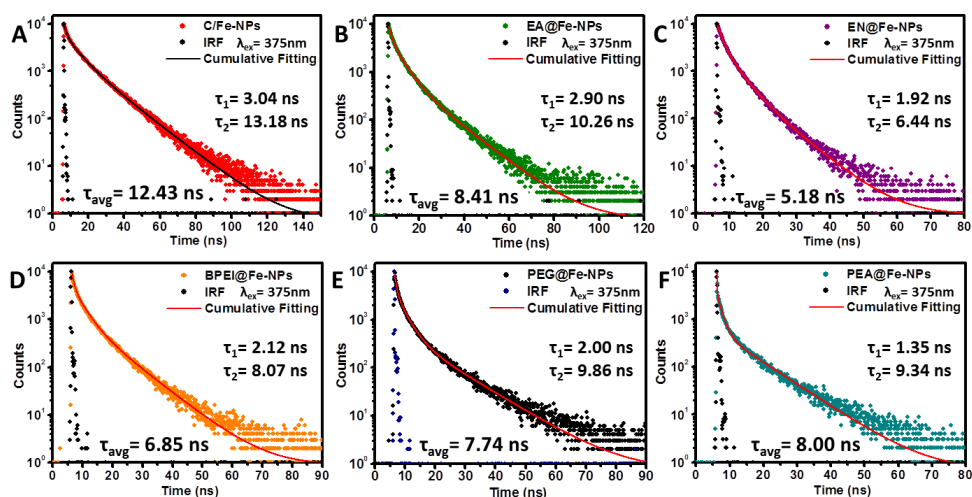
The analysis of the liquid-state PL spectra of EA@Fe-NPs, EN@Fe-NPs, PEG@Fe-NPs and BPEI@Fe-NPs further revealed their excitation-wavelength dependent emissive behaviour in the range of  $350 < \lambda_{\text{ex}} < 500$  nm as well as excitation-wavelength independent fluorescence at  $275 < \lambda_{\text{ex}} < 325$  nm, as presented in **Figure 4.39**. On the contrary, the  $\lambda_{\text{ex}}$ -dependent emission spectra and weak luminescent properties were recorded for PEA@Fe-NPs with the lowest carbon content (**Figure 4.39E**). Overall, the predominant excitation-dependent fluorescence behaviour of C@Fe-NPs may arise from different sizes of nanodomains as well as diversified surface state distributions [17].





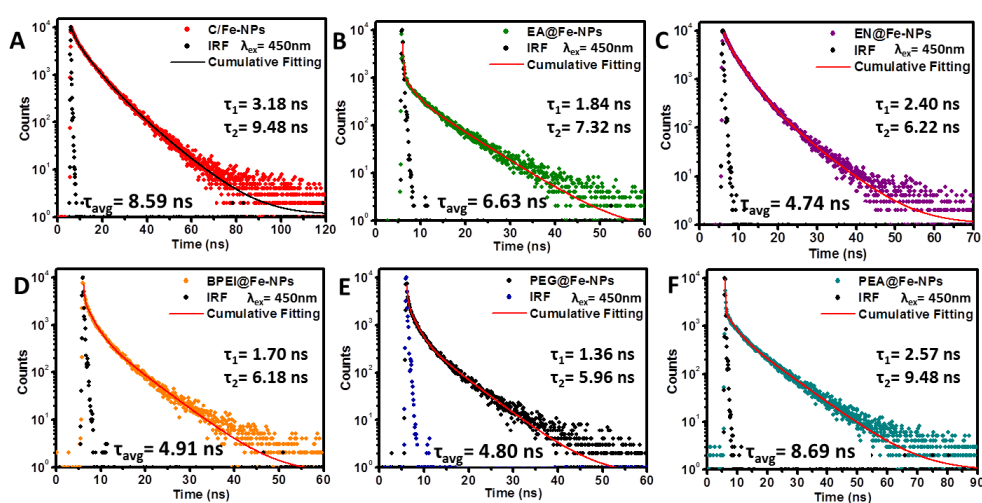
**Figure 4.39** The PL spectra of aqueous dispersions of EA@Fe-NPs (A), EN@Fe-NPs (B), PEG@Fe-NPs (C), BPEI@Fe-NPs (D), PEA@Fe-NPs (E) and C/31Fe-NPs (F) with concentration of 0.01 mg/mL.

The analysis of the PL lifetime decays recorded at  $\lambda_{ex}=375$  nm (**Figure 4.40**) confirmed that the use of EA-rich precursors results in the prolonged average PL lifetimes ( $\tau_{avg}$ ) of C/Fe-NPs ( $\tau_{avg}=12.43$ ns) or EA@Fe-NPs ( $\tau_{avg}=8.41$  ns) than other C@Fe-NPs ( $\tau_{avg}\approx 5-8$  ns). Nevertheless, the lower value of the average PL lifetime of EN@Fe-NPs ( $\tau_{avg}=5.18$  ns) then reported for the pure C-dots derived from EN and CA ( $\tau_{avg}= 14.70$  ns) imply the significant quenching of C-dots luminescence centres by iron oxides domains [70].



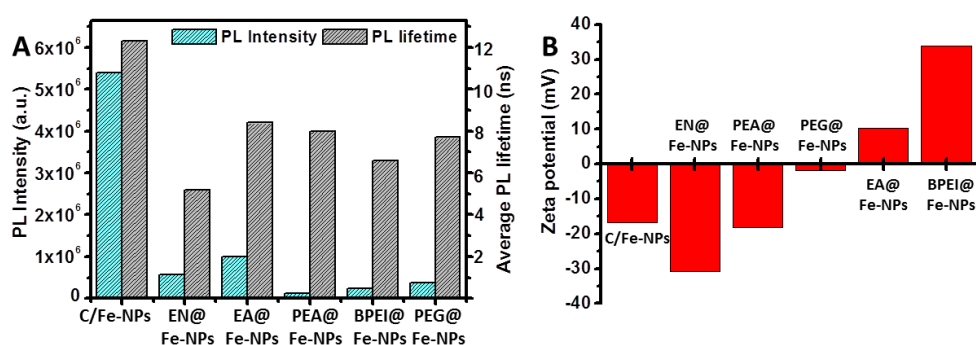
**Figure 4.40** The PL lifetime decays of aqueous dispersions of C/Fe-NPs and C@Fe-NPs recorded at  $\lambda_{ex}$  = 375 nm.

Furthermore, the fluorescence lifetime decays recorded at  $\lambda_{ex}$  = 450 nm revealed a similar trend to the above mentioned results, as demonstrated in **Figure 4.41**. It has been reported that the C-dots derived from PEG<sub>1500</sub> are characterised by the  $\tau_{avg}$  = 4.92 ns at  $\lambda_{ex}$  = 405 nm, which is only insignificantly higher than recorded  $\tau_{avg}$  = 4.80 ns for PEG@Fe-NPs (**Figure 4.41E**), thus neglecting the PL quenching of PEG-derived C-dots by the Fe-NPs [60]. Overall, the exceptional  $\tau_{avg}$  of C@Fe-NPs recorded at  $\lambda_{ex}$  = 375 nm ( $\tau_{avg}$  ≈ 5–8 ns) and  $\lambda_{ex}$  = 450 nm ( $\tau_{avg}$  ≈ 5–9 ns) are longer than reported for many organic dyes ( $\tau$  = 1–5 ns), therefore implying their suitability to be used in the fluorescence lifetime imaging of biological tissues [62, 71].



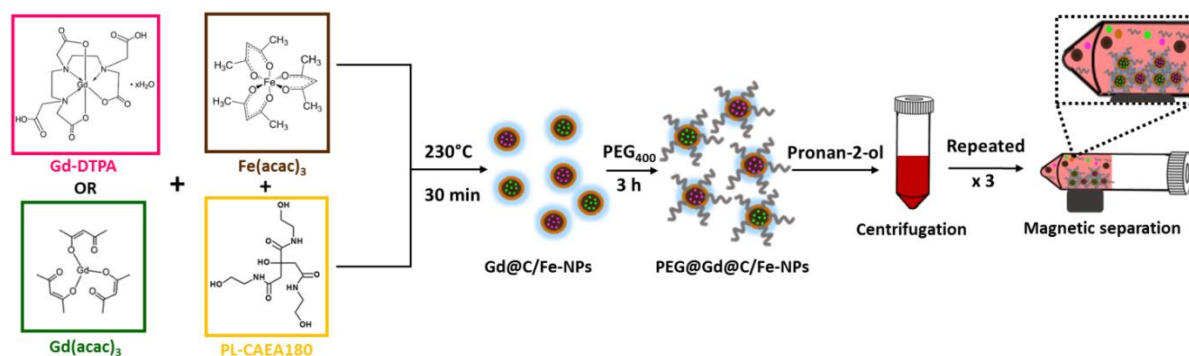
**Figure 4.41** The PL lifetime decays of aqueous solutions of C/Fe-NPs and C@Fe-NPs recorded at  $\lambda_{ex}$  = 450 nm.

The comparative chart gathering the information about the photoluminescence properties of C@Fe-NPs and C/Fe-NPs is presented in **Figure 4.42A**. Among all, the most remarkable optical characteristics are attributed to magnetic C-dots with zeta potential ( $\zeta$ ) value equal to -16.7 mV (**Figure 4.42B**), that suggests both the relatively poor colloidal stability probably related to the aggregation of magnetic nanodomains as well as a significant content of carboxylic groups arising from citric acid or trisodium citrate precursors [20, 21, 26]. Nonetheless, it has been reported that negatively charged hydrophilic groups arising from C-dots impact on the improvement of the stability of Fe-NPs as well as dispersibility of C@Fe-NPs in aqueous media [30]. Among all, the most prominent colloidal stability is attributed to BPEI@Fe-NPs with  $\zeta$ = +33.90 mV, which positive zeta potential value corresponds to the protonation of  $-\text{NH}_2$  groups of cationic polymer BPEI in aqueous solution towards ionized  $-\text{NH}_3^+$  groups [26].



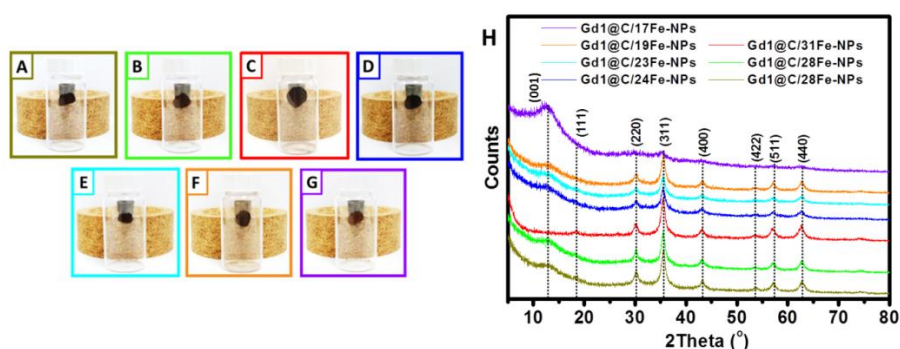
**Figure 4.42** The cumulative chart summarizing the liquid-state optical properties of various carbon-rich magnetic nanoparticles at  $\lambda_{\text{exc}}$ = 375 nm (A) together with zeta potential values of their aqueous dispersions (B).

Likewise, the examination of the XRD patterns for another family of Gd-rich magnetic C-dots (**Figure 4.45H**) demonstrated similar results, while only the powder of Gd2@17C/Fe-NPs do not respond towards an external magnet (**Figure 4.45G**). Overall, these results proved that the magnetic properties of C/Fe-NPs were restored for C/19Fe-NPs through the utilisation of Gd-doping approach. Furthermore, the comparison of the XRD patterns of Gd2@C/Fe-NPs and pure Gd(acac)<sub>3</sub> precursor (Appendix, **Figure A17**) revealed the lack of additional diffraction peaks attributed to free Gd<sup>3+</sup> ions, thus confirmed its complete and stable incorporation into Fe-NPs [46].



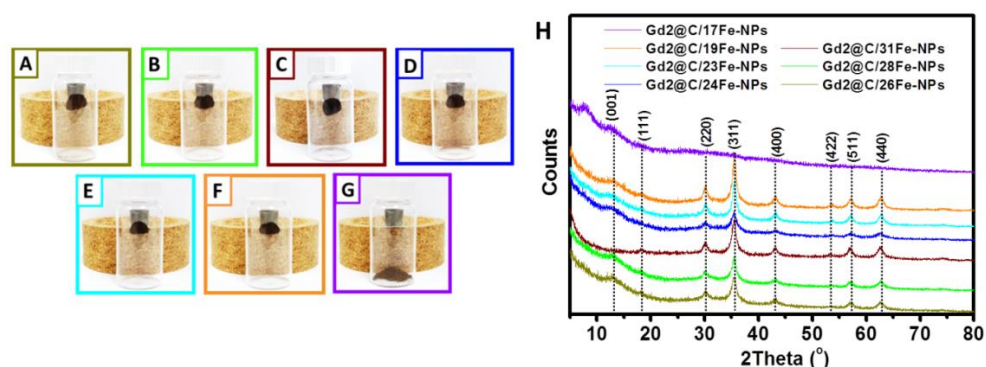
**Figure 4.43** Scheme presenting the synthesis and purification strategies of Gd-doped magnetic C-dots via thermal treatment of Gd-DTPA or Gd(acac)<sub>3</sub>, Fe(acac)<sub>3</sub> and PL-CAEA180 precursors mixtures.

It has been previously reported that the introduction of rare earth elements into the structure of Fe-NPs enhance their optical and magnetic properties. However, this task is not trivial due to a large size of lanthanide ions that hinder the incorporation into the crystalline lattice of magnetite [42]. To this end, the analysis of the XRD patterns of a large family of Gd1@C/Fe-NPs (**Figure 4.44H**) proved the presence of well-pronounced diffraction peaks at  $2\theta \approx 30^\circ, 35^\circ, 42^\circ, 53^\circ, 57^\circ$  and  $63^\circ$  that are corresponding to the (220), (311), (400), (422), (511) and (440) crystal planes of magnetite [20, 23, 27, 30, 31, 36, 40, 41]. The lack of obvious diffraction peaks corresponding to the cubic Gd<sub>2</sub>O<sub>3</sub> further confirmed the complete incorporation of Gd<sup>3+</sup> ions into the tetrahedral and octahedral sites of Fe-NPs as well as suggested the possible substitution of Fe<sup>3+</sup> ions by the Gd<sup>3+</sup> ions that may facilitate the resistance of Gd@C/Fe-NPs towards the oxidation [42, 43]. Besides that, the powders of Gd1@C/Fe-NPs showed a remarkable magnetic response towards external magnet, as demonstrated in **Figure 4.44A-G**.



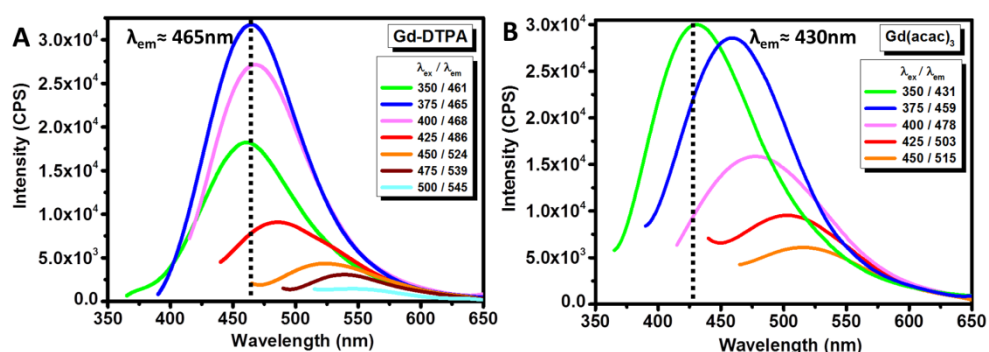
**Figure 4.44** Photos of Gd1@C/Fe-NPs (A-G) with an external magnet along with the X-Ray diffraction patterns of all sample (H).

Likewise, the examination of the XRD patterns for another family of Gd-rich magnetic C-dots (**Figure 4.45H**) demonstrated similar results, while only the powder of Gd2@17C/Fe-NPs do not respond towards an external magnet (**Figure 4.45G**). Overall, these results proved that the magnetic properties of C/Fe-NPs were restored for C/19Fe-NPs through the utilisation of Gd-doping approach. Furthermore, the comparison of the XRD patterns of Gd2@C/Fe-NPs and pure Gd(acac)<sub>3</sub> precursor (Appendix, **Figure A17**) revealed the lack of additional diffraction peaks attributed to free Gd<sup>3+</sup> ions, thus confirmed its complete and stable incorporation into Fe-NPs [46].



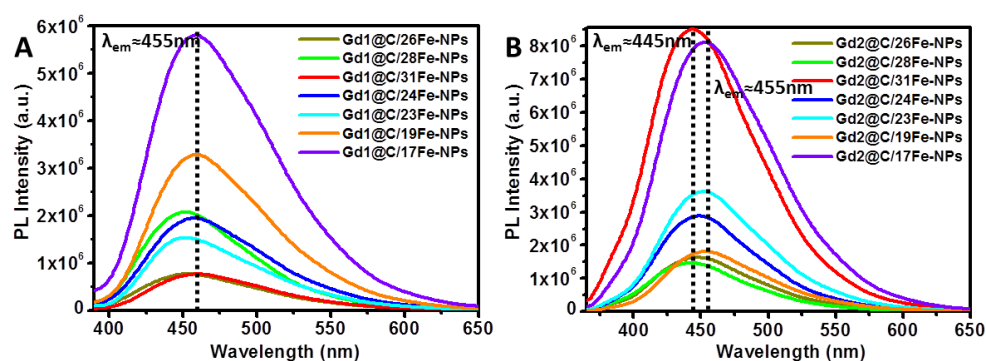
**Figure 4.45** Photos of Gd2@C/Fe-NPs (A-G) with an external magnet together with the X-Ray diffraction patterns of all sample (H).

Besides improvement of magnetic features, gadolinium element contributed also to the change in the optical properties of Gd@C/Fe-NPs. Thus, as demonstrated in **Figure 4.46A**, the Gd-DTPA with the maximum emission peak centered around 465 nm demonstrates the most distinct resemblance to CNP230 ( $\lambda_{em} \approx 460$ nm), while the maximum PL emission for Gd(acac)<sub>3</sub> is shifted towards  $\lambda_{em} \approx 430$ nm.



**Figure 4.46** PL spectra of aqueous solution of Gd-DTPA (A) and Gd(acac)<sub>3</sub> (B) with concentration of 0.1 mg/mL.

Thus, further optical analysis revealed that the position of the maximum emission peak in the PL spectra of Gd1@C/Fe-NPs (**Figure 4.47A**) is dominated by the luminescence arising from CNP230 component, whereas for Gd2@C/Fe-NPs (**Figure 4.47B**) a negligible shifting towards blue-emissive region was observed, as previously noted for pure Gd(acac)<sub>3</sub> precursor (**Figure 4.46B**). Overall, the PL intensities of Gd@C/Fe-NPs are quenched, thus indicating the interfering contribution of two optical modalities. In addition, the analysis of the maximum intensity of the PL emission peaks for Gd1@C/Fe-NPs (Appendix, **Figure A18**) and Gd2@C/Fe-NPs (Appendix, **Figure A19**) synthesized from 1 hour up to 4 hours further confirmed that 3 hours constitute an optimal time for the synthesis of hybrid Gd@C/Fe-NPs as well as suggested the variations in the formation mechanism of both nanosystems.



**Figure 4.47** PL spectra of Gd1@C/Fe-NPs (A) and Gd2@C/Fe-NPs (B) recorded for the maximum emission peak at  $\lambda_{ex}$  = 375 nm. The samples concentration was equal to 0.1 mg/mL.

## 4.4 Conclusion

In conclusion, a large gallery of magnetic C-dots with both magnetic and fluorescent properties was synthesized through a facile one-step and one-pot thermal decomposition method. The impact of iron incorporation into amorphous CNP230, derived from PL-CAEA180 via thermal treatment at 230°C, was investigated for the first time in a very systematic manner. Initially, the detailed structural, thermal and optical analysis proved that the optimum time for the synthesis of magnetic C-dots was between 2 to 3 hours, as these hybrid nanoparticles demonstrated the most remarkable both magnetic as well as fluorescence properties. The detailed physicochemical analysis of a large family of C/Fe-NPs proved that the iron component



impact on the quenching of C-dots fluorescence, while abundant carbon content suppress the magnetic properties. The broad emission ranges in the PL spectra implied the multicolour nature of magnetic C-dots, which was further confirmed by the examination of the results from bioimaging experiment. To that end, the illumination of the HeLa cancer cells with internalized C/Fe-NPs demonstrated the accumulation of these nanoscopic emitters in the cell cytoplasm and perinuclear region. On the other side, the results collected from the magnetometer proved that C/Fe-NPs have a superparamagnetic nature, which is a key requirement in the magnetically-responsive biomedical applications. Thus, the remarkable magnetic features in combination with desired fluorescence and antimicrobial capabilities pave the way for using as-prepared magnetic C-dots as magnetically-guided surveillance probes for the detection and labelling of cancer cells. Besides that, the investigation of the changes of their fluorescence intensity in the presence of metal ions further proved that C/Fe-NPs can be used as optical sensors for the detection of heavy metal based ions. In another approach, the utilisation of gadolinium doping resulted in improvement of magnetic properties of C/Fe-NPs, without significant quenching of their fluorescent properties. Thus, the development of a dual-modal Gd@C/Fe-NPs expand the promising application of magnetic C-dots towards new directions as MRI contrast agents and constituted a facile method to overcome their previous limitation. In addition to all, the use of versatile carbon-rich precursors as the replacement for PL-CAEA180 proved that developed synthetic strategy can be applied to fabricate diverse magneto-fluorescent NPs, which although are less fluorescent possess a superior magnetic features. Overall, it has been proved that the proposed fabrication method can be applied in a different settings, thus giving a promise for a large scale commercialisation of both magnetic C-dots as well as diverse magneto-fluorescent NPs.

## 4.5 References

1. Lu, A.H., E.L. Salabas, and F. Schuth, *Magnetic Nanoparticles: Synthesis, Protection, Functionalization, and Application*. Angew. Chem. Int. Ed. , 2007. **46**: p. 1222 – 1244.
2. Demirer, G.S., A.C. Okur, and S. Kizilel, *Synthesis and Design of Biologically Inspired Biocompatible Iron Oxide Nanoparticles for Biomedical Applications*. J. Mater. Chem. B, 2015. **3**: p. 7831-7849.
3. Shen, L., B. Li, and Y. Qiao, *Fe<sub>3</sub>O<sub>4</sub> Nanoparticles in Targeted Drug/Gene Delivery Systems*. Materials, 2018. **11**: p. 324-353.
4. Xie, L., et al., *Construction of small-sized superparamagnetic Janus nanoparticles and their application in cancer combined chemotherapy and magnetic hyperthermia*. Biomater. Sci., 2020. **8**: p. 1431-1441.
5. Lee, N., et al., *Iron Oxide Based Nanoparticles for Multimodal Imaging and Magnetoresponse Therapy*. Chem. Rev., 2015. **115**: p. 10637–10689.
6. Wu, W., C.Z. Jiang, and V.A.L. Roy, *Designed synthesis and surface engineering strategies of magnetic iron oxide nanoparticles for biomedical applications*. Nanoscale, 2016. **8**: p. 19421-19474.
7. Xu, C., et al., *Applications of Iron Oxide-Based Magnetic Nanoparticles in the Diagnosis and Treatment of Bacterial Infections*. Front. Bioeng. Biotechnol., 2019. **7**: p. 141.
8. Sun, S. and H. Zeng, *Size-Controlled Synthesis of Magnetite Nanoparticles*. J. AM. CHEM. SOC., 2002. **124**: p. 8204-8205.
9. Lobato, N.C.C., M.B. Mansur, and A.M. Ferreira, *Characterization and Chemical Stability of Hydrophilic and Hydrophobic Magnetic Nanoparticles*. Materials Research, 2017. **20**(3): p. 1-11.
10. Itoh, H. and T. Sugimoto, *Systematic control of size, shape, structure, and magnetic properties of uniform magnetite and maghemite particles*. J Colloid Interface Sci., 2003. **265**.
11. Rajan, S.A., M. Sharma, and N.K. Sahu, *Water-to-PEG Variation: Morphology and Hyperthermic Behaviour of Iron Oxide*. J Supercond Nov Magn, 2020. **33**: p. 1603–1609.
12. Yang, S.T., et al., *Carbon Dots for Optical Imaging in Vivo*. J. Am. Chem. Soc. , 2009. **131**: p. 11308–11309.
13. Wang, X., et al., *A Mini Review on Carbon Quantum Dots: Preparation, Properties, and Electrocatalytic Application*. Frontiers in Chemistry, 2019. **7**: p. 1-9.
14. Zhou, J., et al., *Electronic structure and luminescence center of blue luminescent carbon nanocrystals*. Chemical Physics Letters, 2009. **474**: p. 320-324.



15. Han, C., et al., *Multifunctional iron oxide-carbon hybrid nanoparticles for targeted fluorescent/MR dual-modal imaging and detection of breast cancer cells*. *Analytica Chimica Acta*, 2019. **1067**: p. 115-128.
16. Tiwari, A., et al., *Graphitic Carbon Coated Magnetite Nanoparticles for Dual-Mode Imaging and Hyperthermia*. *ACS Appl. Nano Mater.*, 2019. **3**(1): p. 896-904.
17. Zhuo, S., et al., *Facile fabrication of fluorescent Fe-doped carbon quantum dots for dopamine sensing and bioimaging application*. *Analyst*, 2019. **144**: p. 656-662.
18. Lu, N., et al., *Yolk-shell nanostructured Fe<sub>3</sub>O<sub>4</sub>@C magnetic nanoparticles with enhanced peroxidase-like activity for label-free colorimetric detection of H<sub>2</sub>O<sub>2</sub> and glucose*. *Nanoscale*, 2017. **9**: p. 4508-4515.
19. Wang, H. and S. Zhou, *Magnetic and fluorescent carbon-based nanohybrids for multi-modal imaging and magnetic field/NIR light responsive drug carriers*. *Biomater. Sci.*, 2016. **4**(7): p. 1062-1073.
20. Wang, H., et al., *Magnetic iron oxide-fluorescent carbon dots integrated nanoparticles for dual-modal imaging, near-infrared light-responsive drug carrier and photothermal therapy*. *Biomater. Sci.*, 2014. **2**: p. 915-923.
21. Lou, L., et al., *Functionalized magnetic-fluorescent hybrid nanoparticles for cell labelling*. *Nanoscale*, 2011. **3**: p. 2315-2323.
22. Jaiswal, M.K., et al., *A comparative study on thermoresponsive magnetic nanohydrogels: role of surface-engineered magnetic nanoparticles*. *Colloid Polym Sci*, 2012. **290**: p. 607-617.
23. Kumar, A., et al., *One pot synthesis of carbon dots entrenched chitosan modified magnetic nanoparticles for fluorescence based Cu<sup>2+</sup> ion sensing and cell imaging*. *RSC Adv.*, 2016. **6**(64): p. 58979-58987.
24. Anbarasu, M., et al., *Synthesis and characterization of polyethylene glycol (PEG) coated Fe<sub>3</sub>O<sub>4</sub> nanoparticles by chemical co-precipitation method for biomedical applications*. *Spectrochimica Acta Part A: Molecular and Biomolecular Spectroscopy*, 2015. **135**: p. 536-539.
25. Mendes, R.G., et al., *Synthesis and toxicity characterization of carbon coated iron oxide nanoparticles with highly defined size distributions*. *Biochimica et Biophysica Acta*, 2014. **1840**: p. 160-169.
26. Wang, J., et al., *One-pot synthesis of water-soluble superparamagnetic iron oxide nanoparticles and their MRI contrast effects in the mouse brains*. *Materials Science and Engineering C*, 2015. **48**: p. 416-423.
27. Hu, Y., et al., *Preparation and optical properties of magnetic carbon/iron oxide hybrid dots*. *RSC Adv.*, 2017. **7**: p. 41304-41310.

28. Wang, Z., et al., *Synthesis and characterization of a novel magnetic carrier with its composition of Fe<sub>3</sub>O<sub>4</sub>/carbon using hydrothermal reaction*. Journal of Magnetism and Magnetic Materials, 2006. **302**: p. 397–404.
29. Zhang, S., et al., *Preparation of carbon coated Fe<sub>3</sub>O<sub>4</sub> nanoparticles and their application for solid-phase extraction of polycyclic aromatic hydrocarbons from environmental water samples*. Journal of Chromatography A, 2010. **1217**: p. 4757–4764.
30. Liu, X., et al., *Nitrogen-Doped Carbon Quantum Dot Stabilized Magnetic Iron Oxide Nanoprobe for Fluorescence, Magnetic Resonance and Computed Tomography Triple-Modal In Vivo Bioimaging*. Adv. Funct. Mater. , 2016: p. 1–13.
31. Li, B., et al., *One-pot synthesis of polyamines improved magnetism and fluorescence Fe<sub>3</sub>O<sub>4</sub>–carbon dots hybrid NPs for dual modal imaging*. Dalton Trans., 2016. **45**: p. 5484–5491.
32. Ahmadian-Fard-Fini, S., M. Salavati-Niasari, and D. Ghanbari, *Hydrothermal green synthesis of magnetic Fe<sub>3</sub>O<sub>4</sub>-carbon dots by lemon and grape fruit extracts and as a photoluminescence sensor for detecting of E. coli bacteria*. Spectrochimica Acta Part A: Molecular and Biomolecular Spectroscopy 2018. **203**: p. 481–493.
33. Zheng, J., et al., *One-step solvothermal synthesis of Fe<sub>3</sub>O<sub>4</sub>@C core–shell nanoparticles with tunable sizes*. Nanotechnology, 2012. **23**: p. 165601–165609.
34. Wang, H., et al., *Fe<sub>3</sub>O<sub>4</sub>/carbon quantum dots hybrid nanoflowers for highly active and recyclable visible-light driven photocatalyst*. J. Mater. Chem. A, 2014. **2**: p. 15740–15745.
35. Hu, F., et al., *Preparation of Biocompatible Magnetite Nanocrystals for In Vivo Magnetic Resonance Detection of Cancer*. Adv. Mater., 2006. **18**: p. 2553–2556.
36. Guo, Y., et al., *Synthesis of ultrathin carbon dots-coated iron oxide nanocubes decorated with silver nanoparticles and their excellent catalytic properties*. Ceramics International 2017. **43**: p. 7311–7320.
37. Bhattacharya, K. and P. Deb, *Hybrid nanostructured C-dot decorated Fe<sub>3</sub>O<sub>4</sub> electrode materials for superior electrochemical energy storage performance*. Dalton Trans., 2015. **44**: p. 9221–9229.
38. Li, H., et al., *Carbon nanodots: synthesis, properties and applications*. J. Mater. Chem. , 2012. **22**: p. 24230.
39. Beyth, N., et al., *Alternative Antimicrobial Approach: Nano-Antimicrobial Materials*. Evidence-Based Complementary and Alternative Medicine 2015. **2015**: p. 1–16.
40. Jin, H., et al., *Facile self-assembled magnetic nanoparticles/aptamer/carbon dots nanocomposites for highly sensitive up-conversion fluorescence turn-on detection of tetrodotoxin*. Talanta, 2018. **176**: p. 277–283.

41. Wang, M., et al., *A magnetic and carbon dot based molecularly imprinted composite for fluorometric detection of 2,4,6-trinitrophenol*. *Microchimica Acta*, 2019. **186**(86): p. 1-11.
42. Budnyk, A.P., et al., *Gd<sup>3+</sup>-Doped Magnetic Nanoparticles for Biomedical Applications*. *Journal of Spectroscopy*, 2018: p. 1-9.
43. Zhang, G., et al., *Gadolinium-Doped Iron Oxide Nanoprobe as Multifunctional Bioimaging Agent and Drug Delivery System*. *Adv. Funct. Mater.*, 2015. **25**: p. 6101–6111.
44. Zhang, H., et al., *Synthesis and characterization of Gd-doped magnetite nanoparticles*. *Journal of Magnetism and Magnetic Materials*, 2017. **423**: p. 386–394.
45. Douglas, F.J., et al., *Gadolinium-doped magnetite nanoparticles from a single-source precursor*. *RSC Adv.*, 2016. **6**: p. 74500–74505.
46. Huang, Y., et al., *Gadolinium-doped carbon quantum dots loaded magnetite nanoparticles as a bimodal nanoprobe for both fluorescence and magnetic resonance imaging*. *Magnetic Resonance Imaging*, 2020. **68**: p. 113–120.
47. Krysmann, M.J., et al., *Formation mechanism of carbogenic nanoparticles with dual photoluminescence emission*. *J Am Chem Soc*, 2012. **134**(2): p. 747-50.
48. Effenberger, F.B., et al., *Economically attractive route for the preparation of high quality magnetic nanoparticles by the thermal decomposition of iron(III) acetylacetonate*. *Nanotechnology*, 2017. **28**: p. 115603-115611.
49. Wu, W., Q. He, and C. Jiang, *Magnetic Iron Oxide Nanoparticles: Synthesis and Surface Functionalization Strategies*. *Nanoscale Res Lett* 2008. **3**: p. 397–415.
50. Huang, J.H., et al., *Investigation of the Growth Mechanism of Iron Oxide Nanoparticles via a Seed-Mediated Method and Its Cytotoxicity Studies*. *J. Phys. Chem. C* 2008. **112**: p. 15684–15690.
51. Wang, M., et al., *A magnetic and carbon dot based molecularly imprinted composite for fluorometric detection of 2,4,6-trinitrophenol*. *Microchimica Acta*, 2019. **186**: p. 86-97.
52. Polte, J., *Fundamental Growth Principles of Colloidal Metal Nanoparticles – a new Perspective*. *CrystEngComm*, 2015. **17**(36): p. 6809-6830.
53. Chang, J. and E.R. Waclawik, *Colloidal semiconductor nanocrystals: controlled synthesis and surface chemistry in organic media*. *RSC Adv.*, 2014. **4**(45): p. 23505-23527.
54. Xu, C. and S. Sun, *New forms of superparamagnetic nanoparticles for biomedical applications*. *Advanced Drug Delivery Reviews*, 2013. **65**(5): p. 732-743.
55. Thanh, N.T.K., N. Maclean, and S. Mahiddine, *Mechanisms of Nucleation and Growth of Nanoparticles in Solution*. *Chem. Rev.*, 2014. **114**: p. 7610–7630.

56. Vasimalai, N., et al., *Green synthesis of fluorescent carbon dots from spices for in vitro imaging and tumour cell growth inhibition*. Beilstein J. Nanotechnol., 2018. **9**: p. 530–544.
57. Schneider, J., et al., *Molecular Fluorescence in Citric Acid-Based Carbon Dots*. J. Phys. Chem. C, 2017. **121**(3): p. 2014–2022.
58. Reckmeier, C.J., et al., *Aggregated Molecular Fluorophores in the Ammonothermal Synthesis of Carbon Dots*. Chem. Mater., 2017. **29**: p. 10352–10361.
59. Ma, Y.J., et al., *Preparation and characterisation of multifunctional magnetic-fluorescent Fe<sub>3</sub>O<sub>4</sub>/carbon dots/silica composites*. Micro & Nano Letters, 2013. **8**(6): p. 302–304.
60. Xu, Y., et al., *Multifunctional Fe<sub>3</sub>O<sub>4</sub> Cored Magnetic-Quantum Dot Fluorescent Nanocomposites for RF Nanohyperthermia of Cancer Cells*. J. Phys. Chem. C, 2010. **114**: p. 5020–5026.
61. Chowdhuri, A.R., et al., *Carbon Dots Embedded Magnetic Nanoparticles@Chitosan @Metal Organic Framework as a Nanoprobes for pH Sensitive Targeted Anticancer Drug Delivery*. ACS Appl. Mater. Interfaces, 2016. **8**(26): p. 16573–16583.
62. Jin, J., et al., *Self-Assembly of Uniform Spherical Aggregates of Magnetic Nanoparticles through  $\pi$  -  $\pi$  Interactions*. Angew. Chem. Int. Ed. , 2001. **40**(11): p. 2135–2138.
63. Oh, W.K., H. Yoon, and J. Jang, *Size control of magnetic carbon nanoparticles for drug delivery*. Biomaterials, 2010. **31**: p. 1342–1348.
64. Fan, R.J., et al., *Photoluminescent carbon dots directly derived from polyethylene glycol and their application for cellular imaging*. Carbon, 2014. **71**: p. 87–93.
65. Deng, S., et al., *Interactions in fluorescent-magnetic heterodimer nanocomposites*. Nanotechnology, 2010. **21**: p. 145605–145611.
66. Craciun, A.M., et al., *Surface passivation of carbon nanoparticles with p-phenylenediamine towards photoluminescent carbon dots*. RSC Advances, 2016. **6**(62): p. 56944–56951.
67. Patil, U.S., et al., *In Vitro/In Vivo Toxicity Evaluation and Quantification of Iron Oxide Nanoparticles*. Int. J. Mol. Sci., 2015. **16**: p. 24417–24450.
68. Li, L., et al., *Comparative In Vitro Cytotoxicity Study on Uncoated Magnetic Nanoparticles: Effects on Cell Viability, Cell Morphology, and Cellular Uptake*. Journal of Nanoscience and Nanotechnology, 2012. **12**: p. 1–8.
69. Jung, J.H., J.H. Lee, and S. Shinkai, *Functionalized magnetic nanoparticles as chemosensors and adsorbents for toxic metal ions in environmental and biological fields*. Chem. Soc. Rev., 2011. **40**: p. 4464–4474.

70. Dong, X., et al., *Antibacterial effects of carbon dots in combination with other antimicrobial reagents*. PLoS ONE, 2017. **12**(9): p. 1-16.
71. Azam, A., et al., *Antimicrobial activity of metal oxide nanoparticles against Gram-positive and Gram-negative bacteria: a comparative study*. International Journal of Nanomedicine, 2012. **7**: p. 6003–6009.
72. Huang, K.C., et al., *Antimicrobial Applications of Water-Dispersible Magnetic Nanoparticles in Biomedicine*. Current Medicinal Chemistry, 2014. **21**(29).
73. Li, L. and T. Dong, *Photoluminescence Tuning in Carbon Dots: Surface Passivation or/and Functionalization, Heteroatom Doping*. J. Mater. Chem. C, 2018. **6**: p. 7944-7970.
74. Vallan, L., et al., *Supramolecular-enhanced charge-transfer within entangled polyamide chains as origin of the universal blue fluorescence of polymer carbon dots*. J. Am. Chem. Soc., 2018. **140**(40): p. 12862–12869.
75. Xie, Z., et al., *Synthesis and characterization of citrate-based fluorescent small molecules and biodegradable polymers*. Acta Biomaterialia, 2017. **50**: p. 361–369.

# **CHAPTER 5:**

## **Fluorescent chitosan-carbon dots based nanocomposites as nanocarriers for drug delivery applications**

*“The process of scientific discovery is, in effect,  
a continual flight from wonder”*

*Albert Einstein*

## 5.1 Introduction

To date, various organic carbon-rich sources including aromatic compounds, carbohydrates or biomass have been explored for the synthesis of C-dots via bottom-up methods, among which citric acid (CA) constitute the most popular precursor [1]. However, further use of filtration or oxidation treatment is crucial to break down a large carbon clusters from the post-synthesized carbogeous material into nanoscopic domains [2]. Besides that, nitrogen-rich precursors such as ethanolamine (EA) [1, 3], ethylenediamine [4, 5], urea [6, 7], amino acids [1, 8] or beta-amines [9] have been additionally used to uplift the quantum yield values of CA derived C-dots as well as enrich their surface in plentiful surface functional groups. To that end, the content of superficial moieties enable the interactions of C-dots with the bacterial or human cells, facilitate the cellular uptake and thus lower their cytotoxicity [10]. On the other side, strong fluorescence features of C-dots have been applied in the visualisation of either bacterial cells (i.e. *Staphylococcus aureus*, *Escherichia coli*, *Pseudomonas aeruginosa*, *Bacillus subtilis*) or mammalian cancer cells (i.e. HepG2, HeLa, U87, A549, L929, MCF-7) [8, 11-15]. Although the remarkable optical properties of C-dots suspensions have been widely reported, the preparation of nanopowders with strong luminescent properties in a solid-state form still constitute a challenge, due to the self-quenching effect of a large content of conjugated carbogenic domains with  $sp^2$ -hybridization [6]. To this end, the incorporation of highly crystalline C-dots into polymer matrix constitute one of the most popular strategies for preparation of multifunctional nanocomposites with notable photoluminescent properties, both in liquid as well as in a solid-state [16-24]. Among various natural polymers that are considered as a great hosting biomaterials for nanoparticles, chitosan brings a vast attention due to excellent biocompatibility, non-toxicity, eco-friendly nature, good adhesion and low cost of production, which overall facilitate its biomedical application as a carrier with antimicrobial finish for controlled drug delivery [18, 19, 25-29]. More specifically, the chitosan matrix provides a good base for encapsulation of small drug molecules owing to its ability to absorb a large amount of water and form a three-dimensional hydrogel networks [19, 26, 29]. The swelling behaviour of chitosan

hydrogels allow to mimic the structure of living tissues comprising a low interfacial tension with biological fluids [29]. In general, the presence of reactive hydroxyl and amino functional groups in the chitosan structure enhance its susceptibility to chemical modifications with a variety of chemical compounds via covalent linkage, electrostatic attraction or hydrogen bonding [21, 27, 29]. In general, chitosan-based drug carriers that are linked with fluorescent nanotracers are at the centre of attention because of their ability to visualize the path of traceable drug nanocarriers during the delivery to the target site in the body as well as the potential to investigate the biological processes inside the cells [16, 18, 19, 27, 29]. Therefore, the promising application of chitosan-carbon dots nanocomposites as traceable drug delivery nanocarriers constituted an inspiration for this project, which was focused on development of novel CS-CNPs nanocomposites and testing their potential to release a model drug from the chitosan matrix in a controlled manner.

## **5.2 Novelty and predominance over existing materials**

The novelty of this work is associated with three different aspects. First, a novel approach leading to the fabrication of highly fluorescent yellow nanopowder from previously reported crude CNP300, derived from the CA/EA precursors mixture at 300°C, was explored for the first time. The utilisation of severe oxidative conditions during the post-synthesis treatment facilitated the separation of green emissive colour from the crude CNP300 (referred hereafter as CNP300oxG) that constitute a blend of blue and green emissive molecular fluorophores. Although some reports noted the preparation of fluorescent C-dots-based powders [6, 30-38], the presented approach has not been explored yet and could open the doors for a large scale modification of existing fluorophore-rich carbon dots for promising application in photonics and optoelectronics [39]. Second, the fabrication of chitosan-based nanocomposites with C-dots covalently embedded into their polymer matrices proved that polymer network constitute an effective diluent matrix that suppresses an undesired self-quenching effect of C-dots. Besides some reports related to similar phenomenon [16-24], this work further explored the predominant optical properties of CS-CNPs, in contrast to pure C-dots. Third, the evaluation of antimicrobial properties of various C-dots derived



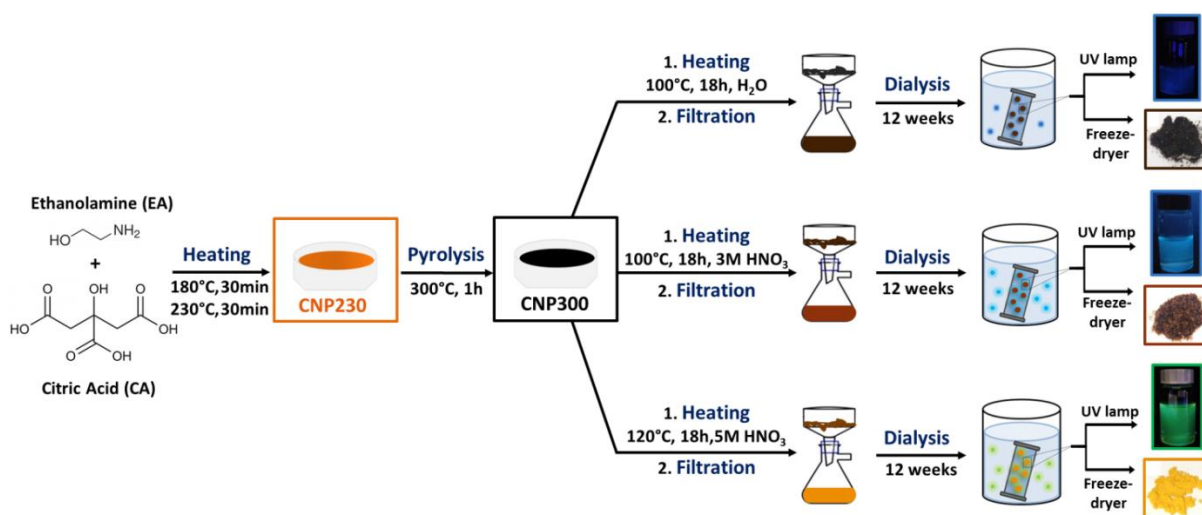
from either CA/EA precursors mixture or biomass against *Escherichia coli* and *Staphylococcus aureus* was undertaken in order to estimate their ability to enhance the antimicrobial effect of commonly used antibiotic (i.e. vancomycin).

Despite previous reports notifying that silica [40] or polymers [41] as solid matrices can facilitate the incorporation of C-dots and modulate their solid-state PL properties, those approaches cannot prevent the quenching effect that originates from the aggregation of carbon nanodomains [42]. Thus, resistant to self-quenching yellow nanopowders with broad emission capabilities overcome this limitation, both as powders or while incorporated into chitosan matrix. Additionally, in the midst of advantages is also an ease of adaptability of proposed oxidative treatment for other highly crystalline and fluorophore-rich C-dots, thereby expanding their optical properties in a solid-state form. Nevertheless, the use of dialysis method as a separation strategy constitute a limitation for a large scale production of CNP300oxG, while the filtration strategy is more time efficient.

## 5.3 Results and discussion

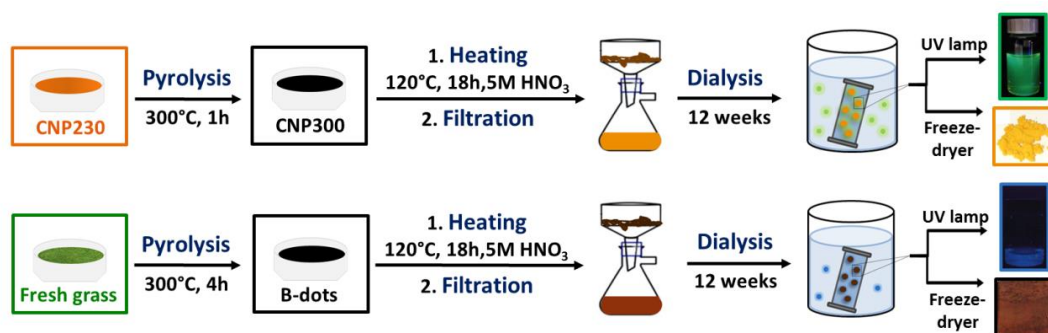
### 5.3.1 Carbon dots as a highly fluorescent nanotracers

The summary of synthetic and purification strategies that were utilised for the generation of various types of carbogenic nanoparticles (CNPs) derived from CA/EA precursors mixture is highlighted in **Figure 5.1**. After pyrolytic treatment of CNP230 at 300°C, the post-synthesized carbogeneous material was dissolved in distilled water, 3M HNO<sub>3</sub> or 5M HNO<sub>3</sub> and further heated at around 100°C, in order to break a large carbon clusters into nanosized particles. Afterwards, all suspensions were firstly filtered and then dialysed to remove unreacted nitric acid as well as to ensure a uniform size distribution of C-dots in the final nanomaterial. The final products were labelled as CNP300non-ox, CNP300oxB and CNP300oxG, while using water, 3M HNO<sub>3</sub> or 5M HNO<sub>3</sub> as dispersant. Although only blue-emissive behaviour was previously reported for CNP300 [43], the implementation of a harsh oxidative strategy led to fabrication of novel CNP300oxG with green luminescence in liquid-state as well as bright yellow colour of a solid powder.



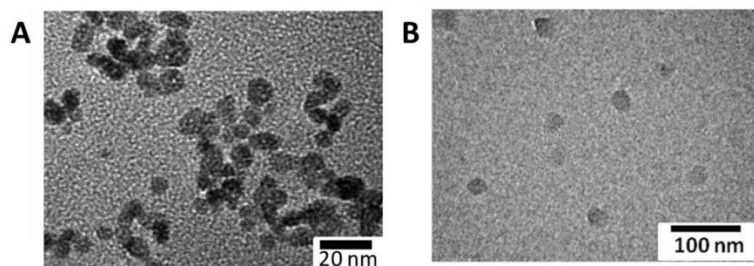
**Figure 5.1** The scheme presenting both the synthetic and purification routes that lead to fabrication of photoluminescent suspensions ( $\lambda_{\text{ex}}=365\text{nm}$ ) and powders derived from the pyrolytic treatment of CA/EA precursors mixture.

Nevertheless, in order to confirm whether the changes in the colour of CNP300ox nanopowders are associated with the presence of molecular fluorophores or the complete oxidation of carbogenic cores, the same to above mentioned strategy (**Figure 5.2**) was applied for the C-dots derived from the fresh grass (referred hereafter as B-dots), as an exemplary biomass source [3].



**Figure 5.2** The scheme showing the same synthesis and purification approaches applied for fluorophore-rich (CNP300) and biomass-derived (B-dots) photoluminescent suspensions and powders.

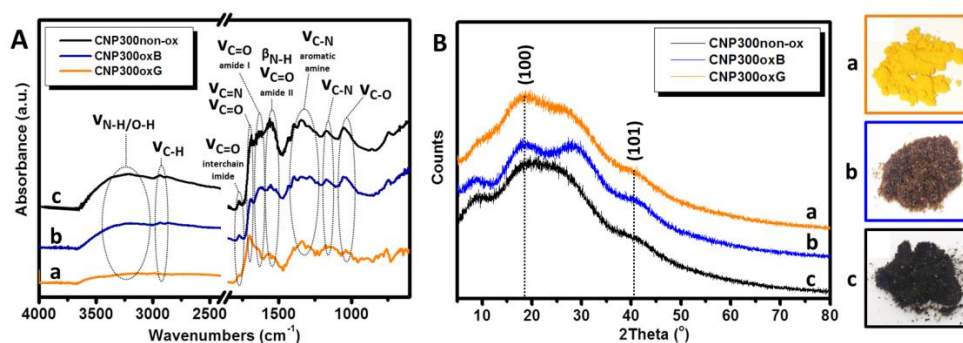
In regard to literature reports, the size of CNP300 is around 8 nm (**Figure 5.3A**). On the other side, an average diameter of B-dots is equal to 25-30 nm (**Figure 5.3B**). To that end, both types of C-dots show potential to be further utilised in biomedical applications [3, 43].



**Figure 5.3** TEM images of CNP300 (A - Adapted from [43]) and B-dots (B - Adapted from Ref. 3).

In order to assess the abundance of surface functional groups that have an impact on the fluorescence phenomena as well as enable conjugation of C-dots with drug molecules [1, 4], the FTIR spectra of CNP300non-ox, CNP300oxB and CNP300oxG were collected. Thus, as presented in **Figure 5.4A**, the absorption bands of CNP300 are centered around  $3549\text{-}3026\text{cm}^{-1}$  (O-H and N-H stretching vibrations of hydroxyl and amine groups),  $2980\text{-}2939\text{cm}^{-1}$  ( $-\text{CH}_2$  and  $-\text{CH}_3$  vibrations),  $1770\text{cm}^{-1}$  (C=O stretching of the imide group),  $1698\text{-}1689\text{cm}^{-1}$  (C=N and C=O),  $1635\text{-}1625\text{cm}^{-1}$  (C=O stretching of amide I),  $1553\text{-}1540\text{cm}^{-1}$  (C=O stretching of amide II and N-H bending),  $1457\text{-}1339\text{cm}^{-1}$  (C-N stretching of aromatic amine),  $1177\text{-}1173\text{cm}^{-1}$  (C-N stretching) and  $1053\text{-}1036\text{cm}^{-1}$  (C-O stretching), whereas the presence of amide and imide groups play a key role in their further coupling with biomolecules [4, 12, 14, 43-47]. In addition, the bands around  $1600\text{cm}^{-1}$  refer to characteristic peaks of benzene skeleton vibrations, thus confirm the presence of isolated  $\text{sp}^2$  clusters [1, 4, 14, 44, 45, 48]. In regard to assessment of the nature of their carbogenic cores that can be either highly graphitic or amorphous, the X-Ray Powder Diffraction analysis was conducted. To that end, the XRD patterns of CNP300non-ox, CNP300oxB and CNP300oxG (**Figure 5.4B**) demonstrate the presence of broad diffraction peaks centered at  $2\theta \approx 19.5^\circ$  together with a shoulder centered at  $2\theta \approx 41.4^\circ$ . In fact, these peaks are attributed to (100) and (101) planes, which correspond to a higher number of oxygen-rich groups [49]. Besides that, a significant broadening of diffraction peaks as well as the presence of two peaks maxima at  $19^\circ$  and  $30^\circ$  are related to both ultra-small size of CNP300ox as well as the change in the lattice structure of carbon dots due to their surface passivation [8, 50]. Overall, the XRD analysis confirmed that all CNP300 species are formed of a highly disordered and cross-linked polyaromatic carbon domains that are surrounded by

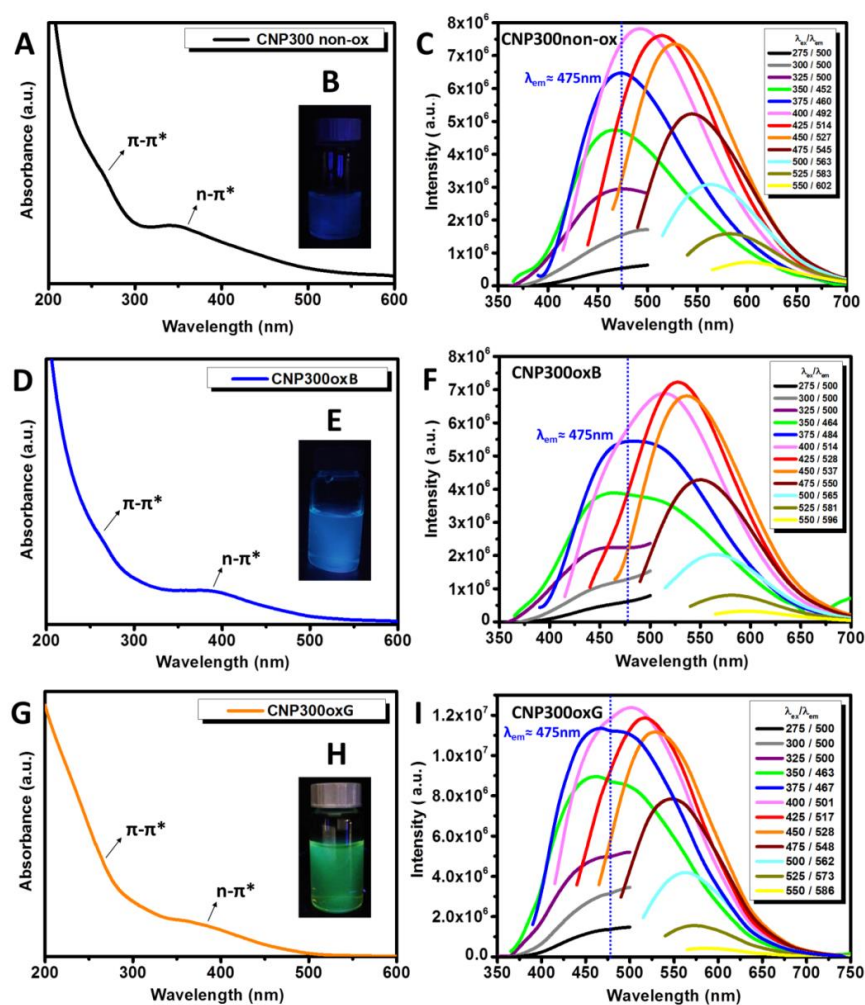
amorphous carbon network with plentiful oxygen-containing groups [1, 45, 48, 49, 51, 52].



**Figure 5.4** FTIR spectra (A) and XRD patterns (B) of CNP300oxG (a), CNP300oxB (b) and CNP300non-ox (c) together with the photos of corresponding powders.

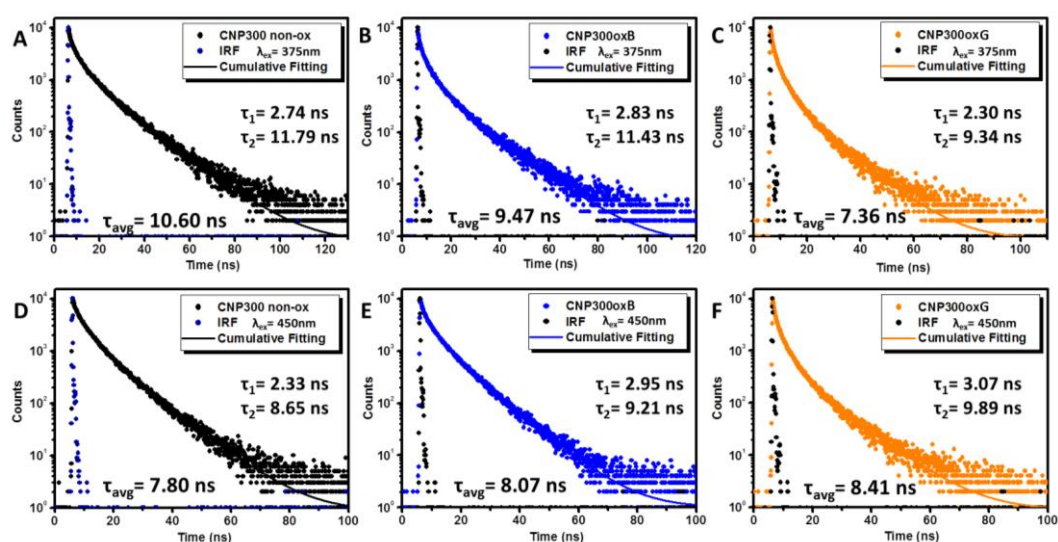
In reference to optical properties, the UV-Vis spectra of CNP300non-ox (**Figure 5.5A**) and CNP300ox (**Figure 5.5D,G**) further exhibit two absorption features: a less pronounced shoulder around 250 nm corresponding to  $\pi$ - $\pi^*$  transitions of C=C bond of polymeric carbon domains as well as a well-pronounced peaks ca. 350 nm (CNP300non-ox) or 390 nm (CNP300ox) attributed to  $n$ - $\pi^*$  edge transitions of carbonyl and amine surface functional groups [1, 4, 5, 14, 15, 47, 48, 53-56]. In general, the  $n$ - $\pi^*$  transitions are related to both nitrogen-doping as well as surface functionalization at the edge of carbon core, which impact on the enhanced emission of C-dots [46]. Under the UV irradiation the colours of aqueous dispersions of CNP300non-ox (**Figure 5.5B**) and CNP300oxB (**Figure 5.5E**) are dark and light blue, respectively, whereas for the CNP300oxG a bright green emission is observed (**Figure 5.5H**). In regard to literature reports, it has been reported that the CA-rich carbon dots display a blue fluorescence, while the significant N-doping can shift the luminescence of C-dots towards green-emissive region [1, 7, 8, 14, 45-48, 54, 55, 57]. The PL spectra of CNP300non-ox (**Figure 5.5C**), CNP300oxB (**Figure 5.5F**) and CNP300oxG (**Figure 5.5I**) revealed their dual emissive mode that is attributed to the excitation-independent phenomena at  $275\text{nm} \leq \lambda_{\text{ex}} \leq 375\text{nm}$  as well as the excitation-dependent phenomena at  $400\text{nm} \leq \lambda_{\text{ex}} \leq 550\text{nm}$ . Importantly, the  $\lambda_{\text{ex}}$  independent or dependent contributions arise from either the presence of molecular fluorophores or carbogenic cores, respectively [43, 46, 52]. In regard to literature reports, CA-based C-dots typically exhibit an excitation-dependent

photoluminescence behaviour, while the excitation-independent emission imply that the surface of carbon dots is relatively uniform and well-passivated [1, 4, 8, 14, 15, 45, 46, 48, 52, 54, 56]. Moreover, the characteristic red-shift of the emission peaks is observed from  $\lambda_{em} \approx 460$  nm (blue emission) to  $\lambda_{em} \approx 625$  nm (red emission) while the  $\lambda_{ex}$  is above 375 nm [4, 43]. This phenomenon may be attributed to the variations in the distribution of surface emissive trap sites formed by diversified functional groups as well as different particle sizes [48, 52, 56]. Overall, the optical properties of all three species are relatively similar implying the intrinsic relationship among particular nanoemitters. On the other side, the only difference related to the colour of luminescence emission suggest the variations in the sizes CNP300 or diverse extent of the surface defects [54].



**Figure 5.5** Liquid-state UV-Vis spectra (A,D,G), photos under UV illumination (B,E,H) and PL spectra(C,F,I) of 0.1 mg/mL aqueous dispersions of CNP300non-ox (A-C), CNP300oxB (D-F) and CNP300oxG (G-I).

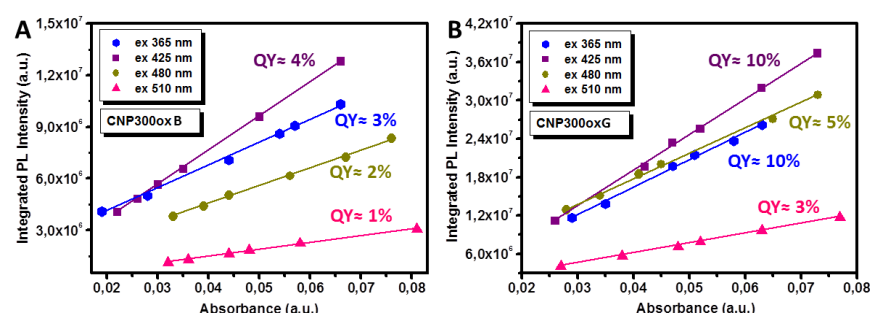
Furthermore, the fluorescence decay dynamics of CNP300non-ox (**Figure 5.6A,D**), CNP300oxB (**Figure 5.6B,E**) and CNP300oxG (**Figure 5.6C,F**) were investigated at different emission wavelengths. In all cases, the PL decay curves were fitted with bi-exponential function while the calculated average PL lifetimes ( $\tau_{avg}$  = 7.36-10.60 ns) were prolonged in contrast to previously reported for C-dots derived from CA and various amino acids ( $\tau_{avg}$  = 7.2ns) [46, 50]. Among all, the  $\tau_{avg}$  = 10.06 ns for CNP300non-ox (**Figure 5.6A**) constitute an agreement with previous reports related to CA-derived C-dots [14]. The elemental analysis of prepared CNP300oxB determined their composition as 45.74%C, 13.12%N, 5.92%H and 35.22%O, while the elemental composition of CNP300oxG indicated the content of 48.17%C, 13.83%N, 5.30%H and 32.70%O. These results are relevant to elemental composition of previously reported CA/amine derived carbon dots and suggest that the larger content of oxygen and hydrogen in CNP300oxB, which may suggest the significant content of citrazinic acid (CTA) molecular fluorophore with the maximum emission peak recorded at  $\lambda_{ex}$ =375 nm [9]. Thus, it is believed that the lack of post-synthesis oxidative treatment impact on dominant contribution of CTA and prolonged PL lifetime for CNP300non-ox at  $\lambda_{ex}$ =375 nm (**Figure 5.6A**). On the other hand, the prolonged PL lifetime of CNP300oxG at  $\lambda_{ex}$ =450 nm (**Figure 5.6F**) may correspond to the surface states of C-dots enriched in plentiful amine groups, as confirmed by the elemental analysis results [4].



**Figure 5.6** Fluorescence lifetime decay curves of 0.1 mg/mL aqueous dispersions of CNP300non-ox, CNP300oxB and CNP300oxG at  $\lambda_{ex}$  = 375 nm (A,B,C) and  $\lambda_{ex}$  = 450 nm (D,E,F).



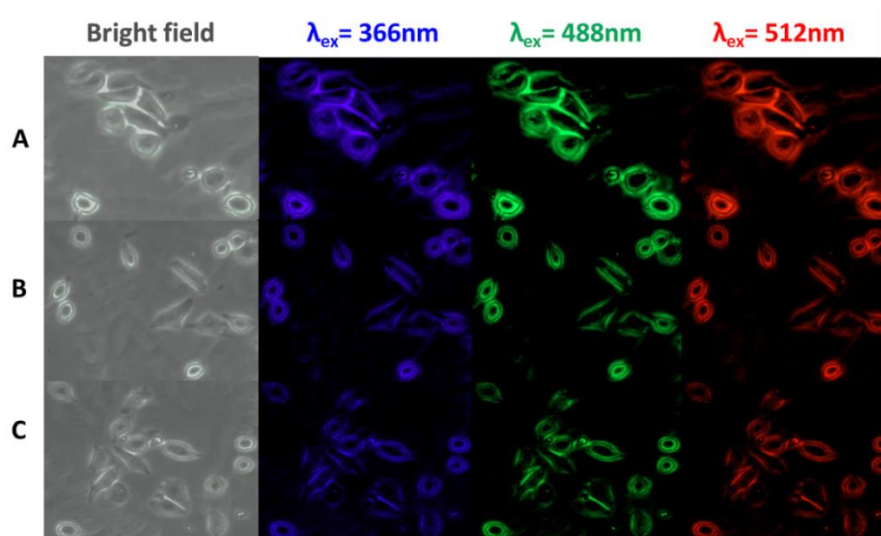
Moreover, the experimental evaluation of quantum yields (QY) of CNP300oxB (**Figure 5.7A**) and CNP300oxG (**Figure 5.7B**) was done in accordance to reference dyes with well-known optical efficiencies, such as anthracene ( $\lambda_{\text{ex}} = 365$  nm), fluorescein ( $\lambda_{\text{ex}} = 425$  nm), rhodamine 6G ( $\lambda_{\text{ex}} = 480$  nm) and rhodamine B ( $\lambda_{\text{ex}} = 510$  nm) (Appendix, **Figure A9**). In regard to the literature statements, C-dots derived only from CA are characterized by the QY ranging from 2.2% up to 3.2% at  $\lambda_{\text{ex}} = 365$  nm [15, 52]. The consistency with these values for CNP300oxB may be subjected to prolonged dialysis procedure, which led to removal of a large amount of CTA molecular fluorophore. On the other side, CNP300oxG with QY $\approx$ 10% at  $\lambda_{\text{ex}} = 365$  nm are characterized by higher optical efficiency that several carbon dots derived from CA and amino acids (3.1%  $\leq$  QY  $\leq$  8.9%,  $\lambda_{\text{ex}} = 360$  nm) or CA/EA-derived CNP300 with QY $\approx$ 4% at  $\lambda_{\text{ex}} = 365$  nm or CAEA-dots with QY $\approx$ 8.5% at  $\lambda_{\text{ex}} = 323$  nm [1, 8, 43, 46]. In contrast to CNP300oxB, a significant increment of the QY for CNP300oxG may be attributed to larger nitrogen content [15]. Nevertheless, the analysis of the QY values as well as the results gathered from elemental analysis leads to conclusion that the increment of N content has a substantial impact on higher PL quantum yields as well as prolonged PL lifetime [52].



**Figure 5.7** The plots of integrated PL intensity of CNP300oxB (A) and CNP300oxG (B) as a function of optical absorbance at 365 nm, 425 nm, 480 nm and 510 nm with calculated quantum yield values.

The above discussed PL spectra as well as fluorescence lifetime decays confirmed that CNP300 possess promising for cellular imaging optical features, which have a significant importance in development of traceable drug nanocarriers. Furthermore, the bioimaging experiments proved that the uptake of CNP300oxG (**Figure 5.8A**), CNP300oxB (**Figure 5.8B**) and CNP300non-ox (**Figure 5.8C**) impacted on the illumination of HeLa cells with blue, green and red colours, upon their excitation at 366 nm, 488 nm and 512 nm, respectively. In contrast, no visible luminescence was

detected in the control cells under the same conditions. Overall, the fluorescence microscopy images show the potential application of CNP300 as bioimaging probes [8, 14, 15], due to the multicolour emission capabilities that have been widely reported for CA-derived C-dots [8, 12, 14, 15, 44, 47, 52, 56].

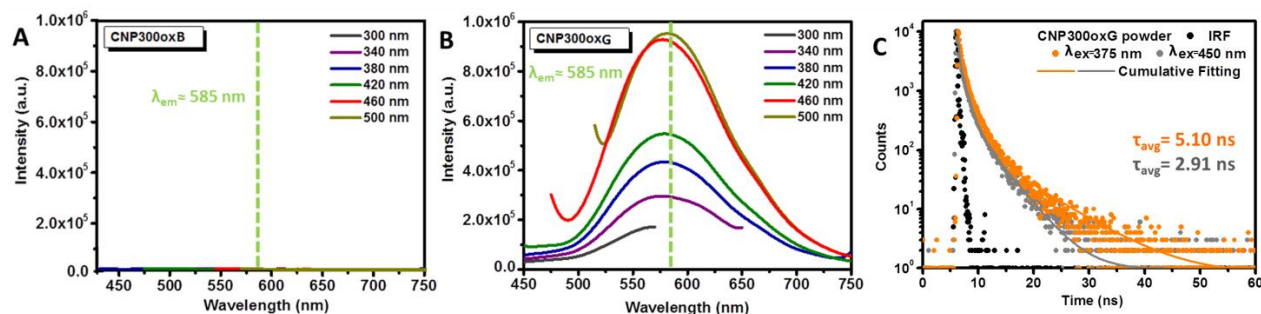


**Figure 5.8** Fluorescent microscope images of HeLa cancer cell line incubated with 50 µg/mL of CNP300oxG (A), CNP300oxB (B) and CNP300non-ox (C) under the bright field, UV, blue and green excitation wavelengths.

Besides liquid-state photoluminescence properties, the CNP300oxG nanopowder show a remarkable optical features in a solid-state form. In detail, the solid-state emission spectra of CNP300oxG demonstrates the excitation-wavelength independent PL behaviour at  $300\text{nm} \leq \lambda_{\text{ex}} \leq 500\text{nm}$ , with all of the emission peaks centered around 585 nm, as displayed in **Figure 5.9B**. Importantly, it has been reported that the larger content of oxygen-rich and nitrogen-rich functional groups hinder the growth of  $\text{sp}^2$ -hybridized nanodomains during the carbonization process, thereby can play an important role in suppressing the quenching of C-dots in a powder form [6]. On the contrary, CNP300oxB do not reveal the PL properties in a powder form (**Figure 5.9A**) and this phenomenon may be related to highly crystalline structure of C-dots as well as a significant content of  $\text{sp}^2$ -hybridized nanodomains that are prone to the self-quenching [6]. In complementary analysis, the solid-state fluorescence lifetime dynamics of CNP300oxG nanopowder (**Figure 5.9C**) revealed the multiexponential property, which suggest that different emissive sites may be present on the surface of

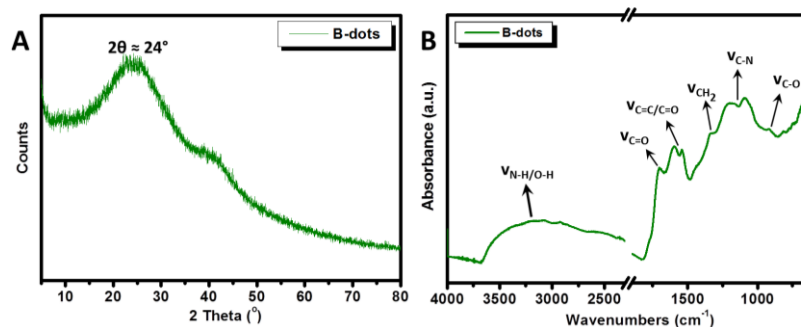


CNP300oxG [14]. Overall, the prolonged  $\tau_{\text{avg}}$  at  $\lambda_{\text{ex}} = 375$  nm suggest the predominance of CNP300oxG nanopowder above many organic dyes.



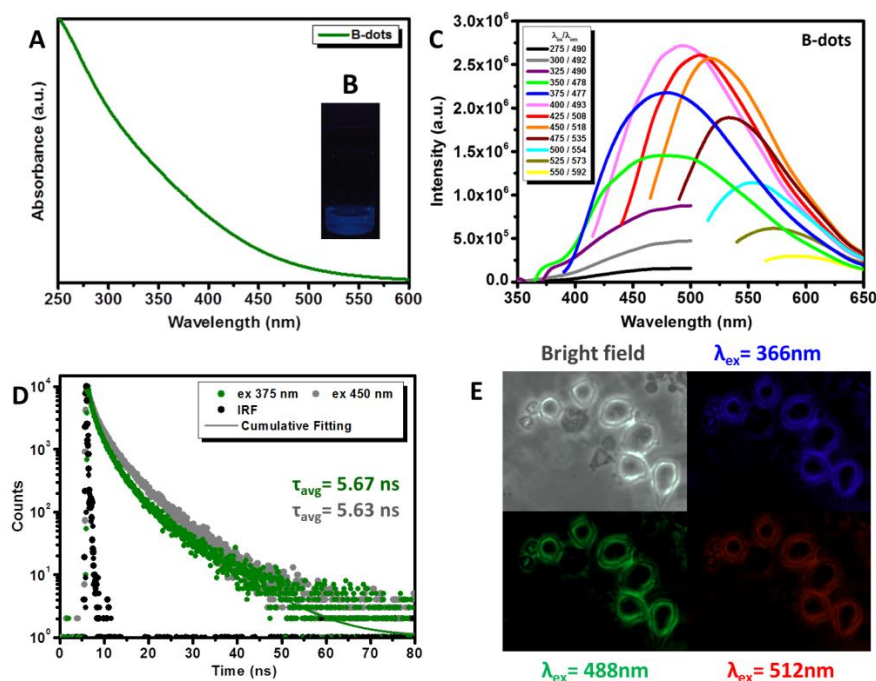
**Figure 5.9** The solid-state PL spectra of CNP300oxB (A) and CNP300oxG (B) together with the PL lifetime decays of CNP300oxG recorded at  $\lambda_{\text{ex}} = 375$  nm and  $\lambda_{\text{ex}} = 450$  nm (C).

Subsequently, the analysis of structural and optical properties of grass-derived B-dots was undertaken in order to determine whether harsh oxidative treatment is changing the colour of fluorophore-rich C-dots or could be also applied for carbon dots derived from the crude biomass source. Thus, as presented in **Figure 5.10A**, the XRD pattern of B-dots display a broad diffraction peak around  $2\theta \approx 24^\circ$ , which indicates the amorphous nature of B-dots [58, 59] and constitute an agreement with previous reports [60]. In addition, the analysis of their FTIR spectra (**Figure 5.10B**) proved the presence of absorption bands at 3590-3056  $\text{cm}^{-1}$  (O-H stretching vibration), 1720  $\text{cm}^{-1}$  (C=O stretching vibration), 1635  $\text{cm}^{-1}$  (C=C bending vibration), 1314  $\text{cm}^{-1}$  ( $\text{CH}_2$  bending vibration), 1141  $\text{cm}^{-1}$  (C-N stretching vibration) and 1036  $\text{cm}^{-1}$  (C-O stretching vibration), which play an important role in combination of nanoscopic particles with other molecules [58, 61-64].



**Figure 5.10** XRD pattern (A) and FTIR spectra (B) of B-dots.

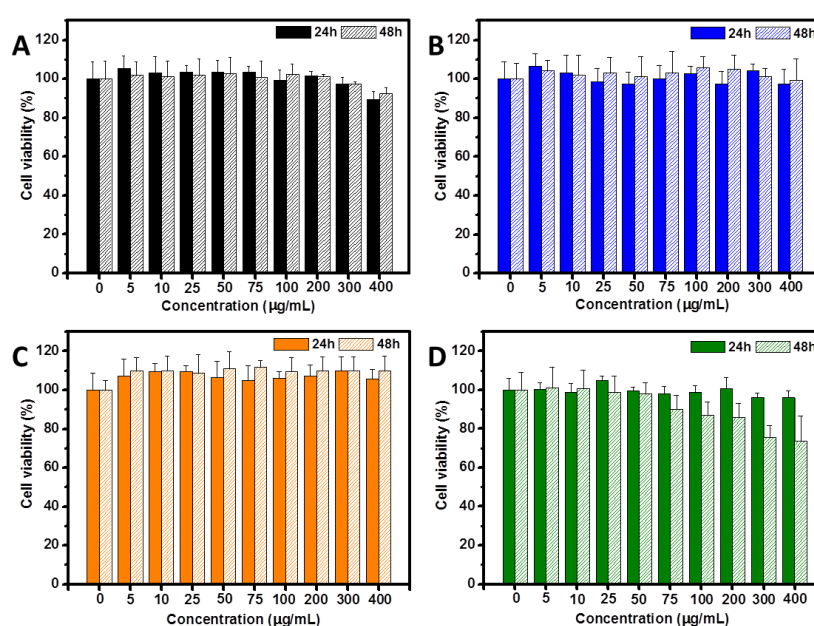
In reference to optical properties of B-dots, the UV-Vis absorption spectra (**Figure 5.11A**) displays a broad absorption band that is relevant to previous report regarding the preparation of blue-emissive C-dots (**Figure 5.11B**) from leaves [65], whereas a lack of obvious absorption peak suggest relatively broad size distribution of carbon nanodomains [57]. On the other side, the PL spectra (**Figure 5.11C**) reveals an excitation-wavelength dependent fluorescence behaviour that may be related to either the presence of emissive traps on the B-dots surface or variable particles size [66]. In addition, the average fluorescence lifetime (**Figure 5.11D**) being around 5.65 ns is relevant to former ones for C-dots derived from potatoes ( $\tau = 5.65$  ns) and significantly longer than for C-dots derived from other natural sources, including the lotus leaves ( $\tau = 2.33$  ns), pine needles ( $\tau = 2.62$  ns), oriental plane leaves ( $\tau = 2.54$  ns) or Boswellia bark extract ( $\tau = 4.2$  ns) [65, 67]. In contrast to CNP300, a significantly shorter average PL lifetime reflect an ultrafast exciton recombination processes, while electron transfer achieved in nanoseconds is highly desired in bioimaging applications [67]. Therefore, B-dots have a significant potential to be used as fluorescent probes in cellular imaging application, while exhibit a multicolour imaging capabilities at different excitation wavelengths (**Figure 5.11E**) [67].



**Figure 5.11** The UV-Vis spectra (A), photo under the UV illumination (B), PL spectra (C) and PL lifetime decays (D) of aqueous dispersion of B-dots with concentration of 0.1 mg/mL. The fluorescence microscopy images (E) showing the multicolour nature of B-dots after being internalized by HeLa cells.

In order to assess the suitability of all above mentioned C-dots for potential biomedical applications, their *in vitro* toxicity against representative HeLa cancer cell line was evaluated with the use of MTT assay. As demonstrated in **Figure 5.12A**, the negligible fall of cell viability was observed for CNP300non-ox, which resulted in total cell viability of 90.36% after 24 hours and 92.52% after 48 hours of incubation. On the other side, the study involving the CNP300oxB (**Figure 5.12B**) and CNP300oxG (**Figure 5.12C**) demonstrated that the HeLa cells viability was kept above 96% after their exposure to CNP300ox with concentration up to 400  $\mu\text{g/mL}$ , thus confirmed the negligible cytotoxicity of CNP300ox [14, 15, 52]. It has been previously reported that the incubation of HeLa cells with CA/EA-derived C-dots for 48 hours impacted on the viability exceeding the 90%, at concentration as high as 600  $\mu\text{g/mL}$  [56]. In addition, other research groups reported that the incubation of HeLa cells with CA-derived C-dots at concentrations ranging from 100 to 800  $\mu\text{g/mL}$  resulted in either 80% cells viability or more than 90% cells viability, depending on the selected amine-based precursor [8, 48]. On the other hand, the overall cell viability of 96% was observed for

HeLa cells incubated with B-dots solutions for 24 hours (**Figure 5.12D**), at concentrations up to 400  $\mu\text{g/mL}$ . Nonetheless, the incubation for 48 hours under the same conditions caused the reduction of cells viability up to 73.65%, which presumably may be related to larger size of B-dots than CNP300 as well as their affinity to aggregate. Nevertheless, these results are still in agreement with previous reports and indicate that the incorporation of C-dots do not have a significant impact on the growth of HeLa cells [12, 44, 55]. Overall, the CNP300 with abundant content of surface functional groups demonstrate better permeability through the cell membrane [48].



**Figure 5.12** The MTT assay results presenting the viability of HeLa cells incubated with various concentrations of CNP300non-ox (A), CNP300oxB (B), CNP300oxG (C) and B-dots (D) for 24 and 48 hours. The data is expressed as a mean  $\pm$  SD of triple experiments while percentage of cell viability is represented comparatively to untreated controls.

Besides evaluation of cytotoxicity against mammalian cells, the antimicrobial studies were carried out against Gram-negative *Escherichia coli* and Gram-positive *Staphylococcus aureus* to estimate the extent of antibacterial effect of CNP300 and B-dots. Thus, the results presented in **Table 5.1** demonstrated that carbon dots enriched in plentiful surface functional groups, such as CNP300oxB, CNP300oxG and B-dots, do not cause an instant killing of microorganisms, while their antimicrobial efficiency after

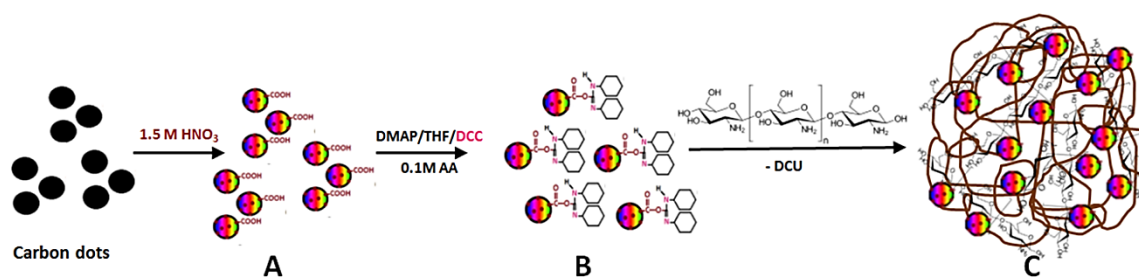
24 hours is above 99.9%. To that end, it is believed that the presence of positively charged end groups ( $-\text{NH}_3^+$ ) on the C-dots pavement is especially favoured by negatively charged surface of *E.coli* and impact on faster antimicrobial action after 2 hours [68]. Overall, these results proved that C-dots can efficiently inhibit the bacterial growth and reduce the possible risks imposed on public health and environment [18, 28, 29, 69].

**Table 5.1** The results from antimicrobial studies presenting the reduction of *E.coli* and *S.aureus* colonies incubated with various C-dots for 24 hours at 37°C

Nanoparticles	<i>Escherichia coli</i>		<i>Staphylococcus aureus</i>	
	% decrease		% decrease	
	2h	24h	2h	24h
B-dots	95.8	99.9	80.7	99.9
CNP300 non-ox	99.6	99.8	99.8	99.9
CNP300oxB	99.0	99.9	89.2	99.9
CNP300oxG	99.3	99.9	76.1	99.9

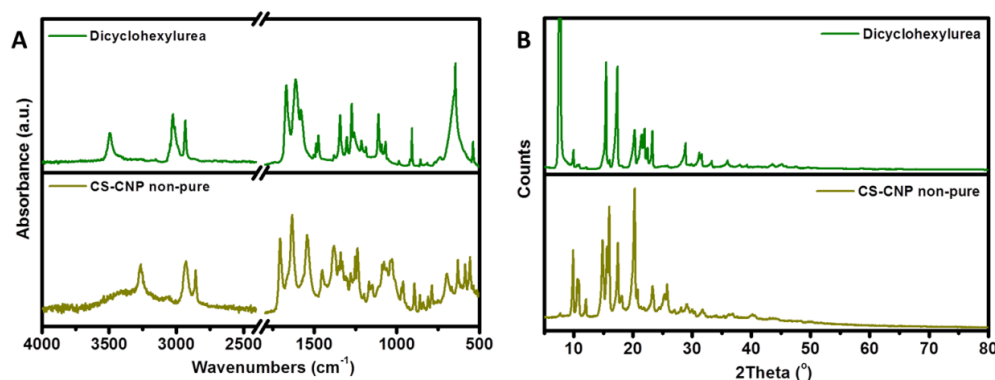
### 5.3.2 Biocompatible nanocomposites based on chitosan and carbon dots

The selected synthesis procedure and utilized precursors mixture for the fabrication of CNP300 have an impact on the content of carboxyl, amino and hydroxyl functional groups on their surface. The abundance of various moieties on CNP300 surface not only impart their dispersibility in aqueous solvents but also allow their further conjugation with various biomolecules (i.e. chitosan) via covalent interactions between  $-\text{COOH}$  and  $-\text{NH}_2$  functional groups, which lead to the generation of amide linkage via carbodiimide chemistry [70]. Thus, the same approach was applied for fabrication of novel types of chitosan-based nanocomposites with embedded into polymer matrix either CNP300oxB (CS-CNP300oxB NCs) or CNP300oxG (CS-CNP300oxG NCs), as schematically presented in **Figure 5.13**.



**Figure 5.13** Scheme presenting a coupling reaction between fluorescent carbon dots (A) and DCC reagent (B) followed by precipitation of DCU side product and generation CS-CNP nanocomposite (C).

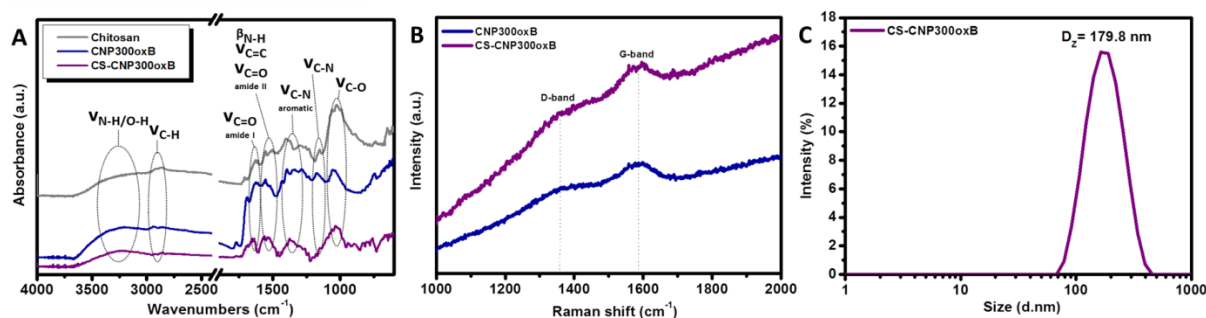
Overall, the significant drawback of the reactions involving the use of carbodiimide reagents is the precipitation of a white side product named as dicyclohexylurea (DCU) during the synthesis process. Therefore, the developed synthetic procedure needed to be carefully optimized to efficiently eliminate the DCU content from the post-reaction mixture. Thus, for each batch of products the FTIR spectra (**Figure 5.14A**) and XRD patterns (**Figure 5.14B**) were recorded to evaluate the purity of CS-CNP300ox. The non-pure products which matched the FTIR spectra (**Figure 5.14A**) and XRD pattern (**Figure 5.14B**) of dicyclohexylurea (DCU) were further discarded.



**Figure 5.14** FTIR spectra (A) and XRD patterns (B) of non-pure CS-CNP nanocomposite (dark yellow colour) containing a co-product dicyclohexylurea (green colour).

The FTIR spectra of pure CS-CNP300oxB (**Figure 5.15A**) show plentiful absorption bands around  $3350\text{cm}^{-1}$  ( $-\text{OH}$  and  $-\text{NH}_2$  stretching vibrations),  $2869\text{cm}^{-1}$  ( $-\text{CH}_2$  and  $-\text{CH}_3$  vibrations),  $1695\text{cm}^{-1}$  ( $\text{C}=\text{O}$  amide I stretching),  $1652\text{cm}^{-1}$  ( $\text{C}=\text{C}$  aromatic stretching),  $1557\text{cm}^{-1}$  ( $\text{N}-\text{H}$  bending vibration and  $\text{C}=\text{O}$  amide II stretching),  $1374\text{cm}^{-1}$  ( $\text{C}-\text{N}$  aromatic stretching) and  $1029\text{cm}^{-1}$  ( $\text{C}-\text{O}$  stretching), similarly to the FTIR spectra of its

counterparts [71]. However, the absorption band of CNP300oxB at  $1625\text{cm}^{-1}$  is shifted towards  $1652\text{cm}^{-1}$  in CS-CNP300oxB, which indicates the increment of C=C stretching arising from conjugated carbon domains [16, 19, 26]. Moreover, an appearance of characteristic for chitosan absorption bands in the FTIR spectrum of CS-CNP300oxB suggests the successful introduction of carbon dots into polymeric matrix [24]. On the other side, the disappearance of the absorption bands around  $1708\text{ cm}^{-1}$  for CS-CNP300oxB NCs may be related to successful amidation reaction between  $-\text{COOH}$  groups of CNP300oxB as well as the amine groups of chitosan [24]. The Raman spectra of both CNP300oxB and CS-CNP300oxB nanocomposite are displayed in **Figure 5.15B**. Although, the presence of only part of distinct characteristic D band (around  $1354\text{ cm}^{-1}$ ) and G band (around  $1595\text{ cm}^{-1}$ ) can be directly detected, the intensity ratio between D and G band is not well pronounced. Thus, this phenomenon imply an imperfect carbonization and the presence of amorphous structures, which may correspond to non-carbonized components, including polymer chains or plentiful surface functional groups [51]. Moreover, the presence of more apparent G bands and less pronounced D bands implied that mainly  $\text{sp}^2$  carbon networks with some  $\text{sp}^3$  hybridized carbons constitute a part of carbogenic nanoparticles structure [44]. In addition, the DLS analysis confirmed that the CS-CNP300oxB have a hydrodynamic size around  $179.8\text{ nm}$  in water (**Figure 5.15C**).

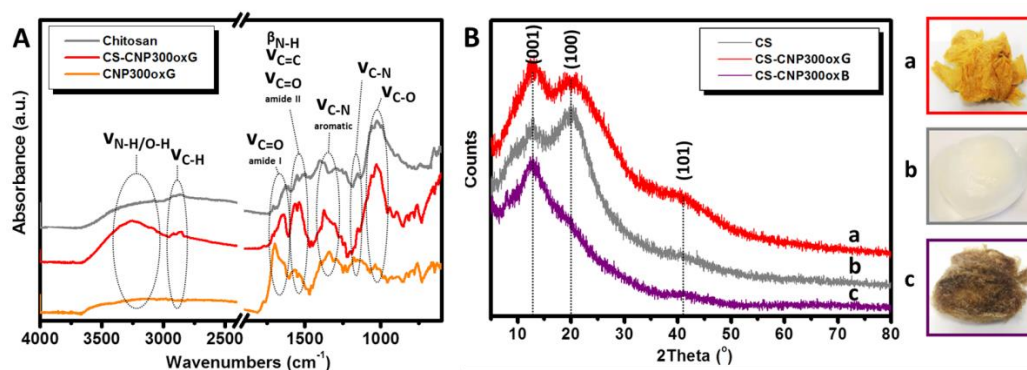


**Figure 5.15** FTIR spectra (A), Raman spectra (B) and the liquid-state particles size distribution measured by DLS (C) for CS-CNP300oxB and CNP300oxB.

Similarly, the FTIR spectra of pure CS-CNP300oxG (**Figure 5.16A**) demonstrated the abundance of absorption bands, corresponding to the hydroxyl and amine groups ( $3259\text{cm}^{-1}$ ),  $-\text{CH}_2$  and  $-\text{CH}_3$  groups ( $2851\text{cm}^{-1}$ ), C=O stretching of amide I ( $1644\text{cm}^{-1}$ ),



C=O/C=C stretching and N-H bending ( $1567\text{cm}^{-1}$ ), C=O stretching of amide II ( $1537\text{cm}^{-1}$ ), C-N aromatic stretching ( $1373\text{cm}^{-1}$ ), C-O stretching ( $1030\text{cm}^{-1}$ ) [23]. In contrast to pure chitosan as well as CNP300oxG, the absorption band of CS-CNP300oxG around  $1700\text{cm}^{-1}$  is red shifted towards lower frequencies. Therefore, this phenomenon may be related to the hydrogen bonding between the functional groups of chitosan and carbogenic nanoparticles [23, 71]. In addition, the enhancement of the absorption band around  $1567\text{cm}^{-1}$  of CS-CNP300oxG in contrast to its counterparts clearly prove the formation of covalent bonding between chitosan monomers and carbogenic nanoparticles [52]. On the basis of XRD patterns (**Figure 5.16B**) of CS-CNP300oxG nanocomposite and chitosan (**Figure 5.16a-b**) a significantly wide diffraction peaks in the range of  $20^\circ$  to  $40^\circ$  suggest the presence of highly cross-linked polymer skeletons [51]. In detail, the intense peak around  $20^\circ$  arises from enlarged interlayer spacing caused by steric hindrance from amorphous  $\text{sp}^3$  carbon as well as the abundant surface functional groups in both chitosan and CS-CNP300oxG [6]. Otherwise, a well pronounced diffraction peaks around  $14^\circ$  for CS-CNP300oxB (**Figure 5.16c**) corresponds to the ordered structures of graphite carbon, thereby highlight the highly crystalline nature of this type of nanocomposite [51].



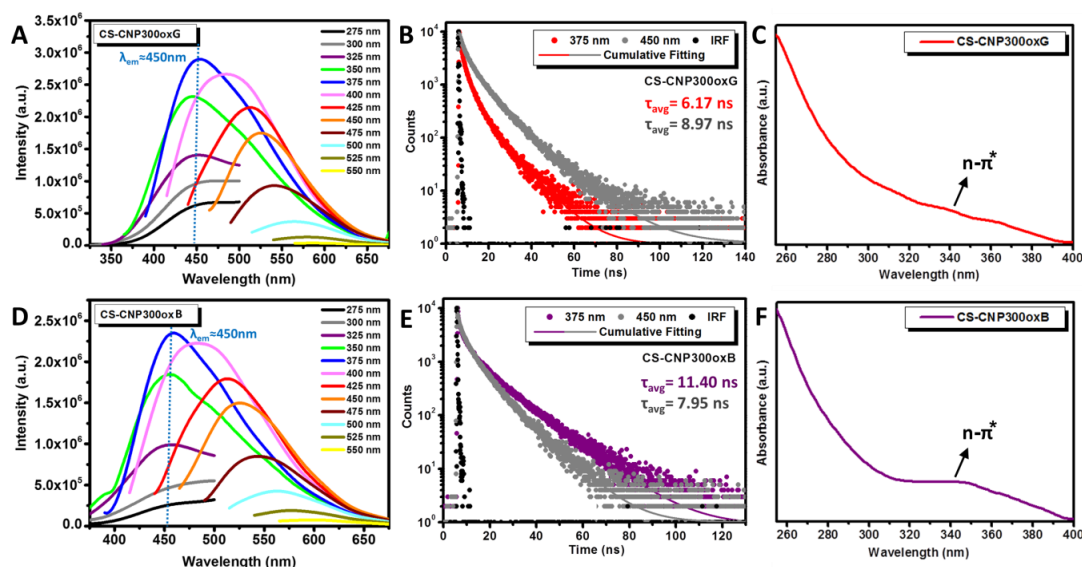
**Figure 5.16** FTIR spectra of CS-CNP300oxG and its components (A) together with the XRD patterns (B) of CS-CNP300oxG (a), chitosan (b) and CS-CNP300oxB (c) along with the photos of their powders.

In reference to optical properties, the UV-Vis absorption spectra of CS-CNP300oxB (**Figure 5.17F**) displays a broad absorption band centered around 350 nm, which originates from  $n\text{-}\pi^*$  transitions of oxygen-rich and nitrogen-rich edge groups as well as  $\pi\text{-}\pi^*$  transitions in  $\text{sp}^2$ -hybridized carbogenic domains [6, 14, 26]. On the other side, a lack of distinctive absorption band in the UV-Vis spectra of CS-CNP300oxG (**Figure**



**5.17C)** may be related to amorphous character of this nanocomposite (**Figure 5.16a**), while the crystalline structure of CS-CNP300oxB (**Figure 5.16c**) have higher content of  $sp^2$ -hybridized carbon domains. The PL spectra (**Figure 5.17A,D**) and fluorescence decay dynamics (**Figure 5.17B,E**) of CS-CNP nanocomposites were investigated at different emission wavelengths. In general, the incorporation of carbon dots into polymer matrix resulted in diminished PL intensity of recorded emission spectra for CS-CNP300oxG (**Figure 5.17A**) and CS-CNP300oxB (**Figure 5.17D**) in contrast to the pure CNP300oxB (**Figure 5.5F**) and CNP300oxG (**Figure 5.5I**) components. Additionally, mixed excitation-independent PL character ( $275\text{nm} \leq \lambda_{\text{ex}} \leq 375\text{nm}$ ) and the excitation-dependent feature ( $400\text{nm} \leq \lambda_{\text{ex}} \leq 550\text{nm}$ ) together with biexponential behaviour of CS-CNP NCs imply the presence of two different emissive sites: molecular states induced by covalently bonded onto C-dots surface molecular fluorophores as well as surface states arising from the content of N-rich functional groups on C-dots pavement [46]. The general comparison between the PL decay dynamics of pure CNP300ox and CS-CNP NCs revealed that the incorporation of CNP300oxB with dark brown colour and  $\tau_{\text{avg}} = 9.47\text{ns}$  at  $\lambda_{\text{ex}} = 375\text{ nm}$  (**Figure 5.6B**) into chitosan matrices resulted in prolongement of the average PL lifetime of CS-CNP300oxB up to  $11.40\text{ ns}$  (**Figure 5.17E**). Presumably, this phenomenon can be related to reduced quenching effect between  $sp^2$  carbogenic domains while using chitosan matrix as a dispersant. Interestingly, no significant differences were observed at  $\lambda_{\text{ex}} = 450\text{ nm}$  for the same materials, likely due to the occurrence of the highest emission peak of CTA fluorophore at  $\lambda_{\text{ex}} = 375\text{ nm}$  (**Figure 5.17D**). On the other hand, the green-emissive mode of CNP300oxG corresponds to prolonged PL lifetime ( $\tau_{\text{avg}} = 8.41\text{ns}$ ) at longer excitation wavelengths ( $\lambda_{\text{ex}} = 450\text{ nm}$ ) (**Figure 5.6F**), which is only insignificantly increased ( $\tau_{\text{avg}} = 8.97\text{ns}$ ) for CS-CNP300oxG (**Figure 5.17B**) under the same conditions. However, at  $\lambda_{\text{ex}} = 375\text{ nm}$  the CS-CNP300oxG is characterized by the  $\tau_{\text{avg}} = 6.17\text{ns}$  (**Figure 5.17B**), which reveal the quenching effect of luminescence characteristics of pure carbon dots counterparts with  $\tau_{\text{avg}} = 7.36\text{ns}$  (**Figure 5.6D**). In fact, the prolonged  $\tau_{\text{avg}}$  of CS-CNP300oxG at  $\lambda_{\text{ex}} = 450\text{ nm}$  (**Figure 5.17B**) reveal the substantial contribution of surface states upon longer excitation wavelengths. On the other side, its shorter PL lifetime at

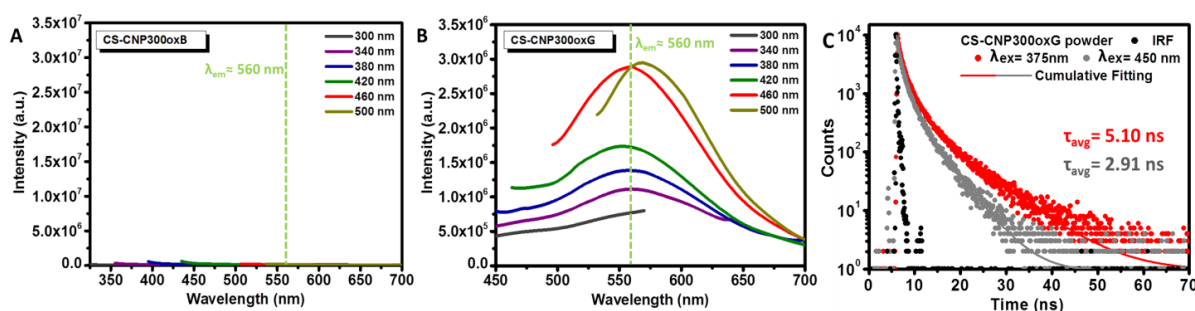
$\lambda_{\text{ex}}=375$  nm (**Figure 5.17B**) is closely associated with both surface domains as well as carbon-core [4]. Overall, the PL lifetime values for both CNP300ox as well as CS-CNPs NCs are significantly longer than the auto cell fluorescence (1-3 ns), which give a promise for utilizing them as selective nanoprobe for PL lifetime imaging applications [50].



**Figure 5.17** PL spectra (A,D), PL lifetime decays (B,E) and UV-Vis spectra (C,F) of CNP300oxB and CS-CNP300oxG. The concentration of aqueous dispersions was equal to 0.1 mg/mL.

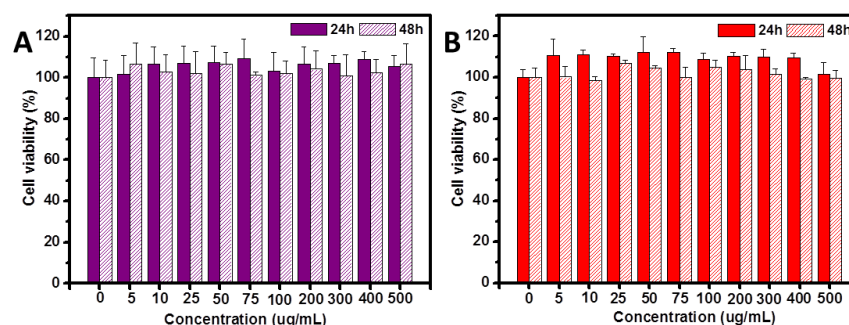
Furthermore, the solid-state PL spectra of CS-CNP300oxG (**Figure 5.18B**) display a broad emission peaks centered at around 560nm, which correspond to green-emissive region. Moreover, a notable shift of the maximum  $\lambda_{\text{em}}$  from around 585nm for pure CNP300oxG (**Figure 5.9B**) up to 560nm for CS-CNP300oxG (**Figure 5.18B**) additionally confirm the successful conjugation of carbon nanodomains with polymeric components. To this point, the enhancement of CS-CNP300oxG fluorescence intensity ( $I_{\text{PL}} \approx 3.0 \times 10^6$  a.u.), in contrast to pure CNP300oxG ( $I_{\text{PL}} \approx 1.0 \times 10^6$  a.u.), suggest that chitosan acts as a diluent matrix that suppress the self-quenching of CNPs. Owing to the fact that polymer matrices usually diminish the optical performance by absorbing light, the presented results suggest the promising utilization of CS-CNP300oxG in polymers industry. Thus, incorporation of C-dots into polymeric matrices prevents their agglomeration and facilitate the generation of nanocomposites with enhanced fluorescent properties. On the contrary, a negligible PL emission intensity was

recorded for crystalline CS-CNP300oxB powder (**Figure 5.18A**), thereby suggesting a larger content of conjugated  $sp^2$  domains than in CS-CNP300oxG [6]. Furthermore, the analysis of the PL lifetime dynamics of CS-CNP300oxG in a powder form (**Figure 5.18C**) reveal that the insignificant changes in  $\tau_1$  values as well as a notable decrement of  $\tau_2$  values for the PL decay curves recorded from  $\lambda_{ex}=375\text{nm}$  to  $\lambda_{ex}=450\text{nm}$  clearly indicate the dominant contribution of molecular states in solid-state CS-CNP NCs [46]. In contrast to liquid-state PL lifetime dynamics recorded at  $\lambda_{ex}=375\text{nm}$  ( $\tau_{avg}=6.17\text{ns}$ ) and  $\lambda_{ex}=450\text{nm}$  ( $\tau_{avg}=8.97\text{ns}$ ) (**Figure 5.17B**), the  $\tau_{avg}$  of CS-CNP300oxG powder is mainly reduced at  $\lambda_{ex}=450\text{nm}$  ( $\tau_{avg}=2.91\text{ns}$ ) (**Figure 5.18C**), which imply that extended  $sp^2$  domains conjugation in CS-CNP nanosystem enhance the degree of light-quenching in a solid-state [6].

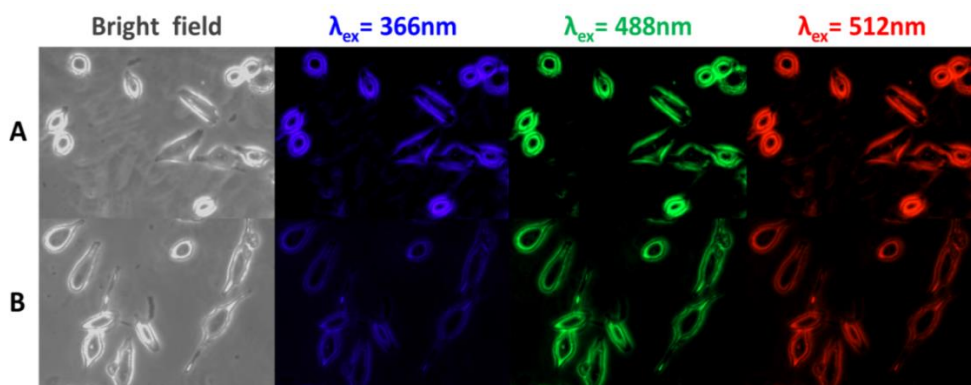


**Figure 5.18** The solid-state PL emission spectra of CS-CNP300oxB (A) and CS-CNP300oxG (B) together with the PL lifetime decays of CS-CNP300oxG recorded at  $\lambda_{ex}=375 \text{ nm}$  and  $\lambda_{ex}=450 \text{ nm}$  (C).

Likewise to the above discussed CNP300, the cytotoxicity studies of CS-CNP nanocomposites were performed against HeLa cancer cell line. As presented in **Figure 5.19**, the *in vitro* toxicity data revealed that the cells viability after their incubation with diversified concentrations of CNP300oxB (**Figure 5.19A**) and CNP300oxG (**Figure 5.19B**) were even slightly higher than that of control group. Therefore, these results confirmed not only a negligible cytotoxicity of these nanocomposites but also an excellent cytocompatibility, which do not impact on the suppression of the cell growth. Therefore, the approaches leading to the fabrication of cytocompatible nanocomposites that are based on non-toxic carbogenic nanoparticles rather than toxic semiconductor quantum dots give a promise for their commercial utilization in both biomedicine as well as biotechnology fields [57].

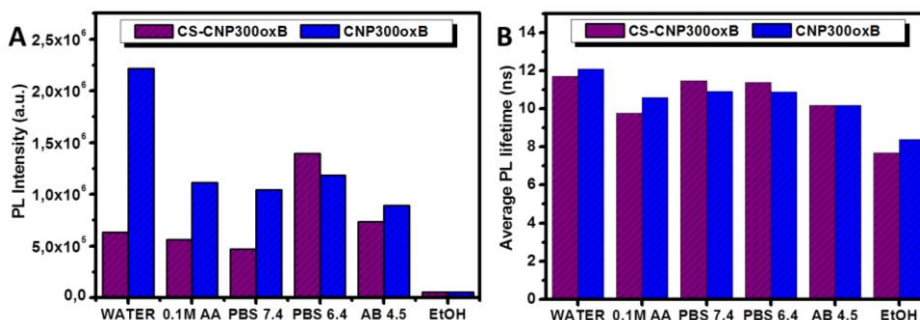


**Figure 5.19** The results from MTT assay showing the viability of HeLa cells incubated with various concentrations of CS-CNP300oxB (A) and CS-CNP300oxG (B) for 24 and 48 hours. The data is presented as a mean  $\pm$  SD of triple experiments and percentage of cell viability is relative to untreated control cells. Furthermore, the uptake of CS-CNP300oxB and CS-CNP300oxG (**Figure 5.20**) by the cancer cells was monitored by fluorescence microscope. To this point, the HeLa cells were incubated with 100  $\mu\text{g/mL}$  of both CS-CNP nanocomposites for 24 hours at 37°C. Subsequently the HeLa cells illuminated by different lasers revealed the multicolour emission capabilities (blue, green, red) while excited at 366nm (blue emission), 488nm (green emission) and 512nm (red emission). In agreement to the bioimaging results of CNP300ox, the fluorescence signals were recorded mainly in the cell membrane as well as cytoplasmic area, especially around the perinuclear region with the negligible PL intensity arising from the cell nucleus. In addition, the accumulation of CS-CNP NCs in the cytoplasm of HeLa cells may indicate that these nanoemitters utilize a passive diffusion mechanism to enter the cells [44]. Therefore, the conducted bioimaging experiments proved the suitability of CS-CNP NCs to be used as a promising fluorescent nanomarkers for both *in vivo* as well as *in vitro* biomedical applications [12, 47, 56].



**Figure 5.20** Fluorescence microscopy images representing the cellular uptake of 100  $\mu\text{g/mL}$  CS-CNP300oxG (left) and CS-CNP300oxB (right) by HeLa cells.

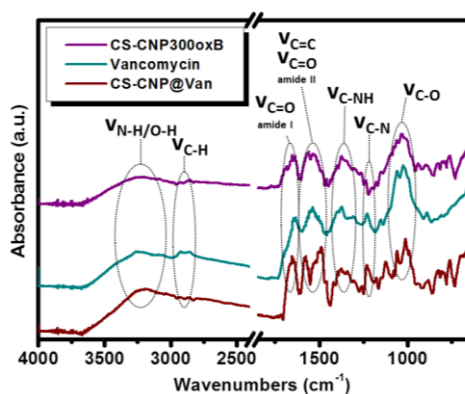
The fluorescence stability of exemplary CS-CNP300oxB nanocomposite was also evaluated at various pH (**Figure 5.21**). In general, the collected results clearly indicated that the PL lifetime features of CS-CNP300oxB as well as CNP300oxB (**Figure 5.21B**) are relatively uniform ( $\tau_{\text{avg}} \approx 10\text{-}11\text{ns}$  at  $\lambda_{\text{ex}} = 375\text{nm}$ ) at various pH. On the contrary, significant changes were observed for the PL emission intensity of CS-CNP300oxB and CNP300oxB NPs (**Figure 5.21A**) at neutral pH, whereas diminished fluorescence emission intensity of CS-CNP might be attributed to poor dispersibility in water. Although the dispersibility of chitosan at acidic pH is complete, the lower PL intensity values for presented CS-CNP300oxB could be related to the quenching effect in acidic pH. Overall, the high PL intensity of CS-CNP300oxB in a wide range of pH confirmed its potential to be used for biomedical applications, such as cellular imaging or as a trackable drug delivery nanocarriers [4, 43].



**Figure 5.21** The comparison between the PL intensity of the maximum emission peaks (A) as well as the average PL lifetimes (B) of CS-CNP300oxB and CNP300oxB in various solvents.

### 5.3.3 Fluorescent CS-CNPs nanocarrier for traceable drug delivery application

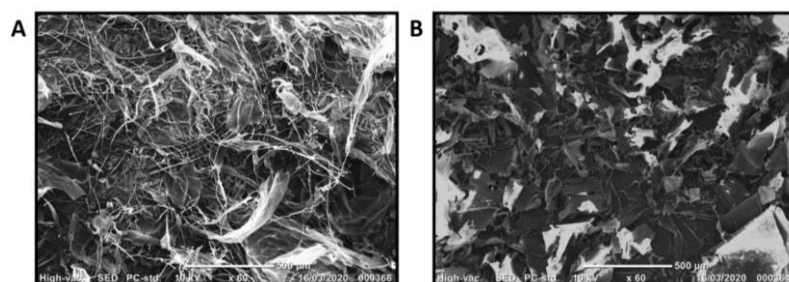
Vancomycin is a glycopeptide antibiotic which has a strong bactericidal activity against many bacterial infections caused by Gram-positive bacteria [72]. Thus, this antibiotic was chosen a model drug for development of drug delivery nanosystem based on CS-CNP NCs. The structural insight into antibiotic loaded CS-CNP NCs (referred hereafter as CS-CNP@Van) was gained by the FTIR spectroscopy, as presented in **Figure 5.22**. The FTIR spectra of vancomycin displayed a characteristic vibrational bands at  $3192\text{cm}^{-1}$ ,  $1653\text{cm}^{-1}$  and  $1577\text{cm}^{-1}$  which correspond to phenolic O-H group, aromatic C=C bond and N-H bonds from amine groups [73]. On the other side, the infrared spectra of CS-CNP@Van exhibited the presence of absorption bands arising from pure CS-CNP component without relevant shifting. However, the intensification of the band centered at  $1504\text{cm}^{-1}$  (C=O amide II vibrational stretching) together with its significant shifting in accordance to pure vancomycin proved the successful covalent conjugation of CS-CNP300oxB with antibiotic molecules. Besides that, other absorption bands of CS-CNP@Van are centered around  $3264\text{cm}^{-1}$ ,  $2927\text{cm}^{-1}$ ,  $1644\text{cm}^{-1}$ ,  $1556\text{cm}^{-1}$ ,  $1372\text{cm}^{-1}$ ,  $1058\text{cm}^{-1}$  and correspond to  $-\text{OH}$  and  $-\text{NH}_2$  stretching vibrations,  $-\text{CH}_2$  and  $-\text{CH}_3$  vibrations, C=O stretching vibrations, C=C stretching vibrations, N-H bending vibrations and C-O stretching vibrations, respectively [74].



**Figure 5.22** FTIR spectra of CS-CNP@Van, vancomycin and CS-CNP300oxB.

The SEM analysis facilitated the investigation of the morphology of pure CS-CNP300oxB (**Figure 5.23A**) as well as CS-CNP@Van nanocarrier (**Figure 5.23B**). To this point, CS-CNP300oxB possess a fibrous and permeable structure while the rough and

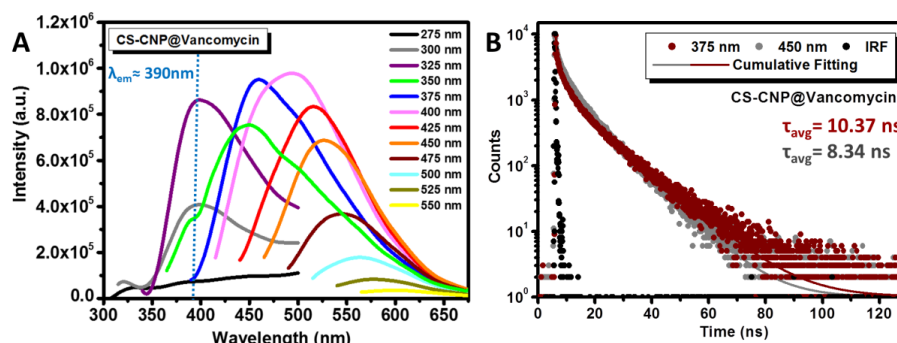
unsmooth surface is characteristic for vancomycin loaded CS-CNP NCs [72]. The structure with similar morphology to presented CS-CNP@Van has been reported before for vancomycin loaded chitosan composite scaffold [74].



**Figure 5.23** SEM images of CS-CNP300oxB (A) and CS-CNP@Van nanocarrier (B).

Furthermore, the investigation of fluorescence decay dynamics (**Figure 5.24B**) as well as the PL emission spectra (**Figure 5.24A**) allowed concluding the extent of interactions between vancomycin molecules and CS-CNP NCs in a liquid state. The average PL lifetime of CS-CNP@Van recorded at  $\lambda_{ex}=375\text{nm}$  ( $\tau_{avg}=10.37\text{ns}$ ) is notably shorter than  $\tau_{avg}$  of CS-CNP300oxB being equal to 11.40ns, under the same conditions. Thus, these results may suggest that vancomycin molecules could act as a quencher for the CTA fluorophore, which is additionally confirmed by reduced PL intensity of the emission peak recorded at  $\lambda_{ex}=375\text{nm}$  ( $I_{PL}\approx 1.0\times 10^6$ ) (**Figure 5.24A**), accordingly to its antibiotic-free counterpart ( $I_{PL}\approx 2.3\times 10^6$ ) (**Figure 5.17D**). In addition, the excitation-independent PL behaviour of CS-CNP@Van is blue-shifted towards the UV light range ( $275\text{nm}\leq \lambda_{ex}\leq 325\text{nm}$ ) with maximum  $\lambda_{em}\approx 390\text{nm}$  (**Figure 5.24A**) in contrast to CS-CNP300oxB with maximum  $\lambda_{em}\approx 450\text{nm}$  (**Figure 5.17D**). On the other side, the PL emission spectra recorded at various excitation wavelengths confirmed the  $\lambda_{ex}$ -dependent emission behaviour of CS-CNP@Van, owing to the gradual shifting of emission peaks from  $\lambda_{ex}=275\text{ nm}$  (blue-emissive region) to  $\lambda_{ex}=550\text{ nm}$  (red-emissive region). This phenomenon implies the presence of a series of emissive traps between  $\pi^*$  and  $\pi$  states of C-dots and thereby cause a variable emissive mode after illumination with specific  $\lambda_{ex}$  [8]. Moreover, the average PL lifetime calculated as 8.34ns at  $\lambda_{ex}=450\text{nm}$  is longer than for CS-CNP300oxB with  $\tau_{avg}=7.95\text{ ns}$ , thus suggesting the generation of more surface states by aromatic molecules of vancomycin. Overall, it is worth to mention

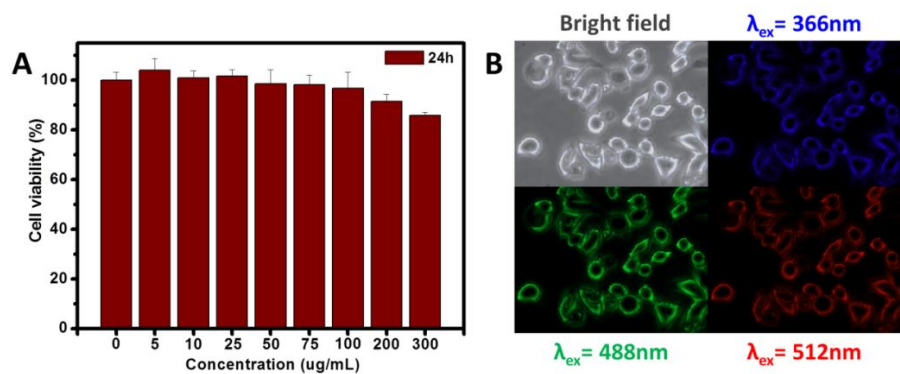
that the values of the PL lifetime components are only giving information about the relative emission strength but not relate precisely to the quantum yields [46].



**Figure 5.24** PL spectra (A) and PL lifetime decays (B) of 0.1 mg/mL aqueous dispersion of CS-CNP@Vancomycin recorded at various excitation wavelengths.

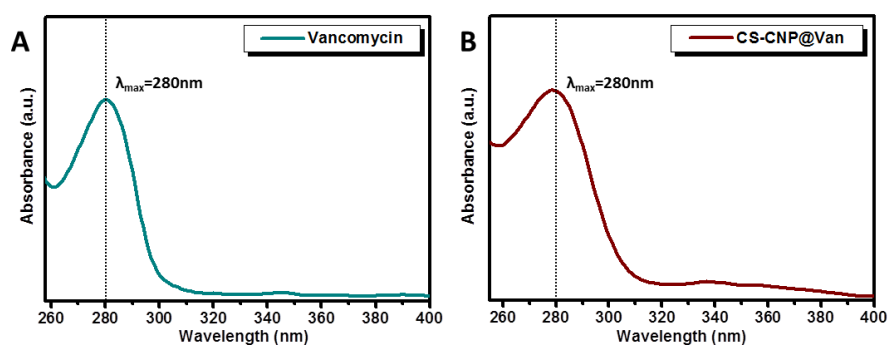
The cytotoxicity studies of CS-CNP@Van (**Figure 5.25A**) were evaluated with the use of HeLa cell line and showed the gradual decrement of cells viability up to around 86% after their incubation with CS-CNP@Van (300  $\mu\text{g/mL}$ ), in reference to untreated control cells (0  $\mu\text{g/mL}$ ). Nevertheless, a more concise toxicity studies should be performed for specific bacterial as well as human cells, in order to fully explore the antimicrobial potential of this nanosystem at the site of infection. Additionally, as presented in **Figure 5.25B**, the CS-CNP@Van nanosystem can successfully penetrate the membrane of HeLa cells and illuminate their cytoplasm with blue ( $\lambda_{ex}=366\text{nm}$ ), green ( $\lambda_{ex}=488\text{nm}$ ) and red ( $\lambda_{ex}=512\text{nm}$ ) colours. In contrast, no visible luminescence was recorded in the control cells under the bright field. Importantly, lack of fluorescence quenching after conjugation of antibiotic molecules with CS-CNP NCs suggest the suitability of carbon-based nanocomposites to be used as a fluorescent nanotracers in targeted drug delivery applications as well as cellular imaging of bacterial cells. Interestingly, some reports noted that the conjugation of C-dots with antibiotic molecules enrich the surface of carbon nanoemitters with functional groups, thereby improve their multicolour capabilities in the cellular labelling [11].





**Figure 5.25** The cytotoxicity from MTT assay of HeLa cells incubated with CS-CNP@Van for 24 hours at various concentrations (A) together with fluorescence microscopy images of HeLa cells with internalized CS-CNP@Van (B) under the bright field and ultraviolet, blue and green  $\lambda_{ex}$ .

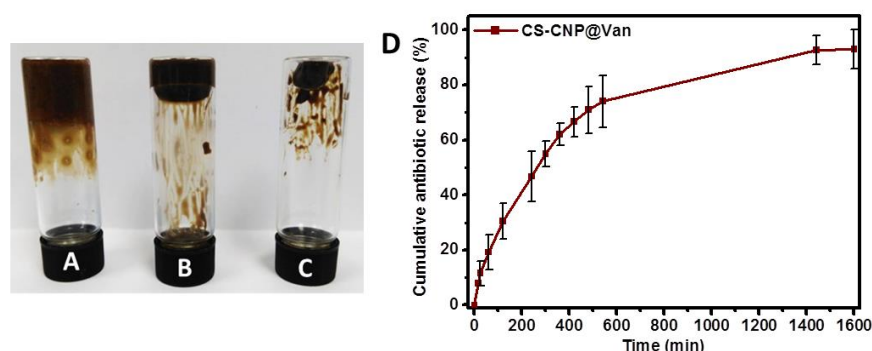
In order to prove the suitability of CS-CNP nanocarrier for potential drug release purposes the release of vancomycin antibiotic from CS-CNP@Van nanosystem was carefully investigated (**Figure 5.26D**). As demonstrated in **Figure 5.26A**, the absorption spectra of vancomycin solution displays absorption peak centered at 280 nm, which similarly is pronounced in the UV-Vis spectra of CS-CNP@Van (**Figure 5.26B**). Additionally, the UV-Vis spectra of CS-CNP@Van reveals a wide absorption band ranging from 320 nm to 400 nm, which correspond to  $n-\pi^*$  transitions [14].



**Figure 5.26** The UV-Vis spectra of pure vancomycin (A) as well as CS-CNP@Van nanosystem (B).

The controlled release of antibiotic from CS-CNP@Van nanosystem was achieved due to the gelation features of chitosan matrix. In detail, at concentration 9.5wt% CS-CNP@Van exists in a liquid state (**Figure 5.27A**), while the increment of the concentration up to 16.5wt% leads to the formation of viscous sol (**Figure 5.27B**), which further forms a concise hydrogel at concentration 24.5wt% (**Figure 5.27C**). Thus, owing to chitosan swelling behaviour, *in vitro* drug release studies demonstrated a

controlled release of vancomycin from CS-CNP@Van nanosystem at elevated pH of 7.4 (**Figure 5.27D**). These results are prolonged in comparison to the release of free vancomycin antibiotic which last up to 7 hours [72]. Therefore, the incorporation of vancomycin into CS-CNP NCs hydrogel played a crucial role in delaying the antibiotic release [72, 74, 75]. Nevertheless, it is believed that further optimisation of the synthetic protocol by modulation of chitosan content could impact on the sustained vancomycin release.



**Figure 5.27** The photos showing the gelation behaviour of CS-CNP@Van at concentration of 9.5wt% (A), 16.5wt% (B) and 24.5wt% (C) together with the drug release profile of vancomycin antibiotic from CS-CNP@Van nanosystem (D).

## 5.4 Conclusion

In summary, the presented work demonstrated a novel strategy to produce highly fluorescent C-dots nanopowder from previously reported crude CNP300, derived from the CA/EA precursors mixture at 300°C, as well as novel chitosan based nanocomposites with embedded C-dots inside their structure. The results from the physicochemical characterisation proved that the utilisation of a harsh oxidative conditions impacted on the shifting of fluorescence colour from blue-emissive region (CNP300oxB) up to green emissive region (CNP300oxG). Further implementation of the same strategy for grass-derived carbon dots proved that the changes in the colour of C-dots based nanopowder were associated with the presence of molecular fluorophores than only modification of the surface states defects. The calculation of the quantum yields for the CNP300ox with various extent of surface functional groups provided a quantitative assessment of their optical efficiencies, and proved that the novel strategy can improve the QY approximately by the factor of 2. Thus, this strategy

could be further applied for other fluorophore-rich carbon dots and give a prospective for the expanding their potential use in the solid-state applications. In addition to the results proving their negligible toxicity towards cancer cells, the bioimaging results confirmed the multicolour nature of presented carbogenic nanoemitters as well as their successful internalization and accumulation in the perinuclear region of HeLa cells. On the top of that, the antimicrobial studies confirmed their remarkable antibacterial properties, which nowadays have a significant importance when the spread of infectious diseases become a threat to human health and development of novel antimicrobial materials is in the centre of attention for many researchers. Furthermore, the synthesis of novel nanocomposites based on biopolymer chitosan with incorporated carbon dots led to generation of effective nanocarrier for the controlled release of vancomycin antibiotic, which due to its remarkable optical properties could also help to monitor the route of drug delivery inside the body. Conclusively, the values of the average PL lifetimes of all prepared nanomaterials and nanocomposites are significantly prolonged in comparison to many organic dyes, which together with non-toxic nature and antimicrobial finish prove their suitability to be utilized for *in vitro* and *in vivo* bioimaging applications as well as traceable drug delivery nanosystems.

## 5.5 References

1. Fang, Q., et al., *Luminescence origin of carbon based dots obtained from citric acid and amino group-containing molecules*. Carbon, 2017. **118**: p. 319-326.
2. Kelarakis, A., *From highly graphitic to amorphous carbon dots: A critical review*. MRS Energy & Sustainability, 2014. **1**(2): p. 1-15.
3. Krysmann, M.J., A. Kelarakis, and E.P. Giannelis, *Photoluminescent carbogenic nanoparticles directly derived from crude biomass*. Green Chem., 2012. **14**: p. 3141–3145.
4. Dhenadhayalan, N., et al., *Unravelling the Multiple Emissive States in Citric Acid-Derived Carbon-Dots*. J. Phys. Chem. C 2016, 120, 2, 1252–1261, 2016. **120**(2): p. 1252–1261.
5. Hsu, Y.F., Y.H. Chen, and C.W. Chang, *The spectral heterogeneity and size distribution of the carbon dots derived from time-resolved fluorescence studies*. Phys. Chem. Chem. Phys., 2016. **18**(43): p. 30086-30092.
6. Yoo, H.J., B.E. Kwak, and D.H. Kim, *The Self-Quenching Origin of Carbon Dots and the Guideline for Its Solid-State Luminescence*. The Journal of Physical Chemistry, 2019. **123**(44): p. 27124-27131.
7. Gu, S., et al., *Microwave Growth and Tunable Photoluminescence of Nitrogen-doped Graphene and Carbon Nitride Quantum Dots*. Journal of Materials Chemistry C, 2019. **7**(18): p. 5468-5476.
8. Sarkar, S., et al., *Amino acid functionalized blue and phosphorous-doped green fluorescent carbon dots as bioimaging probe*. RSC Adv., 2015. **5**: p. 65913-65921.
9. Meng, X., et al., *Supramolecular nanodots derived from citric acid and beta-amines with high quantum yield and sensitive photoluminescence*. Optical Materials, 2018. **77**: p. 48-54.
10. Dong, X., et al., *Carbon Dots as Potent Antimicrobial Agents*. Theranostics, 2020. **10**(2): p. 671-686.
11. Lin, F., Y.W. Bao, and F.G. Wu, *Carbon Dots for Sensing and Killing Microorganisms*. Journal of Carbon Research, 2019. **5**(2): p. 1-21.
12. Zheng, M., et al., *Preparation of highly luminescent and color tunable carbon nanodots under visible light excitation for in vitro and in vivo bio-imaging*. Journal of Materials Research, 2015. **30**(22): p. 3386-3393.
13. Zheng, X., et al., *Single and repeated dose toxicity of citric acidbased carbon dots and a derivative in mice*. RSC Adv., 2015. **5**: p. 91398-91406.
14. Li, L.S., et al., *Highly fluorescent carbon dots synthesized with binary dopants for “turn off” and “turn off-on” sensing and cell imaging*. Sensors and Actuators B, 2018. **268**: p. 84–92.

15. Wang, J., S. Su, and J. Qiu, *Biocompatible Carbon Dots with Diverse Surface Modification*. MRS Advances, 2016. **1**(19): p. 1333-1338.
16. Kandra, R. and S. Bajpai, *Synthesis, mechanical properties of fluorescent carbon dots loaded nanocomposites chitosan film for wound healing and drug delivery*. Arabian Journal of Chemistry, 2020. **13**: p. 4882–4894.
17. Justin, R., et al., *Biodegradable and conductive chitosan – graphene quantum dot nanocomposite microneedles for delivery of both small and large molecular weight therapeutics*. RSC Adv., 2015. **5**: p. 51934-51946.
18. Omid, M., A. Yadegari, and L. Tayebi, *Wound dressing application of pH-sensitive carbon dots/chitosan hydrogel*. RSC Adv., 2017. **7**: p. 10638–10649.
19. Mathew, S.A., et al., *Luminescent chitosan/carbon dots as an effective nano-drug carrier for neurodegenerative diseases*. RSC Adv., 2020. **10**: p. 24386–24396.
20. Huang, Q., et al., *Carbon dots and chitosan composite film based biosensor for the sensitive and selective determination of dopamine*. Analyst, 2013. **138**: p. 5417–5423.
21. Baruah, U., A. Konwar, and D. Chowdhury, *A sulphonated carbon dot–chitosan hybrid hydrogel nanocomposite as an efficient ion-exchange film for  $\text{Ca}^{2+}$  and  $\text{Mg}^{2+}$  removal*. Nanoscale, 2016. **8**: p. 8542–8546.
22. Han, E., et al., *Development of tyrosinase biosensor based on quantum dots/chitosan nanocomposite for detection of phenolic compounds*. Analytical Biochemistry, 2015. **486**: p. 102–106.
23. Mallakpour, S. and E. Khadem, *Linear and nonlinear behavior of crosslinked chitosan/N-doped graphene quantum dot nanocomposite films in cadmium cation uptake*. Science of the Total Environment, 2019. **690**: p. 1245–1253.
24. Sheng, Y., et al., *pH-sensitive drug delivery based on chitosan wrapped graphene quantum dots with enhanced fluorescent stability*. Materials Science & Engineering C, 2020. **112**: p. 110888-110895.
25. Janus, Ł., et al., *Chitosan-Based Carbon Quantum Dots for Biomedical Applications: Synthesis and Characterization*. Nanomaterials, 2019. **9**(274): p. 1-13.
26. Konwar, A., et al., *Green Chitosan-Carbon dots nanocomposite Hydrogel Film with superior properties*. Carbohydrate Polymers, 2015. **115** p. 238-245.
27. Hasanzadeh, M., N. Shadjou, and M. Marandi, *Graphene Quantum Dots Functionalized by Chitosan and Cyclodextrin: An Advanced Nanocomposite for Sensing of Multi-Analytes at Physiological pH*. Journal of Nanoscience and Nanotechnology, 2017. **17**: p. 4598–4607.
28. Liu, H., et al., *A functional chitosan-based hydrogel as a wound dressing and drug delivery system in the treatment of wound healing*. RSC Adv., 2018. **8**: p. 7533-7549.

29. Ali, A. and S. Ahmed, *A review on chitosan and its nanocomposites in drug delivery*. International Journal of Biological Macromolecules 2018. **109**: p. 273–286.
30. Shen, C.L., et al., *In-situ embedding of carbon dots in a trisodium citrate crystal matrix for tunable solid-state fluorescence*. Carbon, 2018. **136**: p. 359-368.
31. Wang, H.J., et al., *A self-quenching-resistant carbon dots powder with tunable solid-state fluorescence and their applications in light-emitting diodes and fingerprints detection*. Dyes and Pigments, 2018. **159**: p. 245–251.
32. Wang, H.J., et al., *Facile microwave synthesis of carbon dots powder with enhanced solid-state fluorescence and its applications in rapid fingerprints detection and white light-emitting diodes*. Dyes and Pigments, 2019. **170**: p. 107623.
33. Wang, D., W.U. Khan, and Y. Wang, *Solid-State Carbon Dots with Efficient Cyan Emission towards White LEDs*. Chem. Asian J., 2019. **14**: p. 286-292.
34. Wang, H.J., et al., *Novel yellow solid-state fluorescent-emitting carbon dots with high quantum yield for white light-emitting diodes*. Spectrochimica Acta Part A: Molecular and Biomolecular Spectroscopy, 2021. **250**: p. 119340.
35. Wei, J.Y., et al., *Scalable Synthesis of Green Fluorescent Carbon Dot Powders with Unprecedented Efficiency*. Adv. Optical Mater., 2020: p. 1-7.
36. Mai, X.D., Y.T.H. Phan, and V.Q. Nguyen, *Excitation-Independent Emission of Carbon Quantum Dot Solids*. Advances in Materials Science and Engineering, 2020: p. 1-5.
37. Zheng, Y., et al., *Facile Preparation of Stable Solid-State Carbon Quantum Dots with Multi-Peak Emission*. Nanomaterials, 2020. **10**: p. 1-10.
38. Yu, T., et al., *A rapid microwave synthesis of green-emissive carbon dots with solid-state fluorescence and pH-sensitive properties*. R. Soc. open sci. , 2018. **5**: p. 180245.
39. Ren, J., L. Stagi, and P. Innocenzi, *Fluorescent carbon dots in solid-state: From nanostructures to functional devices*. Progress in Solid State Chemistry, 2020: p. 100295.
40. Peng, D., et al., *A novel monodisperse SiO<sub>2</sub>@C-dot for the rapid and facile identification of latent fingerprints by self-quenching resistant solid-state fluorescence*. Dalton Trans., 2018. **47**: p. 5823-5830.
41. Tian, Y., et al., *Green low-cost carbon nanodots-polyurethane composites with novel anisotropic anti-quenching mechanism for strain sensing*. Applied Physics, 2019.
42. Song, H., et al., *High production-yield solid-state carbon dots with tunable photoluminescence for white/multi-color light-emitting diodes*. Science Bulletin, 2019. **64**: p. 1788–1794.

43. Krysmann, M.J., et al., *Formation mechanism of carbogenic nanoparticles with dual photoluminescence emission*. J Am Chem Soc, 2012. **134**(2): p. 747-50.
44. Ding, H., et al., *Highly Efficient Red-Emitting Carbon Dots with Gram-Scale Yield for Bioimaging*. Langmuir, 2017. **33**(44): p. 12635–12642.
45. Iqbal, A., et al., *Carbon dots prepared by solid state method via citric acid and 1,10-phenanthroline for selective and sensing detection of Fe<sup>2+</sup> and Fe<sup>3+</sup>*. Sensors and Actuators B, 2016. **237**: p. 408–415.
46. Gao, F., et al., *Rational design of high quality citric acid-derived carbon dots by selecting efficient chemical structure motifs*. Carbon 2017. **112**: p. 131-141.
47. Zhuo, Y., et al., *One-step synthesis of high quantum-yield and excitation-independent emission carbon dots for cell imaging*. Materials Letters, 2015. **139**: p. 197–200.
48. Bhaisare, M.L., et al., *Synthesis of fluorescent carbon dots via microwave carbonization of citric acid in presence of tetraoctylammonium ion, and their application to cellular bioimaging*. Microchim Acta, 2015. **182**: p. 2173–2181.
49. Genc, R., et al., *High-Capacitance Hybrid Supercapacitor Based on Multi-Colored Fluorescent Carbon-Dots*. Scientific Reports 2017. **7**: p. 11222-11236.
50. Wang, D., et al., *Facile and Scalable Preparation of Fluorescent Carbon Dots for Multifunctional Applications*. Engineering, 2017. **3**: p. 402–408.
51. Tao, S., et al., *The polymeric characteristics and photoluminescence mechanism in polymer carbon dots: A review*. Materials Today Chemistry, 2017. **6**: p. 13-25.
52. Zhai, X., et al., *Highly luminescent carbon nanodots by microwave-assisted pyrolysis*. Chem. Commun., 2012. **48**: p. 7955–7957.
53. Wang, J., et al., *Highly fluorescent carbon dots as selective and visual probes for sensing copper ions in living cells via an electron transfer process*. Biosensors and Bioelectronics, 2017. **97**: p. 157–163.
54. Wang, Z., et al., *Fluorescence sensor array based on amino acid derived carbon dots for pattern-based detection of toxic metal ions*. Sensors and Actuators B 2017. **241**: p. 1324–1330.
55. Zhou, M., et al., *Synthesis of highly photoluminescent carbon dots via citric acid and Tris for iron(III) ions sensors and bioimaging*. Talanta, 2015. **143**: p. 107–113.
56. Hu, Y., et al., *How do nitrogen-doped carbon dots generate from molecular precursors? An investigation of the formation mechanism and a solution-based large-scale synthesis*. J. Mater. Chem. B, 2015. **3**: p. 5608-5614.
57. Zhang, Z., et al., *One-pot synthesis of fluorescent nitrogen-doped carbon dots with good biocompatibility for cell labeling*. Luminescence, 2017. **32**(8): p. 1488-1493.

58. Deka, M.J., et al., *Carbon dots derived from water hyacinth and their application as a sensor for pretilachlor*. Heliyon, 2019. **5**(6): p. 1-8.
59. Sabet, M. and K. Mahdavi, *Green Synthesis of High Photoluminescence Nitrogen-doped Carbon Quantum Dots from Grass via a Simple Hydrothermal Method for Removing Organic and Inorganic Water Pollutions*. Applied Surface Science, 2018. **463**: p. 283-291.
60. Meng, W., et al., *Biomass-Derived Carbon Dots and Their Applications*. Energy Environ. Mater., 2019. **2**(3): p. 172-192.
61. Geetha, V., R. Vijayaraghavan, and S.N. Chakravarthula, *Boswellia ovalifoliolata bark extract derived carbon dots for selective fluorescent sensing of Fe<sup>3+</sup>*. Journal of Environmental Chemical Engineering, 2019. **7**: p. 1-9.
62. Singh, J., et al., *Highly Fluorescent Carbon Dots Derived from Mangifera indica Leaves for Selective Detection of Metal Ions*. Science of The Total Environment, 2020. **720**: p. 1-31.
63. Simsek, S., M.O. Alas, and R. Genc, *Evaluation of the physical properties of fluorescent carbon nanodots synthesized using Nerium oleander extracts by microwave-assisted synthesis methods*. J Mater Res Technol., 2019. **8**(3): p. 2721–2731.
64. Pourreza, N. and M. Ghomi, *Green synthesized carbon quantum dots from Prosopis juliflora leaves as a dual off-on fluorescence probe for sensing mercury (II) and chemet drug*. Materials Science & Engineering C, 2019. **98**: p. 887–896.
65. Zhu, L., et al., *Plant leaf-derived fluorescent carbon dots for sensing, patterning and coding*. J. Mater. Chem. C, 2013. **1**: p. 4925-4933.
66. Alex, A.M., et al., *Carbon dots: A green synthesis from Lawsonia inermis leaves*. Materials Today: Proceedings, 2020. **26**: p. 716-719.
67. Mehta, V.N., et al., *Preparation of multicolor emitting carbon dots for HeLa cell imaging*. New J. Chem., 2014. **38**: p. 6152-6160.
68. Abu Rabe, D.I., et al., *The dominant role of surface functionalization in carbon dots' photo-activated antibacterial activity*. Int J Nanomedicine, 2019. **14**: p. 2655-2665.
69. Dong, X., et al., *Antibacterial effects of carbon dots in combination with other antimicrobial reagents*. PLoS ONE, 2017. **12**(9): p. 1-16.
70. Pawar, S., et al., *Functionalized Chitosan–Carbon Dots: A Fluorescent Probe for Detecting Trace Amount of Water in Organic Solvents*. ACS Omega, 2019. **4**: p. 11301–11311.
71. Ou, J., et al., *Well-Dispersed Chitosan-Graphene Quantum Dots Nanocomposites for Electrochemical Sensing Platform*. Journal of The Electrochemical Society, 2015. **162**(12): p. 884-889.



72. Mahmoudian, M. and F. Ganji, *Vancomycin-loaded HPMC microparticles embedded within injectable thermosensitive chitosan hydrogels*. Prog Biomater, 2017. **6**: p. 49–56.
73. Saidykhan, L., et al., *Development of nanoantibiotic delivery system using cockle shell-derived aragonite nanoparticles for treatment of osteomyelitis*. International Journal of Nanomedicine, 2016. **11**: p. 661–673.
74. Zhang, J., et al., *In vivo drug release and antibacterial properties of vancomycin loaded hydroxyapatite/chitosan composite*. Drug Delivery, 2012. **19**(5): p. 264–269.
75. Kalhapure, R.S., et al., *pH-responsive chitosan nanoparticles from a novel twin-chain anionic amphiphile for controlled and targeted delivery of vancomycin*. Colloids and Surfaces B: Biointerfaces 2017. **158**: p. 650-657.

# **CHAPTER 6:**

## **General conclusion and future work**

*“The whole of science is nothing more  
than a refinement of everyday thinking”*

*Albert Einstein*

## 6.1 General conclusion

In general, this thesis outlines novel strategies for the preparation of C-dots based nanosystems that combine a unique set of intrinsic properties arising from carbogenic counterparts. To date, several researchers suggested the use of semiconductor quantum dots (SQDs) with remarkable luminescent properties for application in biomedical fields (i.e. *in vivo* fluorescence imaging). However, the content of heavy metals in their structure has a significant impact on the overall cytotoxicity, thus rise a medical concerns. On the other side, environmentally benign carbon dots with similar tunable fluorescence behaviour are superior to conventionally used SQDs or fluorescent organic dyes, owing to their bio-friendly nature, negligible toxicity, easy-to-modify surface, excellent cytocompatibility, cost efficient production, remarkable colloidal stability as well as facile purification strategies. Nevertheless, the fabrication of C-dots based nanomaterials hold some limitations, among which can be distinguished time efficient synthetic procedures, tedious purification strategies, the self-quenching effect in aggregated powder form, the quenching behaviour after conjugation with other NPs and so forth. Therefore, in this work a large galleries of different C-dots based nanosystems were developed to address those challenges as well as the changes in their structural, morphological, optical and magnetic properties were compressively investigated in detail.

For instance, the development of a large gallery of photoactive suspensions and powders via pyrolytic treatment of binary CA/urea precursors mixture and followed by the use of two standard size separation strategies (i.e. filtration and dialysis) led to fabrication of novel four distinct families of photoluminescent C-dots, in which the emissive signal predominantly arises from C-dots with embedded fluorophores, a blend of molecular fluorophores, a mixture of C-dots with unbound molecular fluorophores as well as cyanuric acid-rich C-dots. Importantly, the selected separation strategies favoured the predominance of different molecular fluorophores in the post-purified materials, which impacted on either blue or green luminescence of the aqueous dispersions of C-dots. Among both, especially filtration strategy holds a promise for being used on a large scale during the synthesis of colour-tunable carbon-

rich powders with excessive content of molecular fluorophores. Besides that, the oxidation of carbogenic residue from the filtration step resulted in generation of another type of fluorescent species, thus complied with the rules of green chemistry that aim to limit the environmental wastes. The detailed examination of the optical properties proved that those nanoscopic emitters constitute an ideal candidates for the bioimaging applications, while their sensitive nature towards external pH variations pave the way for application as optical sensors. Overall, urea-based C-dots could be used as fluorescent probes for monitoring of the intercellular pH variations or for detecting the alerting changes in the early stage of diseases.

In another example, a novel large family of magnetic C-dots with both magnetic and fluorescent properties was synthesized through one-pot thermal decomposition of iron-rich and carbon-rich precursors. The demonstrated synthetic approach proved that iron component impact on the quenching of C-dots fluorescence, while abundant carbon content suppress the magnetic properties. Nevertheless, this limitation was addressed by the simple modification of synthetic protocol via addition of gadolinium component into C/Fe-NPs matrix, which improved their magnetic properties without compromising their optical features. Furthermore, the use of different carbon precursors (i.e. amines, polyetheramine, polymers) proved that proposed synthetic strategy can be used for a wide range of carbon sources, thereby give a promise for a large scale commercialisation. Overall, advanced superparamagnetic capabilities, remarkable fluorescent properties and excellent antimicrobial performance suggested their suitability to be used as a magnetically-guided surveillance probe for the detection and labelling of cancer cells.

At last, novel approaches were used for the development of highly fluorescent C-dots based nanopowders as well as chitosan-based C-dots nanocomposites without self-quenching effect in a solid-state form. The use of harsh oxidative conditions for modification of crude carbogeneous material derived from the mixture of CA/ethanolamine facilitated the separation of blue-emissive and green-emissive fluorescent fractions as well as changed the colour of carbon-rich nanopowders from brown to yellow. Subsequent implementation of the same strategy for a grass-derived

carbon dots suggested that the strong oxidative treatment led to molecular changes in fluorophores structure, thereby this strategy could be further expanded for other types fluorophore-rich C-dots powders. Importantly, biological studies further confirmed that C-dots are characterised by negligible toxicity and have a remarkable antimicrobial properties, whereas the bioimaging experiments confirmed their multicolour nature after being internalized by the cancer cells. In addition, the incorporation of C-dots into chitosan matrix led to generation of effective nanocarriers for the controlled release of vancomycin antibiotic. To that end, the remarkable optical properties of C-dots help to monitor the route of drug administration inside the body, thus can be applied as nanotracers in trackable drug delivery nanosystems.

## 6.2 Future work

Despite the detailed exploration of various synthetic strategies leading to generation of versatile C-dots based nanosystems, their potential has not been fully explored yet. The presented protocols could be used as a guideline for further modification of precursors mixtures, synthesis conditions or purification strategies.

Importantly, the stability studies should be conducted for all C-dots based nanosystems prior their potential *in vivo* applications. To this end, special emphasis should be given to investigation of the impact of daily and ultraviolet light, pH, storage conditions, temperature, humidity as well as variable concentrations of their liquid suspensions over prolonged period of time (i.e. 6-12 months).

Although the results from the *in vitro* toxicity studies confirmed their negligible cytotoxicity against model HeLa cell line, more systematic studies should be further conducted against particular healthy or cancer cell lines. Knowing that the uptake of nanoparticles is carried out by spleen or liver and followed by the elimination via excretion pathway, the special emphasis should be given to subsequent *in vitro* toxicity testing against HEK293 or HepG2 cell lines that are derived from kidneys and liver, respectively. After successful completion of this task, the use of animal models (e.g. mice, rats) could be considered to examine the suitability of these nanoemitters for multimodal *in vivo* imaging application.

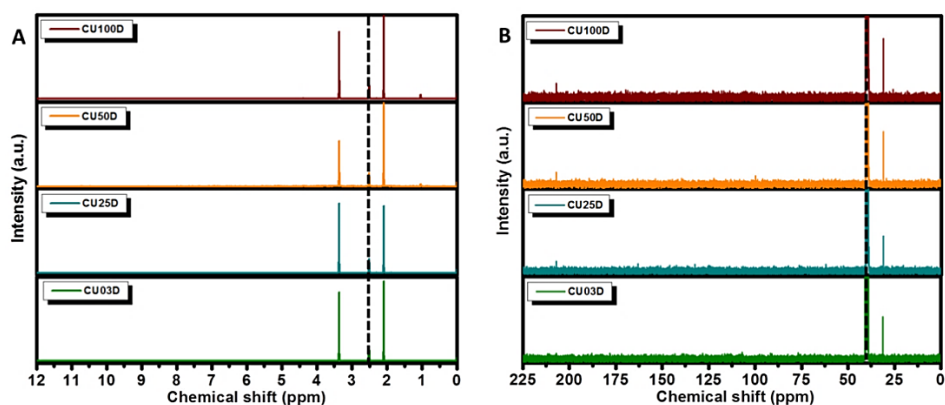
Besides proposed biomedical applications, the remarkable optical and structural properties of as-prepared nanomaterials hold a promise for their further exploration in clinical settings. Especially, the effectiveness of hybrid Gd-doped magnetic C-dots or other versatile magneto-fluorescent NPs could be tested for hyperthermia application in cancer treatment, contrast agents in magnetic resonance imaging or surveillance probes for multimodal imaging. On the other side, the hydrogels based on chitosan/C-dots NCs have potential to be applied as dressings with optical tracking for wound healing applications. In regard to pure C-dots, their further modification with specific biomolecules (i.e. peptides) could target their *in vivo* action towards particular organs where their application as a sensitive optical nanoprobe for detection of particular diseases could be tested in real-time.

# **CHAPTER 7:**

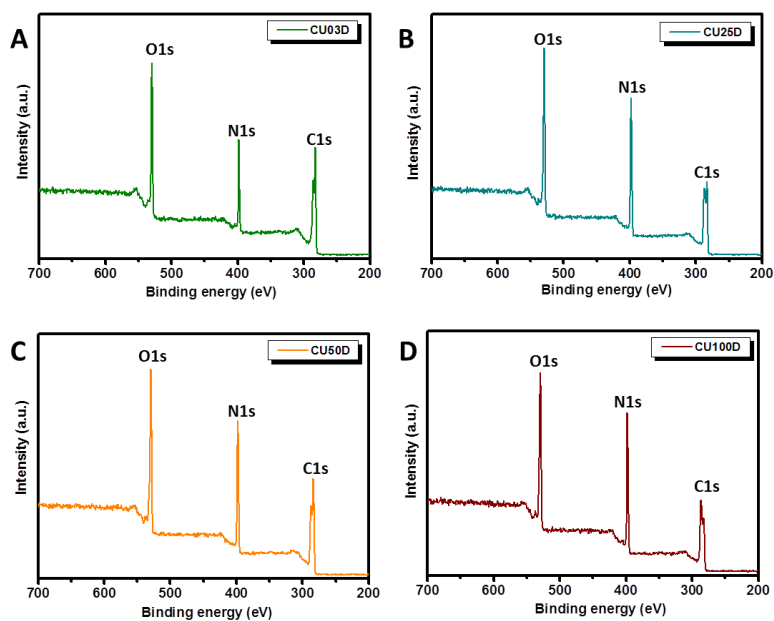
## **Appendices**

**Table A1.** Elemental analysis results for D-series CU-dots

Material	D-series			
	C	H	N	O
CU03D	47%	4%	21%	28%
CU25D	45%	4%	25%	26%
CU50D	44%	3%	28%	25%
CU100D	40%	3%	33%	24%

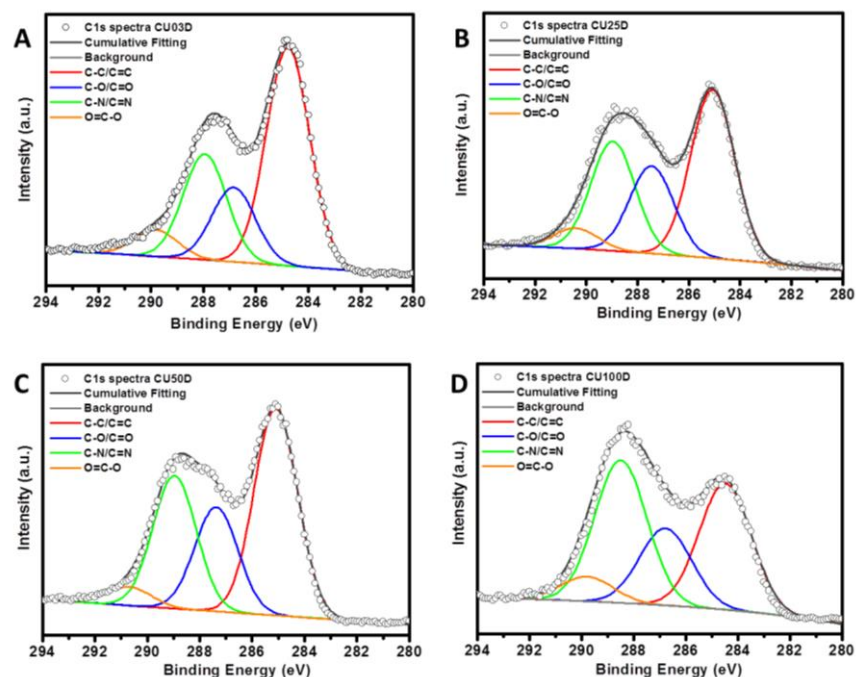


**Figure A1.** The  $^1\text{H}$ -NMR (A) and  $^{13}\text{C}$ -NMR (B) spectrum of D-series CU-dots. The d-DMSO solvent peaks are marked as dashed black line.

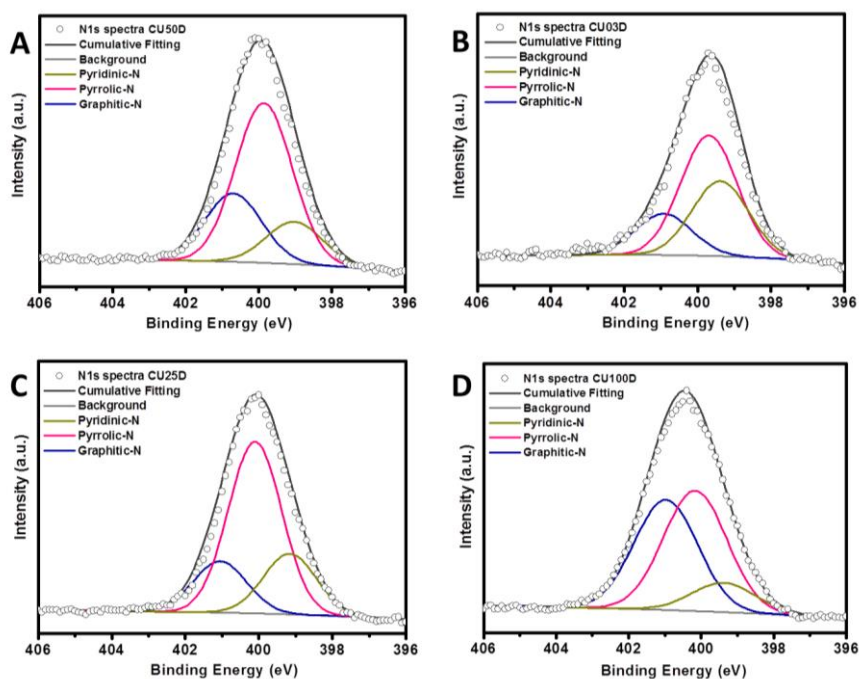


**Figure A2.** Full-scan XPS survey spectra of CU03D (A), CU25D (B), CU50D (C) and CU100D (D).

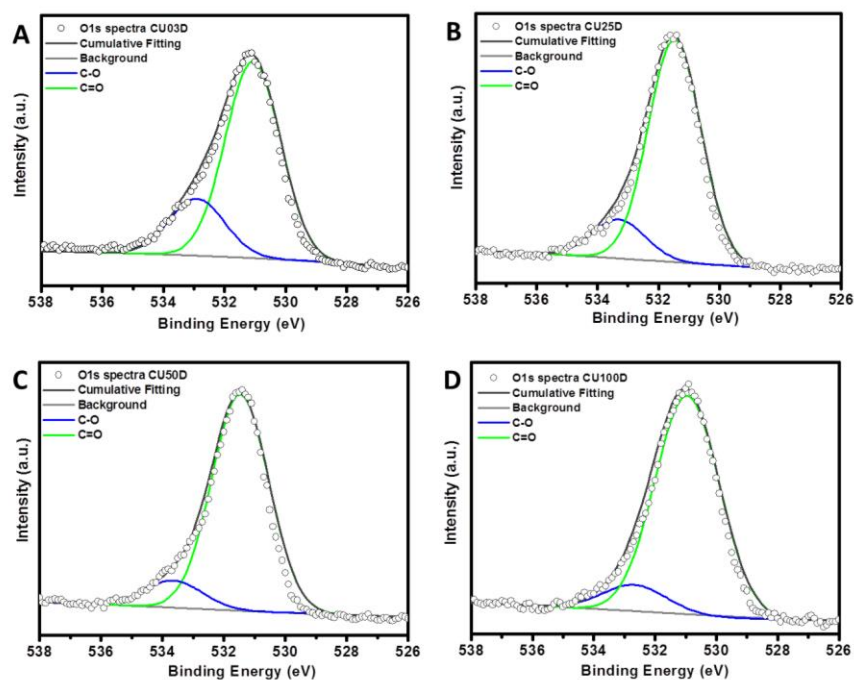




**Figure A3.** C1s XPS spectra of CU03D (A), CU25D (B), CU50D (C) and CU100D (D). The points represent the experimental data and the lines correspond to the fitted curves.



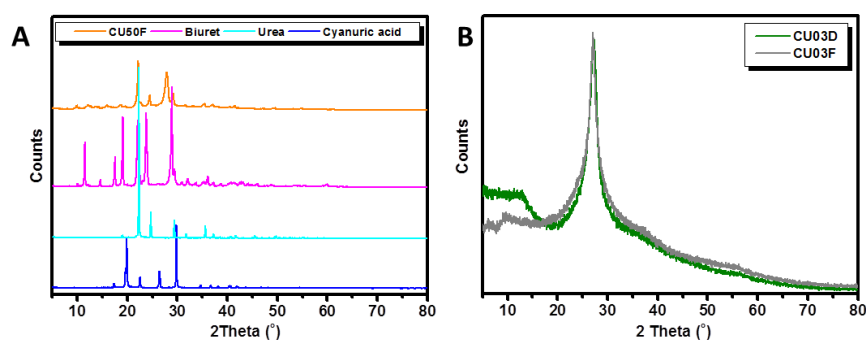
**Figure A4.** N1s XPS spectra of CU03D (A), CU25D (B), CU50D (C) and CU100D (D). The points represent the experimental data and the lines correspond to the fitted curves.



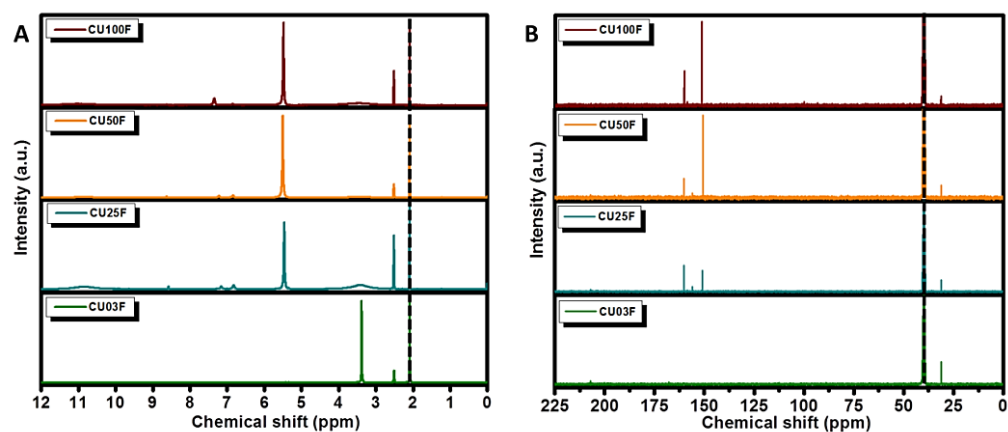
**Figure A5.** O1s XPS spectra of CU03D (A), CU25D (B), CU50D (C) and CU100D (D). The points represent the experimental data and the lines correspond to the fitted curves.

**Table A2.** Elemental analysis results for F-series CU-dots

Material	F-series			
	C	H	N	O
CU03F	36%	4%	31%	29%
CU25F	31%	4%	35%	30%
CU50F	30%	4%	37%	29%
CU100F	29%	5%	38%	28%



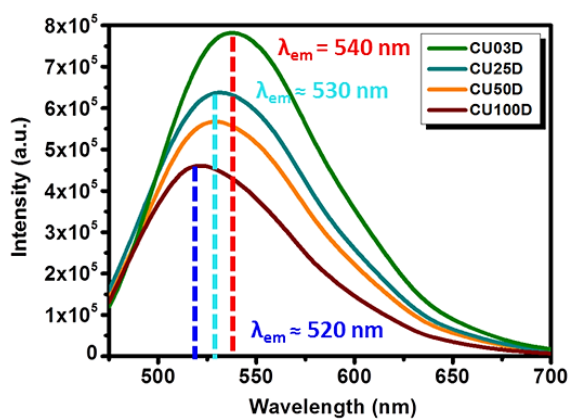
**Figure A6.** The XRD pattern of CU50F nanopowder along with the diffraction patterns of biuret, urea and cyanuric acid (A) as well as XRD pattern of CU03 materials (B).



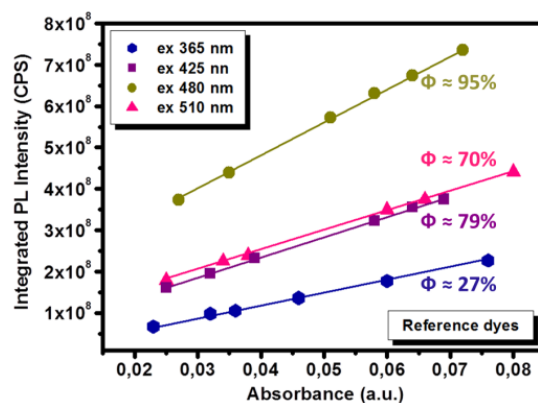
**Figure A7.** The  $^1\text{H}$ -NMR (A) and  $^{13}\text{C}$ -NMR (B) spectrum of F-series CU-dots. The d-DMSO solvent peaks are marked as dashed black line.

**Table A3.** Elemental analysis results for all series of CU50 nanomaterials

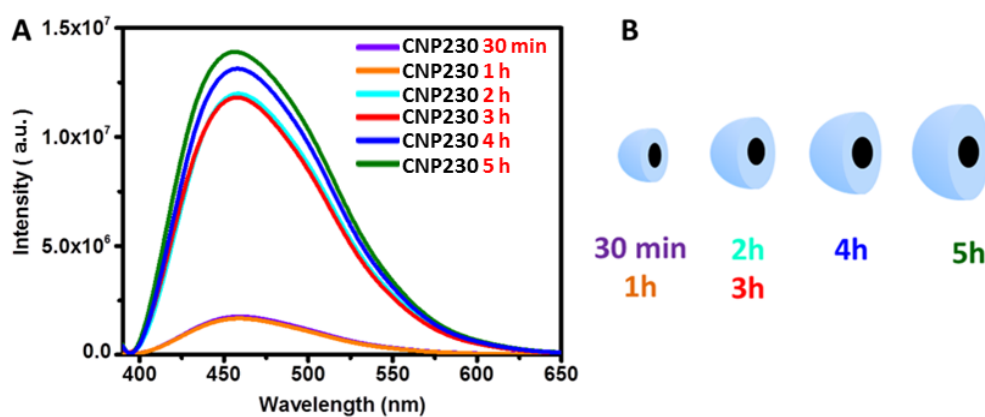
Material	D, D1, F, F1-series			
	C	H	N	O
CU50F1	33%	2%	31%	34%
CU50F1-pre	32%	4%	36%	28%
CU50D	44%	3%	28%	25%
CU50F	30%	4%	37%	29%



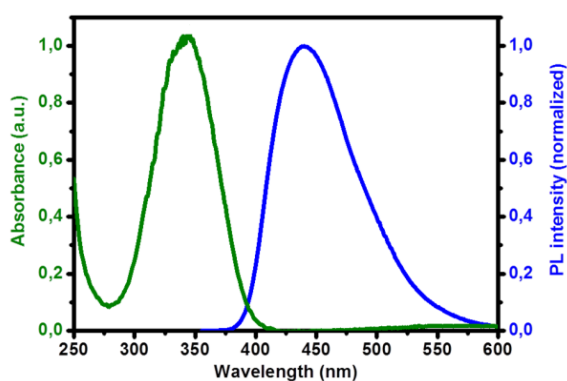
**Figure A8.** PL spectra of the emission peaks recorded at  $\lambda_{\text{ex}} = 460\text{nm}$  for aqueous dispersions of D-series CU-dots. The concentration of the solutions was equal to 0.1 mg/mL.



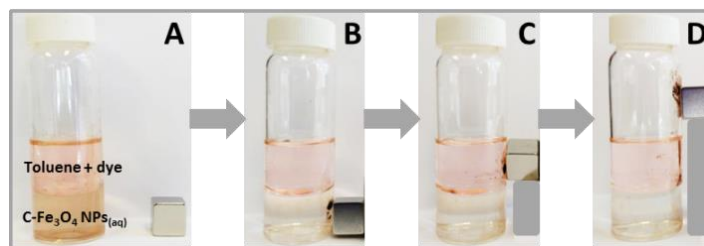
**Figure A9.** The graphical representation of the integrated PL intensity of anthracene ( $\lambda_{\text{ex}}=365$  nm), fluorescein ( $\lambda_{\text{ex}}=425$  nm), rhodamine 6G ( $\lambda_{\text{ex}}=480$  nm) and rhodamine B ( $\lambda_{\text{ex}}=510$  nm) dispersed in EtOH as a function of optical absorbance with corresponding quantum yield values.



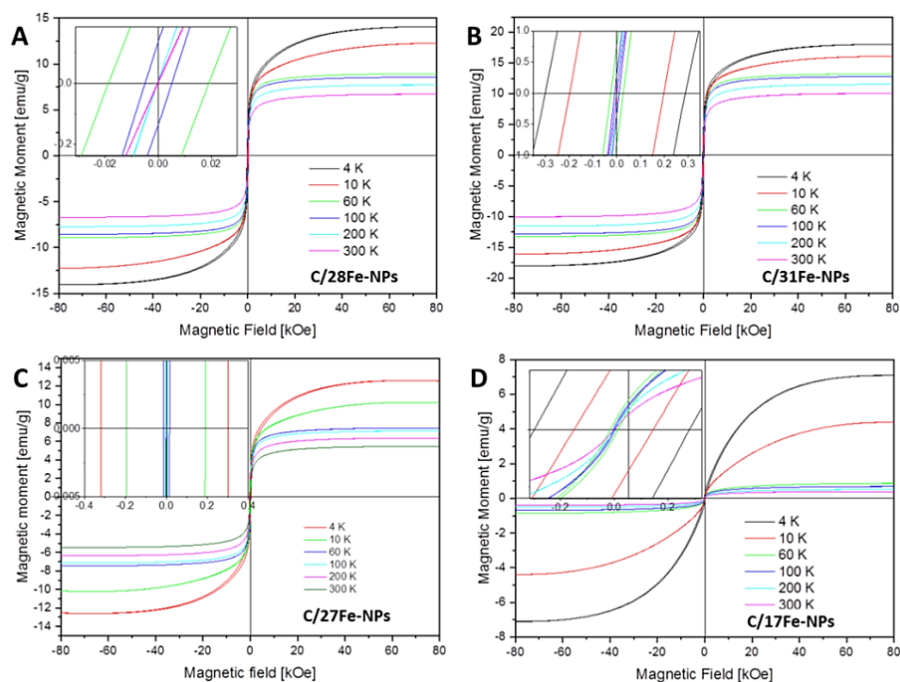
**Figure A10.** PL spectra presenting the maximum emission peak with  $\lambda_{\text{ex}} = 375$  nm of aqueous dispersion of CNP230 synthesized by varied time (A) and the scheme showing the fluorophore outer layer (B).



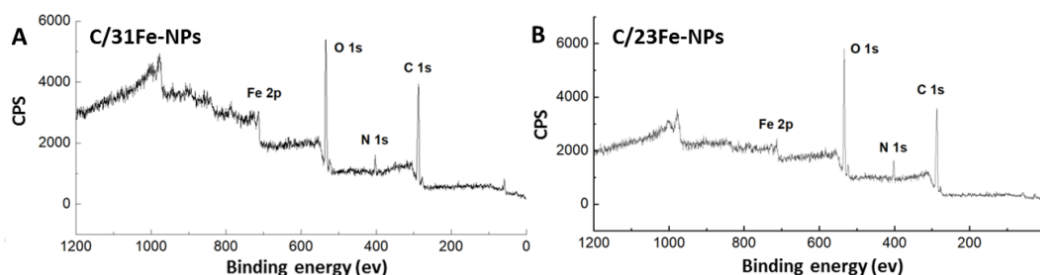
**Figure A11.** The absorption (green colour) as well as photoluminescence emission (blue colour) peak recorded at  $\lambda_{\text{ex}}=375$  nm of pure citrazinic acid fluorophore.



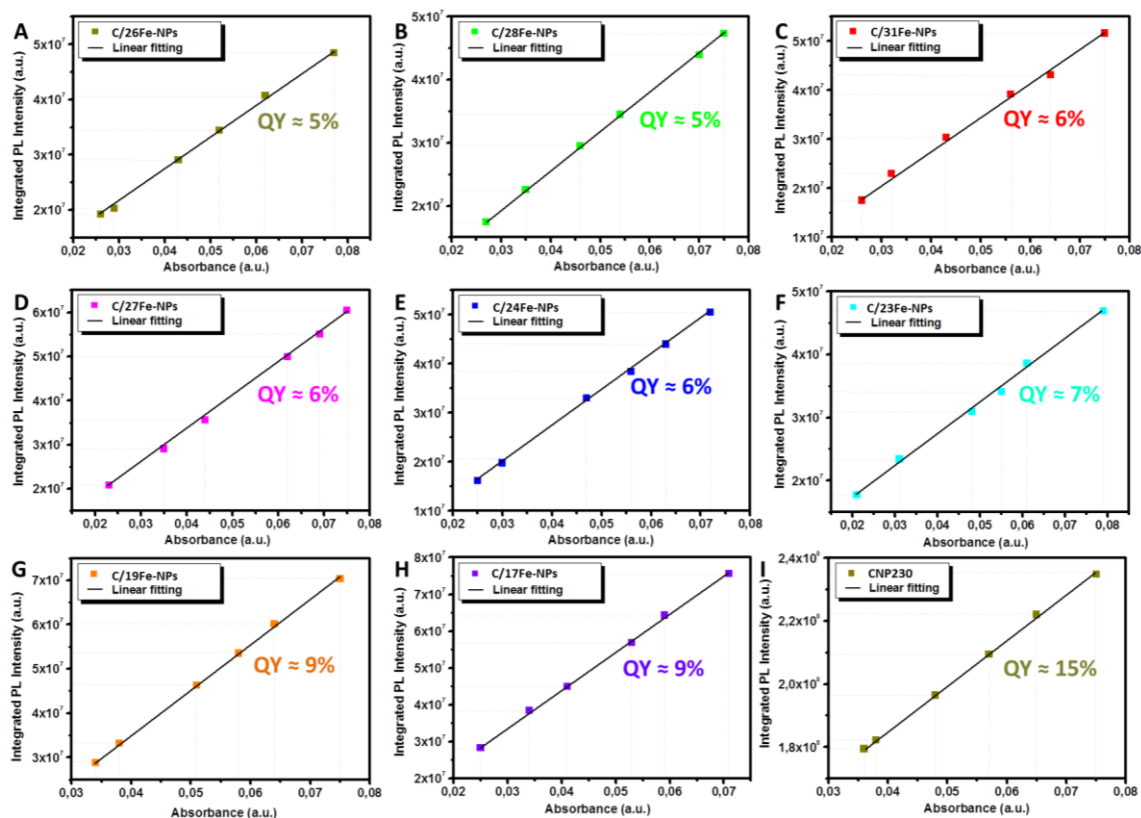
**Figure A12.** Photos showing the response of C/31Fe-NPs towards an external magnet while being dispersed in water (A), toluene (B) and air (C).



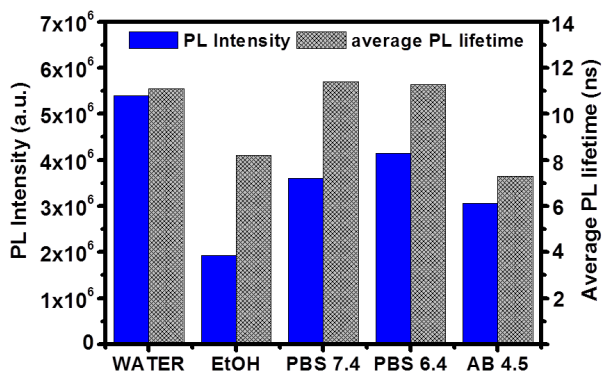
**Figure A13.** Magnetization results of 2.1 mmol (A), 1.9 mmol (B), 1.7 mmol (C) and 1.1 mmol (D) C-Fe<sub>3</sub>O<sub>4</sub> nanoparticles at temperature range of 4 K-300 K. The inset represents the enlarged area of the initial measurements.



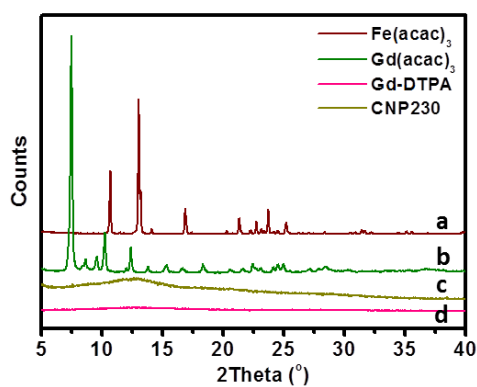
**Figure A14.** The XPS surveys of C/31Fe-NPs (A) and C/23Fe-NPs (B).



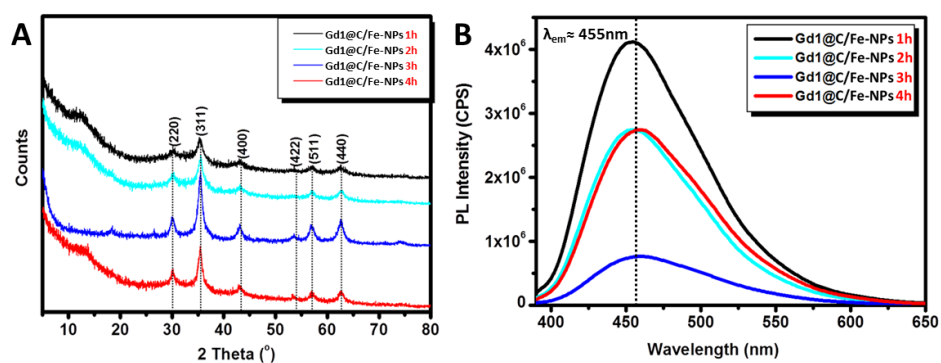
**Figure A15.** The plots of integrated PL intensity of various magnetic C-dots in water as a function of optical absorbance at 365 nm with calculated quantum yield values.



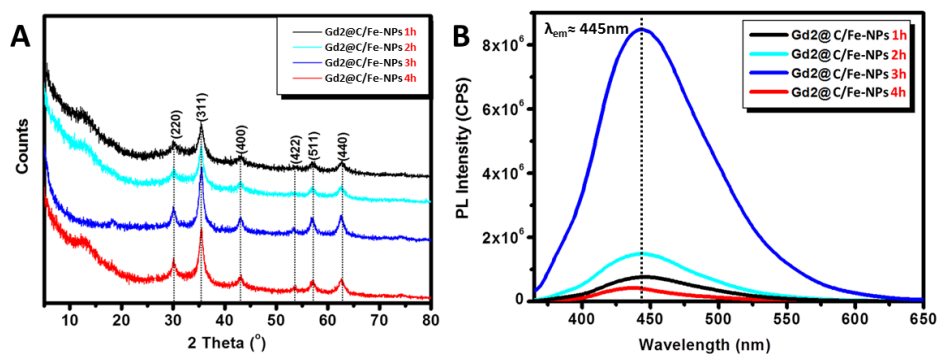
**Figure A16.** The graph presenting the effect of various solvents on the PL intensity and the average PL lifetime of C/31Fe-NPs solutions recorded at  $\lambda_{ex} = 375\text{nm}$ . The concentration of the samples was equal to 0.01 mg/mL.



**Figure A17.** The XRD patterns of CNP230 (c) together with iron-rich (a) and gadolinium-rich (a,d) precursors.



**Figure A18.** The XRD patterns (A) and PL spectra (B) of Gd1@C/Fe-NPs synthesized from 1 hour up to 4 hours. The concentration of aqueous solutions was equal to 0.01 mg/mL.



**Figure A19.** The XRD patterns (A) and PL spectra (B) of Gd2@C/Fe-NPs prepared from 1 hour up to 4 hours. The concentration of aqueous dispersions was equal to 0.01 mg/mL.